

Numerical Modeling of a Bridge System & Its Application for
Performance-Based Earthquake Engineering

HyungSuk Shin

A dissertation submitted in partial fulfillment
of the requirements for the degree of

Doctor of Philosophy

University of Washington

2007

Program Authorized to Offer Degree: Civil & Environmental Engineering

UMI Number: 3265411

INFORMATION TO USERS

The quality of this reproduction is dependent upon the quality of the copy submitted. Broken or indistinct print, colored or poor quality illustrations and photographs, print bleed-through, substandard margins, and improper alignment can adversely affect reproduction.

In the unlikely event that the author did not send a complete manuscript and there are missing pages, these will be noted. Also, if unauthorized copyright material had to be removed, a note will indicate the deletion.

UMI[®]

UMI Microform 3265411

Copyright 2007 by ProQuest Information and Learning Company.

All rights reserved. This microform edition is protected against unauthorized copying under Title 17, United States Code.

ProQuest Information and Learning Company
300 North Zeeb Road
P.O. Box 1346
Ann Arbor, MI 48106-1346

University of Washington
Graduate School

This is to certify that I have examined this copy of a doctoral dissertation by

HyungSuk Shin

and have found that it is complete and satisfactory in all respects,
and that any and all revisions required by the final
examining committee have been made.

Chair of the Supervisory Committee:



Pedro Arduino

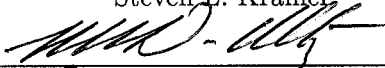
Reading Committee:



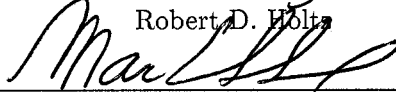
Pedro Arduino



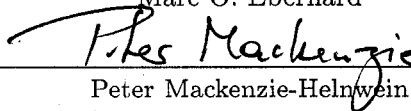
Steven L. Kramer



Robert D. Holtz



Marc O. Eberhard



Peter Mackenzie-Helnwein

Date:

April 27, 2007

In presenting this dissertation in partial fulfillment of the requirements for the doctoral degree at the University of Washington, I agree that the Library shall make its copies freely available for inspection. I further agree that extensive copying of this dissertation is allowable only for scholarly purposes, consistent with "fair use" as prescribed in the U.S. Copyright Law. Requests for copying or reproduction of this dissertation may be referred to Proquest Information and Learning, 300 North Zeeb Road, Ann Arbor, MI 48106-1346, 1-800-521-0600, or to the author.

Signature Hyunah Shi

Date 04-27-2007

University of Washington

Abstract

Numerical Modeling of a Bridge System & Its Application for Performance-Based
Earthquake Engineering

HyungSuk Shin

Chair of the Supervisory Committee:
Professor Pedro Arduino
Civil & Environmental Engineering

Many bridges have been damaged during earthquakes. The severity of the recorded damage varies from column failures and bridge deck collapse due to joint unseating to pile and abutment foundation failure due to lateral spreading. In most of these cases, soil-pile-structure interaction (SPSI) has played an important role. SPSI is affected by soil conditions (e.g., competent soil or liquefiable soil) and loading conditions (e.g., earthquake intensity, motion characteristics, and shaking orientation). In this context, two bridges with different soil and loading conditions were considered focusing on different aspects of their response. One was a two-span portion of a bridge supported by drilled-shaft foundations embedded in competent soil (dry dense sand) and subjected to shaking in the transverse direction. The other represented a typical five-span highway bridge system supported by pile group foundations embedded in liquefiable soils and subjected to shaking in the longitudinal direction.

In the first part of this research, centrifuge experimental tests and OpenSees numerical simulations were performed to understand and validate numerical modeling strategies to capture soil-pile-structure interaction of bridge structures. The study included shaking in several directions, pile embedment lengths, and various levels of nonlinearity. Sensitivity studies were conducted for a bent and a single pile to study the effect of soil motion and p - y spring parameter variation on the superstructure and pile response. For a prototype

bridge model, the soil and p - y spring models verified in the centrifuge simulation study were coupled with a reinforced concrete bridge model (Ranf 2007, Johnson et al. 2006 and Ramirez et al. 2007). Using the prototype reinforced concrete bridge model an equivalent-cantilever approach was investigated to understand appropriate fixity depths and to provide a reasonable dynamic SPSI approximation for motions with different intensity.

In the second part of this research, the PEER PBEE methodology was applied to a typical highway bridge system founded in liquefaction-susceptible soils. A comprehensive numerical model was developed for the bridge system by coupling a well-defined OpenSees bridge model (Mackie and Stojadinovic 2003) with various types of SPSI modeling components, including: pile, pile cap, and abutment structures. Using the comprehensive bridge model, the global bridge behavior and the effect of lateral spreading on the bridge were investigated. In this study, various sources of uncertainties were considered, including: earthquake motion uncertainty, model parameter uncertainty, and soil spatial variability uncertainty. Motions corresponding to four different hazards are used to evaluate record-to-record uncertainties. From this study, structural and geotechnical Engineering Demand Parameters (EDPs) related to bridge damage were identified and relative efficiencies for several Intensity Measures (IMs) were investigated. Parameters that influence the bridge performance were investigated through sensitivity analysis and Tornado diagrams. Then, First-Order Second-Moment (FOSM) analyses were performed to estimate parametric uncertainties. Gaussian stochastic random fields for clay and liquefiable soils were generated to investigate spatial variability uncertainties. Using the combined EDP uncertainties with IM hazard curves and the PEER PBEE framework, EDP hazard curves were developed for several EDPs.

TABLE OF CONTENTS

	Page
List of Figures	iv
List of Tables	xii
Chapter 1: Introduction	1
1.1 Background	1
1.2 Objectives of the Research	6
1.3 Dissertation Organization	8
Chapter 2: Seismic Soil-Pile-Structure Interaction on Bridge Structures	10
2.1 Introduction	10
2.2 Soil-Pile Interaction Modeling	10
2.3 P-y Curves	12
2.4 Pile Response to Lateral Loads	25
2.5 Pile Group Response to Lateral Loads	28
2.6 Axially Loaded Single Pile	35
2.7 SPSI and Structural Stiffness	40
2.8 Soil-Abutment-Bridge Interaction	42
2.9 Summary	43
Chapter 3: Performance Based Earthquake Engineering	46
3.1 Introduction	46
3.2 Performance Based Earthquake Engineering Methodology	46
3.3 Numerical Integration of Uncertainties in PBEE Framework	48
3.4 Selection of IMs	54
3.5 Uncertainty Integration Approximation	57
3.6 Summary	59
Chapter 4: Physical and Numerical Modeling of Bridge Structures	60
4.1 Introduction	60

4.2	Centrifuge Test Concept	61
4.3	Bridge Structure Models in Centrifuge Tests	62
4.4	Numerical Modeling of Centrifuge Tests	71
4.5	Summary	77
Chapter 5:	Dynamic Response of Two-Span Bridge and Bent Structures Embedded in Dense Sand	80
5.1	Introduction	80
5.2	Soil Response in Centrifuge Experiments and Numerical Simulations	80
5.3	Response of Two-column Bent and Single Pile Structures	89
5.4	Two-Span Bridge Response in Centrifuge Experiments and Numerical Simulations	95
5.5	Summary	105
Chapter 6:	Response of Bridge Bents with Different Pile Embedment Lengths and Shaking Orientations	110
6.1	Introduction	110
6.2	Response of Two-column Bents Subjected To Various Orientation of Shaking	110
6.3	Response of Bridge Structures with Various Pile Embedment Lengths	116
6.4	Summary	128
Chapter 7:	SPSI Approximation Using Equivalent-Cantilever Bridge Model	133
7.1	Equivalent Depth-to-Fixity Depth Approach for SPSI Simplification	134
7.2	Equivalent Depth-to-Fixity of Prototype Bridge	137
7.3	Dynamic Response of Equivalent Cantilever Bridge Model	139
7.4	Summary of Dynamic Response of Prototype and Equivalent Cantilever Bridge Model and Analytical Estimation of Fixity Depth	144
Chapter 8:	Seismic Response of A Typical Highway Bridge in Liquefiable Soil	149
8.1	Introduction	149
8.2	Target Bridge System	149
8.3	Numerical Modeling of the Target Bridge System	152
8.4	Seismic Response of Bridge System and Engineering Demand Parameters	162
8.5	Summary and Conclusions	180
Chapter 9:	Application of PBEE to A Typical Highway Bridge in Liquefiable Soil	187
9.1	Introduction	187

9.2	Input Motions and Intensity Measures	188
9.3	EDPs of Bridge System	193
9.4	Uncertainties in EDP Estimation	195
9.5	Record-to-record Uncertainty	199
9.6	Model Parameter Uncertainty	199
9.7	Spatial Variability Uncertainty of Soil	212
9.8	EDP Hazard Curves	217
9.9	Summary and Conclusions	228
Chapter 10: Summary, Conclusions and Recommendations for Future Research . .		231
10.1	Introduction	231
10.2	Summary and Conclusions	232
10.3	Recommendations for Future Research	241
Bibliography		244
Appendix A: Sensitivity of Two-Column Bent and Single Pile Structures		252

LIST OF FIGURES

Figure Number	Page
1.1 Bridge failures in recent earthquakes	2
1.2 Bridge failures in recent earthquakes	3
2.1 Static and dynamic Beam-on-Nonlinear-Winkler-Foundation (BNWF) model	11
2.2 Back-calculated $p-y$ curves for sand from field tests - after Reese et al. (1975)	14
2.3 Back-calculated $p-y$ curves for stiff clay from field test - after Reese et al. (1974)	15
2.4 Cyclic response of a rigid pile in soft clay - after Matlock (1970)	15
2.5 Comparison of ultimate soil resistance of soft clay (Matlock 1971) and sand (Reese et al. 1974)	19
2.6 Suggested ultimate soil resistance for cohesionless soil	19
2.7 Back-calculated $p-y$ behavior during shaking - after Wilson et al. 2000	21
2.8 Relationship between residual strength and corrected SPT resistance (Seed and Harder, 1990)	23
2.9 Pile foundation failure of Yachiyo bridge due to kinematic loading - after Hamada (1992)	27
2.10 Schematic of pile alignment in a group	29
2.11 Design line for p -multipliers - after Mokwa (1999)	30
2.12 Schematic of rotational soil resistance due to pile cap rotation	31
2.13 Pile group load test results and calculated results for fixed pile cap and free pile head - after Mokwa (1999)	32
2.14 Illustration of axial load transfer in a pile - after Vijayvergiya (1997)	36
2.15 Typical load-movement characteristics of an axially loaded pile - after Vijayvergiya (1997)	37
2.16 Normalized $t-z$ (or $f-z$) curve for clay and sand - after Vijayvergiya (1997)	38
2.17 Normalized $q-z$ curve for sand and clay - after Vijayvergiya (1997)	40
2.18 Lateral stiffness of column with and without rotational restraint at the top	41
2.19 Schematic of seat-type abutment structure components and bridge deck-abutment-soil interaction	44

2.20	Simplified abutment load-deflection characteristic using initial stiffness and ultimate resistance in Caltrans' guideline - after SDC (2004)	45
3.1	Schematic IM hazard curve from PSHA	49
3.2	Construction of fragility curves from IM-EDP correlations (demand model) .	51
3.3	Construction of EDP hazard curve from IM hazard curve and fragility curves	52
3.4	Schematic illustration of sufficiency in IMs	55
3.5	Schematic illustration of IM efficiency	56
3.6	Schematic illustration of demand models according to various schemes of ground motion selection	58
4.1	Schematic drawing and test setup of CFG1	63
4.2	Schematic drawing and test setup of CFG2	64
4.3	Schematic drawing and test setup of CFG3	65
4.4	Structural embedment lengths and clear heights	66
4.5	Recorded centrifuge base motions	70
4.6	Convention used for local translation and rotation in the superstructure . . .	71
4.7	Modeling of soil-pile-structure interaction in a single pile using p - y , t - z , and Q - z springs	74
4.8	Material models for soil, interface springs and pile in OpenSees	75
4.9	Modeling of two-column bents (Bent-L, Bent-M, Bent-S, Bent-LL-Hy, Bent-SS-Hy)	76
4.10	Modeling of oriented two-column bents (Bent-00, Bent-30, Bent-60, and Bent-90)	78
4.11	Modeling of Bent-LS-Hy and Bent-LS-Lt	78
4.12	Modeling of a two-span bridge with different bent clear column heights and rotational mode	79
5.1	Shear wave velocity profile for soil in centrifuge container and in OpenSees soil model	82
5.2	Free-field accelerometer array in CFG3 test (prototype scale)	82
5.3	Mode shapes for two-dimensional soil model container (based on the initial soil stiffness before shaking)	84
5.4	Mode shapes for one-dimensional soil column model (based on the initial soil stiffness before shaking)	84
5.5	Transfer function between soil (2.6 m) and base in CFG3 and 2-D soil model simulation: frequency sweeping motion, $a_{max} = 0.25g$	85
5.6	Transfer function between soil (2.6 m) and base in CFG3 and 1-D soil model simulation: frequency sweeping motion, $a_{max} = 0.25g$	86

5.7	Soil response spectra corresponding to soil motion recorded in CFG3 at 2.78m depth and from simulations (1-D shear beam soil model and 2-D container soil model)	87
5.8	Recorded and simulated free-field array acceleration time histories in CFG3 soil: Northridge motion, $a_{max} = 0.25g$	88
5.9	Superstructure acceleration time histories for Bent-M2 obtained from centrifuge test and numerical simulations (CFG1)	90
5.10	Superstructure acceleration response spectra for Bent-M2 obtained from centrifuge test and numerical simulations (CFG1)	91
5.11	Maximum pile bending moments for Bent-M2 obtained from centrifuge test and numerical simulations (CFG1)	91
5.12	Superstructure acceleration time histories for sPile-1 obtained from centrifuge test and numerical simulation (CFG1)	92
5.13	Superstructures acceleration response spectra for sPile-1 obtained from centrifuge test and numerical simulations (CFG1)	92
5.14	Maximum pile bending moments for sPile-1 obtained from centrifuge test and numerical simulations (CFG1)	93
5.15	Nonlinear response of superstructure and soil at 2.6m obtained from centrifuge tests and numerical simulations	94
5.16	Consistency (repeatability) of centrifuge tests (Bent-M2 in CFG1 and Bent-00 in CFG2) - Northridge events	96
5.17	Superstructure response in Bent-90 and sPile-2 in CFG2 - Northridge events	97
5.18	Bending moment of a bent and a single pile structure with no superstructure inertial mass in OpenSees (Northridge 0.75g)	97
5.19	Acceleration response spectra of superstructure response before and after bridge deck connection for Northridge motion, $a_{max} = 0.10g$	99
5.20	Response of superstructure, and pile and soil at 2.6m depth in centrifuge test (CFG1) for Northridge motion events ($a_{max} = 0.25g$ and $0.79g$)	100
5.21	Centrifuge and OpenSees bridge deck acceleration time histories at three bent locations for Northridge event, $a_{max} = 0.25g$	102
5.22	Centrifuge and OpenSees bridge deck acceleration time histories at three bent locations for Northridge event, $a_{max} = 0.74g$	102
5.23	Centrifuge and OpenSees bridge superstructure response and pile bending moments for Northridge event, $a_{max} = 0.25g$	103
5.24	Centrifuge and OpenSees maximum bending moments below ground surface and the corresponding depths for a two-span bridge subjected to Northridge events with different intensities; $a_{max} = 0.08g, 0.25g, 0.60g,$ and $0.77g$	104

5.25	Centrifuge and OpenSees maximum soil resistance: Northridge events, $a_{max}=0.25g$, $0.60g$, and $0.77g$: the centrifuge back-calculated soil resistance data was provided by Ilankatharan (Ilankatharan et al., 2006)	105
6.1	Centrifuge and OpenSees acceleration response spectra at bent top in bridge transverse and longitudinal direction - Northridge event, $a_{max}=0.25g$	112
6.2	Centrifuge and OpenSees maximum pile bending moment envelopes (M_{xx} and M_{yy}) and maximum principal bending moments ($\sqrt{M_{xx}^2 + M_{yy}^2}$) in oriented bents - Northridge event, $a_{max}=0.25g$	113
6.3	Bent orientation effect on recorded and simulated peak horizontal acceleration at the bent top in two local directions - Northridge event, $a_{max}=0.08g$, $0.25g$, $0.60g$, and $0.77g$	114
6.4	Rotation response of oriented bent superstructure - Northridge event, $a_{max}=0.77g$	115
6.5	Comparison of superstructure acceleration time histories for Bent-LL-Hy (pile embedment length = 12.0 D) and Bent-SS-Hy (pile embedment length = 5.0D) in centrifuge test	118
6.6	Comparison of superstructure response spectra for Bent-LL-Hy (pile embedment length = 12.0 D) and Bent-SS-Hy (pile embedment length = 5.0D) in centrifuge test	118
6.7	Centrifuge and OpenSees superstructure acceleration response for Bent-LL-Hy and Bent-SS-Hy subjected to Northridge motion, $a_{max} = 0.25g$	119
6.8	Centrifuge and OpenSees superstructure acceleration response for Bent-LL-Hy and Bent-SS-Hy subjected to sweeping motion, $a_{max}=0.41g$	120
6.9	Centrifuge and OpenSees bending moments for Bent-LL-Hy (embedment length = 12.0D)	121
6.10	Centrifuge and OpenSees bending moments for Bent-SS-Hy (embedment length = 5.0D)	121
6.11	Structure response spectra for three single piles subjected to Northridge events ($a_{max} = 0.04g$, $0.25g$, and $0.74g$) and frequency sweeping event ($a_{max} = 0.41g$): pile embedment lengths = 12.0D, 7.5D, and 5.0D. For the moderate Northridge motion ($a_{max} = 0.25g$), sPile-S superstructure response data could not be measured appropriately due to instrumentation malfunction. . .	123
6.12	Centrifuge and OpenSees superstructure acceleration time histories for three single pile structures (embedment lengths = 12.0 D, 7.5 D, and 5.0 D) subjected to Northridge motion event, $a_{max} = 0.74g$	124
6.13	Centrifuge and OpenSees superstructure acceleration response spectra for three single pile structures (embedment lengths = 12.0 D, 7.5 D, and 5.0 D) subjected to Northridge motion event, $a_{max} = 0.74g$	125

6.14	Centrifuge and OpenSees maximum bending moments for sPile-L (embed- ment length = 12.0D) subjected to varying intensity motions	125
6.15	Comparison of centrifuge superstructure response spectra for Bent-LS-Hy and Bent-LS-Lt (with different pile embedment lengths = 12.0D and 5.0D) in CFG3	127
6.16	Comparison between centrifuge and OpenSees superstructure acceleration response for LS-Hy subjected to sweeping motion, $a_{max}=0.41g$	129
6.17	Comparison between centrifuge and OpenSees superstructure acceleration response for Bent-LS-Lt subjected to sweeping motion, $a_{max}=0.41g$	130
6.18	Comparison between centrifuge and OpenSees maximum bending moments for Bent-LS-Hy (embedment lengths = 12.0 D and 5.0 D) subjected to varying intensity motions	131
6.19	Comparison between centrifuge and OpenSees maximum bending moments for Bent-LS-Lt (embedment lengths = 12.0 D and 5.0 D) subjected to varying intensity motions	131
7.1	Representation of soil-pile system by equivalent fixed-based cantilever (after Chai 2002)	135
7.2	Prototype bridge shear force and bending moment distributions in Bent-S at different times during shaking (Coyote Lake 1979, Gilroy #6, $a_{max} = 0.167g$)	138
7.3	Locations of pile bending moments for different intensity shaking: small shak- ing = Coyote Lake 1979, Gilroy #6 ($a_{max} = 0.167g$) and strong shaking = Loma Prieta 1989, Gilroy Historic ($a_{max} = 0.691g$)	141
7.4	Maximum shear force on prototype and fixed bridge models (I-880 four haz- ards, 40 motions)	143
7.5	Time histories of bending moment and shear force at column top (Bent-S): small shaking = Coyote Lake 1979, Gilroy #6 ($a_{max} = 0.167g$) and strong shaking = Loma Prieta 1989, Gilroy Historic ($a_{max} = 0.691g$)	145
7.6	Time histories of displacement relative to base (Bent-S): small shaking = Coyote Lake 1979, Gilroy #6 ($a_{max} = 0.167g$) and strong shaking = Loma Prieta 1989, Gilroy Historic ($a_{max} = 0.691g$)	146
7.7	Bending moment and shear force at column top (Bent-S): small shaking = Coyote Lake 1979, Gilroy #6 ($a_{max} = 0.167g$) and strong shaking = Loma Prieta 1989, Gilroy Historic ($a_{max} = 0.691g$)	147
7.8	Time histories displacement relative to base (Bent-S): small shaking = Coyote Lake 1979, Gilroy #6 ($a_{max} = 0.167g$) and strong shaking = Loma Prieta 1989, Gilroy Historic ($a_{max} = 0.691g$)	148
8.1	Target Bridge System (dimensions in meters)	150
8.2	Structure configuration	150

8.3	Layer definition and identification	152
8.4	SPT profiles of loose sand layer below both embankments	153
8.5	Variation of undrained shear strength of clay layer across bridge	154
8.6	Recommended loose sand material parameters in OpenSees and interpolations	156
8.7	Modeling of soil-structure interaction in OpenSees	158
8.8	p - y spring parameters: ultimate lateral resistance (p_{ult})	161
8.9	p - y spring parameters: y_{50}	162
8.10	Modeling of bridge deck-abutment-soil interaction in OpenSees	163
8.11	Horizontal and vertical displacements of bridge and pore water pressure ratio in soil (after earthquake) - Northridge 1994, $a_{max} = 0.25g$: Magnification factor = 20	165
8.12	Horizontal and vertical displacements of bridge and pore water pressure ratio in soil (after earthquake) - Erzincan, Turkey 1992, $a_{max} = 0.70g$: Magnifica- tion factor = 20	166
8.13	Time histories of of shear strain profile below left and right abutment - Northridge 1994, $a_{max} = 0.25g$	167
8.14	Time histories of shear strain profile below left and right abutment - Erzincan, Turkey 1992, $a_{max} = 0.70g$	167
8.15	Permanent soil displacement profiles at pile foundation and slope toe loca- tions for 10 motions	168
8.16	Pore pressure ratio time histories in liquefiable soil	169
8.17	Spatial and temporal variation of pore pressure profile below right abutment in liquefiable soil - Northridge 1994, $a_{max} = 0.25g$	170
8.18	Effect of soil element out-of-plane thickness on slope toe and pile cap lateral displacement - Erzincan, Turkey 1992, $a_{max} = 0.70g$	171
8.19	Schematic drawing of 3-D embankment deformation	172
8.20	Displacement of each bridge column at top and bottom and drift ratios (col- umn height = 6.7m) - Erzincan motion, Turkey 1992, $a_{max} = 0.70g$	174
8.21	Acceleration time histories and response spectra at soil base and pile cap - Northridge motion 1994, $a_{max} = 0.25g$	175
8.22	Abutment and bridge deck movements	177
8.23	Bridge deck and abutment interaction force-displacement - Erzincan motion, Turkey 1992, $a_{max} = 0.70g$	178
8.24	Location of maximum pile bending moment in Pile 0 at the left abutment . .	180
8.25	Location of maximum pile curvatures in Pile 4 and Pile 5 at the right abutment	181
8.26	Maximum pile bending moments and lateral soil resistance during earthquake - Erzincan motion, Turkey, $a_{max} = 0.70g$	182

8.27	<i>p-y</i> time histories during earthquake excitation - Erzincan motion, Turkey, $a_{max} = 0.70g$	183
8.28	<i>p-y</i> curves during earthquake excitation - Erzincan motion, Turkey, $a_{max} = 0.70g$	184
8.29	Pile cap resistance curves - Erzincan motion, Turkey, $a_{max} = 0.70g$	185
9.1	Example of an input motion used in the comprehensive bridge study (Erzincan, Turkey 1992, $a_{max} = 0.70g$)	189
9.2	PGA hazard curve used in OpenSees simulations	190
9.3	IM hazard curves	194
9.4	Correlation between lateral pile cap displacement and curvature from simulations for Northridge 1994, 0.2557g; unit of curvature = 1/m	196
9.5	Components of total uncertainty in EDP estimation	198
9.6	EDP-IM relationships for right abutment slope residual vertical settlement	200
9.7	EDP-IM relationships for Pier 4 maximum drift	201
9.8	IM Efficiency	202
9.9	Tornado diagrams for four maximum EDPs: Temblor 1966 motion at Parkfield ($a_{max} = 0.47g$)	208
9.10	Gradient of a response over variation of a input parameter ($\frac{\partial g}{\partial X_i}$)	212
9.11	Inherent soil variability - after Phoon and Kulhawy (1999)	213
9.12	Illustration of autocorrelation effect on residual variation - after Baecher and Christian (2003)	214
9.13	Example of generated Gaussian fields	216
9.14	Stochastic friction angle field in loose sand layer	218
9.15	EDP hazard curves for maximum Pier 4 drift and residual Pile Cap 4 lateral displacement	226
9.16	Effect of IM efficiency on EDP hazard curves	229
A.1	<i>p-y</i> spring parameter regions for sensitivity study	255
A.2	Effect of soil motion on bent response - Northridge motion, $a_{max} = 0.25g$	257
A.3	Effect of soil motion on single pile response - Northridge motion, $a_{max} = 0.25g$	258
A.4	Effect of soil motion on bent response - Sweeping motion, PGA = 0.50g	260
A.5	Effect of soil motion on single pile response - Sweeping motion, PGA = 0.50g	261
A.6	Simple estimation of natural periods of bent and single pile structures	262
A.7	Natural period variation of single pile structure during shaking (eigenvalue analysis results)	263
A.8	Effect of p_{ult} change (p_{ult}) in greater-than-3D depth on bent superstructure response - Northridge motion, $a_{max} = 0.25g$	264

A.9 Schematic drawing of Change of initial stiffness in p - y curve due to change of y_{50} and p_{ult}	265
A.10 Effect of p - y spring stiffness (y_{50}) - bent; Northridge motion ($a_{max} = 0.25g$)	266
A.11 Effect of p - y spring stiffness (y_{50}) - single pile; Northridge motion ($a_{max} = 0.25g$)	267
A.12 Effect of p - y spring stiffness (y_{50}) - bent; Sweeping motion (PGA = 0.50g) .	268
A.13 Effect of p - y spring stiffness (y_{50}) - single pile; Sweeping motion (PGA = 0.50g)	269
A.14 Effect of p - y spring ultimate soil resistance (p_{ult}) - bent; Northridge motion ($a_{max} = 0.25g$)	270
A.15 Effect of p - y spring ultimate soil resistance (p_{ult}) - single pile; Northridge motion ($a_{max} = 0.25g$)	271
A.16 Effect of p - y spring ultimate soil resistance (p_{ult}) - bent; Sweeping motion (PGA = 0.50g)	272
A.17 Effect of p - y spring ultimate soil resistance (p_{ult}) - single pile; Sweeping motion (PGA = 0.50g)	273

LIST OF TABLES

Table Number	Page
2.1 Representative values of ε_{50} for normally consolidated clays - Peck et al. (1974) - after Reese and Van Impe (2001)	16
2.2 Representative values of ε_{50} for overconsolidated clays - after Reese and Van Impe (2001)	16
2.3 Representative values of k_{py} for sand - after Reese and Van Impe (2001)	17
2.4 Recommended <i>p-multipliers</i> for pseudo-static analysis - after Brandenberg (2005)	25
2.5 Typical values of the soil adhesion factor, α - after NAVFAC (1982)	34
2.6 Recommended parameters for Cohesionless Siliceous Soil - after API (1993)	38
4.1 Scaling relationships for centrifuge modeling - after Wood (2004)	61
4.2 Aluminum type in structures	68
4.3 Summary of centrifuge test and simulations	72
7.1 Equivalent depth-to-fixity and depth-to-maximum-moment of prototype bridge based on Chai(2002)'s method	139
8.1 Soil types and properties	151
8.2 SPT profiles below embankments	153
8.3 Summary of PDMY material parameter values used for cohesionless soil	157
8.4 Summary of PIMY material parameter values used for cohesive soil	158
9.1 Magnitude-corrected <i>PGA</i>	190
9.2 I-880 Input motion characteristics (four hazards)	191
9.3 Intensity Measures	192
9.4 IM hazard curve coefficients for I-880 input motions	193
9.5 EDP list	197
9.6 Summary of EDP median coefficients and record-to-record uncertainty for power-law median response model, $EDP = a IM^b$	203
9.7 Input Parameter Uncertainties	205
9.8 Coefficient of correlation for the input parameters	210
9.9 Summary of parametric uncertainty	211

9.10	Summary of spatial variability uncertainty (loose sand + clay)	219
9.11	Summary of spatial variability uncertainty (loose sand)	220
9.12	Summary of spatial variability uncertainty (clay)	221
9.13	Summary of total EDP uncertainty - percentage is calculated by the ratio of individual uncertainty to total uncertainty	223
9.14	Summary of EDP hazard curve: exponential coefficients	225
9.15	Summary of EDP at different return periods	227
A.1	Structures, motions, and base variable values used in sensitivity study	254
A.2	Sensitivity study variables	255
A.3	Ratio of Near-Surface Soil Resistance to Maximum Inertial Force, R_{rs}	274

ACKNOWLEDGMENTS

I would like to appreciate Dr. Pedro Arduino for his valuable guidance and tremendous supports throughout this research as well as his advices and encouragements. I would like to thank my reading committee members for their reviewing and advices, especially Dr. Steven Kramer who was involved in the same research projects and provided helpful guidance, comments and suggestions.

I am grateful for the financial support from the Pacific Earthquake Research Center (PEER) and George E. Brown, Jr. Network for Earthquake Engineering Simulation (NEES).

Most of this research could not be completed without many collaborative efforts and helps from other researchers. Mahadevan Illankatharan and Dr. Bruce Kutter at University of California, Davis worked together for centrifuge tests and shared great ideas and helps. Dr. Tyler Ranf and Dr. Marc Eberhard at University of Washington provided a calibrated bridge structure model. Dr. Kevin Mackie at University of Central Florida provided a typical highway bridge model for PBEE research. The PBEE study was also possible and improved by the work with PEER geotechnical research team (Dr. Ross Boulanger at University of California, Davis, Christian Ledzma and Dr. Jonathan Bray at University of California, Berkeley, Azadeh Bozorgnadeh and Dr. Scott Ashford at University of California, San Diego, and other many researchers). I would like to thank all of them. I would like to make a special thank Dr. Mackenzie-Helnwein for allowing to use the Center for Computational Biomechanics so that tremendous amount of computation time could be reduced.

I would like to acknowledge my family, friends, and colleagues for their supports, encouragements and friendships. Finally, I would like to deeply thank Wookeun Shin and my officemate, Roy MayField, for their precious encouragements and friendships.

DEDICATION

To my wife, Seung Hee

Chapter 1

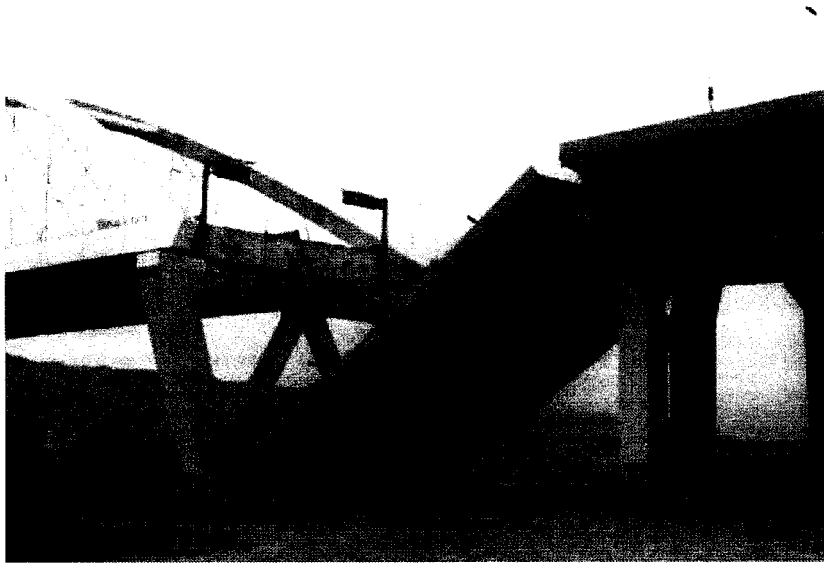
INTRODUCTION

1.1 Background

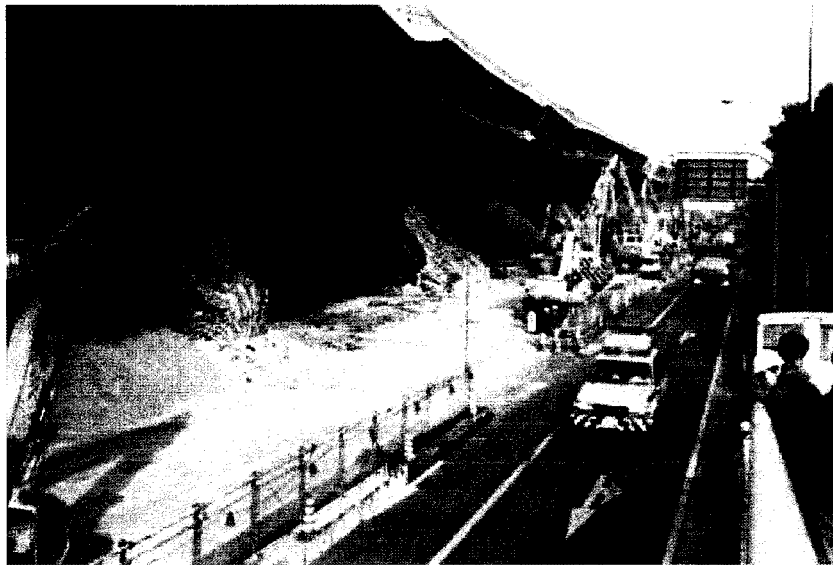
Many bridges are subject to damage and failure due to earthquake excitations. Figures 1.1 and 1.2 show examples of situations where this damage has resulted in loss of lives and significant economic losses. The pattern and severity of damage to a particular bridge can vary depending on bridge structure type and supporting system, including foundation and ground conditions. The response of soils beneath and adjacent to bridge sites can play an important role in the level of damage sustained by the bridge. For example, large relative span movements in the longitudinal direction can cause joint unseating and collapse. These relative displacements increase with out-of-phase bridge column movement and rotation of skewed bridge spans. Excessive bridge displacements, such as in viaducts, can lead to pounding with adjacent structures and cause impact damage. Bridge damage can also result from column failure due to lack of flexural ductility, or column shear failure, showing plastic hinges or shear cracking. This damage may become severe when a pile foundation fails due to liquefaction or lateral spreading, thereby causing a loss of support or extensive lateral loading on piles, bridge columns, and abutments.

The performance of a bridge system due to seismic excitations may be influenced by the interaction with its supporting system. When earthquake energy propagates through the soil, the foundation shaking induces inertial forces in the superstructure which, in turn, influence the foundation response. This soil-pile-structure interaction (SPSI) effect changes the actual input motion at the supports and can significantly affect the response of the bridge.

Although many research studies on SPSI have been done over several decades, the full



(a) Unseating of bridge span, Nishinomiya-ki bridge, Kobe earthquake 1995



(b) Column failure of the Hanshin expressway, Kobe earthquake 1995

Figure 1.1: Bridge failures in recent earthquakes



(a) Abutment failure at Rio Banano bridge, Costa Rica earthquake 1990



(b) Loss of support due to liquefaction, Rio Viscaya bridge, Costa Rica earthquake 1990

Figure 1.2: Bridge failures in recent earthquakes

extent of the interaction mechanisms are not fully understood; particularly when the bridge, foundation, and/or soil exhibit nonlinear response. Nonlinear response is particularly likely to occur for the strong ground motions that bridges are designed to resist, and even more likely when liquefiable soils are present.

This lack of understanding often leads to a significant level of conservatism and simplification in design and analysis. In many cases, foundations are strategically designed to remain elastic by adding a large amount of excess strength - this conservative approach avoids the difficulty of post-earthquake inspection and high repair costs (Chai, 2002), but, adds to design and construction costs. In other cases, structural engineers use simple foundation springs or simplified lateral supporting systems to consider SPSI in their analysis. In general, these simplifications are not sufficient and/or appropriate to obtain an accurate estimate of the structural response and performance, especially when highly nonlinear soil behavior is expected.

As mentioned above, SPSI involves the interaction among three bridge system components: the structure, the pile foundation, and the surrounding soil. Understanding of the interaction effects between these components have often been achieved with partial completeness in structural laboratory tests without realistic foundation systems, or from pile loading tests in the field without realistic earthquake loading or superstructure interaction. Thus, inclusion of all three components with realistic earthquake loading in experiments and numerical analysis is necessary to understand, not only each interaction component, but also the global system response. For this reason, centrifuge testing has been one of the preferred physical modeling techniques, especially for SPSI problems, since various input motions can be applied to full configuration of structures embedded in different soil conditions.

Modeling of soil-pile interaction in bridges is complicated mainly due to the slenderness of typical pile configurations and the nonlinear behavior of the surrounding soils. Rigorous numerical simulations of the interaction problem require three-dimensional (3-D) dynamic finite element models (FEM) capable of accurately representing the nonlinear, inelastic behavior of both soils and structural materials. However, 3-D simulations are still computationally expensive and require the use of advanced constitutive models and robust interface

contact elements between the soil and pile. As an alternative, Winkler foundation spring models have been widely used in practice. Even using the simplified Winkler approach, the structural modeling of an entire bridge/foundation/soil system is not a simple task since it still requires good 2-D or 3-D nonlinear structural models, as well as soil models capable of representing the soil behavior, including liquefaction and/or large strain effects accurately. Additional problems arise in coupling all the required components (i.e., soil, pile, and structure) in an analysis. This is particularly important in cases where the structure is not oriented to the primary axis of earthquake shaking, when nonuniform pile lengths are used, or where highly nonlinear response such as that produced by liquefaction or lateral spreading is expected.

Moreover, in current seismic design and assessment, instead of looking for a binary decision (i.e., safe or unsafe), the performance of the structural and geotechnical system becomes more meaningful, particularly to owners or other stakeholders when it can be expressed in terms of a continuous measure of performance. Reliable estimation of performance depends on using well-defined structural/geotechnical models that can account for soil-pile-structure interaction effects, as well as, uncertainties in earthquake motions and soil properties. These requirements lead to extensive numerical exercises based on advanced analytical tools and probabilistic methods. In this context, the Pacific Earthquake Engineering Research Center (PEER) has developed a probabilistic framework and analytical tool (OpenSees) that provides the necessary means for performance-based evaluation. This framework is capable of describing both physical damage and earthquake losses considering a wide range of ground motion hazards and soil-structure response levels. It thereby provides a more complete and consistent picture of bridge performance than the procedures upon which current bridge design is based.

In PBEE methodologies, which usually involve the evaluation of seismic hazards and economic losses, the characterization of uncertainties in each of a series of interim steps is important since they all influence the final results. In particular, the uncertainties in the relationship between ground motions and bridge response depend on the manner in which the ground motion is defined and the accuracy with which the response can be computed for a given measure of ground motion intensity. Reducing uncertainty in these quantities leads

to smaller uncertainties associated with earthquake motion and more economic designs. The PBEE evaluation should include several sources of uncertainties including earthquake motion uncertainties, model parameter uncertainties, spatial variability uncertainties, and analysis model uncertainties.

Mackie and Stojadinovic (2003) performed PBEE analyses for typical highway bridges founded on good soil conditions and demonstrated the application of the PEER PBEE methodology to bridges including important aspects of bridge behavior. However, for performance estimation of a bridge system with realistic soil conditions, including liquefaction-susceptible soils, appropriate modeling of soil-pile-structure interaction and soil-abutment-bridge interaction under lateral spreading is needed to accurately estimate the bridge response and to capture realistic force boundary conditions at the pier base and bridge deck ends. This could lead to the identification of global damage mechanisms, which would not be captured by the simplified analyses commonly used in contemporary practice design.

1.2 Objectives of the Research

In this context, this dissertation aims to develop an improved understanding of soil-pile-structure interaction (SPSI) in bridge structures for more accurate estimation of bridge performance. A secondary goal is to validate approximate methods for SPSI by calibrating its parameters against data obtained from a series of high-quality centrifuge tests. The final objective is to estimate bridge performance hazards considering several sources of uncertainties using the PBEE framework developed by the Pacific Earthquake Engineering Research (PEER) center.

To achieve these goals, two bridges with different soil conditions and loading conditions were considered focusing on different aspects of their response. The first bridge was a two-span portion of a bridge supported by drilled shaft foundations embedded in competent soil (dry dense sand) and subjected to shaking in the transverse direction. The second bridge represented a typical five-span highway bridge system supported by pile group foundations embedded in liquefiable soils and subjected to longitudinal shaking.

For the first bridge study, several centrifuge experimental tests and numerical simulations using the OpenSees finite element program were performed to understand and validate the

modeling of soil-pile-structure interaction of bridge structures. For the second bridge study, SPSI mechanisms of the bridge structure subjected to lateral spreading were investigated and the PEER PBEE methodology was applied considering various sources of uncertainties from earthquake motions, model parameters, and soil spatial variability. Details of the tasks required to complete each objective are summarized below.

1.2.1 Study of a Bridge in a Good Condition of Soil

A bridge founded in dry sand would normally be thought of as being relatively straightforward to design (in the case of a new bridge) or evaluate (in the case of an existing bridge). Nevertheless, the experimental and analytical investigation of a bridge founded in such desirable soil conditions can help identify and understand the basic mechanisms of soil-pile interaction and their effects on structural response. The main elements included in this study are:

1. Investigation of the behavior of the two-span bridge and several bent structures to various levels of earthquake motion. The investigation considered several complicated conditions that can be encountered in a bridge structure, by performing centrifuge tests and numerical simulations using the OpenSees finite element platform.
2. Validation of dynamic Beam-on-Nonlinear-Winkler-Foundation (BNWF) models based on conventional p - y springs for typical earthquake scenarios using the results obtained from centrifuge experiments and numerical simulations.
3. Evaluation of p - y spring parameter sensitivities on the response of bent structures to improve the confidence on the use of p - y springs using the verified numerical model.
4. Investigation of an *Equivalent-depth-of-fixity* method to provide a reasonable SPSI approximation and to understand the effect of motion intensity on the appropriate fixity-depth using a calibrated reinforced concrete bridge model (Ranf, 2007).

1.2.2 Study of a Bridge Subjected to Lateral Spreading

Because bridges are often constructed to cross bodies of water, they are frequently located in areas susceptible to soil liquefaction. Reliable design/evaluation of such bridges requires that the complicated effects of liquefaction be considered. Liquefaction affects many aspects of the seismic performance of bridges - it affects earthquake ground motions, it affects soil-pile interaction, and it introduces damage mechanisms that would not otherwise exist. Evaluation of the performance of a bridge on liquefiable soil provides an even more rigorous set of conditions under which to evaluate performance, and allows evaluation of the additional level of damage associated with liquefaction. The main elements included in this study are:

1. Development of a comprehensive numerical model of a complete bridge system in liquefaction-susceptible soil, including various SPSI modeling strategies for several bridge components such as pile groups and abutment structures. This model was intended to capture appropriate local and global bridge behavior and bridge damage mechanisms.
2. Use of the bridge model to obtain various sources of uncertainties from earthquake motions, model parameters, and spatial variability in bridge performance estimation considering a range of near-fault motions.
3. Identification of efficient Intensity Measures (IMs) as measures of bridge response in order to reduce the record-to-record uncertainty.
4. Integration of all bridge performance results and uncertainties with seismic hazard in a PBEE framework to evaluate the bridge performance hazard.

1.3 Dissertation Organization

Chapter 2 presents a review on p - y curves for different soils, the effects of liquefaction and lateral spreading on soil-pile interaction, and of factors that influence pile response.

The chapter also describes the response of pile groups with pile cap and abutment-soil interaction. A brief introduction to t - z and q - z curves is also included.

Chapter 3 reviews the PBEE methodology developed by the Pacific Earthquake Engineering Research (PEER) Center, considerations for ground motion selection, and numerical integration of uncertainties in the PBEE framework.

Chapter 4 describes the series of centrifuge tests performed for several bridge structures and their numerical modeling using OpenSees.

Chapter 5 presents centrifuge experimental test results and their corresponding numerical simulations for a two-span bridge, a two-column bent, and single pile structures.

Chapter 6 presents centrifuge experimental test results and their corresponding numerical simulations for a variety of structures including bents subjected to different orientations of shaking, and bents and single pile structures with different pile embedment lengths.

Chapter 7 describes an investigation on the equivalent fixity-depth that provides reasonable estimate of SPSI. These analyses were based on the simulation of a prototype bridge, which included the soil and p - y spring model verified in the centrifuge test and a calibrated reinforced bridge model.

Chapter 8 describes a target bridge system on liquefiable soil and its numerical modeling in OpenSees. The global and local response of the bridge system is presented in detail.

Chapter 9 describes a PBEE evaluation of a bridge system on liquefiable soil subjected to ground motions corresponding to four hazard levels. A variety of factors contributing to uncertainties in ground motions and bridge response are investigated and described. By combining these uncertainties and including the seismic hazard in the PEER PBEE framework, EDP hazard curves were developed for several bridge EDPs.

Chapter 10 presents a summary and conclusions of this research and recommendations for future research.

Appendix A presents results of a sensitivity study on p - y spring parameters for bents and single pile structures.

Chapter 2

SEISMIC SOIL-PILE-STRUCTURE INTERACTION ON BRIDGE STRUCTURES**2.1 Introduction**

Typical bridges consist of the bridge structure, pile/drilled shafts or spread footing foundations, abutment structures, and the supporting soil. During earthquakes, the individual components interact with each other and affect the global response of the bridge. In this literature review, relevant aspects related to lateral soil-pile interaction and soil-abutment-bridge interaction are discussed. Since p - y curves are important in modeling soil-pile-structure interaction, this topic is covered in detail. Other topics reviewed in this chapter includes the lateral response of piles and pile groups, soil-pile-structure interaction associated with structural stiffness, and soil-abutment-bridge interaction.

2.2 Soil-Pile Interaction Modeling

Soils and pile foundations interact with each other under both static and dynamic loading conditions. The interaction is complex, and complete evaluation requires resources that are rarely available to practicing engineers. As a result, simplified models, which attempt to capture the main aspects of soil-pile interaction, have been developed. These models have been shown to work well for static and relatively slow cyclic loads (such as wave loads, typically encountered in pile-supported offshore structures), and can also be applied, with consideration of inertial effects, to problems including seismic soil-pile interaction. This section introduces the static/dynamic Beam-on-Nonlinear-Winkler-Foundation (BNWF) method, often referred as p - y *method*, which is commonly used to model soil-pile interaction.

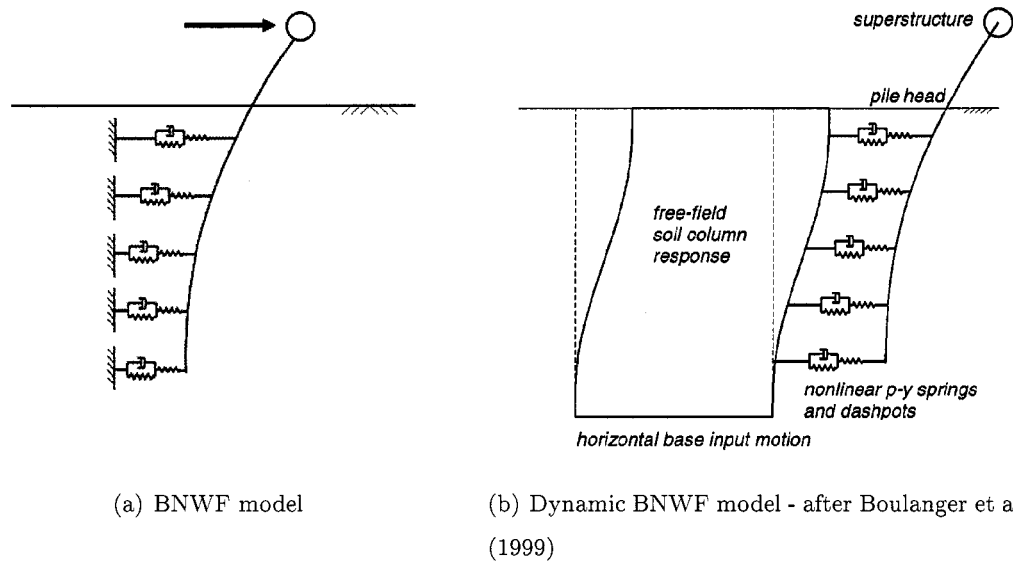


Figure 2.1: Static and dynamic Beam-on-Nonlinear-Winkler-Foundation (BNWF) model

2.2.1 Static and Dynamic Beam-on-Nonlinear-Winkler-Foundation (BNWF) Models

The analysis of laterally loaded piles is complicated due to the long and slender configuration of piles, the nonlinear response of the surrounding continuous soils, and the interface where the soil is in contact with the pile. Rigorous simulation of the interaction problem requires three-dimensional (3-D) finite element models (FEM), which are computationally expensive, and require the use of advanced constitutive models to capture localized soil response. They also require the use of robust contact elements to capture soil and pile interaction effects such as gapping and sliding [e.g., Petek (2006)]. As an alternative, Winkler foundation models have been widely used in practice. In these models the pile is treated as a beam supported on a Winkler spring foundation, i.e., a series of independent horizontal and vertical nonlinear springs distributed along the pile. For this reason, these models are often referred as *Beam-on-Nonlinear-Winkler-Foundation* (BNWF) models. Figure 2.1a shows a schematic of a BNWF model.

During earthquakes, shear waves propagate through the soil applying kinematic forces to the pile foundation. The foundation shaking induces inertial forces in the superstructure.

The inertial forces affect the foundation response and the soil movement. The soil motion around the pile, where soil-pile interaction occurs, is referred to as *near-field* motion. The soil motion recorded far from the pile is referred as *far-field* or *free-field* motion. In coupled simulations, where the pile and soil are connected together by interface springs, it is assumed that a soil column provides the free-field motion and the soil-pile-structure interaction occurs at the interface springs. Alternatively, free-field motions can be calculated separately along the pile depth and the corresponding displacement time histories can be applied to p - y springs. This idea is illustrated in the dynamic Beam-on-Nonlinear-Winkler-Foundation (BNWF) model shown in Figure 2.1b.

2.3 P - y Curves

To completely define the BNWF model it is important to establish accurate p - y curves. In this section two cases are considered: i) a pile subjected to monotonic and cyclic loads at the pile head, and ii) a pile embedded in liquefiable soil and subjected to earthquake excitations and lateral spreading. To analyze the first case, conventional p - y curves are introduced. For the earthquake problem, since there are not yet well-established p - y curves for liquefiable soil, several experimental observations are discussed.

2.3.1 Conventional p - y Curves for Piles Subjected to Static and Cyclic Loading

To capture the lateral response of piles, soil reaction force versus pile displacement (i.e., p - y) relationships are commonly used together with beam elements in static and dynamic BNWF models. In general these curves are based on field tests, laboratory model tests, and analytical solutions. The pile displacement (y) and soil resisting force per unit length (p) can be back-calculated from measured or calculated bending moments by double-differentiating and double-integrating the governing equilibrium differential equation. That is,

$$p = \frac{d^2}{dz^2} M(z) \quad (2.1)$$

and, assuming linear bending behavior,

$$\frac{d^2}{dz^2} y = \frac{M(z)}{EI} \quad (2.2)$$

where p is the lateral resistance on the pile, y is the lateral pile displacement, M is the pile bending moment, EI is the flexural rigidity of the pile, and z is the vertical distance measured along the pile. Many researchers have performed static and cyclic lateral load tests on full-scale and model piles in different soils with the purpose of evaluating p - y curves - e.g. Matlock (1970) for soft clay, Reese et al. (1974) for sand, Reese et al. (1975) for stiff clay below the ground water table, Reese et al. (1981) for stiff clays above the ground water tables, etc. As a result, several p - y curve criteria have been proposed for sands and clays. Additional field load tests and analytical and numerical evaluation of p - y response have brought more confidence to the use of these curves (Reese et al., 1981). Although there is some criticism of the BNWF model due to its limitations for capturing all soil continuum effects (in particular the coupling between p - y and t - z springs), the back-calculated p - y curves themselves reflect the continuum condition and have been successfully used in many projects. Wang and Reese (1998) suggested that the error incurred using discrete curves is a second-order effect; taking into account the difficulty of precisely predicting the relevant properties of the soil, especially next to the pile where the soil properties are strongly affected by the pile installation problem.

Back-calculated p - y Curves for Sand, Stiff Clay, and Soft Clay

Figures 2.2 and 2.3 show back-calculated p - y curves for cohesionless and cohesive soils obtained from field tests. The envelope curves can be characterized mainly by their initial stiffness and ultimate resistance; which is mobilized at large displacements. The initial stiffness and ultimate soil resistance increase with depth in a uniform granular soil; since the soil stiffness and confinement increase with depth. The characteristics of the p - y curve depend on soil type, loading condition, and ground water location since they reflect the nonlinear shearing characteristics of the soil. Figure 2.2 clearly shows the ultimate lateral soil resistance of a sand under cyclic loading is smaller than that obtained for static loading. This pattern is more clear in stiff clays, as shown in Figure 2.3. However, the difference between sand and stiff clays subjected to cyclic loading is that the ultimate resistance of sands stays constant after a peak value is reached while the ultimate resistance in stiff clays

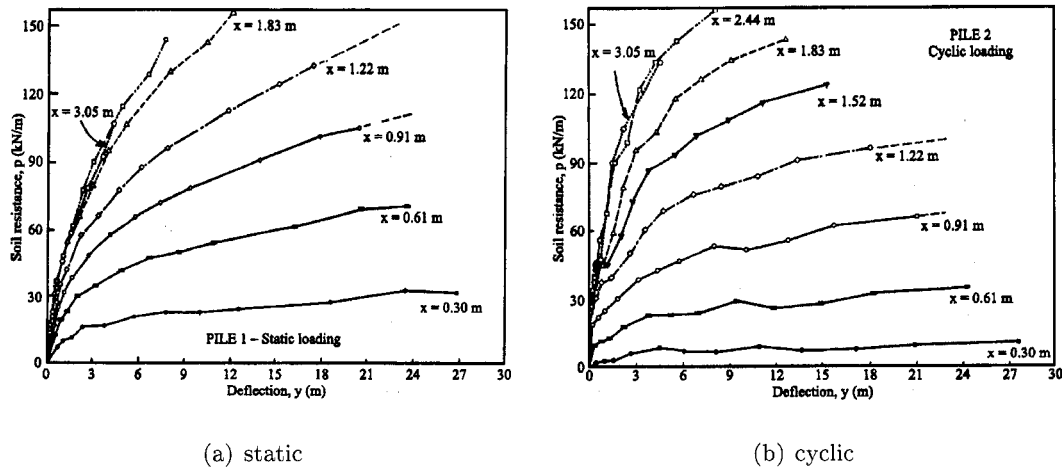


Figure 2.2: Back-calculated p - y curves for sand from field tests - after Reese et al. (1975)

decreases significantly after the peak value.

In soft clays, the soil resistance increases with pile displacement reaching a constant ultimate resistance under static loading, while the ultimate resistance becomes smaller under cyclic loading. An important feature observed in soft clays subjected to cyclic loading is the formation of gaps between the pile and the soil near the ground surface. Figure 2.4 shows experimental p - y curves for soft clays subjected to cyclic loading.

From experimental observations, Reese, Matlock, and other researchers proposed several p - y curve construction methods for various soil types, ground water conditions, and loading types. Details on these methods are summarized in the following subsections.

Initial Stiffness of p - y Curves

The initial stiffness of p - y curves may have little consequence for most pile analysis (Reese and Van Impe, 2001). The reason is that when a pile is subjected to large lateral loading, most of the reaction occurs near the ground surface where the mobilized lateral soil resistance is close to the ultimate resistance; which is mobilized at displacement levels that are beyond the initial p - y curve portion. The cases where the initial p - y curve stiffness can be important is when piles are subjected to vibratory loading or when piles are installed in

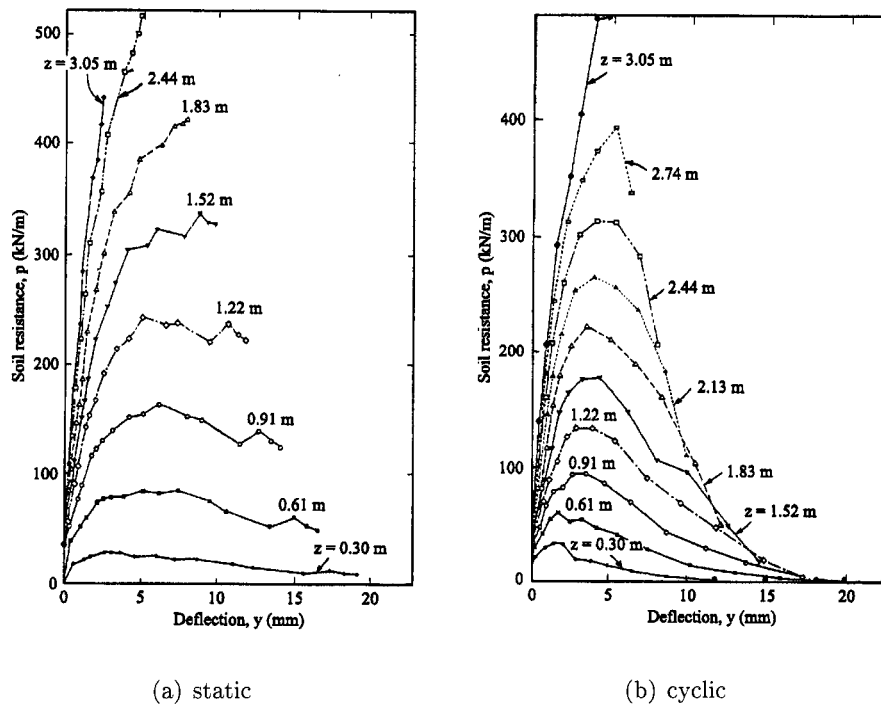


Figure 2.3: Back-calculated p - y curves for stiff clay from field test - after Reese et al. (1974)

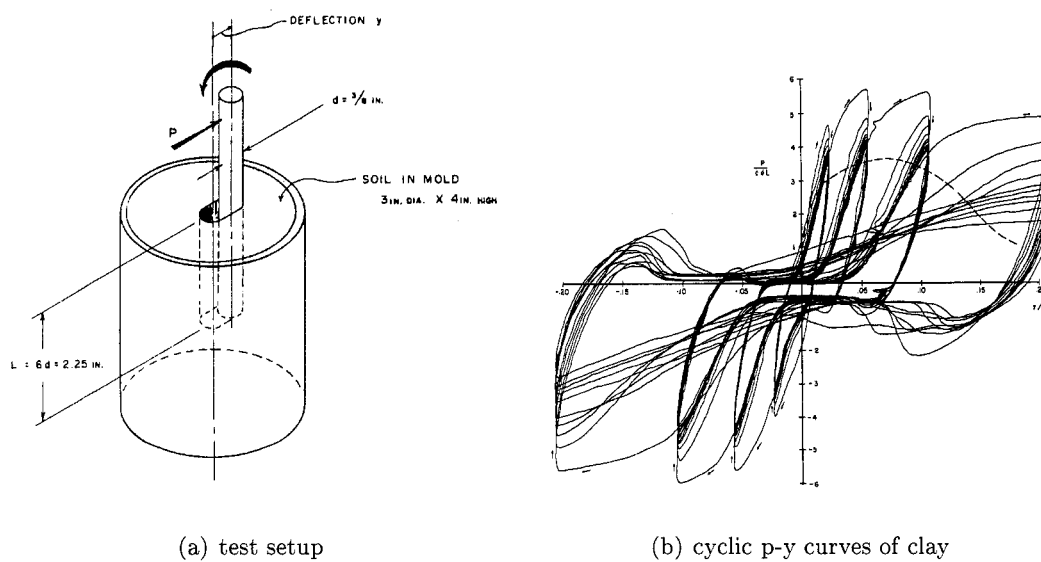


Figure 2.4: Cyclic response of a rigid pile in soft clay - after Matlock (1970)

Table 2.1: Representative values of ε_{50} for normally consolidated clays - Peck et al. (1974) - after Reese and Van Impe (2001)

clay	average undrained shear strength, (kPa)	ε_{50}
soft clay	< 48	0.020
medium clay	48 - 96	0.010
stiff clay	96 - 192	0.005

Table 2.2: Representative values of ε_{50} for overconsolidated clays - after Reese and Van Impe (2001)

	average undrained shear strength, (kPa)	ε_{50}
overconsolidated	50 - 100	0.007
clay	100 - 200	0.005
	300 - 400	0.004

brittle soils.

The initial stiffness is often defined in terms of indirect parameters. For clays, the displacement at which half of the ultimate soil resistance is mobilized, called y_{50} , is used to define the initial p - y stiffness. y_{50} for clays is usually defined as

$$y_{50} = 2.5 \varepsilon_{50} D \quad (2.3)$$

where, ε_{50} represents the strain corresponding to one-half of the undrained strength and D is pile diameter. Tables 2.1 and 2.2 present typical ε_{50} values for normally- and over-consolidated clays.

For sands, Reese et al. (1974) suggest an initial p - y stiffness equal to k_{py} times depth. Table 2.3 presents typical k_{py} values for sands.

Ultimate Resistance of p - y Curves

Ultimate soil resistances are calculated using two simple mechanisms based on limit equilibrium analysis. For near-surface p - y curves, a three-dimensional sliding surface wedge

Table 2.3: Representative values of k_{py} for sand - after Reese and Van Impe (2001)

	k_{py} for submerged sand	k_{py} for above GWT
loose sand	5.4 MN/m ³	6.8 MN/m ³
medium sand	16.3 MN/m ³	24.4 MN/m ³
dense sand	34.0 MN/m ³	61.0 MN/m ³

is considered. For deeper p - y curves, a two-dimensional flowing soil failure mode around the pile in a horizontal plane is considered. In both cases, the ultimate resistance is a function of pile diameter, depth (or overburden), and soil strength parameters. Matlock (1970) proposed ultimate resistance expressions for clays. In his analysis Matlock recognized the ultimate resistance for clays at deeper depths is strongly affected by cohesion and pile diameter and it is insensitive to depth. Therefore, the following expressions were proposed to evaluate the ultimate resistance for piles in soft clays at shallow and deeper depths.

$$p_{ult} = \begin{cases} \left[3 + \frac{\gamma'}{c_u z + \frac{J}{b} z} \right] c_u b & \text{for shallow depths} \\ 9 c_u b & \text{for deeper depths} \end{cases} \quad (2.4)$$

where γ' is the average effective soil unit weight, c_u is the undrained shear strength of the soil at depth z , b is pile diameter or width, and J is an experimentally determined coefficient (0.5 for soft clay and 0.25 for medium stiff clay).

Similarly, Reese et al. (1974) suggested ultimate resistance expressions for sands. In their analysis, theoretically calculated values (p_s) are factored by experimental coefficients that vary with loading type and depth. The expressions for ultimate resistance are

$$p_{ult} = \begin{cases} A_s p_s & \text{for static loading} \\ A_c p_s & \text{for cyclic loading} \end{cases} \quad (2.5)$$

where A_s or A_c are experimental factors associated with loading type and depth (Reese et al., 1974). The value of p_s is calculated by

$$p_s = \begin{cases} \gamma z \left[\frac{K_0 z \tan \phi \sin \beta}{\tan(\beta - \phi) \cos \alpha} + \frac{\tan \beta}{\tan(\beta - \phi)} (b + z \tan \beta \tan \alpha) \right. \\ \quad \left. + K_0 z \tan \beta (\tan \phi \sin \beta - \tan \alpha) - K_a b \right] & \text{for shallow depths} \\ K_a b \gamma z (\tan^8 \beta - 1) + K_0 b \gamma z \tan \phi \tan^4 \beta & \text{for deeper depths} \end{cases} \quad (2.6)$$

where $\alpha = \phi/2$; $\beta = 45 + \phi/2$; $K_0 = 0.4$, $K_a = \tan^2(45 - \phi/2)$, $b =$ pile diameter or width, $\phi =$ soil friction angle at depth z , and $\gamma' =$ soil unit weight.

Recently, Zhange et al. (2005) proposed a method to calculate the ultimate soil resistance for cohesionless soil considering the normal and side resistance that develops around the pile. To evaluate the normal resistance, they suggested a method originally proposed by Fleming et al. (1992) such that $p_u = K_p^2 \gamma z b$. To evaluate the side resistance an additional term is included. The total ultimate resistance is then expressed as

$$p_u = (\eta K_p^2 \gamma z + \xi K \gamma z \tan \delta) b \quad (2.7)$$

where, $\eta = 0.8$ and $\xi = 1.0$ for a circular pile; $\eta = 1.0$ and $\xi = 2.0$ for a square section pile (Briaud and Smith, 1983), $\delta =$ interface friction angle between pile and soil, and $b =$ pile diameter. In their study, they compared several small-scale pile tests and centrifuge test results performed by Barton and Finn (1983). Their results showed that Broms (1964a)'s ultimate resistance expression, as shown in Figure 2.6, underpredicts the ultimate lateral resistance at all depths while the method of Reese et al. (1974) underpredicts ultimate lateral resistances at shallower depths, but overpredicts the ultimate lateral resistance at deeper depths. Figure 2.6 compares patterns of several suggested ultimate lateral soil resistance distributions for cohesionless soil.

2.3.2 *p-y Curves for Liquefiable Soil*

In the previous subsection, conventional *p-y* curves were introduced. These curve were developed mainly from experimental tests where the pile head was loaded monotonically or cyclically. Since the applied loading rate was slow in most cases, there was no excess pore water pressure built-up in the saturated soil around the pile. However, when a pile is

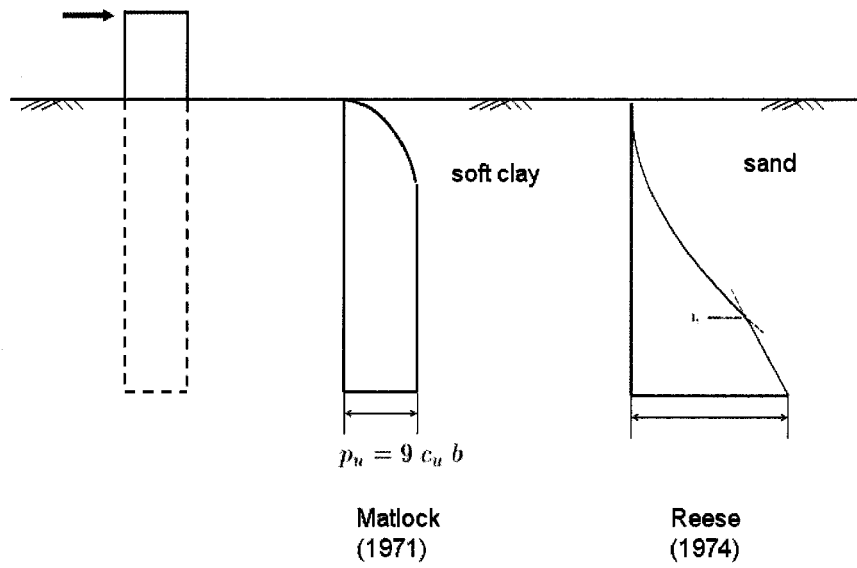


Figure 2.5: Comparison of ultimate soil resistance of soft clay (Matlock 1971) and sand (Reese et al. 1974)

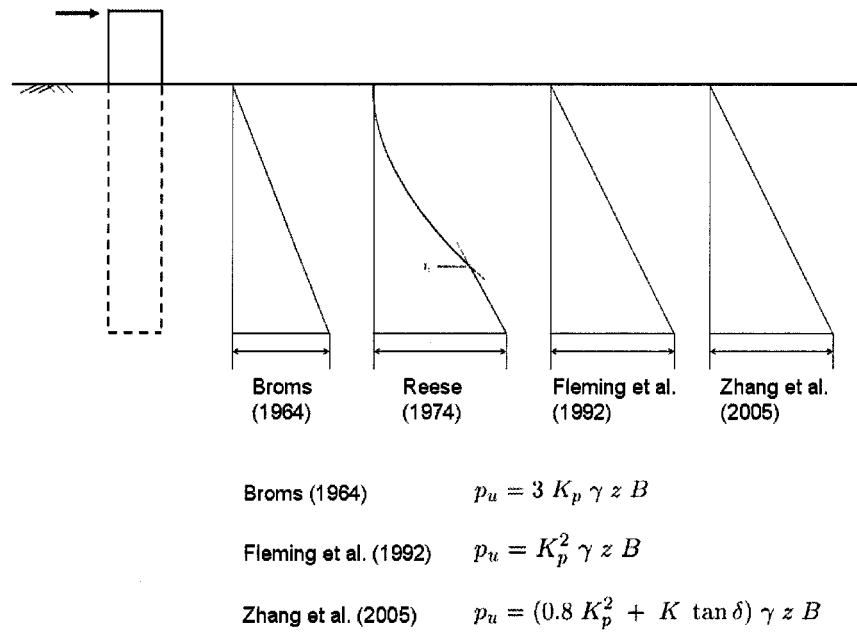


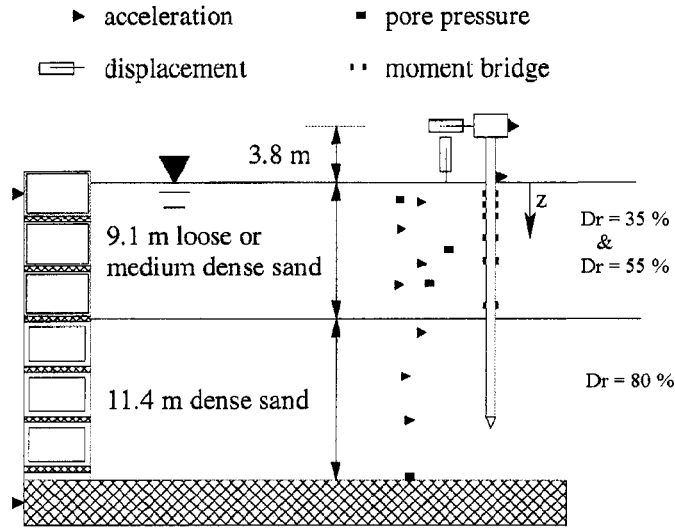
Figure 2.6: Suggested ultimate soil resistance for cohesionless soil

subjected to earthquake shaking, the soil around the pile may liquefy, if susceptible, and the soil resistance may change due to pore water pressure generation. This is an important aspect, particularly for deep foundations on liquefiable soils. In this section, recent studies on the lateral resistance of piles in liquefiable soil are discussed.

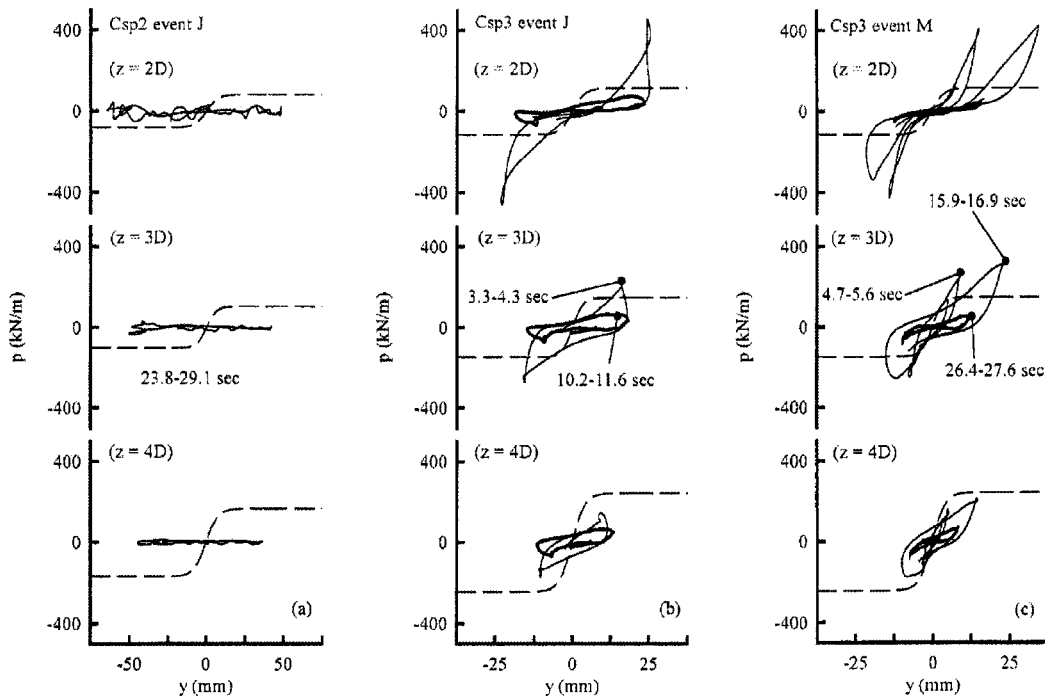
Back-calculated p - y Curves for Piles in Level Ground Liquefiable Soils

When the soil around a pile is liquefied the soil resistance around the pile changes. To better understand these changes several types of dynamic experiments have been recently performed including: i) centrifuge tests (Dobry et al., 1995; Wilson et al., 2000), ii) large scale laminar shear box shaking tests (Tokimatsu et al., 2001), and iii) full scale field blasting tests (Rollins et al., 2005; Weaver et al., 2005; Berber and Rollins, 2005).

Among the results obtained from these tests, it is worth examining the p - y curves back-calculated from the centrifuge tests performed by Wilson et al. (2000). Some of these results are shown in Figure 2.7. The figure illustrates observed p - y curve pattern in liquefiable soils. In these tests, different soil densities were used. From these results it was observed that the lateral soil resistance was similar to that observed during undrained tests, showing degradation and hardening of the lateral soil resistance due to pore water pressure generation and dissipation. After liquefaction, denser sands showed larger lateral resistance than loose sands. Medium dense sands showed a progressive softening of lateral resistance with pore pressure increase with number of cycles, especially near the ground surface. The p - y behavior was softest when the pore pressure ratio was high and when the lateral displacements were smaller than those corresponding to past peak values. When dilation occurred at large pile displacements in medium dense to dense sands, the lateral soil resistance against pile increased to a level that was sometimes greater than the ultimate resistance of the non-liquefiable soil. This effect can be correlated to the pore pressure drop associated with dilation under rapid, undrained loading conditions. In addition, the lateral resistance was affected by the amount of pile displacement, loading rate, and degree of pore pressure dissipation. Similar patterns were observed in other experimental tests.



(a) Centrifuge test set up



(b) Back-calculated curves - Dr = 35 % and *SantaCruz** motion ($a_{max,base}=0.45g$); Dr = 55 % and Kobe motion ($a_{max,base}=0.22g$); ; Dr = 55 % and *SantaCruz** motion ($a_{max,base}=0.41g$)

Figure 2.7: Back-calculated p - y behavior during shaking - after Wilson et al. 2000

Lateral Soil Pressure on Piles due to Lateral Spreading

When a soil in a slope, or at the base of a slope, undergoes liquefaction, the driving shear stresses induced by gravity in the soil deposit may cause permanent strains to accumulate in one preferential direction, and thereby lead to lateral spreading. The accumulated soil deformation during shaking can induce large amounts of kinematic forces on the pile foundation, which may result in severe damage to foundations and structures such as a bridges or port facilities.

To analyze piles subjected to lateral spreading, the lateral force induced by the liquefied layer must be considered. This can be done assuming a constant pressure distribution independent of the amount of soil displacement, or by using spring forces that depend on imposed soil displacements. In both approaches, the lateral force applied to the pile depends on the liquefied soil properties, distribution of soil displacement, and the velocity of the lateral flow (Wang and Reese, 1998). Among these factors, the strength of the liquefied soil is most important.

To estimate the liquefiable soil resistance, the conventional soil resistance without liquefaction is scaled by a *p-multiplier* that account for a simplified distribution of pore pressure ratio along the pile. *p-multipliers* for fully liquefied soils vary depending on the test conditions (Dobry et al., 1995; Wilson, 1998). For example, the Japan Road Association (JRA, 2002) guidelines suggests a 30% of total overburden stress times pile diameter for the lateral pressure imposed by the liquefiable soil with an additional reduction factor associated with the distance from the waterfront.

Another way to estimate the kinematic load on the pile from lateral spreading is to assume that the liquefied sand behaves as an undrained soil with a certain residual shear strength. Among several ways to estimate the residual strength, the in-situ test approach is commonly used. This method is based on correlations between SPT resistance and back-calculated shear strengths from flow slide case histories (Seed, 1986; Stark and Mesri, 1992; Seed and Harder, 1990). Figure 2.8 shows one of these correlations. Unfortunately, this approach includes considerable uncertainties due to the variability of soil and stress conditions in the case histories.

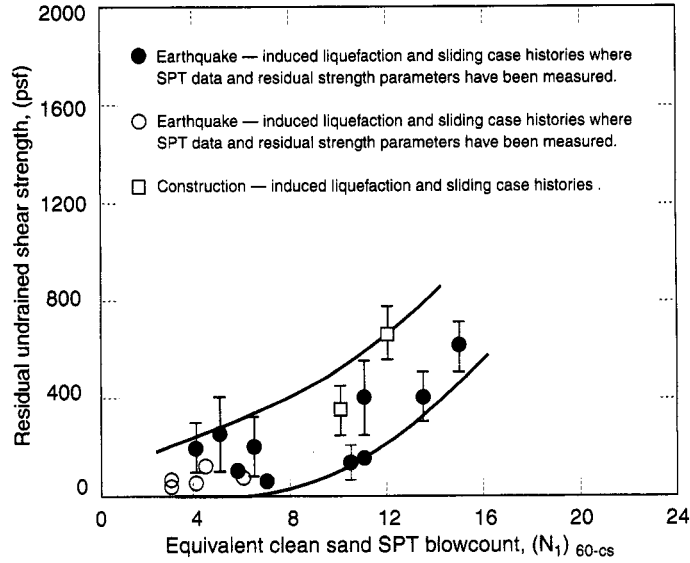


Figure 2.8: Relationship between residual strength and corrected SPT resistance (Seed and Harder, 1990)

As another approach, the use of normalized shear strengths (S_r/σ'_{v0}) is widely accepted and has shown to have several advantages. However, normalized shear strengths vary considerably for different soils (Kramer, 1996).

As an improved in-situ method approach, Kramer (2006) proposed a hybrid residual strength model that accounts for uncertainties using different weights that depends on documentation quality. The probabilistic form of the residual strength in this hybrid model is expressed as

$$S_r(P) = \exp [\overline{\ln S_r} + \Phi^{-1}(P) \sigma_{\ln S_r}] \quad (2.8)$$

where,

$$\overline{\ln S_r} = -8.444 + 0.109 \overline{N} + 5.379 (\overline{\sigma'_{v0}})^{0.1}$$

$$\sigma_{\ln S_r} = \sqrt{\sigma_m^2 + 0.00073 \overline{N}^2 COV_N^2 + 4.935 (\overline{\sigma'_{v0}})^{0.2} COV_{\sigma'_{v0}}^2}$$

$$\sigma_m^2 = 1.627 + 0.00073 \overline{N}^2 + 0.0194 \overline{N} - 0.027 \overline{N} (\overline{\sigma'_{v0}})^{0.1} - 3.099 (\overline{\sigma'_{v0}})^{0.1} + 1.621 (\overline{\sigma'_{v0}})^{0.2}$$

P = the probability of non-exceedance (i.e. the percentile value)

σ'_{v0} = vertical effective stress in atm

$$\overline{N} = (N_1)_{60}$$

$$COV_N = 0.3$$

$$COV_{\sigma'_{v0}} = 0.05$$

Approximation of Liquefiable p - y Curves

As discussed previously, the lateral resistance of liquefiable soil against piles cannot be simply defined using conventional p - y backbone envelopes. Moreover, the resistance is found to be strongly correlated to the characteristics of the undrained soil behavior; which depends on density, displacement history and displacement level, depth (i.e., confining pressure), and other factors. Several researchers have tried to encapsulate these effects within the pore pressure ratio, r_u , and establish approximate p - y curves based on this parameter; since the pore pressure change and phase transformation effects (contraction and dilation) governs the undrained soil behavior. In this approximation, the lateral resistance is assumed to be inversely proportional to pore pressure ratio (r_u) in a degradation parameter (often also called p -multiplier).

Dobry et al. (1995) used this inverse relationship to capture the response observed in centrifuge pseudo-static tests of single pile embedded in liquefiable leveled ground soil ($D_r \approx 40\%$). Using measured pore pressure ratio distributions with depth to evaluate the degradation of the p - y curves, pile bending moments were predicted reasonably well. Using a similar approach, Wilson (1998) concluded that p -multipliers ranging from 0.1 to 0.2 for $D_r \approx 40\%$ and from 0.25 to 0.35 for $D_r \approx 55\%$ in pseudo-static analysis give reasonable results for representative peak loading cycles on a single pile. In a recent work Brandenberg (2005) recommended more refined p -multiplier values to account for liquefaction effects in pseudo-static analysis for different $(N_1)_{60-cs}$. These values are shown in Table ??.

Boulanger et al. (2004) performed nonlinear FEM analyses for one of Wilson(1998)'s centrifuge test for a single pile in liquefiable soil. In their finite element model the p - y springs were connected to adjacent soil elements to transfer pore pressure ratio information. The ultimate capacity and tangential stiffness were scaled by a factor of $(1-r_u)$. Their results, particularly those corresponding to the soil profile and superstructure, agreed very

Table 2.4: Recommended p -multipliers for pseudo-static analysis - after Brandenberg (2005)

$(N_1)_{60-cs}$	m_p
< 8	0 to 0.1
8 - 16	0.1 to 0.2
16 - 24	0.2 to 0.3
> 24	0.3 to 0.5

well with the experimental results showing reasonably good ability of the model to capture the principal features of the response observed in the centrifuge.

2.4 Pile Response to Lateral Loads

In the preceding section, characteristics of conventional p - y curves were discussed focusing on initial stiffness and ultimate soil resistance. Although Figures 2.5 and 2.6 illustrate the distribution of ultimate lateral resistances with depth, the actual lateral soil resistance may not follow the full ultimate resistance distribution over the pile depth. In most cases, pile deflection, especially for long flexible piles, is greatest near the ground surface and large portions of the lateral soil reaction occurs near the surface. Therefore, maximum bending moments occur near or around 1.25D to 3.3D from the surface (Chai and Hutchinson, 2002). During earthquakes, piles are also subjected to inertial loading in addition to kinematic loading. The inertial loading affects predominantly the response of the soil and pile near the ground surface, while the kinematic loading influences the pile response over its lengths; depending on the soil conditions where the pile is embedded and their earthquake response characteristics such as lateral resistance degradation due to liquefaction and lateral spreading. This section discusses the response of piles to monotonic and cyclic loads including details on pile response in layered soils with liquefiable soil.

2.4.1 Pile Response due to Static/Cyclic Lateral Load and Load Transmission

When the load applied to a pile head is increased, the load is transmitted to the soil. If the soil resistance near the surface reaches an ultimate state, the deeper soil takes additional loading. This resistance (re-)distribution process is related to pile stiffness and yielding. When the pile stiffness is high relative to the soil, the pile tends to show a smaller curvature and the soil resistance is mobilized to deeper depths. However, once the pile bending moment is close to the yield moment, a plastic hinge is generated and the lateral load transmitted to deeper depths becomes smaller. Since piles usually don't reach the ultimate bending moment at the initial yielding location and the soil yielding extends progressively downward with increased loads, the plastic hinge location spreads out, rather than remaining concentrated at the initial location (Gerolymos and Gazetas, 2005).

2.4.2 Pile Response Under Pile Head Load

Using simple ultimate soil resistance diagrams (i.e., constant ultimate resistance with depth in clay and linearly increased ultimate resistance with depth in sand as shown in Figures 2.5 and 2.6), Broms (1964b) and Broms (1964a) calculated maximum lateral pile head forces and bending moments for different possible failure modes using different pile lengths (short, intermediate, and long), soil types (cohesive and cohesionless), and pile head conditions (free and fixed). In Broms study, pile length, pile head condition, and soil type give different soil reaction patterns and pile bending moment distributions. For example, short piles mobilize full soil resistance, whereas long piles mobilize ultimate soil resistance only near the ground surface. The bending moment distribution is also affected by the pile head fixity.

2.4.3 Pile Response During Lateral Spreading

The pile bending moment distribution mainly depends on the boundary forces that develop along the pile length. During an earthquake, kinematic loads cause large pile bending moments at the interface between layered soils; where large levels of shear strain concentrate due to different soil stiffness. In many cases, large pile bending moments and

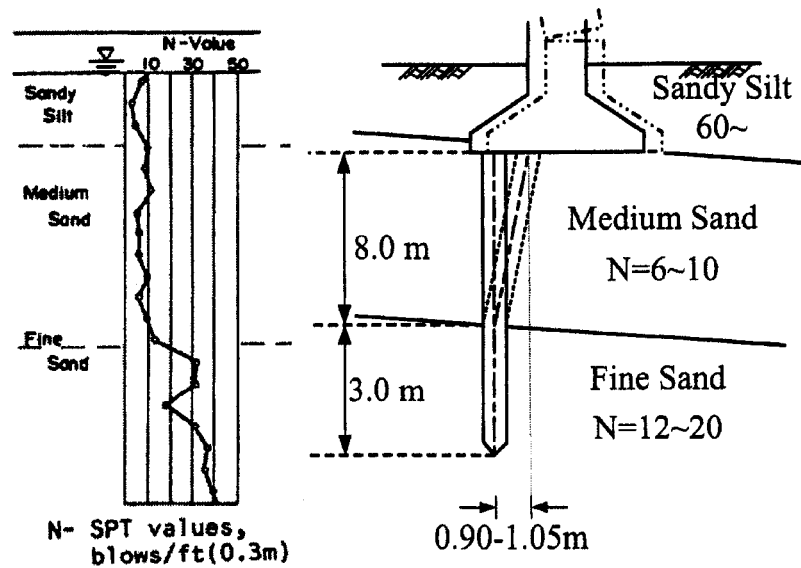


Figure 2.9: Pile foundation failure of Yachiyo bridge due to kinematic loading - after Hamada (1992)

failure have been observed at the interface between these layers. Figure 2.9 shows an example where pile failures occurred at the soil layer interface. Large bending moment concentrations at soil layer interfaces are more obvious when one of the soil layers is liquefied.

When a soil over a non-liquefiable soil is liquefied, the lateral soil resistance varies with the degree of liquefaction. In these cases the underlying non-liquefiable soil may control the pile response due to its rotational restraint effect; which is associated with pile rigidity and embedment length. For this reason, the location of the interface between liquefiable and non-liquefiable layers and the combination of liquefiable and non-liquefiable layers are important factors to evaluate pile response. From centrifuge tests where lateral spreading was considered using different liquefiable layer combinations, Abdoun et al. (2003) observed that maximum bending moments occurred at the interface between the liquefiable and non-liquefiable layers. After the pile bending moment reached a peak value, the moment value decreased with the pile bouncing-back. They also observed that a floating pile installed in a non-liquefiable layer over a liquefiable layer had a maximum bending moment at the top of the liquefiable layer since displacements at the upper non-liquefiable soil exceeded

that of the liquefied lower layer. In cases where piles were embedded in three layers (non-liquefiable layer over liquefiable layer over a non-liquefiable layer), large maximum bending moments occurred at the layer interfaces (i.e. at the top and bottom of the liquefiable layer) although the larger maximum values occurred at the lower interface. In these cases, it was also observed that the measured bending moment distribution within the liquefied layer was nearly linear showing little contribution to the pile bending moment from the liquefied soil pressure. Another observation was that soil densification due to pile driving resulted in larger bending moments than those in cast-in-place piles due to the fact that the densification increased the initial effective stress around the pile.

2.5 Pile Group Response to Lateral Loads

Pile groups consist of rows of piles whose heads are connected by a rigid pile cap. The lateral capacity of pile groups depends on the individual pile capacities, pile spacing, pile installation method, pile cap resistance, and other factors.

2.5.1 Group Effect

The efficiency of an individual pile in a pile group (compared to a single isolated pile) varies mainly depending on pile spacing, pile alignment, and location of the pile in the group. When piles in a group are closely spaced, lateral pile movements affect the soil stresses around the adjacent piles. Figure 2.10 shows two possible pile alignments: in-line and side-by-side. In in-line alignments, a front pile (or leading pile) takes more load than the others and the rear pile (trailing pile) mobilizes less soil resistance. This effect is referred as *shadow effect*. In side-by-side alignments, corner piles located at the corner or at the edge of a pile group take a greater share of the load than the interior piles. This is particularly noticeable when piles are closely spaced. This effect is referred as *edge effect*.

To capture the response of piles in a pile group, group efficiency factors are included in the p - y curves using p -multipliers (Brown et al., 1988). To evaluate these p -multipliers several researchers have performed experimental tests on pile groups using different pile group sizes (i.e., number of rows and piles per row), pile spacing, pile cap rotational conditions, and soil type and density. Mokwa (1999) studied pile group behavior and pile cap

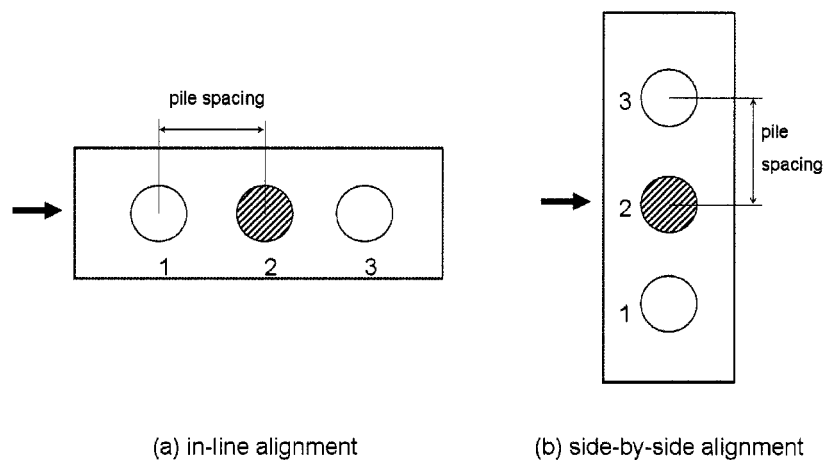
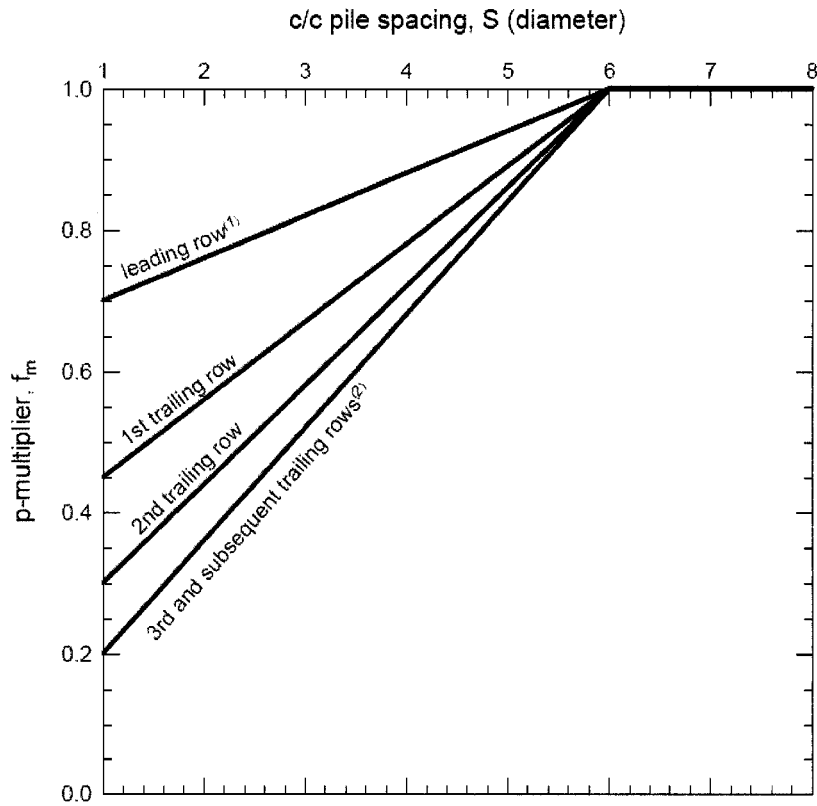


Figure 2.10: Schematic of pile alignment in a group

resistance and completed a comprehensive literature review using 350 journal articles and other publications, including 37 experimental studies (15 full-scale tests, 16 1-g model tests, and 6 centrifuge tests) and approximately 30 analytical studies. Based on these studies, he concluded that pile spacing is the dominant factor affecting pile group response and that group effects are negligible when the center-to-center pile spacing is greater than $6D$ in in-line configurations or greater than $3D$ in the side-by-side configurations. He also concluded that soil type and density does not affect significantly the pile group efficiency, and that efficiency decreases with increasing displacement and becomes constant after a deformation of 5 % of pile diameter. He also developed relationships to estimate pile group efficiencies and *p-multipliers* as a function of pile arrangement and pile spacing. Figure 2.11 shows Mokwa's *p-multipliers* for leading and trailing rows. Other group efficiency values versus pile spacing for different pile alignments in a pile group can be found in Mokwa (1999).

2.5.2 Pile Cap Resistance

The pile cap in a pile group strongly affects the rotational and lateral capacity of the whole foundation. When a pile cap is subjected to lateral loading, the rotational tendency of the pile cap is restrained by the vertical soil resistance that develops along the pile shafts and at the pile tip. This is schematically shown in Figure 2.12. Mokwa (1999) compared



Notes:

- (1) The term row used in this chart refers to a line of piles oriented perpendicular to the direction of applied load.
- (2) Use the f_m values recommended for the 3rd trailing row for all rows beyond the third trailing row.
- (3) Bending moments and shear forces computed for the corner piles should be adjusted as follows:

<u>side by side spacing</u>	<u>corner pile factor</u>
3D	1.0
2D	1.2
1D	1.6

Figure 2.11: Design line for p-multipliers - after Mokwa (1999)

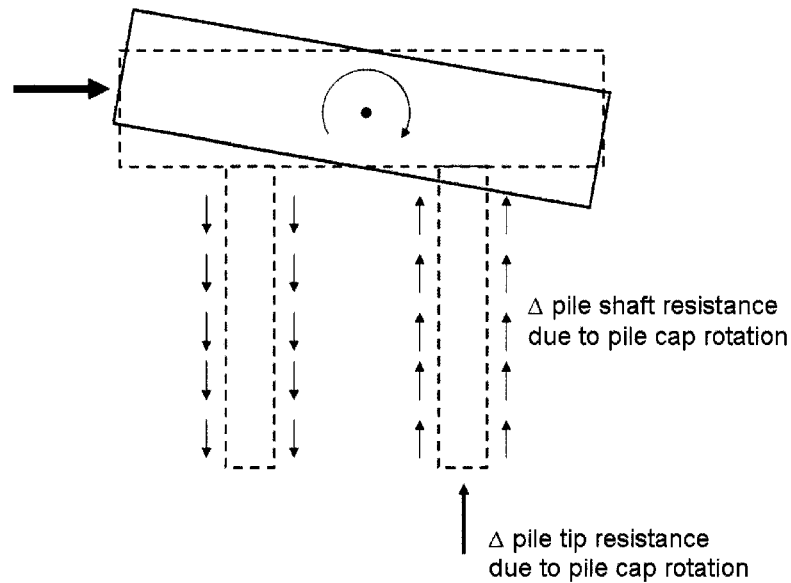


Figure 2.12: Schematic of rotational soil resistance due to pile cap rotation

field load test results for a pile group to numerical simulations based on two cases: i) a fixed-head case (no pile cap rotation) and ii) a free-head case (without any pile cap rotational constraint). Figure 2.13 shows the pile group resistance recorded in the experiment and calculated using these two extreme numerical cases. It is clear from the figure that the experimental results fit in the middle of the two extreme cases; indicating the rotational soil resistance due to the pile axial resistance significantly influences the pile group response.

Pile caps can also mobilize considerable lateral soil resistance themselves when they are subjected to lateral loading. The lateral resistance of the soil against the pile cap movement depends on the passive earth pressure at the front face of the cap, and on the sides and base, sliding resistance and the active pressure on the back face of the cap. Mokwa (1999) found that the sliding resistance and active forces are negligible since the values are small compared to the passive resistance and they tend to offset each other.

To calculate the passive earth pressure resistance, several passive earth pressure theories, such as the log spiral, Rankine, and Coulomb theories can be used. Using Rankine's theory,

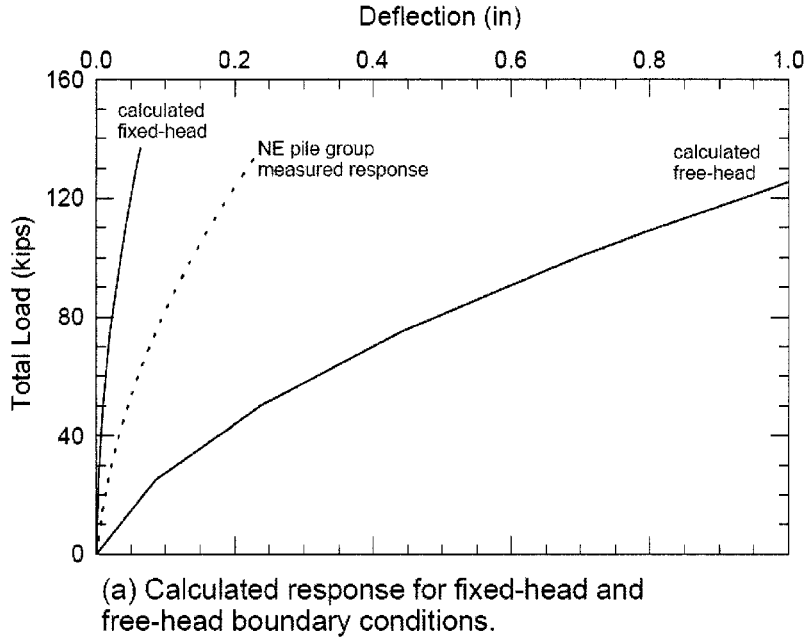


Figure 2.13: Pile group load test results and calculated results for fixed pile cap and free pile head - after Mokwa (1999)

the passive earth pressure at the cap face can be determined by

$$E_p = \frac{1}{2} \gamma H^2 K_p + 2 c H \sqrt{K_p} + q H K_p \quad (2.9)$$

where, $K_p = \tan^2(45 + \phi/2)$, ϕ = friction angle of soil, c = cohesion of soil, q = surcharge pressure, γ = unit weight of soil, and H = height of pile cap.

For large soil-wall friction angles (δ), the log spiral theory gives more accurate results than Rankine or Coulomb's earth pressure theories. This is due to the fact that: i) Rankine's theory does not consider wall friction; resulting in underestimated passive earth pressures, especially at high δ 's, and ii) K_p values from Coulomb's theory are unconservative and can be very inaccurate when the wall friction angle is greater than about 0.4ϕ (Mokwa, 1999). To account for large values of wall friction angle (δ), Mokwa (1999) developed a procedure based on the log spiral theory. In his procedure, the soil weight over a log spiral failure surface and the log spiral center location are determined using an iterative technique. With these values the earth pressure forces ($P_{p\phi}$, P_{pc} , and P_{pq}) are calculated to determine the

earth pressure coefficients shown in Equation 2.10.

$$E_p = \frac{1}{2} \gamma H^2 K_{p\phi} + 2cH \sqrt{K_{pc}} + qH K_{pq} \quad (2.10)$$

where $K_{p\phi} = \frac{2P_{p\phi}}{\gamma H^2}$, $K_{pc} = \frac{P_{pc}}{2cH}$, and $K_{pq} = \frac{P_{pq}}{qH}$

The resulting passive earth pressure force is determined for a unit length of soil in two dimensions. In a real pile cap, or bulkhead, the passive region is wider than in a two-dimensional model. Therefore, larger passive earth pressures are mobilized. The zone of the mobilized soil resistance depends on the friction angle of the soil and depth. To include the three dimensional pile cap effect Mokwa (1999) performed field load tests on bulkheads and measure the pure pile cap lateral resistance without pile lateral resistance. He found that using the log spiral theory, together with Ovesen (1964)'s three-dimensional shape factors, accurate results were obtained for both c - ϕ natural soils and cohesionless crusher run backfill. The Ovesen's 3-D modifying factor (R) is expressed by

$$R = 1 + (K_p - K_a)^{2/3} \left[1.1 E^4 + \frac{1.6B}{1 + 5\frac{b}{H}} + \frac{0.4(K_p - K_a)E^3 B^2}{1 + 0.05\frac{b}{H}} \right] \quad (2.11)$$

where, $B = 1$ for a single pile cap or anchor block, $E = 1 - \frac{H}{z+H}$, and z is embedment depth from the ground surface to the top of the pile cap.

For cohesionless soil, the ultimate earth pressure force, accounting for the 3-D effect, can be expressed by

$$P_{ult,cap} = R E_p b = R (P_{p\phi} + P_{pc} + P_{pq}) b \quad (2.12)$$

where, R is Ovesen's 3-D modifying factor calculated from Equation 2.11, E_p is the 2-D passive earth pressure obtained using Equation 2.10, and b is pile cap width.

For cohesive soils ($\phi = 0$), Mokwa (1999) suggested the so-called $\phi=0$ *sliding wedge method* to calculate passive earth pressure. The method follows Reese's sliding surface wedge approach for a laterally loaded pile and is based on full-scale test results. Equation 2.13 shows a semi-empirical equation for the ultimate passive earth pressure for cohesive soils

$$P_{ult,cap} = \frac{cbH}{2} \left(4 + \frac{\gamma H}{c} + \frac{0.25H}{b} + 2\alpha \right) \quad (2.13)$$

Table 2.5: Typical values of the soil adhesion factor, α - after NAVFAC (1982)

interface soil	soil cohesion, c (psf)	adhesion factor, α
Very soft cohesive soil	0 to 250	1.0
Soft cohesive soil	250 to 500	1.0
Medium stiff cohesive soil	50 to 1000	1.0 to 0.75
Stiff cohesive soil	1000 to 2000	0.75 to 0.5
Very stiff cohesive soil	2000 to 4000	0.5 to 0.3

where α is a factor that accounts for adhesion between the cohesive soil and the wall. Table 2.5 shows typical values for α . Since the three-dimensional and shape effects are implicitly included in the experimental tests, no additional modification factors are needed.

2.5.3 Response of Pile Groups Subjected to Earthquake Loading

The dynamic response of pile groups is complicated by the presence of the pile cap. When the soil is liquefied, the soil-pile-structure interaction becomes even more complicated.

Curras et al. (2001) performed centrifuge tests on a superstructure supported by a pile group founded in an upper clay underlain by dense sand. Using p - y , t - z , and q - z interface springs and conventional group efficiency factors for pile groups, good predictions were obtained. In their study, it was observed that higher nonlinear response due to soil-pile group interaction caused the translational and rotational stiffness to decrease and led to longer first modal periods.

Several researchers have performed centrifuge tests (Abdoun et al., 2003; Brandenber et al., 2005), large shaking table tests (Suzuki et al., 2006; He et al., 2006), and full-scale field blasting tests (Juirnarongrit and Ashford, 2004; Kawamata et al., 2006) to investigate pile group response due to lateral spreading.

From centrifuge tests on two pile groups (2.5D and 4D pile spacing) subjected to lateral spreading, Abdoun et al. (2003) found that the soil between cast-in-place 4D spacing piles was liquefied, but the soil between driven 2.5D spacing piles was not fully liquefied (r_u

≈ 0.8). They also observed that the front and rear piles had similar maximum bending moments. The maximum bending moment values were much smaller than those measured in single piles due to the frame effect associated with axial forces of individual piles.

Kawamata et al. (2006) performed numerical analysis on pile groups subjected to lateral spreading induced by blasting using simplified 1-D and 2-D pile models. The 1-D pile model consisted of a single pile with an equivalent stiffness and p - y springs. The 2-D pile models represented a pile group with two rows of equivalent piles. Using the 2-D simplified model, the rotational resistance of the pile group was included. In their analysis, conventional p - y springs with p -multipliers were used. The recorded ground deformation was applied to the p - y springs and it was assumed that the p - y springs in liquefiable layer had no stiffness. The 2-D simulations were in good agreement with the experimental results.

2.6 Axially Loaded Single Pile

The behavior of an axially loaded pile relies on the skin resistance of the pile (Q_s) and the pile tip (point) resistance (Q_p). The total resistance of a pile (Q_t) is simply expressed by

$$Q_t = Q_s + Q_p \quad (2.14)$$

The load-transfer mechanism is complicated due to several reasons. First, the maximum values of Q_s and Q_p do not occur simultaneously. Second, the induced elastic displacements at different depths along the pile vary and the skin resistance vs. displacement relationship is nonlinear. Finally, the pile tip resistance affects the overall distribution of skin resistance. Figure 2.14 illustrates a typical load transfer mechanism in a single pile. The load transfer is different depending on soil type. In clays, the total resistance of the pile generally reaches a maximum value after some pile movement and then drops gradually to a residual value. In contrast, the total resistance continues to increase at a decreased rate or tends to reach a maximum value. This typical behavior between mobilized total resistance and movement of pile top is shown in Figure 2.15. As it is shown in the figure, the frictional resistance in clays increases rapidly and reaches a maximum value at a small displacement and then decreases gradually and reach a residual value. However, the point resistance in clays continues to

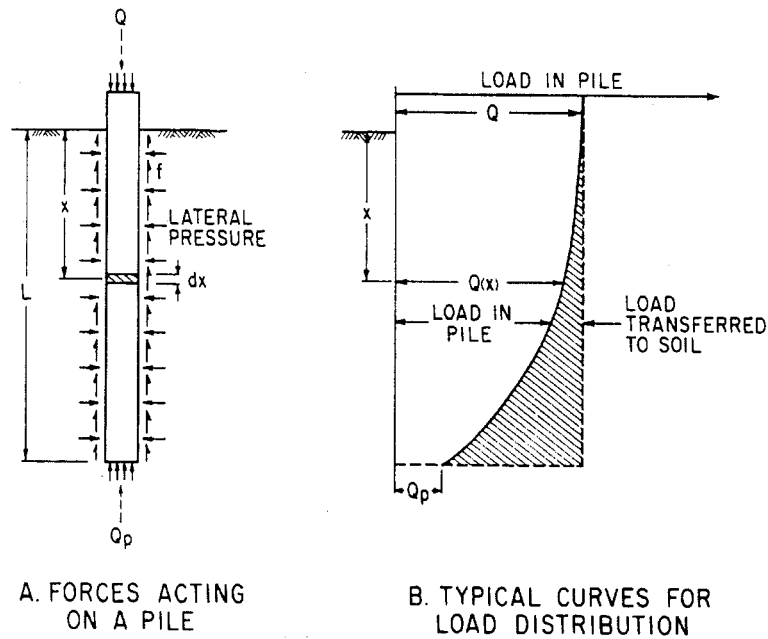


Figure 2.14: Illustration of axial load transfer in a pile - after Vijayvergiya (1997)

increase and reach a maximum value at a relatively larger displacement. This resistance is commonly obtained from end bearing capacity theory. The displacement at which the maximum resistance is obtained is called critical displacement (or movement). On the other hand, the frictional resistance in sands remains almost constant after reaching a peak value. The point resistance for sands continues to increase gradually.

The skin resistance and the point resistance are modeled by t - z curves and q - z curves which are similar to the p - y curves used for lateral soil resistance. Many authors - for example, Coyle and Sulaiman (1967), Vijayvergiya (1997), Parker and Reese (1969), Mosher (1984), and O'Neill and Reese (1999) have investigated field and lab tests and suggested methods or formulas to develop these curves.

2.6.1 Ultimate Skin Resistance (t_{ult}) and Ultimate Point Resistance (q_{ult}) for Sands

Vijayvergiya (1997) proposed a relationship for skin and point resistance for driven piles based on his literature review and experience. The mobilized unit friction resistance for any

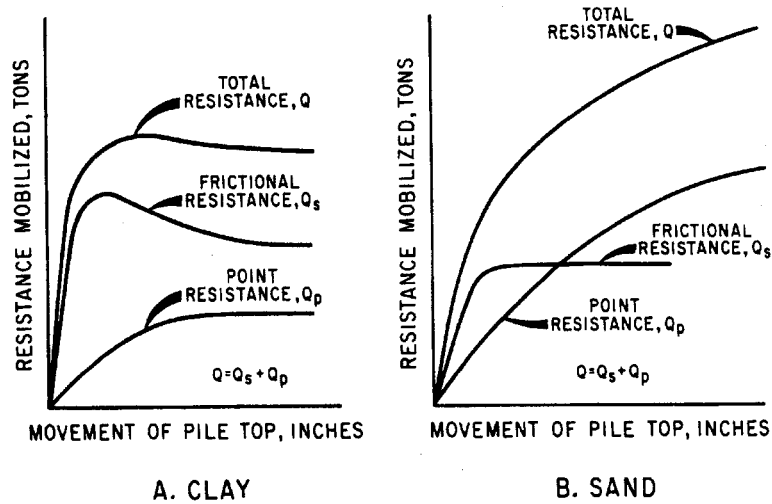


Figure 2.15: Typical load-movement characteristics of an axially loaded pile - after Vijayvergiya (1997)

movement of a pile is expressed in Equation 2.15. The relationship can be used for clay and sand.

$$f = f_{max} \left(2 \sqrt{\frac{z}{z_c} - \frac{z}{z_c}} \right) \quad (2.15)$$

where, f = unit friction mobilized along a pile segment at a displacement (z), f_{max} = maximum unit friction, and z_c = critical displacement corresponding to q_{max} . The value of f_{max} is obtained using Equation 2.16.

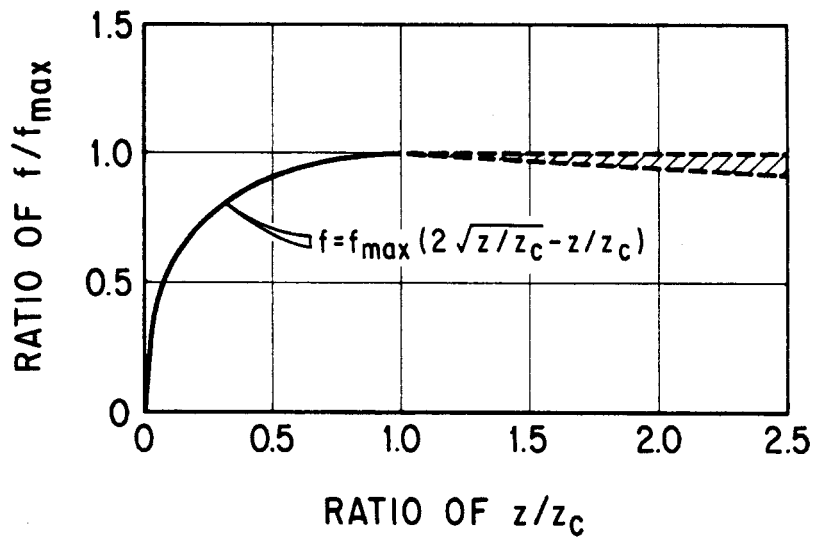
$$f_{max} = K \sigma_v \tan \delta \quad (2.16)$$

where, K = coefficient of lateral earth pressure, σ_v = effective vertical stress, and δ = angle of friction between soil and pile surface. The value of δ is usually approximated by $\delta = \phi - 5$. The value of K for medium dense to dense sand ranges from 0.8 for tension to 1.25 for compression, but the value of K for loose sand may be lower and close to K_a , the coefficient of active lateral earth pressure. Table 2.6 gives API (1993)'s recommendations for the value of δ and limiting values for f_{max} . The value of z_c , where f_{max} is mobilized, ranges from 0.2 to 0.3 in. in both clays and sands. Equation 2.16 is plotted in Figure 2.16.

The mobilized tip resistance for any tip movement, z , can be obtained using the following

Table 2.6: Recommended parameters for Cohesionless Siliceous Soil - after API (1993)

soil type	δ (degree)	f_{max} (kPa)	N_q in Eq. 2.18	q_{max} (kPa)
Clean Sand	30	95.8	40	9580
Silty Sand	25	81.4	20	4790
Sandy Silt	20	67.1	12	2870
Silt	15	47.9	8	1920

Figure 2.16: Normalized t - z (or f - z) curve for clay and sand - after Vijayvergiya (1997)

empirical relationship.

$$q = \left(\frac{z}{z_c}\right)^{1/3} q_{max} \quad (2.17)$$

where, q = tip resistance mobilized at any value of $z < z_c$, q_{max} = maximum tip resistance, and z_c = critical displacement corresponding to q_{max} . The value of q_{max} is determined using Equation 2.18,

$$q_{max} = N_q \sigma_v \quad (2.18)$$

where, N_q = bearing capacity factor, and σ_v = effective vertical stress at the base of the pile. The value of N_q depends on the angle of internal friction of the granular soil. API recommendations of N_q for driven piles in medium dense to dense sand is given in Table 2.6. Vesic (1970) and Kerisel (1964) suggested that the value of q_{max} increases linearly to a limited depth. Beyond certain depths, the values should be limited. Limiting values are also given in Table 2.6. The critical displacement z_c is defined as a vertical displacement at which the maximum unit point bearing of pile tip q_{max} is mobilized. The value of z_c is approximated to 3% to 9% of the diameter for clays and sands (or 0.04 D for clay to 0.06 D for sand). Here, D represents pile diameter. A normalized q - z curve is illustrated in Figure 2.17.

Mosher (1984) proposed another method to evaluate skin resistance and point resistance. The skin resistance f is computed in Equation 2.19 using f_{max} obtained from Castello (1980)'s charts. The tip resistance is calculated in Equation 2.20 using modified equations for different density of sands assuming that q_{max} occurs at 0.25 in.

$$f = \frac{z}{\frac{1}{E_f} + \frac{1}{f_{max}}(z)} \quad (2.19)$$

$$q = \left(\frac{z}{z_c}\right)^m q_{max} \quad (2.20)$$

Here, the value of m is 1/2 for loose sand, 1/3 for medium sand, and 1/4 for medium dense sand. The value of q_{max} is determined from Castello (1980)'s curves. O'Neill and Reese (1999) provided methods for computing the nominal axial resistance for drilled shafts considering various soil types, drainage conditions, and loading directions.

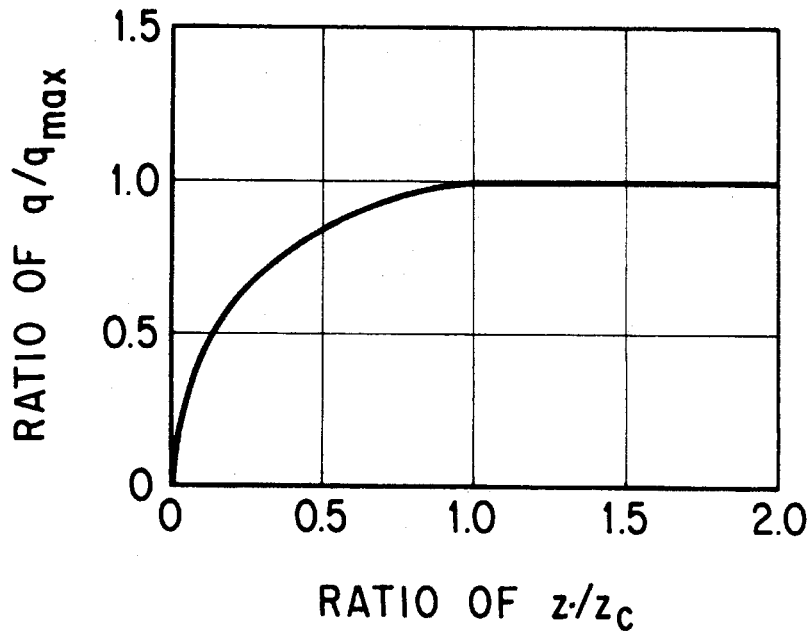


Figure 2.17: Normalized q - z curve for sand and clay - after Vijayvergiya (1997)

2.7 SPSI and Structural Stiffness

The interaction between piles and the surrounding soil also affects the overall stiffness of a soil-structure system. As such, it can affect the dynamic response of that system. This section describes SPSI effects on the superstructure response.

2.7.1 SPSI Effect on Structure Response

In an ideal case where a structural column base is fixed, which could occur when the column is socketed into hardrock, the column stiffness can be calculated using well known equations, as shown in Figure 2.18. However, for the column case of bridges founded on soils, the column base conditions are not fixed. During an earthquake, the structure base supported by a pile or pile group system undergoes translational and rotational movements. The actual stiffness of the columns vary due to changes in structural boundary conditions. The local soil deformation around the pile near the ground surface and the rocking behavior causes energy dissipation and stiffness decrease resulting in longer structure natural periods.

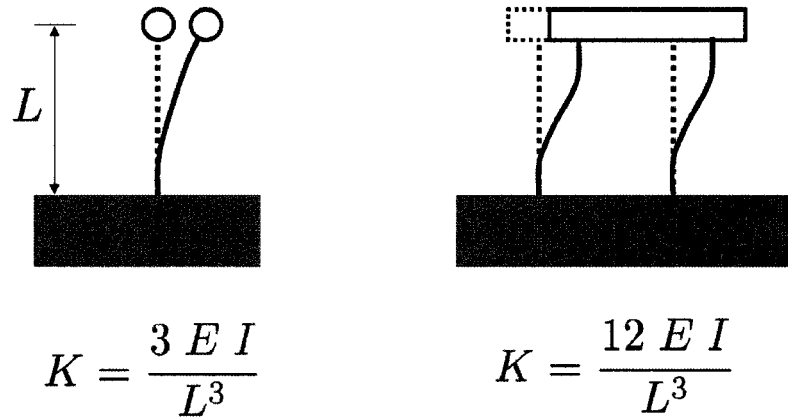


Figure 2.18: Lateral stiffness of column with and without rotational restraint at the top

The frame effect in a pile group provides rotational resistance.

Since SPSI makes the fundamental period of the structure longer, there is a prevailing structural view that this effect is beneficial (i.e., longer periods stay away from the critical period in a design spectrum). However, this beneficial effect is true only when the response spectrum of an earthquake motion is within the design spectrum. When the input motion has large components at frequencies contents that corresponds to the SPSI associated natural periods, and out of the design spectrum critical period, the structure may undergo severe damage. These effects have been observed in many case histories (Gazetas and Mylonakis, 1998).

2.7.2 Other Factors that Influence the Structural Response

As explained above, the structure and pile response is affected by pile section stiffness, and other geometric characteristics such as clear height above the ground surface, pile head rotational constraint, pile embedment length, and degree of rocking.

When the clear height above the ground surface is long, the maximum bending moment occurs near the ground surface. In a structure whose supporting columns have different clear heights, the short column tends to show relatively larger lateral demand due to its larger stiffness.

Pile embedment is another influencing factor. When the pile embedment is long enough and the induced deformations and bending moments are confined to the upper part of the pile, the piles are regarded as 'flexible'; since the overall length of the pile does not significantly affect the response of the pile, (Randolph, 1981). Using elastic beam theory and considering elastic springs with uniform or linearly increasing modulus to represent the soil, a critical length (R_c and R_s) beyond which the pile length no longer significantly affects the response under lateral loading is calculated by

$$l_c \simeq 4 \sqrt[4]{\frac{E I}{k_h}} \quad (2.21)$$

where, E and I are the Young' modulus and the pile cross section moment of inertia of pile, respectively and k_h is the constant horizontal subgrade reaction modulus of the soil and n_h is the rate of increase of horizontal subgrade reaction modulus.

2.8 Soil-Abutment-Bridge Interaction

Bridge abutments can significantly affect the response of a bridge deck by providing longitudinal and transverse resistance and impeding lateral bridge displacement. In this review, the transverse abutment response is not considered. The longitudinal abutment response depends on abutment type, and backfill soil characteristics, and abutment foundation. Typical bridge abutment types include diaphragm abutments, seat abutments, and cast-in-drilled-hole (CIDH) shaft-controlled abutments. To be consistent with current abutment design practice (Caltrans, 2004) at the California Department of Transportation (Caltrans) this review focuses only on seat abutments.

Figure 2.19 shows a schematic drawing of a seat-type abutment and bridge deck-abutment-soil interaction. Seat-type abutments consist of a backwall on a stem wall and wing walls. The structure can be supported by pile foundations or shallow foundations. The bridge deck is seated on bearing pads on top of the stem wall and is separated horizontally from the backwall to provide an initial gap. The bridge deck inertial force is then transmitted through the bearing pad friction to the stem wall until the bridge deck reaches the backwall. To protect the piles from highly nonlinear response or severe damage, the backwall and shear keys are often designed to shear-off in such a way it is easy to retrofit them after

an earthquake. When the deck inertial force increases and the deck comes into contact with the backwall, the lateral resistance derives from the soil resistance on the backwall plus the stem wall and pile. Once the backwall is sheared off, the lateral resistance mainly comes from the mobilized passive earth pressure in the embankment backfill above the level of the backwall failure.

This mechanism is quite complicated and difficult to simulate. Therefore, the abutment reaction is often simplified as a 1-D load-displacement spring that captures the overall interaction between bridge deck and abutment system including backfill soil and gap. For the abutment stiffness and capacity, Caltrans uses empirical relationships developed from full-scale abutment tests conducted at UC Davis (Maroney, 1995). The initial abutment stiffness, including pile, can be expressed as

$$K_{abut} = k_i \times w \times \left(\frac{h_{abut}}{5.5 \text{ ft}} \right) \quad (2.22)$$

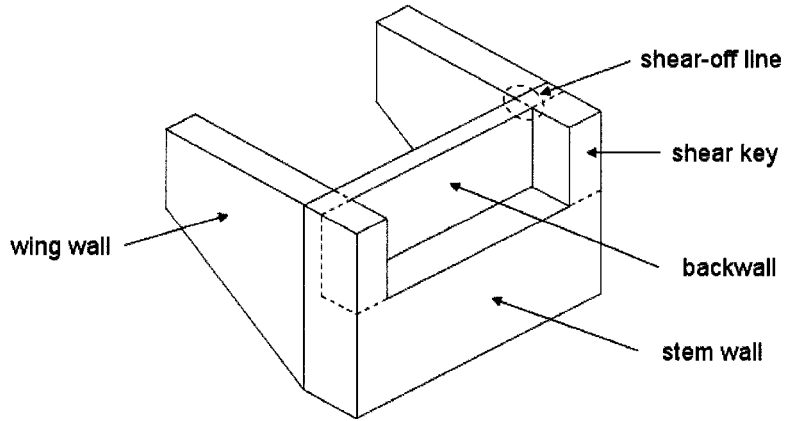
where, k_i is $20.0 \frac{\text{kip/in}}{\text{ft}}$, w is the width of the backwall (ft), and h_{abut} is the height of the backwall (ft). The ultimate abutment capacity due to the backfill soil can be expressed as

$$P_{abut} = A_e \times (5.0 \text{ ksf}) \times \left(\frac{h_{abut}}{5.5 \text{ ft}} \right) \quad (2.23)$$

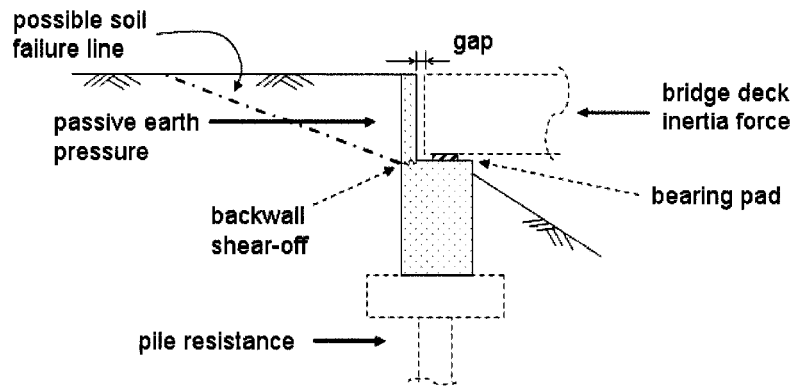
where, A_e = the effective abutment area (ft^2). The coefficient (5.0 ksf) is intended to account for the static shear strength of a typical embankment material. Using the initial stiffness and ultimate capacity, a 1-D load-displacement curve can be approximated using a simple curve as shown in Figure 2.20.

2.9 Summary

This chapter reviewed soil-structure interaction among bridge components with a focus on the interface spring characteristics of piles and pile groups in various soil and loading conditions such as sand, clay, and liquefiable soils subjected to static and dynamic loadings. The soil-pile system response subjected to lateral spreading and factors that can influence the dynamic response characteristics of pile-supported structures were reviewed. Finally, the soil-abutment interaction was briefly discussed.



(a) seat abutment structure components



(b) bridge deck-abutment-soil

Figure 2.19: Schematic of seat-type abutment structure components and bridge deck-abutment-soil interaction

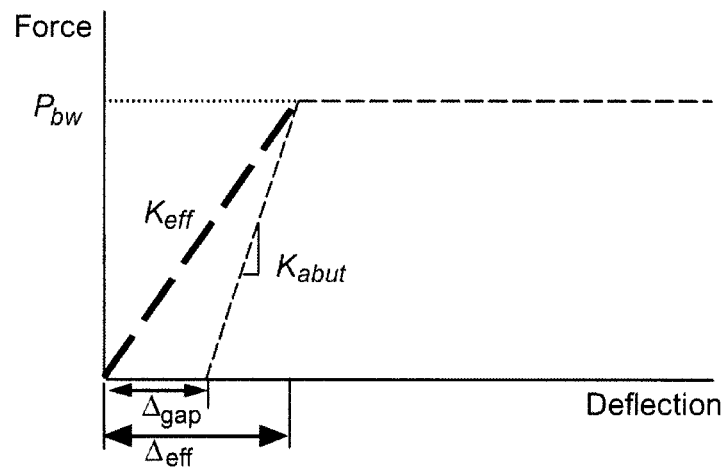


Figure 2.20: Simplified abutment load-deflection characteristic using initial stiffness and ultimate resistance in Caltrans' guideline - after SDC (2004)

Chapter 3

PERFORMANCE BASED EARTHQUAKE ENGINEERING**3.1 Introduction**

The seismic performance assessment of civil engineering facilities allows owners to consider a continuous range of meaningful information in making economical design choices rather than basing design on a binary decision (i.e., safe or unsafe). However, a reliable seismic performance estimation is challenging since it inherently includes uncertainties of earthquake motions and soil-structure response. Prediction of response requires well-defined structural/geotechnical models that can account for soil-structure interaction for a range of geotechnical and structural input parameters. In this context, the Pacific Earthquake Engineering Research Center (PEER) has developed a probabilistic framework and an analytical tool (OpenSees) that allow evaluation of performance taking uncertainties into account quantitatively.

In this chapter, the PEER Performance Based Earthquake Engineering (PBEE) framework is described. Numerical and closed form integration of uncertainties in the PEER framework are discussed. Several characteristics of selected motions and their effect on demand models are briefly investigated.

3.2 Performance Based Earthquake Engineering Methodology

The PEER PBEE framework computes risk as a function of ground shaking through several intermediate steps using the Total Probability Theorem. This risk estimation includes many sources of uncertainties that can be handled probabilistically. The intermediate steps are described in terms of seismic hazard, demand hazard, and damage hazard. The seismic hazard is characterized in terms of an Intensity Measure, IM which describes the level of ground shaking. The demand hazard is some form of response, characterized in terms of an Engineering Demand Parameter, EDP, at the site of interest. The damage hazard results

from these EDP's and it is characterized in terms of a Damage Measure. Finally, the risk is expressed in a form that is useful to decision makers, associated with selected Decision Variables, DV. IMs can be defined by ground motion parameters such as peak ground acceleration (PGA), peak ground velocity (PGV), Arias Intensity (I_a), cumulative absolute velocity (CAV_5), first mode spectral acceleration ($S_a(T_1)$), etc. Possible EDPs could involve column drift ratio, curvatures, shear force, bending moment, and settlement of a supporting system. DMs can be related to structural damage such as cracking, spalling, bar buckling, and column shear failure, or to non-structural damage such as slope failure. DVs can be expressed in terms of repair cost, downtime, repair time, loss of life, and loss of facility capacity among others. The hazard or risk curves for the interim variables (e.g., IM, EDP, DM, or DV) are expressed in terms of a relationship between the variable and its exceedance rate. The exceedance rate can be described by the mean annual frequency (MAF) or return period (T_R). For example, owners can be informed using a DV risk curve that an existing or planned bridge will have x dollars of damage every y years. The mean annual rate of exceedance in the DV risk curve can be obtained combining all the other variables using the total probability theorem, which in discrete form results in,

$$\lambda_{dv_l} = \sum_{k=1}^{N_{dm}} \sum_{j=1}^{N_{edp}} \sum_{i=1}^{N_{im}} P[DV > dv_l | dm_k] P[DM = dm_k | edp_j] P[EDP = edp_j | im_i] \Delta \lambda_{im_i} \quad (3.1)$$

where N_{dm} , N_{edp} , and N_{im} are the number of increments of DM, EDP, and IM, respectively. $P[DV > dv_l | dm_k]$ represents the conditional probability of DV exceeding dv_l at a given dm_k . $P[DM = dm_k | edp_j]$ and $P[EDP = edp_j | im_i]$ represent conditional probabilities of $DM = dm_k$ and $EDP = edp_j$ at given edp_j and im_i , respectively. The $\Delta \lambda_{im_i}$ is an increment of mean annual rate of exceedance in a IM hazard curve. In the PEER PBEE framing equation, each conditional probability term includes the uncertainty between the interim variables at an increment step and contributes to the mean annual rate of exceedance in the DV risk curve.

3.3 Numerical Integration of Uncertainties in PBEE Framework

In this section, details on the process required to integrate the uncertainties that leads to hazard and risk curves are presented.

3.3.1 IM Hazard from PSHA

The process of building up a DV risk curve starts with an IM hazard curve obtained from a Probabilistic Seismic Hazard Analysis (PSHA). In this curve, shown schematically in Figure 3.1, a mean annual rate of exceedance (λ_{IM}) for any particular value of a specified IM for a given site is obtained. If a specific earthquake source is considered, the mean annual rate of exceedance of a certain IM, such as PGA and $S_a(T_1)$, is obtained by multiplying the average rate of threshold magnitude exceedance (ν) by the probability that an IM is greater than a particular IM of interest. The average rate of threshold magnitude exceedance (ν) is determined using recurrence laws considering a certain threshold magnitude such that,

$$\nu = 10^{a-b m_o} \quad (3.2)$$

where, a and b can be obtained from the Gutenberg-Richter recurrence law and m_o is a threshold magnitude. The probability that an IM is greater than a particular IM of interest is calculated considering uncertainties in distance and magnitude for the potential earthquake sources such that,

$$P[IM > im] = \int \int P[IM > im|m, r] f_M(m) f_R(r) dm dr \quad (3.3)$$

where, $P[IM > im|m, r]$ is the probability that an IM level is exceeded for a given magnitude and distance (m and r), usually obtained from attenuation relationships. $f_M(m)$ and $f_R(r)$ are the probability density functions for magnitude and distance, respectively. Considering N_f potential earthquake sources at a site, the total average exceedance rate can be obtained by adding the sources such that,

$$\lambda_{im} = \sum_{i=1}^{N_f} \nu_i \int \int P[IM > im|m, r] f_{Mi}(m) f_{Ri}(r) dm dr \quad (3.4)$$

It is noted that λ_{im} is expressed in 1/time units and it is not a probability since λ_{im} is a multiplication of ν and $P[IM > im]$. If the probability of at least one exceedance of IM

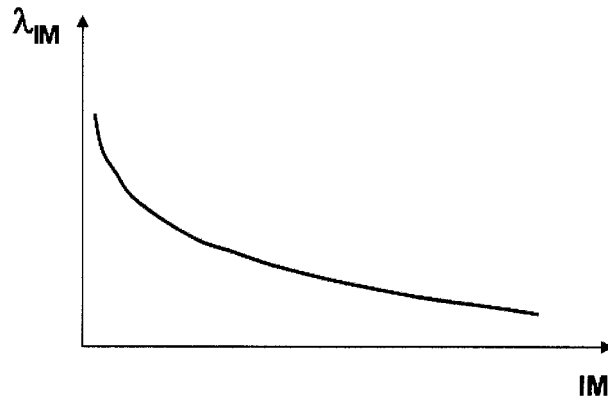


Figure 3.1: Schematic IM hazard curve from PSHA

= im for a certain period (t) of time is of interest, it can be approximated using Poisson's model such that

$$P[N \geq 1] = 1 - e^{-\lambda t} \quad (3.5)$$

Hazard curves can be obtained for specific sources using a PSHA or can also be obtained from USGS hazard websites for several IMs such as PGA and $S_a(T)$ for several return periods (1 %, 2 %, 5 %, 10 %, 20 %, and 50 % in 50 years) and several structural periods (T) (0.1, 0.2, 0.3, 0.5, 1.0, and 2.0 sec). The USGS hazard website can be found at <http://eqint.cr.usgs.gov/eq-men/html/deaggint2002-06.html>.

3.3.2 EDP Hazard

From the IM hazard curve, several IMs that corresponds to target occurrence rates (e.g., $\lambda_{im} = 0.01386$ (1/75), 0.0021 (1/475), and 0.0004 (1/2475) or 50%, 10%, and 2% in 50 years) are determined and used to select and scale input motions. Using these motions in numerical simulations, a relationship between EDP and IM can be obtained. This relationship is referred as *demand model*. Demand models show different levels of dispersion. Therefore, a correlation can be defined in statistical ways. The source of dispersion in the relationship comes from earthquake motion uncertainties, soil and structural property uncertainties,

numerical model uncertainties, etc.

EDP hazard curves can be obtained from the IM hazard curve through numerical integration of the uncertainties in the EDP-IM relationship using Equation 3.6.

$$\lambda_{edp_j} = \sum_{i=1}^{N_{IM}} P[EDP > edp_j | im_i] \Delta\lambda_{im_i} \quad (3.6)$$

The probability term in the equation can be obtained from fragility curves which include EDP uncertainties over an entire IM range. To construct a fragility curve, the data in the EDP-IM relationship is grouped into several im ranges (im_i) over the entire IM range. The number of im intervals defines the number of points in the fragility curve to be constructed. To obtain a smooth fragility curve, a reasonable number of im intervals is needed. The data in each IM group is statistically processed and probability distributions of EDP for different IMs are obtained. Figure 3.2a schematically shows the construction of a fragility curve for a particular EDP(j). In the process, the probability density function for each im_i is integrated over the EDP range that is greater than the selected edp_j (shaded areas in the plot). Other points on the EDP fragility curve are obtained considering other probability functions corresponding to other im_i . This procedure is repeated for the other probability functions at different IMs. Therefore, in a single fragility curve, the probability information of the EDP that is greater than the value of interest is included over the entire range of IMs. The values of $P[EDP > edp_j | im_i]$ in Equation 3.6 represents the fragility curve for a particular edp_j , which is function of an IM. For another fragility curve, the same integration is repeated using an EDP range that is greater than edp_{j+1} over the entire range of IM to construct the appropriate fragility curve. This is schematically shown in Figure 3.2b.

Once all of the fragility curves are obtained, the EDP hazard curve can be calculated by integrating the IM hazard curve and fragility curves using Equation 3.6. The procedure is illustrated in Figure 3.3. First, the IM hazard curve and a fragility curve for a particular edp_j is divided into N_{IM} intensity measure intervals, and the $P(i, j) = P[EDP > edp_j | im_i]$ is multiplied by $\Delta\lambda_{IM_i}$. This procedure is repeated over all the discretized IMs (i.e. $i=1$ to N_{IM}) and all the products are summed to have one point in the EDP hazard curve. To obtain more points in the EDP hazard curve, the integration process is repeated for other edp_{j+1} fragility curves.

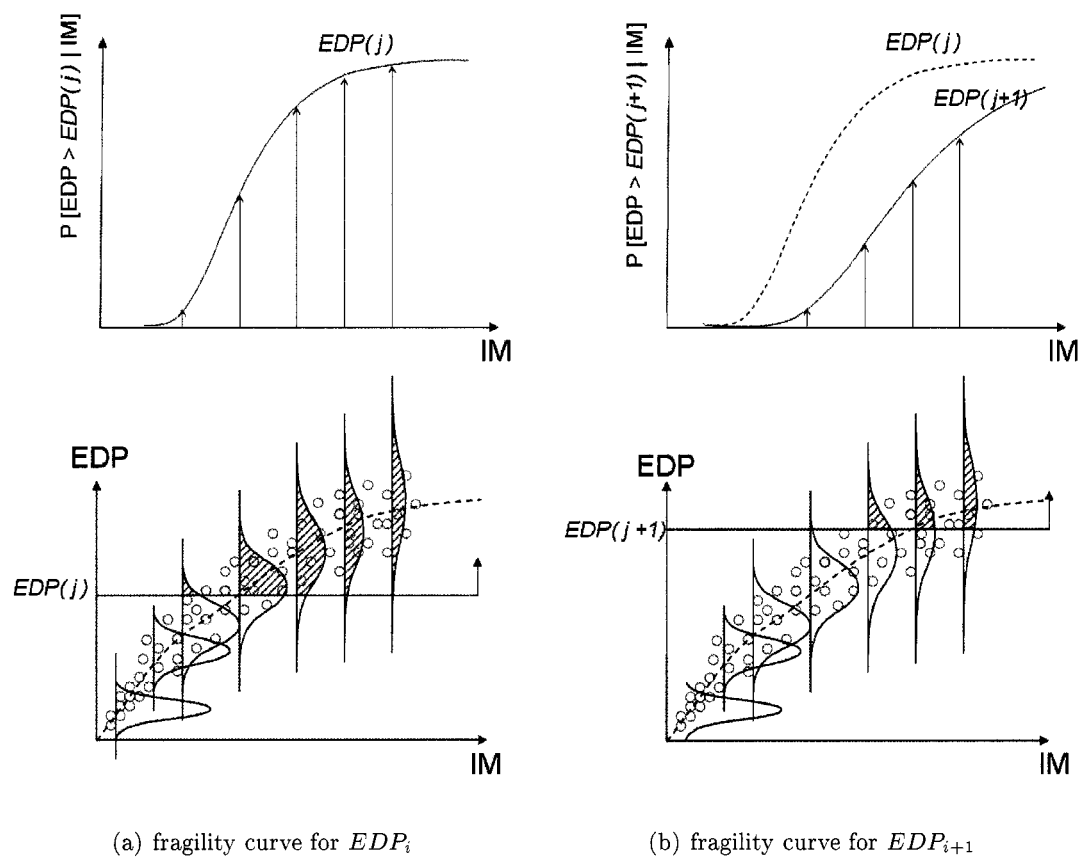


Figure 3.2: Construction of fragility curves from IM-EDP correlations (demand model)

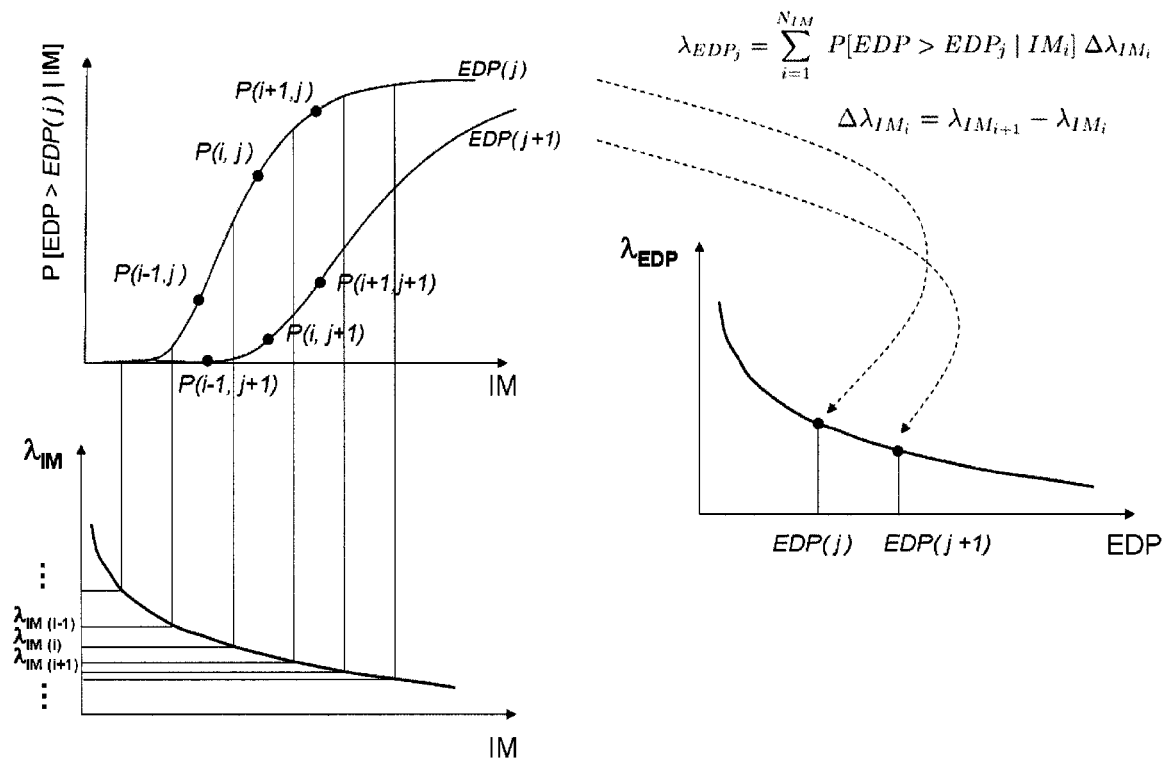


Figure 3.3: Construction of EDP hazard curve from IM hazard curve and fragility curves

3.3.3 DM Hazard

Similarly, the DM hazard curve is obtained by following Equation 3.7 and using the EDP hazard curve and DM-EDP relationship (*damage model* or *capacity model*) that correlate the EDP response into physical descriptions such as cracking, spalling, and fracture. In this procedure, the capacity model can be obtained from an experimental test database (Berry and Eberhard, 2003; Hose et al., 2000) or numerical analyses. Damage often is collected in discrete manner.

$$\lambda_{dm_k} = \sum_{j=1}^{N_{EDP}} P[DM > dm_k | edp_j] \Delta\lambda_{edp_j} \quad (3.7)$$

3.3.4 DV Risk

The DV risk curve is determined from the DM hazard curve and the DM-DV relationship (*decision model*) using Equation 3.8. The correlation between DM and DV is obtained from professional surveys, early earthquake-induced repair cost data, or repair cost estimation from research laboratory and probabilistic estimation for operational cost of highway bridge functionality such as traffic volume, lane and speed reduction or access to emergency vehicles.

$$\lambda_{DV_l} = \sum_{k=1}^{N_{DM}} P[DV > DV_l | DM_k] \Delta\lambda_{DM_k} \quad (3.8)$$

3.3.5 PEER PBEE Framework Equation

The PEER PBEE framework equation (Equation 3.1) can be obtained by combining the individual probability estimation from each intermediate steps into a single equation. Using Equations 3.6 and 3.7 and noting $\Delta P[y > y^* | x] = P[y = y^* | x]$,

$$\begin{aligned} \Delta\lambda_{edp_j} &= \sum_{i=1}^{N_{IM}} \Delta P[EDP > edp_j | im_i] \Delta\lambda_{im_i} \\ &= \sum_{i=1}^{N_{IM}} P[EDP = edp_j | im_i] \Delta\lambda_{im_i} \end{aligned} \quad (3.9)$$

$$\begin{aligned}
\Delta\lambda_{dm_k} &= \sum_{j=1}^{N_{EDP}} \Delta P[DM > dm_k | edp_j] \Delta\lambda_{edp_j} \\
&= \sum_{j=1}^{N_{EDP}} P[DM = dm_k | edp_j] \Delta\lambda_{edp_j}
\end{aligned} \tag{3.10}$$

Then, Equation 3.8 can be expressed in combined form using Equations 3.9 and 3.10 such that

$$\begin{aligned}
\lambda_{dv_l} &= \sum_{k=1}^{N_{dm}} P[DV > dv_l | dm_k] \Delta\lambda_{dm_k} \\
&= \sum_{k=1}^{N_{dm}} P[DV > dv_l | dm_k] \sum_{j=1}^{N_{edp}} P[DM = dm_k | edp_j] \Delta\lambda_{edp_j} \\
&= \sum_{k=1}^{N_{dm}} P[DV > dv_l | dm_k] \sum_{j=1}^{N_{edp}} P[DM = dm_k | edp_j] \sum_{i=1}^{N_{im}} P[EDP = edp_j | im_i] \Delta\lambda_{im_i} \\
&= \sum_{k=1}^{N_{dm}} \sum_{j=1}^{N_{edp}} \sum_{i=1}^{N_{im}} P[DV > dv_l | dm_k] P[DM = dm_k | edp_j] P[EDP = edp_j | im_i] \Delta\lambda_{im_i}
\end{aligned} \tag{3.11}$$

3.4 Selection of IMs

In the PEER equation (Equation 3.1 or 3.11), the deaggregated variables are aggregated by integration over all the selected intermediate variables. Therefore, it is important to ensure the EDPs, DMs, and DVs are not affected by conditional IMs. Earthquake motion characteristics often vary with magnitude and distance. Some EDPs such as liquefaction are influenced by the magnitude and distance effects embedded in the IMs resulting in different EDPs even with similar IMs. Using regression analysis, the residual (regression error) of each EDP with magnitude or distance can be evaluated. If the EDP residuals vary, the motions are not *sufficient* and influence upstream variables. However, if the residual is relatively constant over magnitudes or distances, the EDP responses are independent of magnitudes and distance for the selected IMs and the IM is *sufficient*. This residual variation is schematically shown in Figure 3.4 along with magnitude or distance for sufficient and not-sufficient cases.

Another aspect of a selected motions is its *efficiency*. Earthquake motions can be characterized by several IMs such as PGA , PGV , I_a , CAV_5 , and $S_a(T_1)$. The selected motions

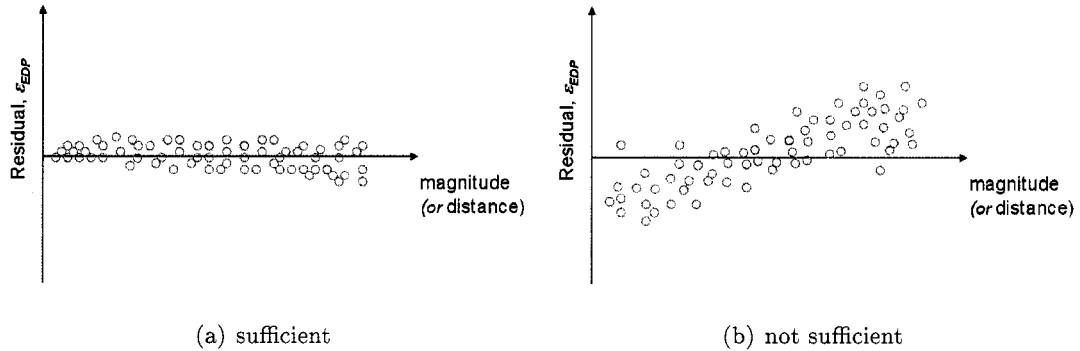


Figure 3.4: Schematic illustration of sufficiency in IMs

can be scaled to have the same IM according to the mean annual exceeding rate of interest for simulations. However, the motions may still have different characteristics such as frequency content, duration, number of cycles, etc resulting in a large variability in EDP-IM relationships. This large variation implies that the IM is *not efficient* and additional motions should be added to have suitable confidence in the probability distribution of EDP-IM relationships. For example, if an EDP probability density function (PDF) for a given IM has a wide dispersion, more effort (i.e., a greater number of motions and simulations) will be required to obtain the necessary confidence on the PDF information. On the other hand, if the motions give less dispersion, the bell-shaped probability distribution will be tall and narrow and a small number of motions is enough to have confidence. In this case, it is said the IM is *efficient*. Efficiency affects the uncertainty in EDP-IM relationships. Use of efficient IMs reduce uncertainties and thereby the EDP hazard curves with smaller return periods result in less conservative risk estimations. More information on *efficiency* and *sufficiency* can be found in Luco and Cornell (2001) and Kramer and Mitchell (2006).

PGA often shows large variability in EDP-IM relationships due to the fact that additional motion characteristics related to the domain response mechanism are not included in PGA. Therefore, $S_a(T_1)$ is commonly used as an improved IM over PGA. However, $S_a(T_1)$ does not account for frequency information at $T \neq T_1$ and period elongation effects due to nonlinear response or soil-structure interaction (Krawinkler and Miranda, 2004). Kramer and Mitchell (2006) found CAV_5 is efficient and sufficient for liquefaction potential estimation.

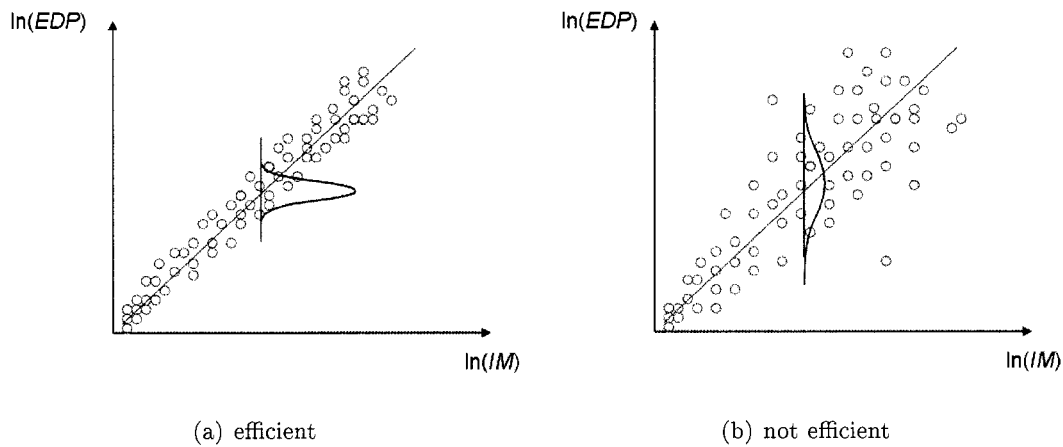


Figure 3.5: Schematic illustration of IM efficiency

The estimation of the median and uncertainty in a demand model (EDP-IM relationship) is affected by the ground motions used in the analysis or numerical simulations. Among several ways to select or scale ground motions the *cloud method*, *stripe method*, and *incremental dynamic analysis (IDA)* are commonly used. Figure 3.6 illustrates these methods using schematic EDP-IM plots. In the cloud method, a wide range of ground motions are selected. Since the cloud method uses motions from which a wide range of IM can be computed, the median and dispersion information of the seismic demand model (EDP-IM relationship) can be obtained for a broad selection.

In the IDA method, motions with selected IMs are incrementally scaled from small to large IMs. This method is the dynamic equivalent to the familiar static pushover analysis. This method provides information on the evolution of the median and dispersion of the demand model with incrementally scaled motions. However, care should be taken when scaling small intensity records by large scale factors.

Finally, in the stripe method, all selected motions are scaled to have the same IM values for selected IMs. This method is a special case of the IDA method. The benefit of the stripe method is that the median and dispersion is not subjected to the regression error of considering an entire IM range. However, the major drawback is that an intensity-dependent demand model cannot be obtained from a single stripe analysis. Mackie and Stojadinovic

(2005b) investigated each method and found that with the same computational effort, the cloud method and IDA method provide similar estimates of the median and dispersion.

3.5 Uncertainty Integration Approximation

Demand models that relate EDPs to IMs can often be approximated by power laws. Therefore, the mean EDP-IM relationship in (natural) log space can be approximated by a linear function. That is,

$$EDP = a (IM)^b \quad (3.12)$$

$$\ln(EDP) = A + B \ln(IM) \quad (3.13)$$

The coefficients in this equation can be obtained from a median relationship using a least-square regression on the demand model data.

For a large range of IMs, the median EDP-IM relationship may not be linear and data dispersion in the demand model may increase due to high nonlinear response in the system. In log space, however, the degree of dispersion over the entire IM range is uniform if a lognormal distribution of EDP at a given IM is assumed. This homoskedasticity assumption facilitates the integration process using a closed form solution (Jalayer, 2003). The IM hazard curve can also be assumed to follow a power law such as,

$$\lambda_{im} = k_o (im)^{-k} \quad (3.14)$$

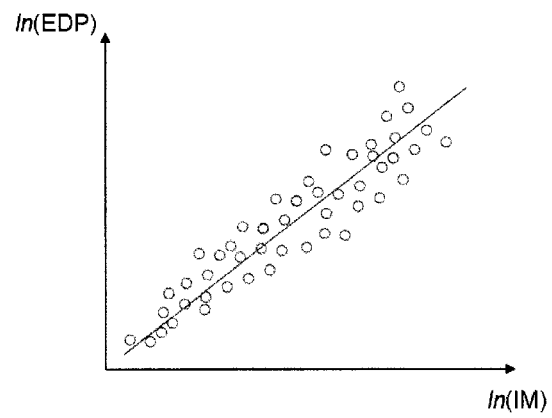
Equation 3.14 can be expressed in log scale as,

$$\ln(\lambda_{im}) = \ln(k_o) - k \ln(im) \quad (3.15)$$

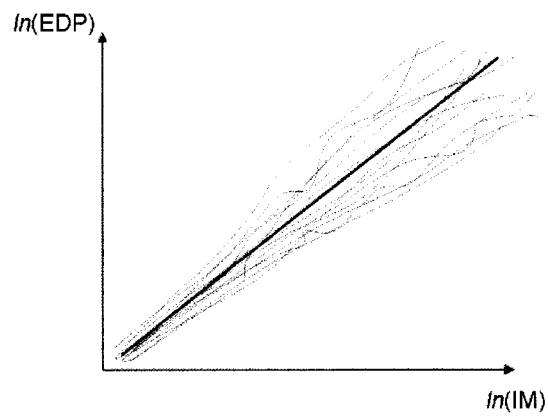
The two unknown coefficients in the equation can be obtained solving Equation 3.14 or 3.15 by substituting IM values and mean annual rates of exceedance for the two hazard levels (e.g. (IM_1, λ_{IM_1}) and (IM_2, λ_{IM_2})). This assumption should be used with care, especially for very low or high IMs.

The combined closed form solution, used to create the EDP hazard curve using these assumptions, can be expressed as

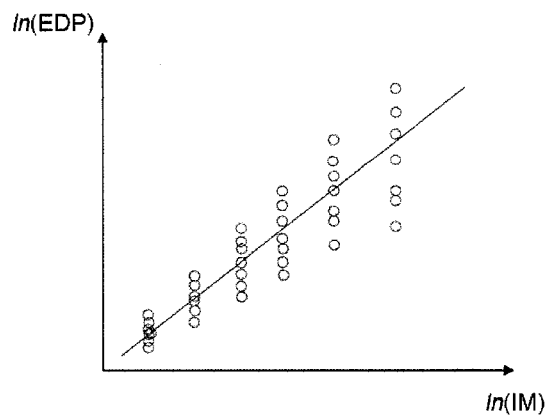
$$\lambda_{edp} = P[EDP > edp|IM] = k_o \left[\left(\frac{edp}{a} \right)^{1/b} \right]^{-k} \exp\left[\frac{1}{2} \frac{k^2}{b^2} \sigma_{\ln(EDP|IM)}^2 \right] \quad (3.16)$$



(a) cloud analysis



(b) incremental demand analysis (IDA)



(c) stripe analysis

Figure 3.6: Schematic illustration of demand models according to various schemes of ground motion selection

In this equation, the first term

$$k_o \left[\left(\frac{edp}{a} \right)^{1/b} \right]^{-k}$$

represents the EDP-IM median relationship and the second term

$$\exp\left[\frac{1}{2} \frac{k^2}{b^2} \sigma_{\ln(EDP|IM)}^2\right]$$

can be seen as an amplification factor on λ_{edp} due to the uncertainty in the EDP-IM relationship. If the $\sigma_{\ln(EDP|IM)}$ is equal to 0, the uncertainty amplifier becomes zero. If $\sigma_{\ln(EDP|IM)}$ is greater than 0, then the value of λ_{edp} is amplified.

Details on the derivation of this equation are described in Jalayer (2003). This closed form solution procedure can be extended to DM hazard curves and DV risk curves using similar assumptions and arguments. Mackie and Stojadinovic (2005a) developed a visual tool that generates the DV risk curves using a closed form solution.

3.6 Summary

This chapter introduced the PEER PBEE framework including the estimation of intermediate variables used in the PBEE framework and corresponding fragility curves. Uncertainty integration through the PBEE framework equation was described. Important aspects such as IM sufficiency and efficiency were discussed for selection of IMs. Finally, a closed form solution is briefly described as an approximate method for obtaining hazard and risk curves.

Chapter 4

PHYSICAL AND NUMERICAL MODELING OF BRIDGE STRUCTURES**4.1 Introduction**

The seismic response of bridges and other structures, particularly those supported by drilled shafts, can be strongly influenced by soil-pile-structure interaction (SPSI). SPSI can be complicated and influenced by many factors including ground motion intensity, directions of shaking, various structural configurations including clear height above the ground surface, embedment length, and pile head rotational constraints.

To evaluate the seismic SPSI in a bridge and bridge components, a series of centrifuge tests were performed in the U.C. Davis centrifuge facility in collaboration with researchers from that institution (Ilankatharan and Kutter 2005). These tests were a part of a larger research program on soil-foundation-structure interaction effects funded by the George E. Brown, Jr. Network for Earthquake Engineering Simulation (NEES) (Wood et al., 2004). The tests described in this dissertation were performed on: i) a two-span bridge with different clear column heights, ii) several two-column bents oriented at different angles with respect to the direction of primary shaking, and iii) several bents and single piles with different pile embedment lengths and masses. These models were subjected to various earthquake motions with different intensities and frequency contents to trigger different levels of system nonlinearity.

The Open System for Earthquake Engineering Simulation (OpenSees) framework was used to simulate the centrifuge response. To represent the centrifuge structures, two- and three-dimensional structural models were attached to 2-D shear beam soil columns and conventional interface springs.

This chapter describes details of the three centrifuge tests and the strategies used in OpenSees to capture the recorded response. Comparisons between the experimental and

Table 4.1: Scaling relationships for centrifuge modeling - after Wood (2004)

Quantity	Full scale (prototype, 1g)	Centrifuge models at N g's
Length	1	$1/N$
Area	1	$1/N^2$
Volume	1	$1/N^3$
Mass density	1	1
Force	1	$1/N^2$
Stress (force/area)	1	1
Time (dynamic event)	1	1
Frequency	1	N

numerical results are presented in Chapter 5 and Chapter 6.

4.2 Centrifuge Test Concept

The basic concept used in centrifuge tests is based on the fact that the response of a scaled soil model is similar to the response of a prototype soil system when the model is subjected to an artificial gravity that increases the stresses to the level of stress in the prototype model. Using this idea, the dimensions of a model are determined based on the selected controlled gravity field. For example, if a model of a prototype structure is built to a $1/N$ scale, then a gravitational acceleration field N times larger than the prototype gravity is required to ensure that the stresses in the model are similar to those experienced in the prototype structure. The increased gravity field can be obtained using the centrifugal accelerations that can be achieved in a centrifuge.

A set of scaling factors can be established for various physical parameters using dimensional analysis and governing equations. These scaling laws are summarized in Table 4.1. The details of these derivations are described in Wood (2004).

This centrifuge approach is useful to evaluate seismic soil-structure-interaction; since it is difficult to test large-scale structural and geotechnical systems in the field with realistic earthquake loading. In this research, the selected centrifuge gravity field was 52g. Therefore,

the prototype dimensions were 52 times larger than the centrifuge specimen dimensions.

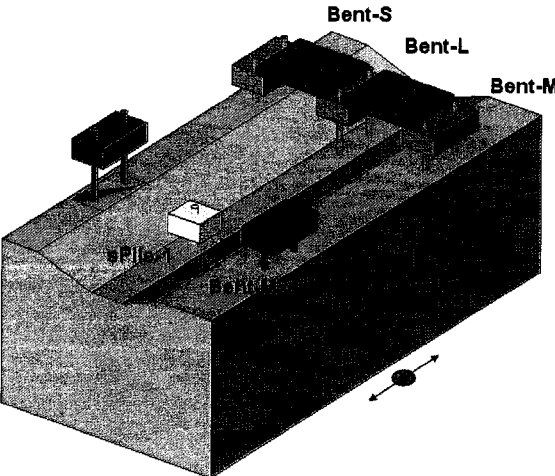
4.3 Bridge Structure Models in Centrifuge Tests

This section briefly discusses the three centrifuge test models performed at the U.C Davis centrifuge facility to investigate SPSI effects on bridge structures. All of the tests were completed in collaboration with the geotechnical research team at the University of California at Davis. Mahadevan Ilankatharan, a co-worker at UC Davis, worked as a primary tester and was in charge of instrumentation, calibration and data processing. Basically, all of the superstructures had accelerometers to measure accelerations in several directions. Piles had pairs of strain gauges at several locations to measure relative strains, hence, pile curvatures. Each centrifuge test had an vertical array of accelerometers in the soil to record the free-field response. Accelerations in the soil and piles were recorded at 2.6 m depth from surface. Centrifuge base accelerations were also recorded in three directions. The instrumentation program and calibration information are not included in this dissertation. Details on the centrifuge tests have been compiled in several centrifuge test data reports published elsewhere (Ilankatharan et al., 2005, 2007a,b).

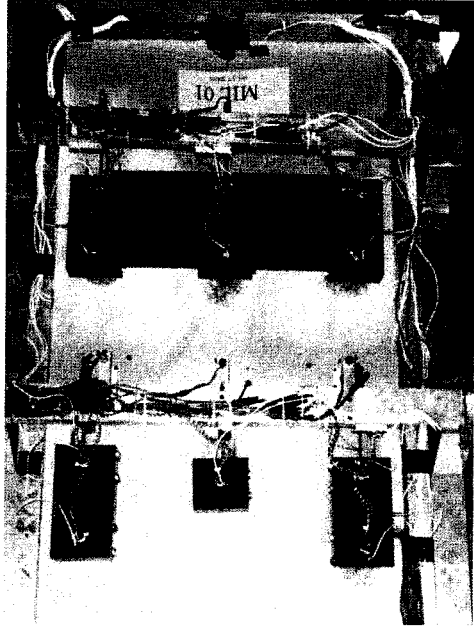
4.3.1 Three centrifuge tests

Schematic drawings of the three centrifuge tests are shown in Figures 4.1a to 4.3a. The final centrifuge test setups are shown in Figures 4.1b to 4.3b.

The first centrifuge test, named CFG1 in Figure 4.1a, included four structural models: a two-span bridge with three two-column-bents, a two-column-bent, a two-column-bent with a pile cap and a single pile. Clear heights above the ground surface for the three bridge bents were 2.6 m, 6.5 m, and 3.9 m and the embedment lengths were 15.6 m, 11.7 m, and 14.3 m in prototype scale, respectively. In this dissertation, the bridge bents are designated based on their clear heights as *Bent-S*, *Bent-L*, and *Bent-M*. The individual bent located in the same soil profile as *Bent-M* is referred as *Bent-M2*. The main purpose of this test was to investigate the effect of clear height above ground on the dynamic response of bridges and on SPSI.

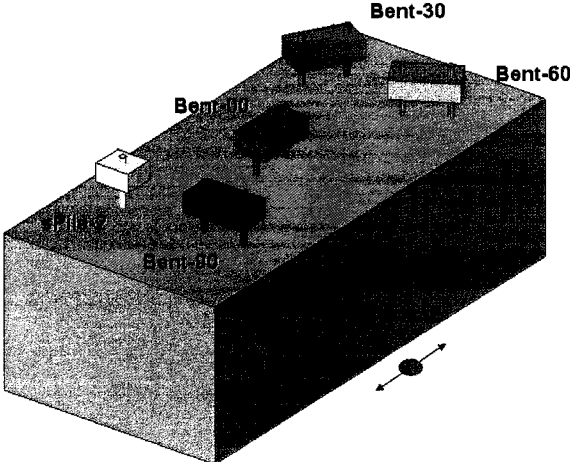


(a) CFG1

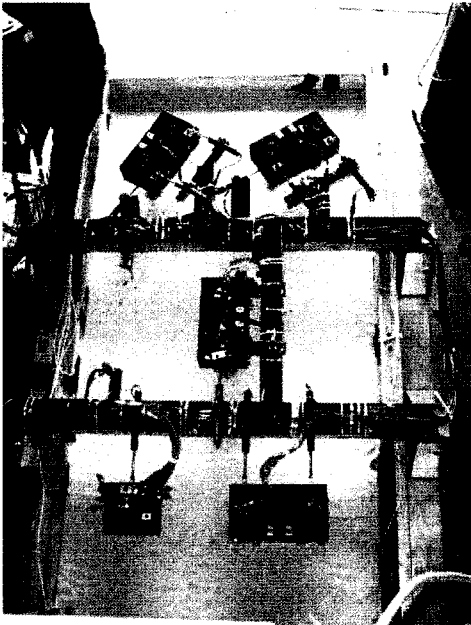


(b) CFG2

Figure 4.1: Schematic drawing and test setup of CFG1

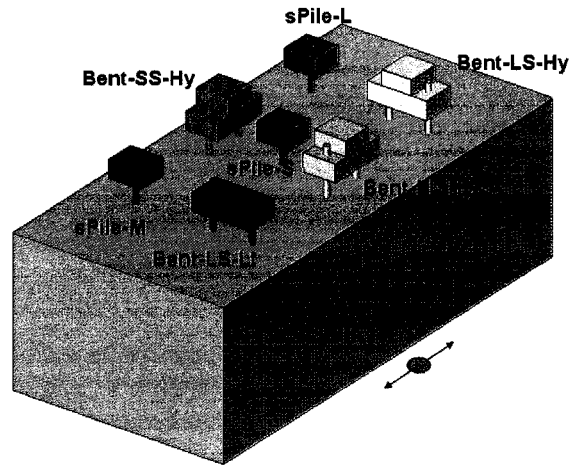


(a) CFG1

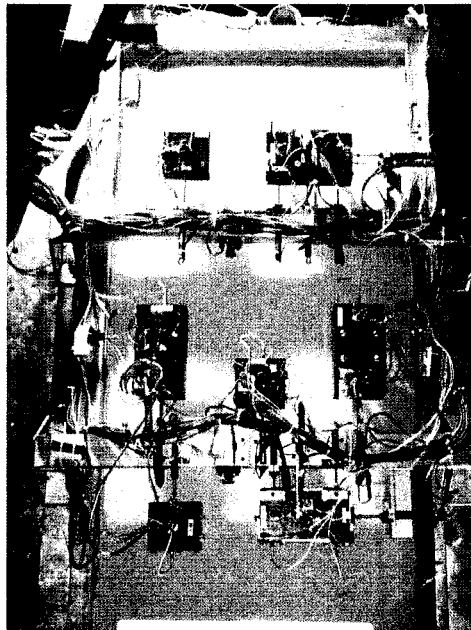


(b) CFG2

Figure 4.2: Schematic drawing and test setup of CFG2

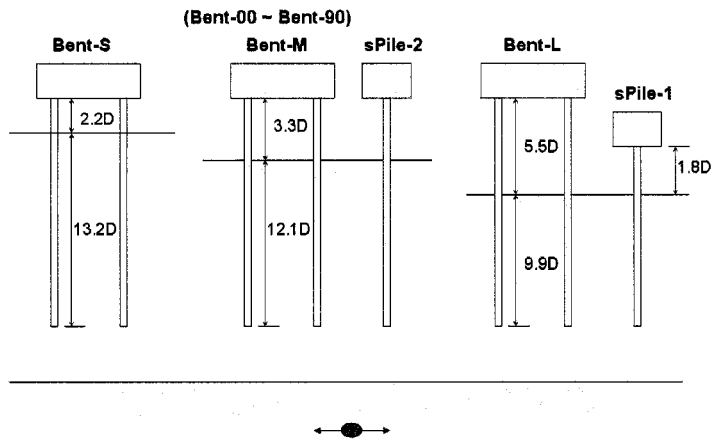


(a) CFG1

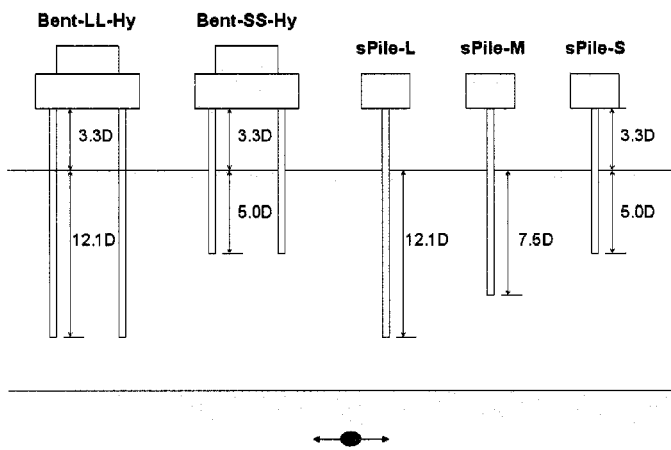


(b) CFG2

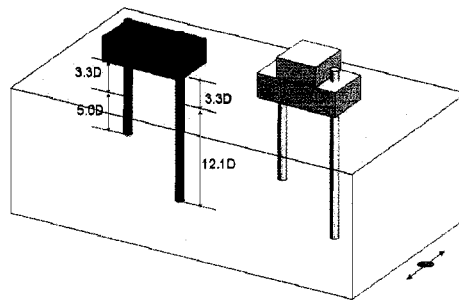
Figure 4.3: Schematic drawing and test setup of CFG3



(a) CFG1 and CFG2



(b) CFG3



(c) CFG3

Figure 4.4: Structural embedment lengths and clear heights

The second centrifuge test, named CFG2 in Figure 4.2a, included four two-column bents and one single pile bent. The bents had the same configuration and structural properties as Bent-M in CFG1. The two-column bents were oriented at 0° , 30° , 60° , and 90° to the primary axis of shaking. In this dissertation, bent designations are chosen according to their orientation. The bent parallel to the shaking direction is designated as *Bent-00*, and is located at the center of the container. The bent with an orientation perpendicular to the shaking direction is designated as *Bent-90*. The purpose of these tests was to study the effect of twisting on the response of oriented bents and the effect of SPSI associated with multi-directional pile shaking.

The third centrifuge test shown in Figure 4.3a included four bridge bents and three single piles. The aim of this test was to trigger larger nonlinear response in the structural and geotechnical components. The four bents were grouped into two groups. The bents in the first group had different pile lengths and similar structural characteristics. One bent (Bent-LS-Hy) had more mass than the other (Bent-LS-Lt). These two bents were designed to be affected by torsion (θ_{zz} in Figure 4.6) and multi-directional lateral soil-pile interaction. The bents in the second group had the same pile lengths and the same (heavy) mass. However, one bent (Bent-SS-Hy) had short piles and the other (Bent-LL-Hy) had long piles. These two bents were designed to trigger higher nonlinear soil-pile system response. The three single piles (sPile-S, sPile-M, sPile-L) were set to have different embedment lengths (short, medium, and long). Embedment lengths for the short, medium, and long piles were 5D, 7.5D, and 12D, respectively; where D represents pile diameter (1.18 m in prototype scale).

Figure 4.4 shows the pile embedment lengths and structural clear heights used in the three centrifuge tests. Since the structures used in each test were very similar with slightly different configurations (such as pile embedment lengths, clear heights, superstructure masses, and shaking orientations), comparisons between each other's recorded response provide important insight on the dynamic response of bridges. For simplicity, in this dissertation, the two-column bents and structures supported by a single pile or drilled shaft are referred as *bent* and *single pile*.

Table 4.2: Aluminum type in structures

Test name	Structure name	Aluminum type
CFG1	sPile-1	6061-T6
	Bent-M2	6061-T6
	Bent-S	6061-T4
	Bent-M	6061-T4
	Bent-L	6061-T4
CFG2	sPile-2	6061-T6
	Bent-00	6061-T6
	Bent-30	6061-T4
	Bent-60	6061-T4
	Bent-90	6061-T6
CFG3	sPile-S	6061-T4
	sPile-M	6061-T6
	sPile-L	6061-T4
	Bent-LL-Hy	6061-T4
	Bent-SS-Hy	6061-T4
	Bent-LS-Hy	6061-T6
	Bent-LS-Lt	6061-T6

4.3.2 Bridge Structures and Piles

The centrifuge bridge piles and superstructure were made of aluminum 6061-T4 ($E = 68.5$ GPa; yield strength = 130 MPa) and aluminum 6061-T6 ($E = 68.5$ GPa; yield strength = 255 MPa). In prototype scale the aluminum tubing cross section had an outer diameter of 0.991m and a wall thickness of 0.0952m. All piles were wrapped with plastic layers resulting in a 1.181m outer diameter. The yield and ultimate bending moment for the T6 pile column were 7890 kN-m and 10500 kN-m, respectively. The yield and ultimate bending moment for the T4 pile column were 4022 kN-m and 5364 kN-m, respectively. The aluminum type used in each structure is summarized in Table 4.2.

4.3.3 Soil

The soil chosen for the centrifuge tests was a Nevada Sand. A target relative density of 80% (1.66 Mg/m^3) was used in all tests. The soil specimens were prepared by dry pluviation

in a flexible shear beam model container. To measure the free-field soil response, several accelerometers were embedded in soil in a vertical array and in a plane array located at a 2D depth ($D = \text{pile diameter}$).

4.3.4 Input Motions

The input motions used in the centrifuge tests were based on the NORTHRIDGE 01/17/94 1231, CENTURY CITY LACC NORTH, 090 (CMG STATION 24389) earthquake motion. This motion has a 0.26g peak acceleration, 0.21 m/sec peak velocity, and 0.07 m peak displacement. The motion was scaled and applied to the centrifuge resulting in 0.08g, 0.25g, 0.59g, and 0.75g peak accelerations at the centrifuge container base. Similar centrifuge base motions were used in all the tests. In this dissertation, the motions are referred, with their peak acceleration, as the Northridge motion. Typical recorded motions at the centrifuge base are shown in Figure 4.5a.

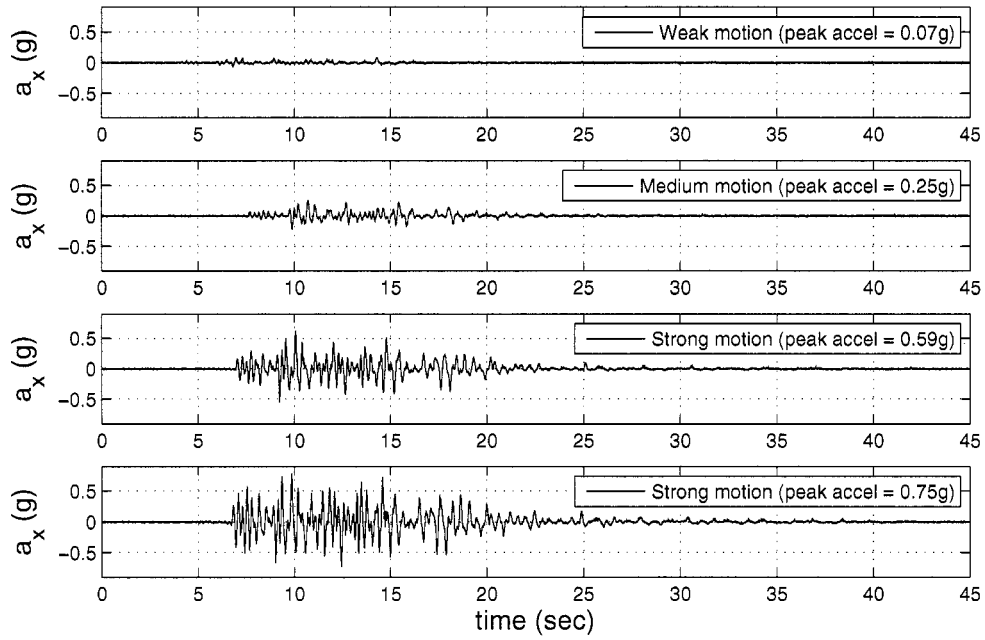
To investigate the effect of motion frequency content on the structural response, several frequency-sweeping motions were generated and applied with different peak accelerations. A couple of these motions are shown in Figure 4.5b. More details on the target and attained base motions can be found in the centrifuge test data reports (Ilankatharan et al., 2005, 2007a,b).

4.3.5 Local axis for superstructure response

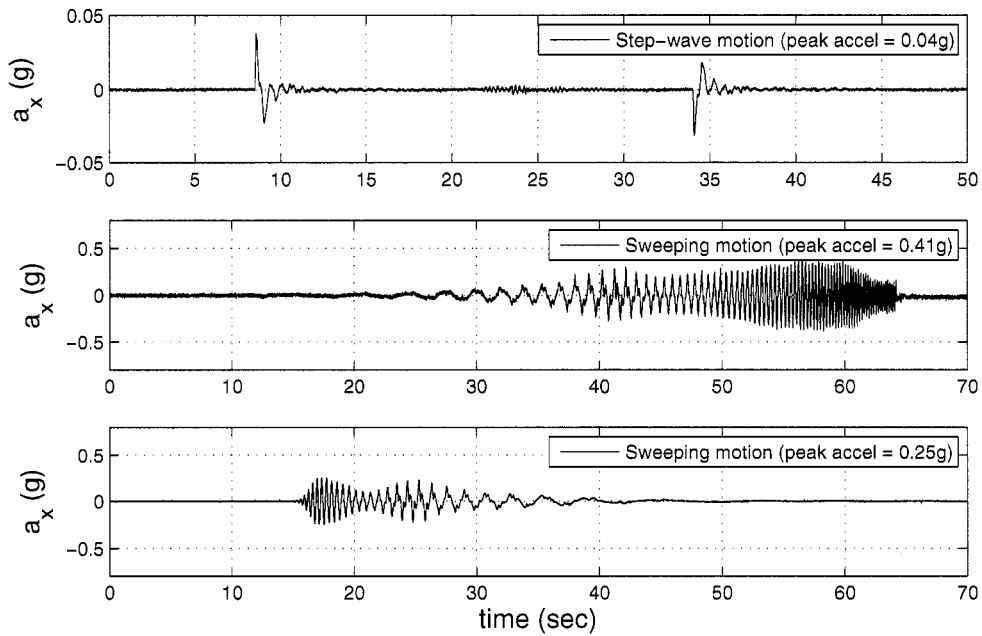
In these series of centrifuge tests, some structures were oriented at different angles with respect to the primary shaking direction. For this reason, six degrees-of-freedom are noted in the superstructure schematic shown in Figure 4.6. The x- and y-directions are referred to the transverse and longitudinal directions of the bridge, respectively.

4.3.6 List of centrifuge test simulations

In the simulation study, several motions were selected among the applied centrifuge test motions to evaluate the capacity of the numerical models to capture different levels of nonlinearity and to investigate the effect of input motion frequency content on the simulated



(a) Northridge motions



(b) Step-wave and frequency sweeping motions

Figure 4.5: Recorded centrifuge base motions

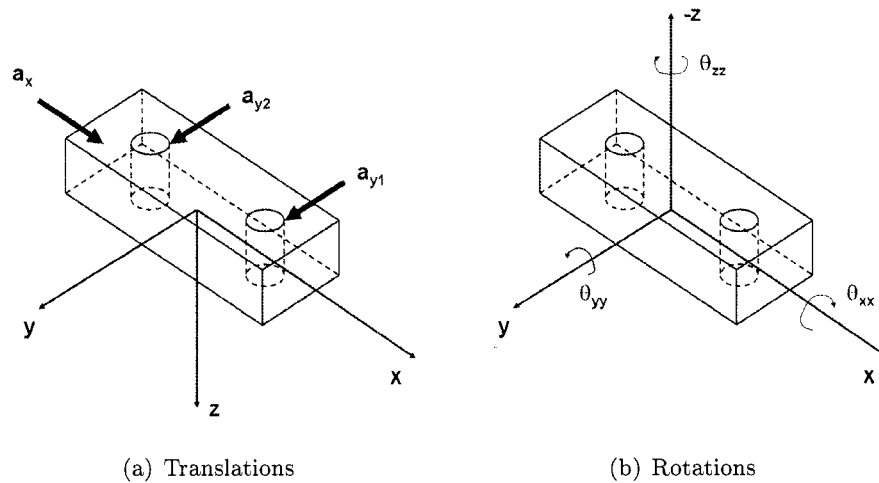


Figure 4.6: Convention used for local translation and rotation in the superstructure

response. Table 4.3 summarizes the structures and input motions used in the simulations. The motion ID can be used to identify the motions in the centrifuge test data reports.

4.4 Numerical Modeling of Centrifuge Tests

This section presents a brief description of the OpenSees finite element program and the numerical models developed to simulate the response recorded in the centrifuge experimental tests.

4.4.1 Open System for Earthquake Engineering Simulation (OpenSees)

OpenSees is a finite element framework developed by the Pacific Earthquake Engineering Research Center (PEER) to simulate the response of structural and geotechnical systems subjected to earthquakes (<http://opensees.berkeley.edu/>).

OpenSees was developed for an open source software using objected-oriented paradigms in C++ so that researchers and developers could easily implement, modify, and add new elements and material models in the finite element platform. The OpenSees input script (user interface) is written in a string-based scripting language, *Tcl*, which allows simulations to be performed using basic language features such as variable substitution and evaluation

Table 4.3: Summary of centrifuge test and simulations

test name	motions used in simulations			structure models			
	type	a_{max} (g)	motion ID	structure	name	embedment	height
CFG1	step-wave	0.100	MIL01-11	single pile	sPile-1	9.9D	1.8D
	Northridge	0.080	MIL01-13	two-column bent	Bent-M2	12.1D	3.3D
		0.250	MIL01-14	two-span bridge	Bent-S	13.2D	2.2D
		0.600	MIL01-15		Bent-L	9.9D	5.5D
		0.740	MIL01-16		Bent-M	12.1D	3.3D
CFG2	step-wave	0.080	MIL02-03	single pile	sPile-2	12.1D	3.3D
	Northridge	0.250	MIL02-11	oriented bents	Bent-00	12.1D	3.3D
		0.600	MIL02-12		Bent-30	12.1D	3.3D
		0.780	MIL02-13		Bent-60	12.1D	3.3D
	sweeping	0.410	MIL02-16		Bent-90	12.1D	3.3D
CFG3	step-wave	0.04	MIL03-02	single pile (short)	sPile-S	5.0D	3.3D
	Northridge	0.25	MIL03-03	single pile (medium)	sPile-M	7.5D	3.3D
		0.74	MIL03-15	single pile (long)	sPile-L	12.1D	3.3D
				long-long heavy bent	Bent-LL-Hy	12.1D	3.3D
	sweeping	0.25	MIL03-11	short-short heavy bent	Bent-SS-Hy	5.0D	3.3D
				long-short heavy bent	Bent-LS-Hy	12D/5D	3.3D
				long-short light bent	Bent-LS-Lt	12D/5D	3.3D

and control structures (e.g., *if*, *for*, *while*).

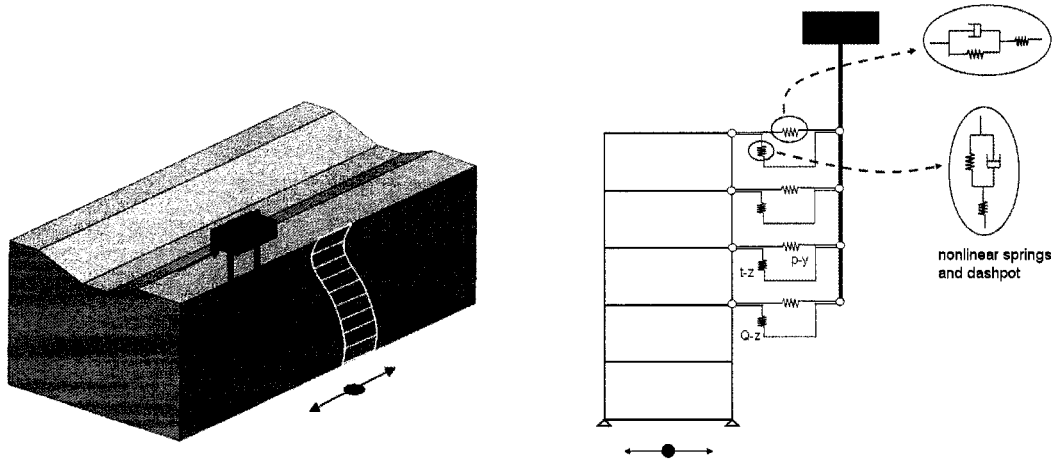
One important aspect of OpenSees is that it is capable of modeling 1-D to 3-D nonlinear structural and geotechnical systems using a variety of different structural and geotechnical material models.

4.4.2 Modeling concept using Dynamic Beam-on-Nonlinear-Winkler Foundation (BNWF) Model

When a pile or a pile-supported structure is subjected to an earthquake, the pile is excited by kinematic forces that originate from the soil motion as well as by inertial forces that come from the superstructure vibration. The soil motion experienced near the pile is usually referred as *near-field* and is associated with soil-pile-structure interaction. The soil motion experienced far enough from the pile to be uninfluenced by nonlinear, local interaction is referred as *far-field* or *free field*. In coupled analyses, where the pile and soil are coupled together by interface springs (p - y , t - z , and q - z), a 1-D shear beam soil column can be used to provide the free-field (far-field) motion and the soil-pile-structure interaction (near-field) can be considered to occur at the interface springs. To capture the free-field motion, the soil element out-of-plane thickness in a 2-D plane strain model was increased so that the soil motion is not affected by the existence of the pile. Figure 4.7 shows a schematic of an OpenSees soil-pile-structure interaction model using p - y springs. t - z and q - z springs are included to account for the vertical soil-pile interaction due to the structural self-weight.

4.4.3 Material Models Used in BNWF Model

Figure 4.8 shows schematics of the material models used in OpenSees to capture the response of a bridge system. The centrifuge soil was modeled using a pressure-dependent elasto-plastic constitutive model, here referred as Pressure Depend Multi Yield (PDMY), proposed by Yang et al. (2003). The interface spring elements consisted of elastic, plastic, and gap components connected in series using API (1993)'s recommended backbone curves for sand and clay (Boulangier et al., 1999). Ultimate lateral soil resistances (p_{ult}) were



(a) Soil-pile-structure interaction

(b) Dynamic BNWF model with interface springs

Figure 4.7: Modeling of soil-pile-structure interaction in a single pile using p - y , t - z , and Q - z springs

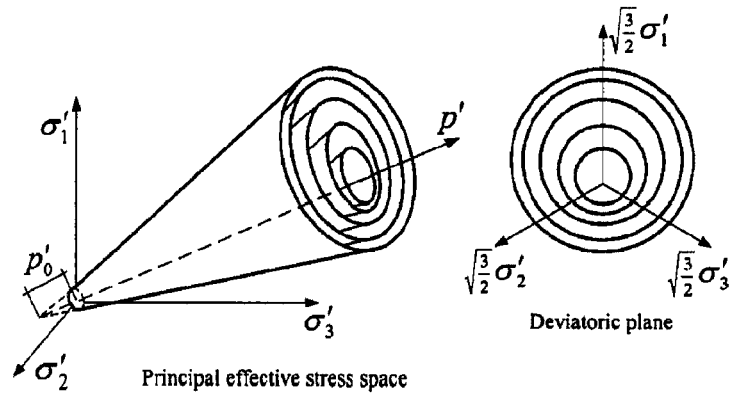
calculated based on overburden stresses obtained from gravity analyses and using Reese's criteria (Reese et al., 1974). Values of y_{50} were calculated by solving API p - y curve in Equation 4.1 for 50% of p_{ult} .

$$p = p_{ult} \tanh \left[\frac{k z}{p_{ult}} y \right] \quad (4.1)$$

where z is depth, k is a coefficient that can be determined from API (1993) charts based on density (or friction angle) and ground water condition. The t - z ultimate frictional shaft resistance (t_{ult}) was obtained using a 0.5 lateral earth pressure coefficient and 32° concrete-soil friction angle, and assuming the friction angle of the soil was 37° . The Q - z ultimate tip resistance (q_{ult}) was evaluated using Coyle and Castello (1981)'s approach. The pile was modeled using nonlinear fiber beam column elements and the plastic tubing was ignored in the fiber section definition.

4.4.4 Modeling of single piles and two-column bents

The single pile structures (sPile-1 in CFG1, sPile-2 in CFG2, and sPile-L, sPile-M, sPile-S in CFG3) were modeled using BNWF models as shown in Figure 4.7b. The two-column



(a) Soil model (Yang et al., 2003)

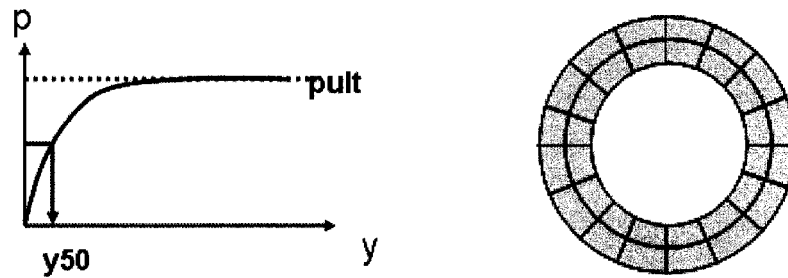
(b) p - y spring model based on API (1993) (c) Nonlinear beam column using fiber section

Figure 4.8: Material models for soil, interface springs and pile in OpenSees

bridge bents (Bent-L, Bent-M, Bent-S in CFG1 and Bent-LL-Hy, Bent-SS-Hy in CFG3) were modeled using a two-column bent structure configuration as shown in Figure 4.9 with the two soil columns allowing vertical rocking.

4.4.5 Modeling of Two-column Bents in CFG2 and CFG3 (Bent-00, Bent-30, Bent-60, Bent-90, Bent-LS-Hy, and Bent-LS-Lt)

Modeling soil-structure interaction of two-column bridge bents excited by an earthquake acting in an arbitrary direction, such as 30° and 60° , is more complicated than modeling the unidirectional excitation case; where the shaking is in the bridge longitudinal or transverse

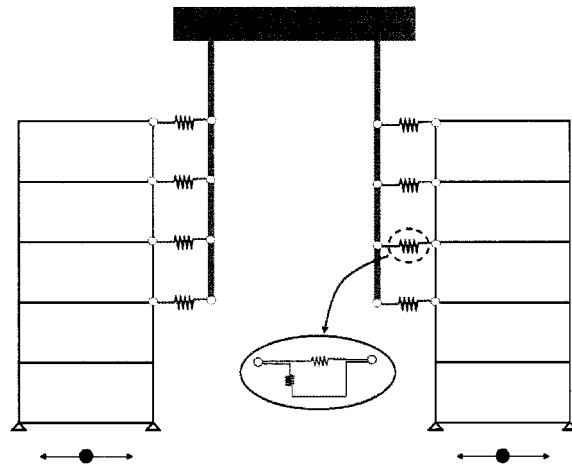


Figure 4.9: Modeling of two-column bents (Bent-L, Bent-M, Bent-S, Bent-LL-Hy, Bent-SS-Hy)

directions. To properly address this problem it is usually necessary to use three-dimensional finite element (FEM) models. However, full 3-D FEM analyses are computationally expensive and require the use of advanced soil constitutive and soil-pile interface models. Therefore, a simplified decoupled approach was used to capture the 3-D response in this study. The selected method was based on two main simplifications. First, two perpendicular lateral p - y springs were used in an effort to capture multi-directional soil-pile interaction assuming the response in the direction parallel to the bent (x-direction in local axis in Figure 4.6) has no effect on the response in the direction perpendicular to the bent (y-direction in Figure 4.6). Second, the free-field response was decoupled in two perpendicular directions. For this purpose, the longitudinal base motion was decomposed into two components; one parallel to the local x-axis and the other parallel to the local y-axis. The decomposed motions were separately used to calculate free-field motions along the pile depth. The resulting free-field (i.e., far-field) motions were applied to pile interface springs (i.e. near-field system) in two directions. The process is schematically shown in Figure 4.10.

The two-column bents supported by one short pile and one long pile (Bent-LS-Hy and Bent-LS-Lt) were modeled using 3-D structures embedded in 2-D soil columns with different

soil conditions as shown in Figure 4.11. The bent structures were connected to soil nodes and fixed nodes in two perpendicular directions using p - y springs.

4.4.6 Modeling of a two-span bridge in CFG1

The bents used to capture the response of the two-span bridge in CFG1 had different clear heights due to different ground surface elevations. This structural configuration led to different lateral stiffness and different lateral response of each bent resulting in twisting of the bridge deck. This response is illustrated in Figure 4.12b. For this reason, the bridge was modeled using a 3-D structure connected to several 1-D soil columns at each bent column location. The bridge column was connected to soil nodes by p - y springs in the transverse direction and to fixed nodes in the longitudinal direction as shown in Figure 4.12. The use of three different soil column heights allowed each bridge bent to be subjected to different freefield motions.

4.5 Summary

This chapter introduced the three centrifuge tests performed in the U.C. Davis centrifuge facility to investigate SPSI of bridge structures subjected to different levels of system non-linearity. The bridge structures include: i) a two-span bridge whose columns have different clear heights, ii) several two-column bents oriented at different angles with respect to the primary shaking direction, and iii) several bents and single piles with different pile embedment lengths and masses. These models were subjected to various earthquake motions with different intensities and frequency content.

The Open System for Earthquake Engineering Simulation (OpenSees) framework was used in all the simulations. Several numerical modeling strategies for the bridge structures with various geometric and loading conditions were described considering two- and three-dimensional structures connected to soil columns through conventional p - y interface springs.

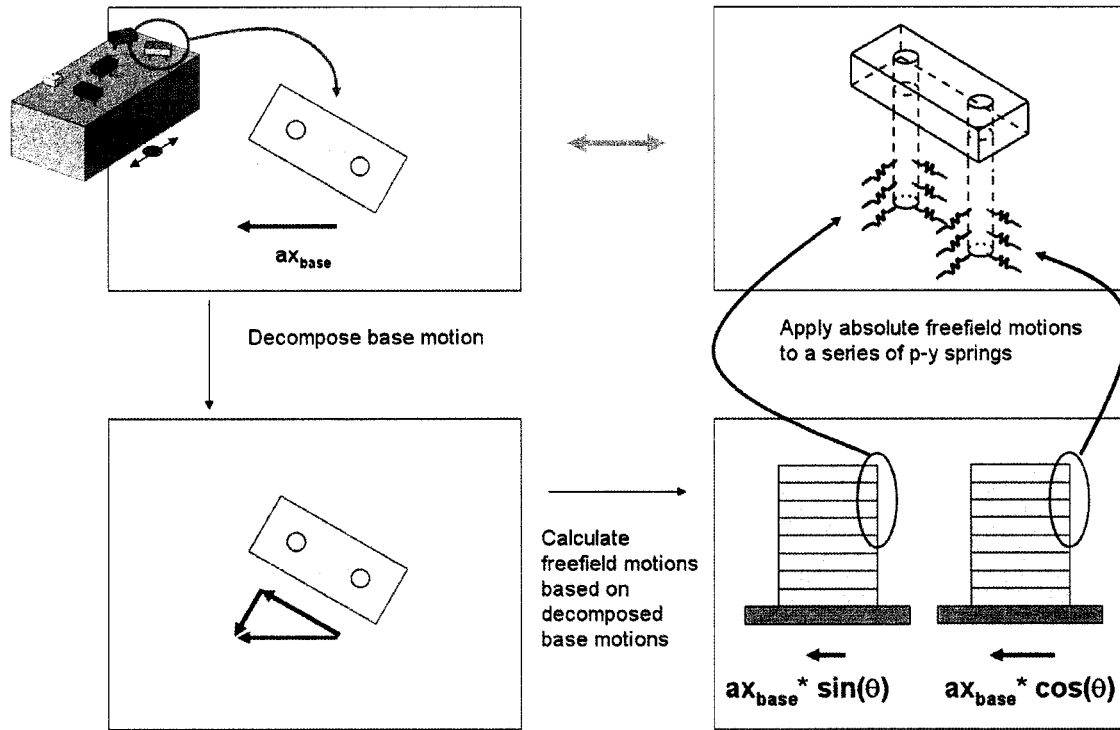


Figure 4.10: Modeling of oriented two-column bents (Bent-00, Bent-30, Bent-60, and Bent-90)

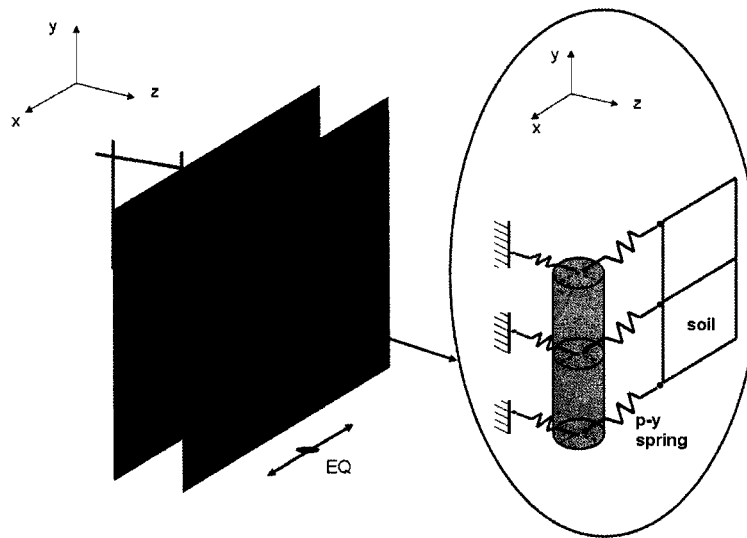
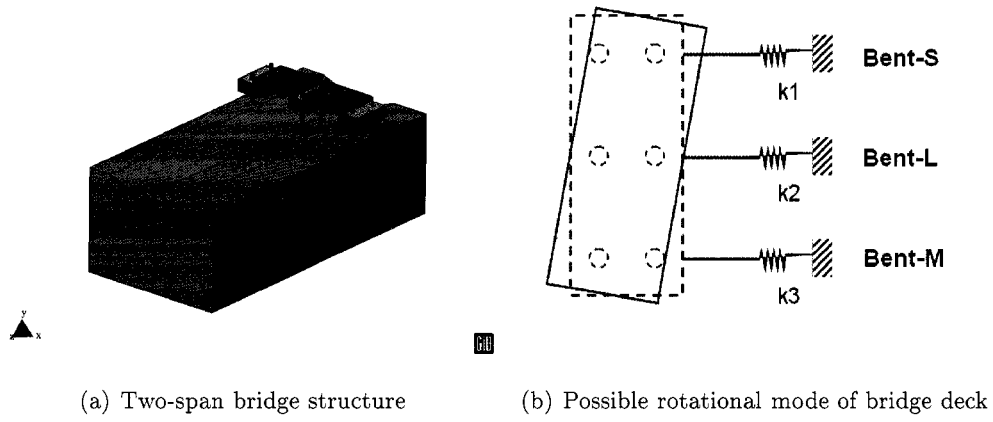
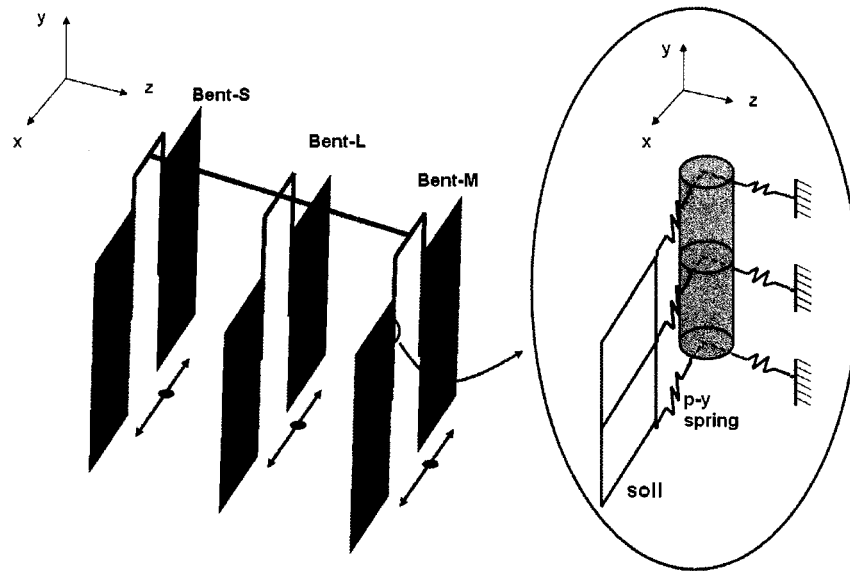


Figure 4.11: Modeling of Bent-LS-Hy and Bent-LS-Lt



(a) Two-span bridge structure

(b) Possible rotational mode of bridge deck



(c) Modeling of bridge in OpenSees

Figure 4.12: Modeling of a two-span bridge with different bent clear column heights and rotational mode

Chapter 5

**DYNAMIC RESPONSE OF TWO-SPAN BRIDGE AND BENT
STRUCTURES EMBEDDED IN DENSE SAND****5.1 Introduction**

The dynamic response recorded in the centrifuge soil, two-column bents, single-pile bents, and two-span bridge was investigated and compared to OpenSees numerical simulations obtained using BNWF models as described in Chapter 4. In this dissertation, the physical response of bridge structures was examined and the capabilities of the BNWF models were evaluated. For this purpose, the soil response recorded in the centrifuge container was compared to the simulated soil response to verify the 1-D shear beam soil model. Then, the OpenSees BNWF models were validated by comparison with centrifuge test results for a bent, a single pile, and a two span bridge.

To better understand the effect of SPSI in these structures, parametric studies were performed for a bent and a single pile structure, focusing on the effect of different soil motions and p - y parameters on the superstructure and pile response. In the sensitivity analysis, the effect of the natural period of the soil-pile system on the structural response was investigated. All the results and discussion are presented in Appendix A.

5.2 Soil Response in Centrifuge Experiments and Numerical Simulations

The soil response to seismic excitation was investigated using a 1-D soil shear beam model in OpenSees. To verify the feasibility of using 1-D soil shear beam model, the simulated response was compared to the centrifuge soil response.

5.2.1 Response of Centrifuge Container Soil and 1-D Shear Beam Soil Model

A simple 1-D shear beam model was used to model the soil in a centrifuge flexible shear beam (FSB) container. In the shear beam soil model, the degrees-of-freedom of the nodes

at the same elevation were equal in the horizontal and vertical directions. To account for the lateral inertial forces due to the mass of the container rings, the inertial mass of the soil was increased by 30 %.

In OpenSees, the shear modulus (G) of the Pressure-Dependent Multi-Yield (PDMY) is determined based on a reference shear modulus and the effective confining pressure at each soil depth, such that

$$G = G_r \left(\frac{p'}{p'_r} \right)^{0.5} \quad (5.1)$$

where G_r represents the reference shear modulus for a particular reference effective confining pressure p'_r ($= 101$ kPa). p' is the actual effective confining pressure at a location. Knowing G , shear wave velocities can be approximated from $G = \rho v_s^2$; where ρ is the soil density and v_s is the shear wave velocity. Considering several reference shear moduli, OpenSees soil shear velocity profiles can be generated. Figure 5.1 shows OpenSees soil shear velocity profiles together with empirical values obtained using Equations 5.2 and 5.3 (Seed and Idriss, 1970; Arulanandan et al., 2000). The coefficient K_2 in Equation 5.2 can be determined from void ratio or relative density. The shear wave velocity profile for the soil used in the centrifuge container was estimated measuring wave travel times between adjacent accelerometers in the accelerometer array; schematically shown in Figure 5.2. The estimated average shear velocity was about 250 m/sec in the CFG3 test specimen. Comparing this value to possible OpenSees shear wave profiles, a $G_r = 91,000$ kPa was chosen as reference soil shear modulus.

$$G_{max} = 1000 K_2 (p')^{0.5} \quad (5.2)$$

$$v_s = 65.8 (p')^{0.5} \quad (5.3)$$

To gain a better understanding on the soil response, the mode shapes for a 2-D soil container model and 1-D shear beam model were evaluated in OpenSees using eigenvalue analyses. The eigenvalue analyses were performed for the initial soil condition before applying the earthquake excitation (i.e., including only self weight). The 2-D soil container model was generated using the soil container dimensions and setting the most outward nodes at each elevation to have the same horizontal degrees-of-freedom. Figures 5.3 and 5.4 illustrate

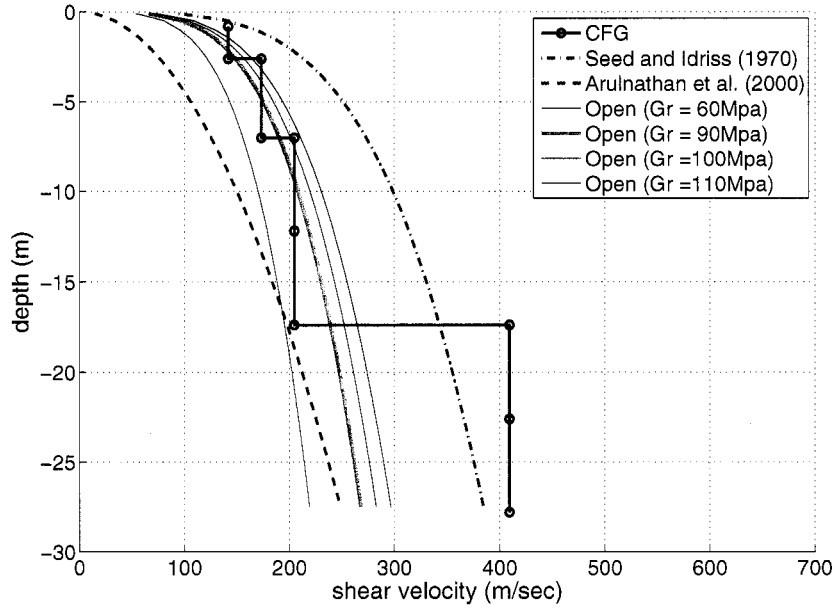


Figure 5.1: Shear wave velocity profile for soil in centrifuge container and in OpenSees soil model

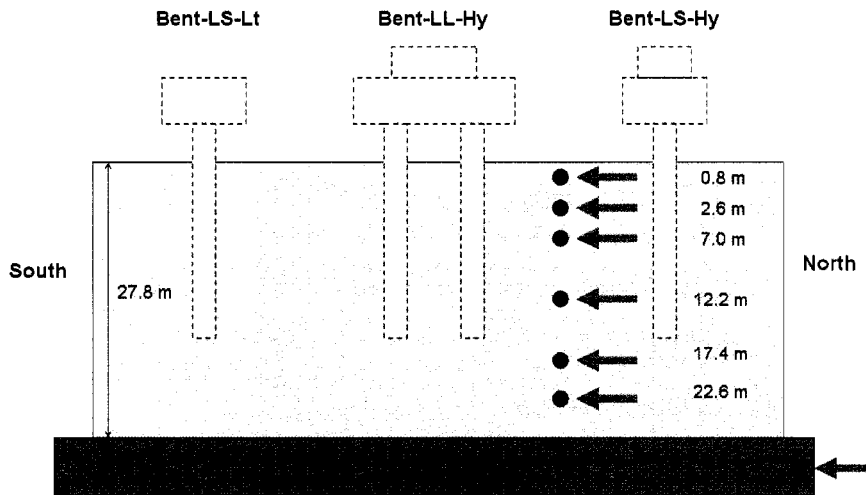


Figure 5.2: Free-field accelerometer array in CFG3 test (prototype scale)

several lateral mode shapes for the 2-D soil container and 1-D shear beam models showing the 2-D soil container model was able to capture various mode shapes including rocking while the 1-D soil model could capture the 1-D vertical shear wave propagation mode. The first natural period of each soil model was 0.515 sec and 0.475 sec, respectively. The actual natural period of the soil in the centrifuge container was investigated using transfer functions (ratio of Fourier amplitudes at 2.6m in the soil and at the base) obtained using the soil response recorded in the centrifuge. A similar approach was used to investigate the first natural period using a 1-D shear beam and the 2-D soil container model simulations. Values of the transfer functions at frequencies greater than 4 Hz are not shown in the figures; since the Fourier amplitude ratios due to very small soil amplitudes produced unrealistic spikes for these large frequencies.

Figure 5.5 shows that the actual natural period of the centrifuge soil was about 0.67 sec (1.5 Hz), which is a little longer than that obtained from the eigenvalue analysis due to soil nonlinearity. This figure shows that the 2-D soil container model captured the natural period well. Figure 5.6 shows the 1-D soil shear beam model gave a slightly shorter natural period (0.57 sec or 1.75 Hz). Figure 5.6 shows that the use of a 1-D soil shear beam model underestimated the response at 1.0 to 1.5 Hz and overestimated the response at 1.5 to 2.4 Hz. Figure 5.7 compares simulation results for the 1-D soil shear beam and 2-D soil container models in terms of acceleration response spectra showing that the centrifuge soil response was better captured by the 2-D soil model than the 1-D soil shear beam model.

To evaluate the feasibility of using the 1-D soil column model, several different intensity motions were considered. Figure 5.8 compares centrifuge and 1-D soil column acceleration time histories. Overall, the 1-D soil column model captured the soil response reasonably well for motions with different levels of intensity and frequency content; even though the peak acceleration is slightly overestimated in the 1-D soil column model. This can be attributed to the shorter fundamental period of the 1-D soil column; which indicates a stiffer soil column system than the 2-D soil container model or centrifuge soil.

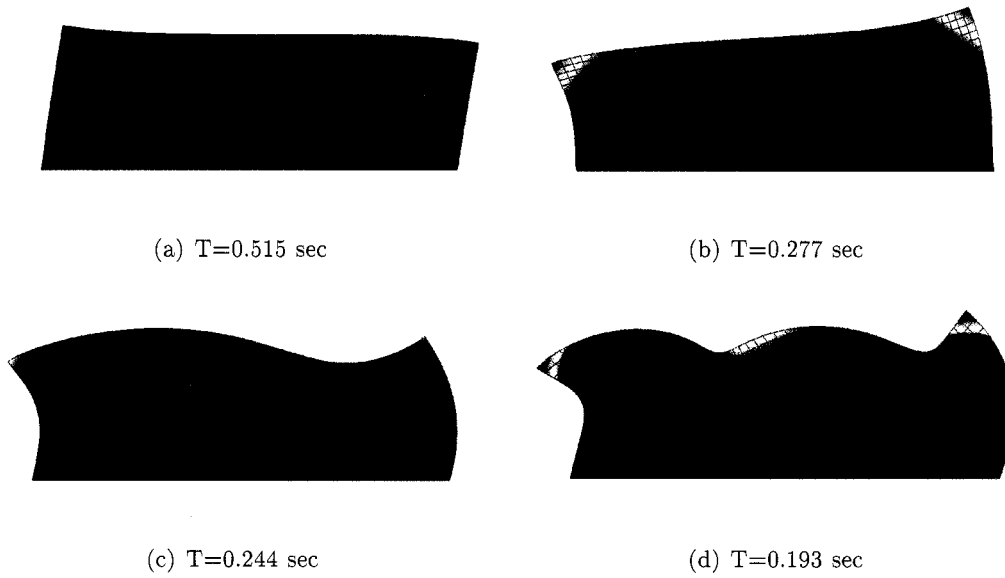


Figure 5.3: Mode shapes for two-dimensional soil model container (based on the initial soil stiffness before shaking)

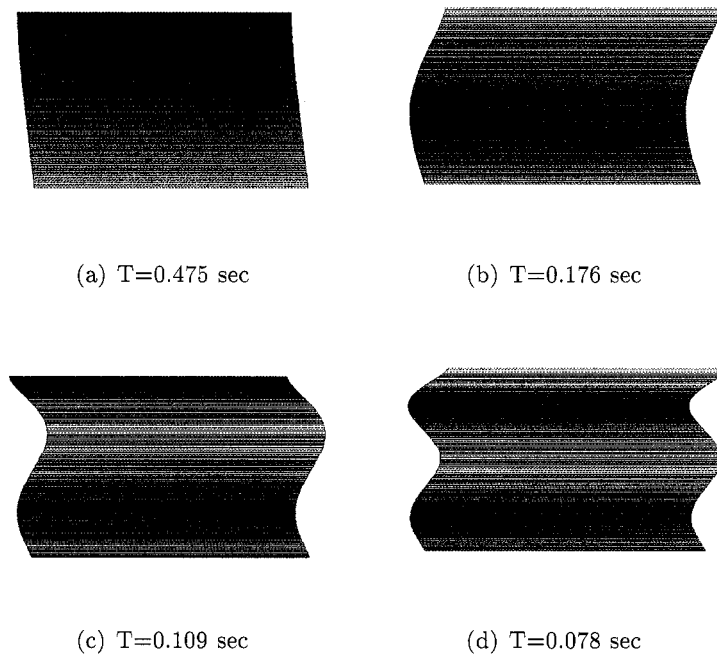


Figure 5.4: Mode shapes for one-dimensional soil column model (based on the initial soil stiffness before shaking)

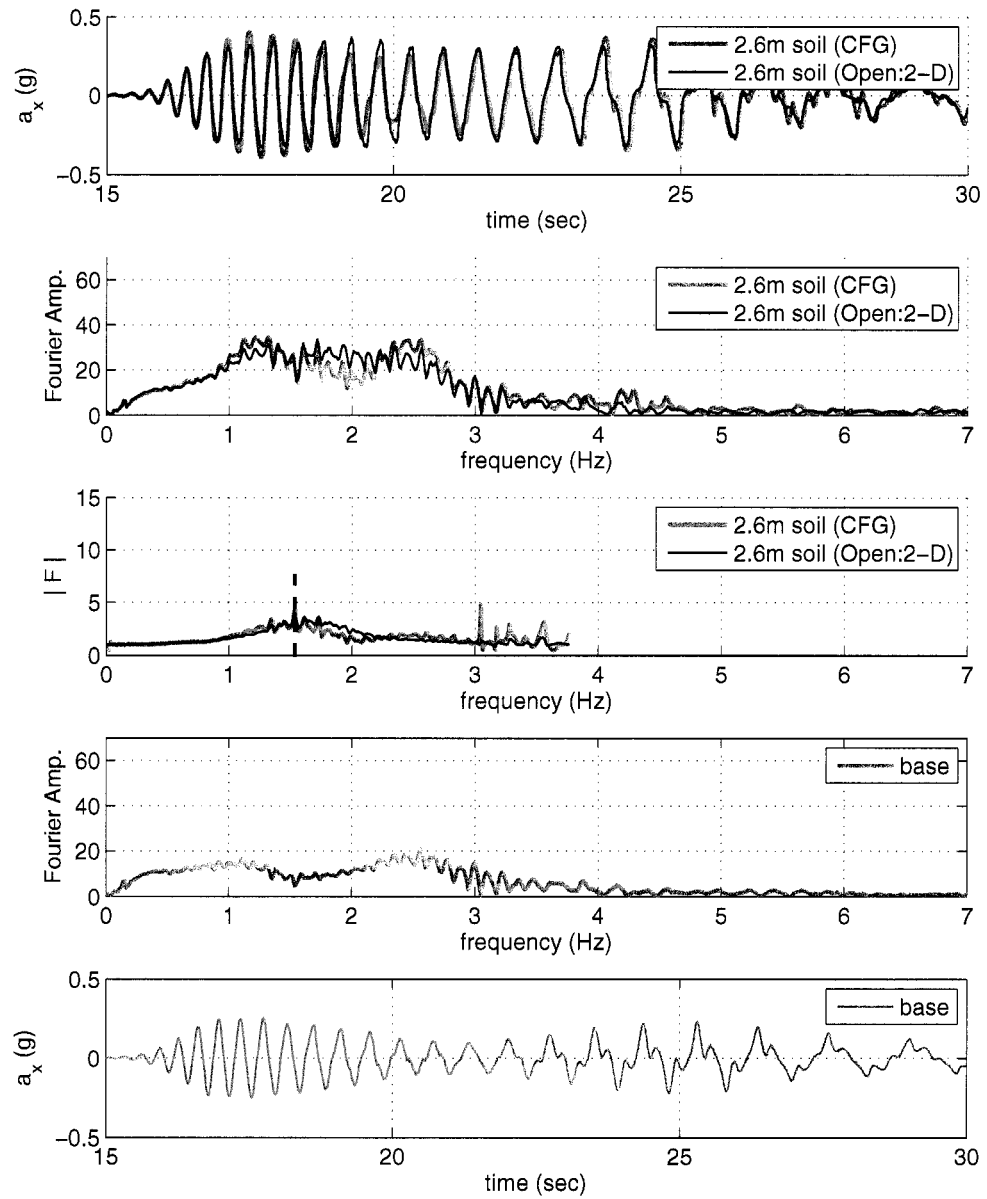


Figure 5.5: Transfer function between soil (2.6 m) and base in CFG3 and 2-D soil model simulation: frequency sweeping motion, $a_{max} = 0.25g$

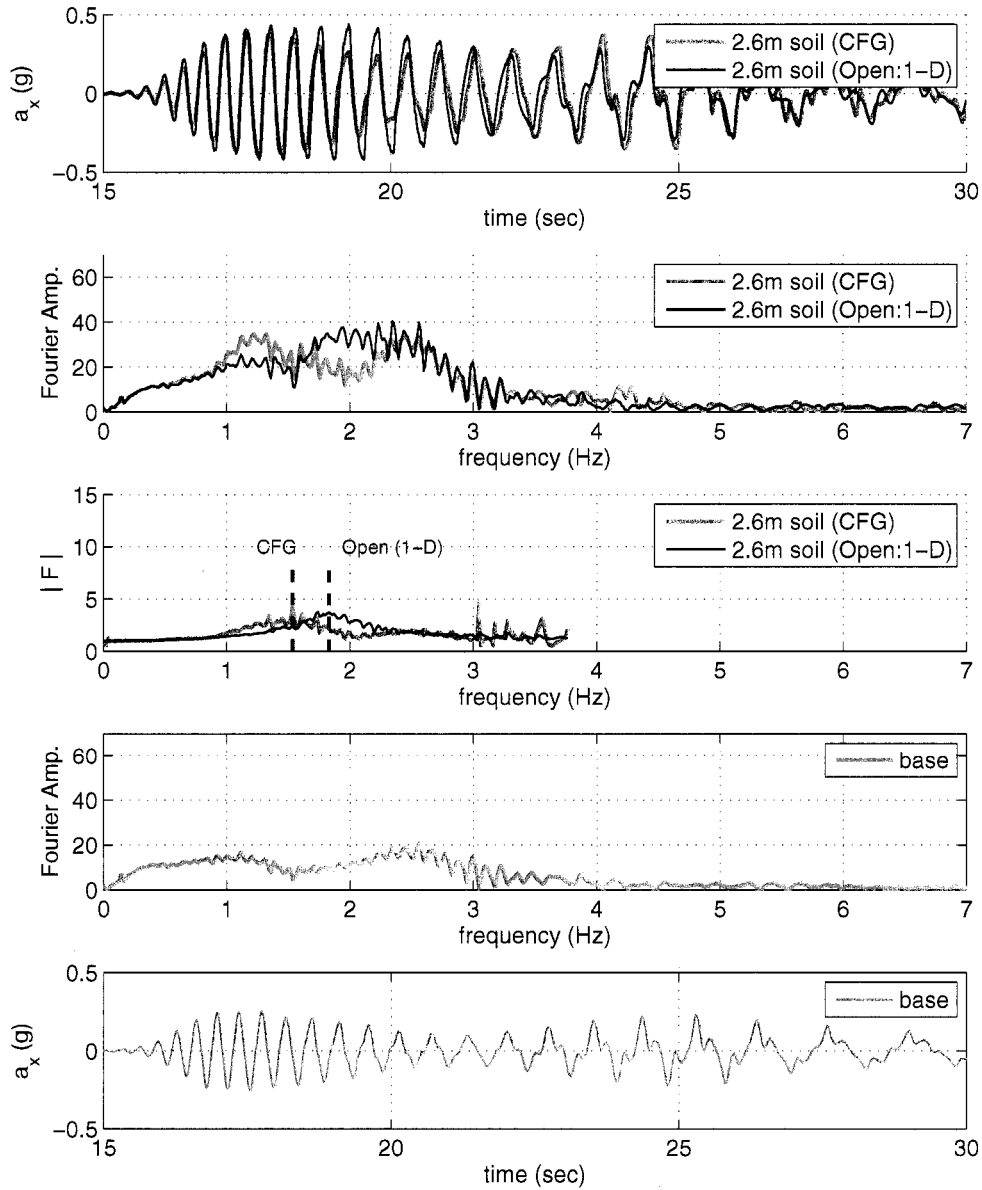


Figure 5.6: Transfer function between soil (2.6 m) and base in CFG3 and 1-D soil model simulation: frequency sweeping motion, $a_{max} = 0.25g$

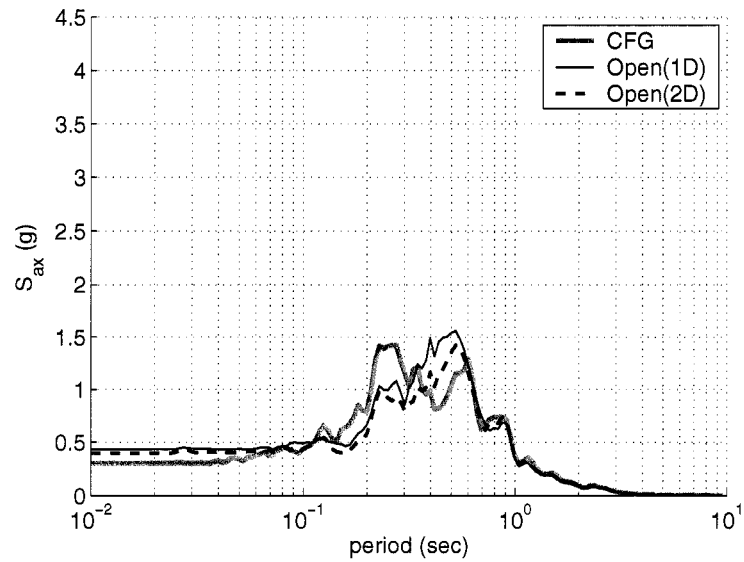
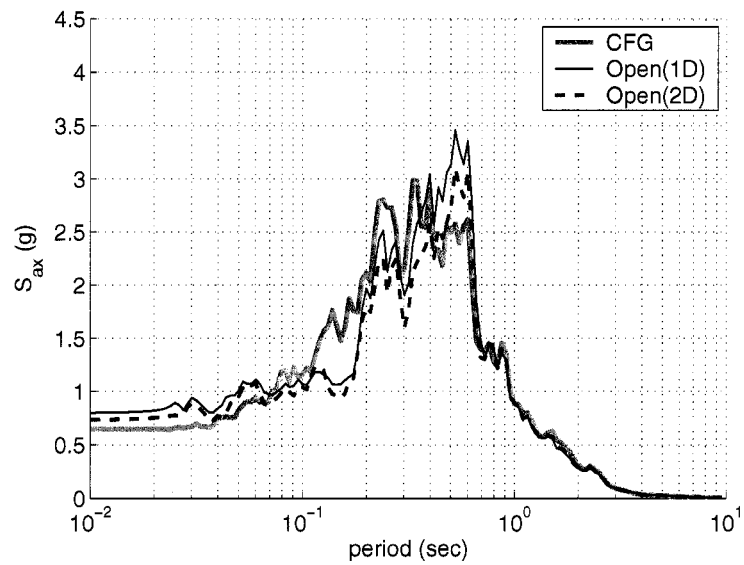
(a) Northridge, $a_{max} = 0.25g$ (CFG3)(b) Northridge, $a_{max} = 0.74g$ (CFG3)

Figure 5.7: Soil response spectra corresponding to soil motion recorded in CFG3 at 2.78m depth and from simulations (1-D shear beam soil model and 2-D container soil model)

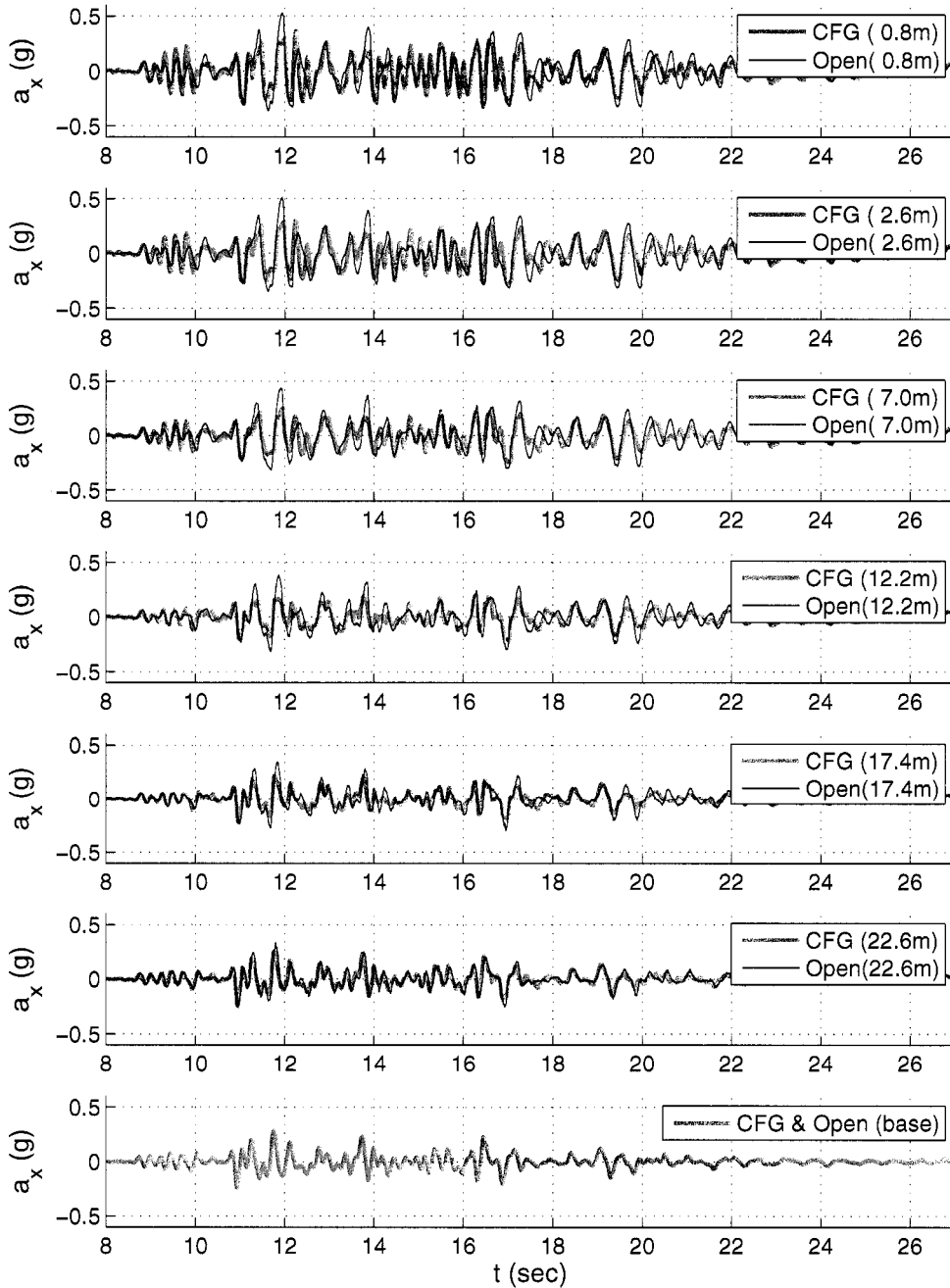


Figure 5.8: Recorded and simulated free-field array acceleration time histories in CFG3 soil: Northridge motion, $a_{max} = 0.25g$

5.3 Response of Two-column Bent and Single Pile Structures

In this section the results obtained from OpenSees simulations and centrifuge tests are compared to investigate the ability of the dynamic BNWF model to capture the response of a two-column bridge bent (Bent-M2 in CFG1) and a single column bent (sPile-1 in CFG1) subjected to shaking in the transverse direction.

5.3.1 Two-Column Bridge Bent Response (Bent-M2 in CFG1)

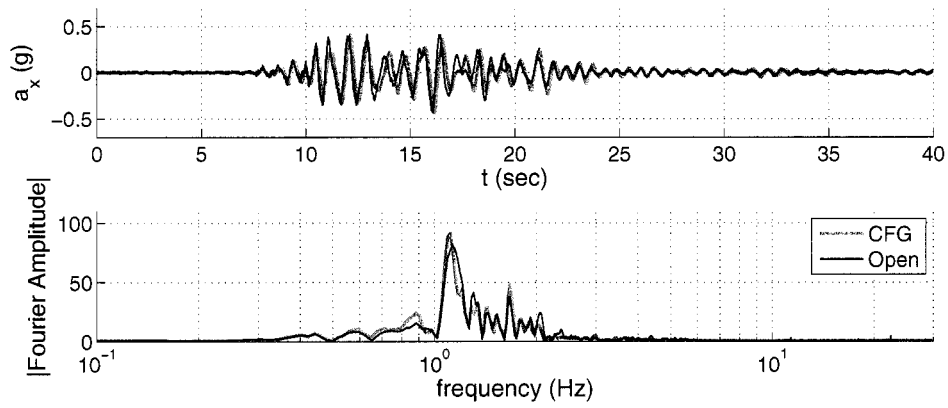
Figures 5.9 through 5.11 compare the centrifuge response of a two-column bridge bent (Bent-M2 in CFG1) to the response predicted by numerical simulation. The figures show that the simulated acceleration time histories, Fourier spectra, and response spectra of the superstructure were in good agreement with the measured centrifuge test results for moderate and strong shaking. The maximum bending moments were also well captured in OpenSees. However, for strong shaking, the location of the simulated maximum bending moment was slightly deeper and larger than that recorded in the centrifuge test.

5.3.2 Single Pile Response (sPile-1 in CFG1)

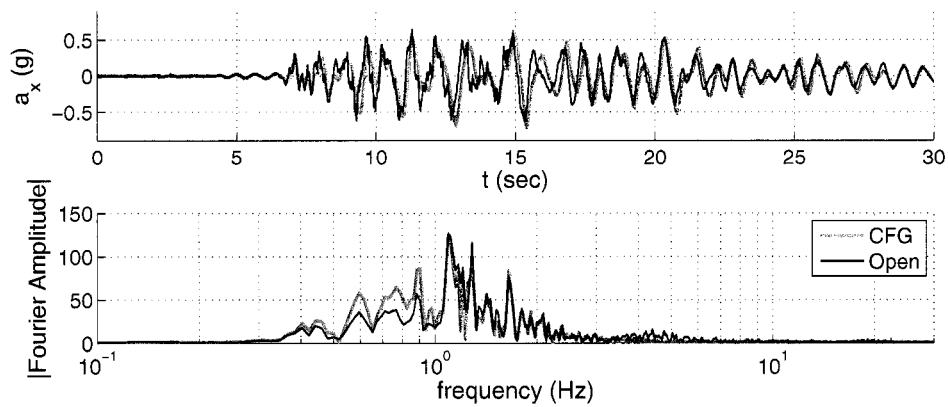
Figures 5.12 and 5.13 compare the centrifuge response of a single pile structure (sPile-1 in CFG1) to that predicted by numerical simulations. The results show that the superstructure response was well captured in OpenSees for both moderate and strong shaking. However, Figure 5.14 shows that the maximum bending moment in OpenSees was underestimated, especially near the ground surface. Extrapolated values from two centrifuge bending moment records above the ground surface were about two times the simulated results. This maximum bending moment difference was not consistent with the well-matched superstructure acceleration response.

5.3.3 Effect of Soil and Structure Nonlinearity on Observed Response

As the motion intensity increased, the response of the soil and structure was affected by the nonlinearity of the soil and structural materials. Figure 5.15 shows peak accelerations in the superstructure and soil (2.6 m depth) for motions with increasing intensity. Since



(a) Northridge motion, $a_{max} = 0.25g$



(b) Northridge motion, $a_{max} = 0.74g$

Figure 5.9: Superstructure acceleration time histories for Bent-M2 obtained from centrifuge test and numerical simulations (CFG1)

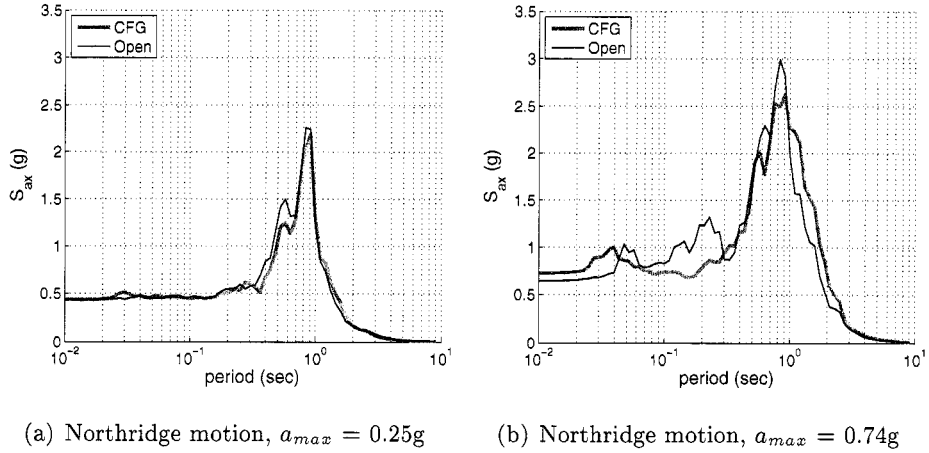


Figure 5.10: Superstructure acceleration response spectra for Bent-M2 obtained from centrifuge test and numerical simulations (CFG1)

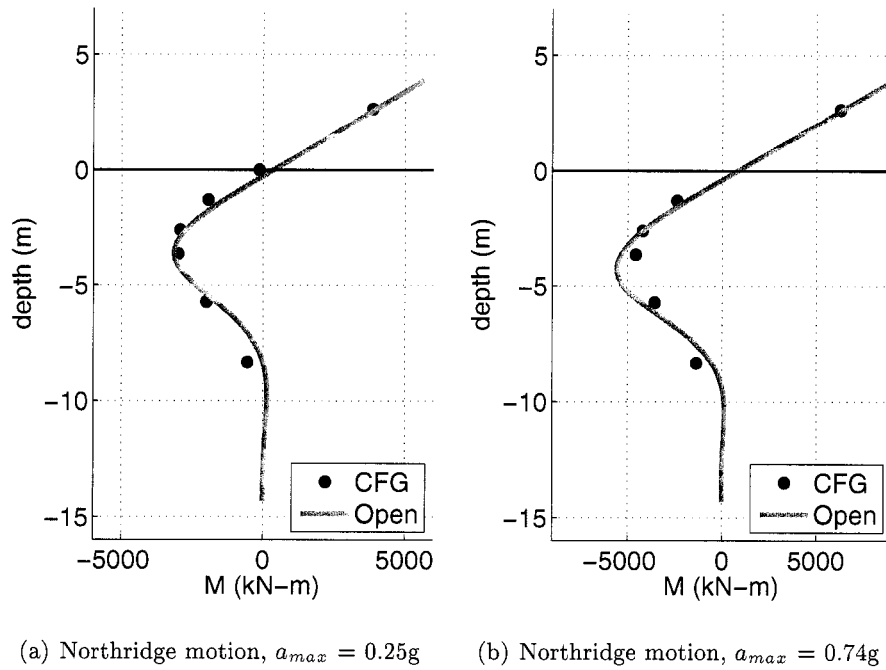


Figure 5.11: Maximum pile bending moments for Bent-M2 obtained from centrifuge test and numerical simulations (CFG1)

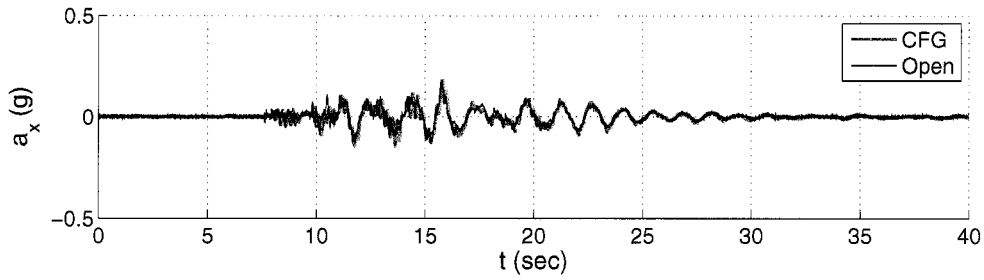
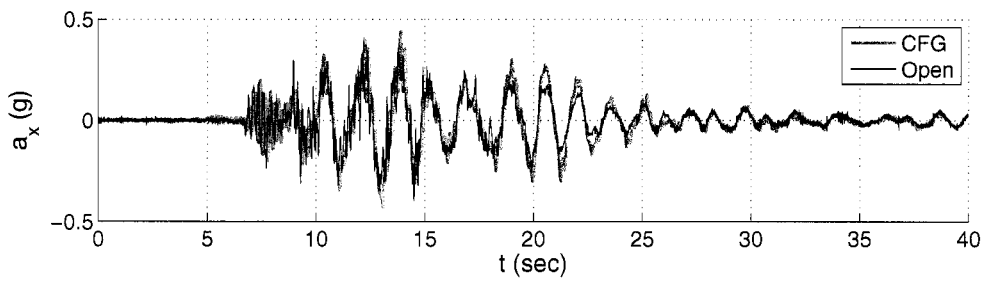
(a) Northridge motion, $a_{max} = 0.25g$ (b) Northridge motion, $a_{max} = 0.74g$

Figure 5.12: Superstructure acceleration time histories for sPile-1 obtained from centrifuge test and numerical simulation (CFG1)

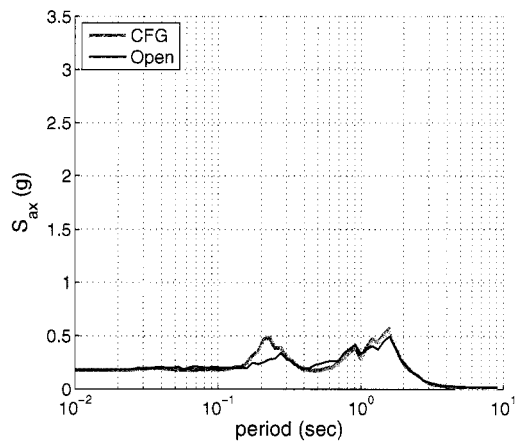
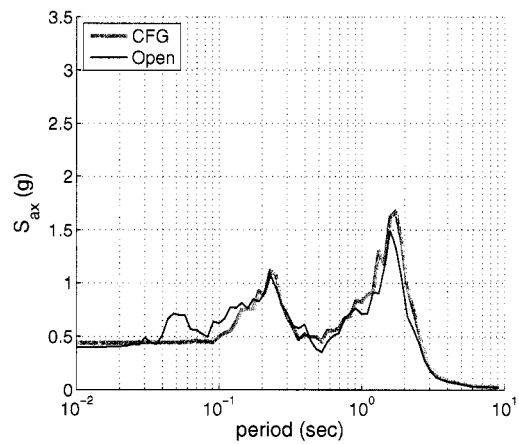
(a) $a_{max} = 0.25g$ (b) $a_{max} = 0.74g$

Figure 5.13: Superstructures acceleration response spectra for sPile-1 obtained from centrifuge test and numerical simulations (CFG1)

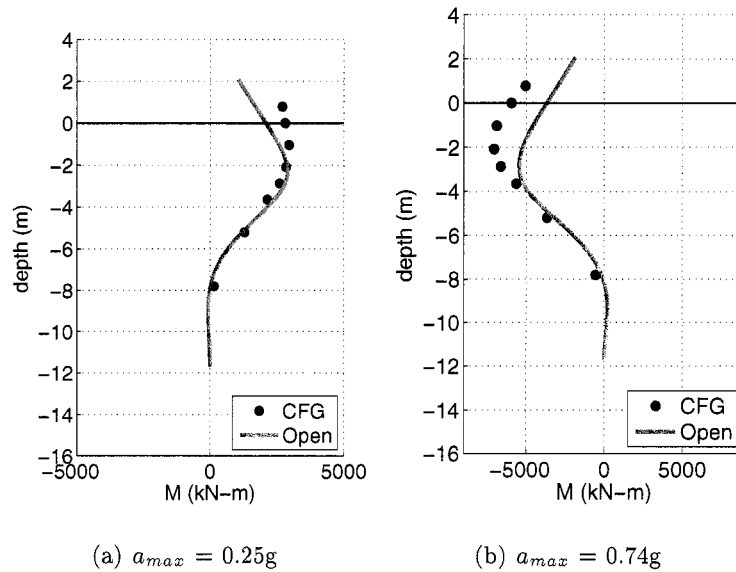
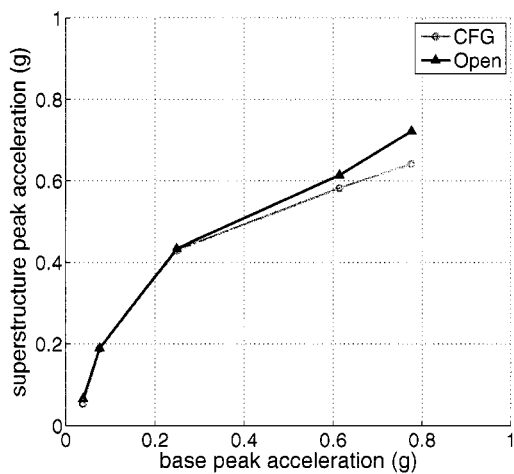


Figure 5.14: Maximum pile bending moments for sPile-1 obtained from centrifuge test and numerical simulations (CFG1)

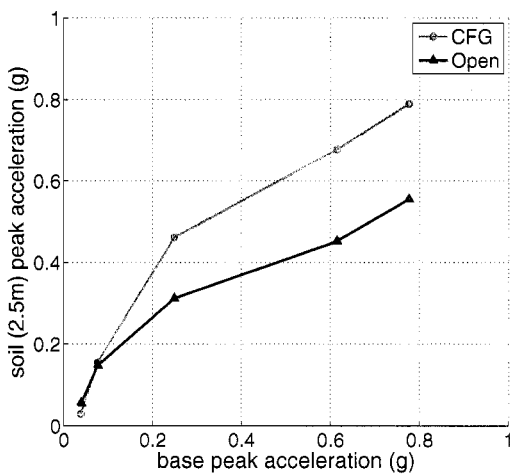
the surface elevations of the soil, where Bent-M2 and sPile-1 were embedded, were different, the soil response measurement locations were different resulting in slightly different peak accelerations; as shown in Figures 5.15b and 5.15d. The variation of peak acceleration in the superstructure and soil due to increasing base peak accelerations shows clear evidence of nonlinear response occurring in the soil-foundation system. The figures also show that the superstructure peak accelerations for the bent and single pile were well captured by the OpenSees simulations for motions with various intensities. However, the soil (2.6 m depth) peak accelerations were overestimated by OpenSees for most motions. The reason for this inconsistency or discrepancy (i.e., good estimation of superstructure response with overestimated soil response) will be investigated later in this chapter.

5.3.4 Consistency (Repeatability) of Centrifuge Test Results

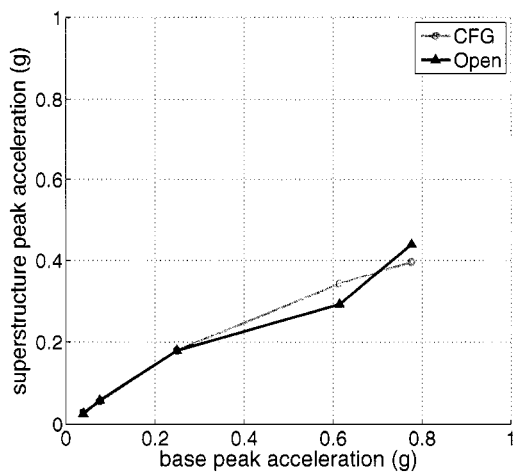
Several structures in different centrifuge tests (e.g., Bent-M2 in CFG1 and Bent-00 in CFG2) were shaken with similar base motions. The response of these structures subjected to similar base motion were compared to investigate consistency (repeatability) of results.



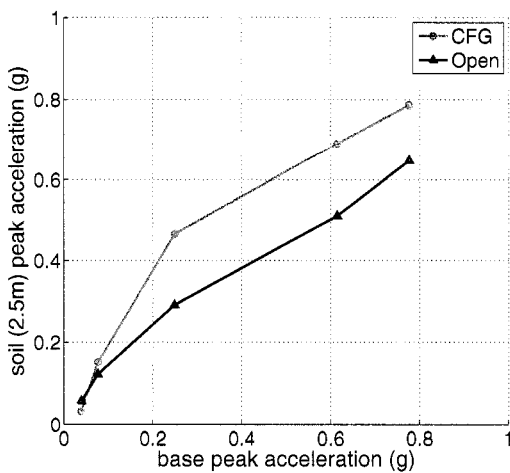
(a) Bent-M superstructure



(b) Soil (2.6m) near Bent-M



(c) sPile-1 superstructure



(d) Soil (2.6m) near sPile-1

Figure 5.15: Nonlinear response of superstructure and soil at 2.6m obtained from centrifuge tests and numerical simulations

Figure 5.16 shows the response spectra for the superstructure, 2.6m-depth soil, and base motions in CFG1 and CFG2 were similar for two different intensity motions, indicating the centrifuge response recorded in two different centrifuge tests was consistent when similar base motions were applied.

Since Bent-90 was subjected to shaking in the longitudinal direction, its response was expected to be similar to that of a single pile with the same tributary mass. Figure 5.17 presents the superstructure response for Bent-90 and sPile-2 in CFG2, showing the response of Bent-90 was slightly larger than that of single pile.

5.3.5 Inertial Effect on Bent and Single Pile Structures

To investigate the contribution of the inertial force on the pile response, the inertial mass was removed in the next series of OpenSees simulations. Figure 5.18 compares pile bending moments obtained from centrifuge tests and OpenSees simulations (without inertial mass) for a strong motion. The figure clearly shows the kinematic contribution to the simulated bending moments was very small indicating the superstructure inertial force controlled the pile behavior. Therefore, it was inferred that the large bending moments near the surface recorded in the centrifuge originated from the superstructure inertial force that developed during shaking.

5.4 Two-Span Bridge Response in Centrifuge Experiments and Numerical Simulations

This section presents numerical and experimental results corresponding to the two-span bridge. The three individual bents were subjected to a small shaking before connecting the bridge deck to the bents. After connecting the bridge deck, various motions were applied to the bridge.

5.4.1 Effect of Bridge Deck Connection to Individual Bent Response

Bent-L, Bent-M, and Bent-S in CFG1 test were subjected to small shaking ($a_{max} = 0.10g$) before and after the bridge deck was connected. The individual bent response recorded in CFG1 test was compared to show the effect of bridge deck connection and

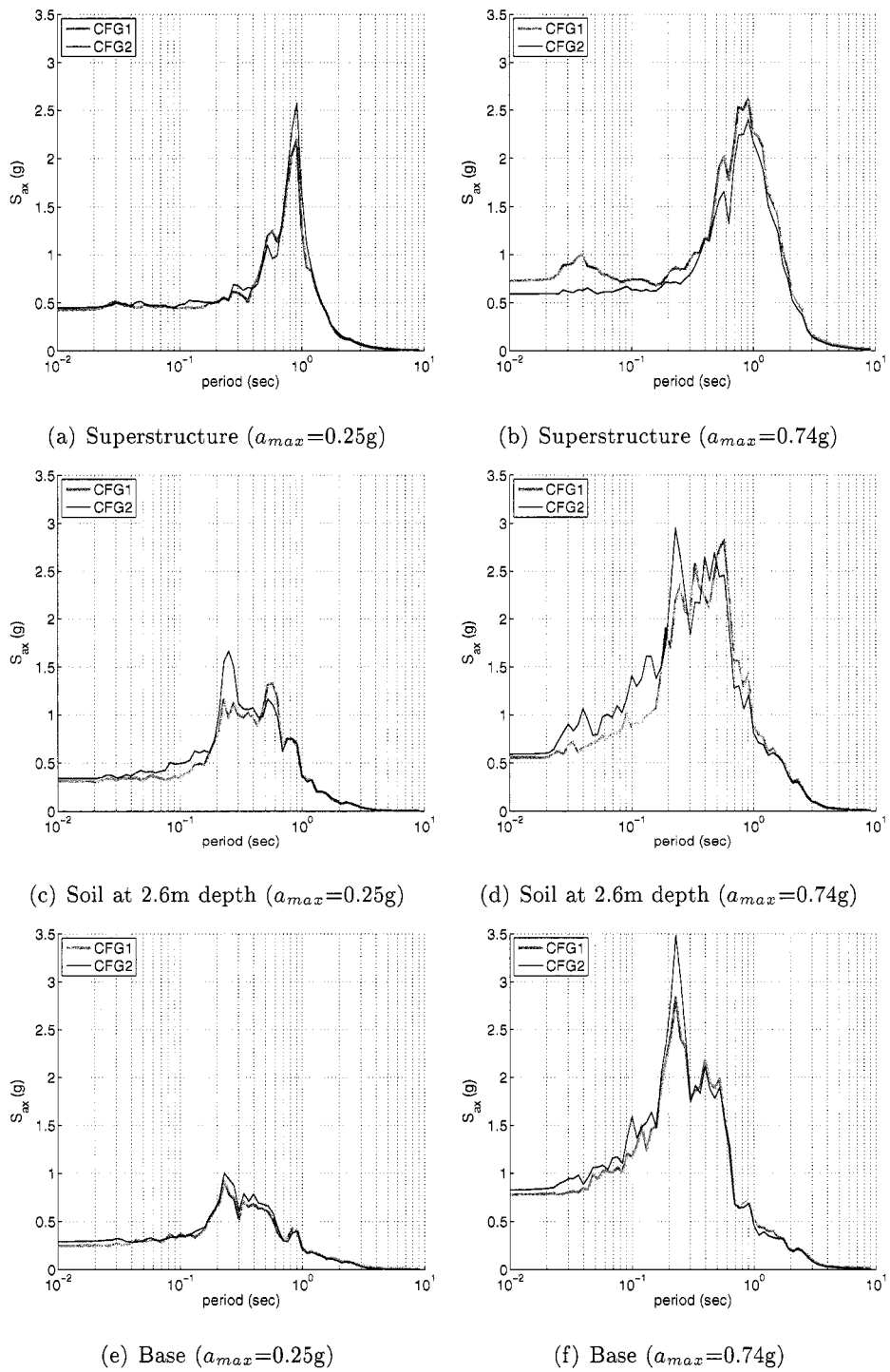


Figure 5.16: Consistency (repeatability) of centrifuge tests (Bent-M2 in CFG1 and Bent-00 in CFG2) - Northridge events

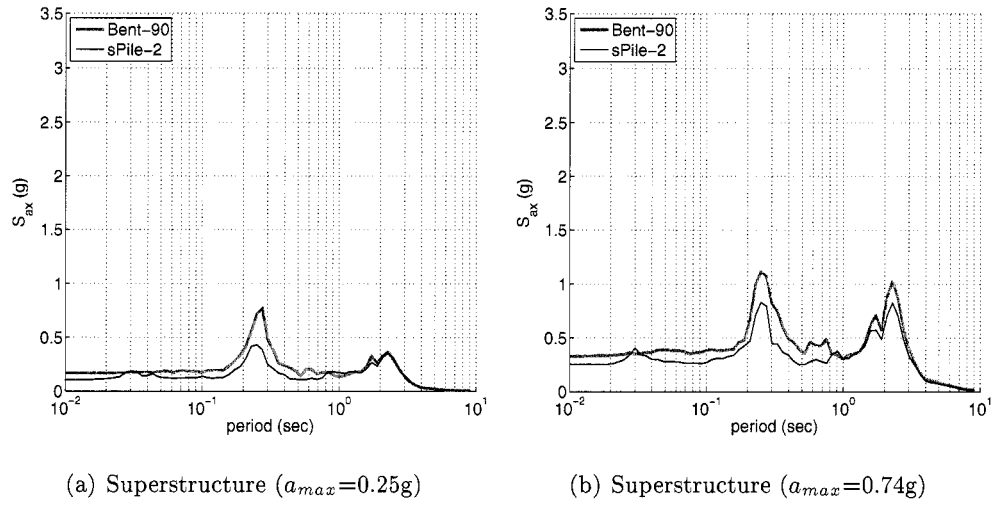


Figure 5.17: Superstructure response in Bent-90 and sPile-2 in CFG2 - Northridge events

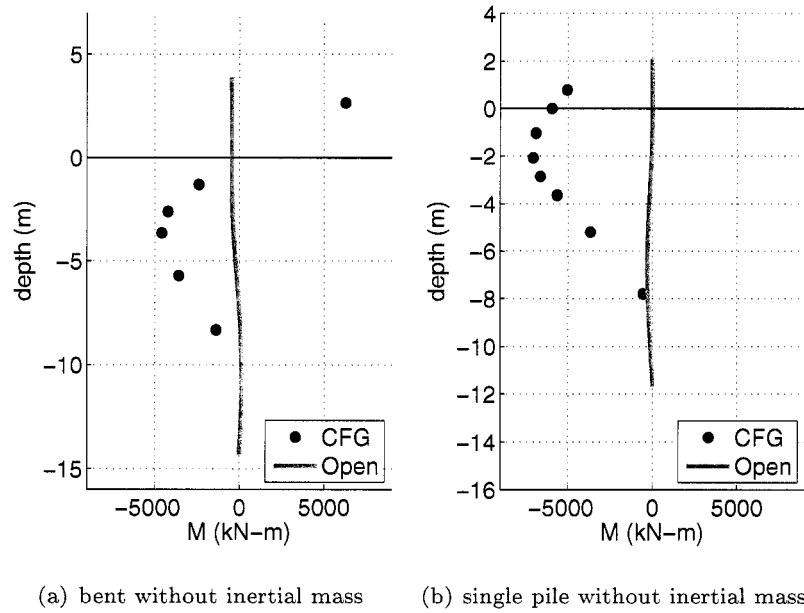


Figure 5.18: Bending moment of a bent and a single pile structure with no superstructure inertial mass in OpenSees (Northridge 0.75g)

bent-to-bent interaction. The response spectra presented in Figure 5.19a clearly show that the bents had different fundamental periods and peak accelerations before deck connection. From the figures, Bent-S had the shortest fundamental period and showed the largest peak acceleration. Bent-L had the largest natural period and showed the smallest peak acceleration. In contrast, Figure 5.19b shows that after connecting the deck the three bents had a similar fundamental period and showed similar peak accelerations; even though Bent-S had a slightly shorter fundamental period than the other bents. The short period observed at Bent-S after connecting the deck was attributed to a larger lateral stiffness due to its short clear height. Figures 5.19c to 5.19e show the effect of bridge-deck-connection on the individual bent response is presented. The figures show that after connecting the deck, Bent-S had a smaller peak acceleration and the same natural period while Bent-L had a larger peak acceleration and shorter natural period. Figure 5.19f shows soil acceleration response spectra at 2.6 m depth indicating the input motions were the same before and after connecting the deck.

5.4.2 Centrifuge Test Results of Two-Span Bridge

After connecting the deck, several moderate to strong shaking motions were applied to the bridge. Figure 5.20 compares the recorded response of the superstructure, pile at 2.6 m depth, and soil at 2.6 m depth at each bent location. The Bent-L pile response at 2.6 m depth was not recorded during the strong shaking event due to an instrumentation malfunction. For moderate shaking (Figure 5.20a, 5.20c, and 5.20e), the three bents showed similar superstructure response while the pile response at 2.6 m depth was different at each bent, especially the peak accelerations. The pile response at 2.6 m depth, shown in Figure 5.20c, represents the near-field motion resulting from soil-pile-structure interaction at that depth. The soil response at 2.6 m depth shown in Figure 5.20e represents the far-field motion which is not affected by this interaction. For strong shaking, the recorded peak acceleration at Bent-M (Figure 5.20b) was smaller than that for the two other structures. The difference can be attributed to the bridge deck rotation that was generated due to different lateral stiffness at each bent.

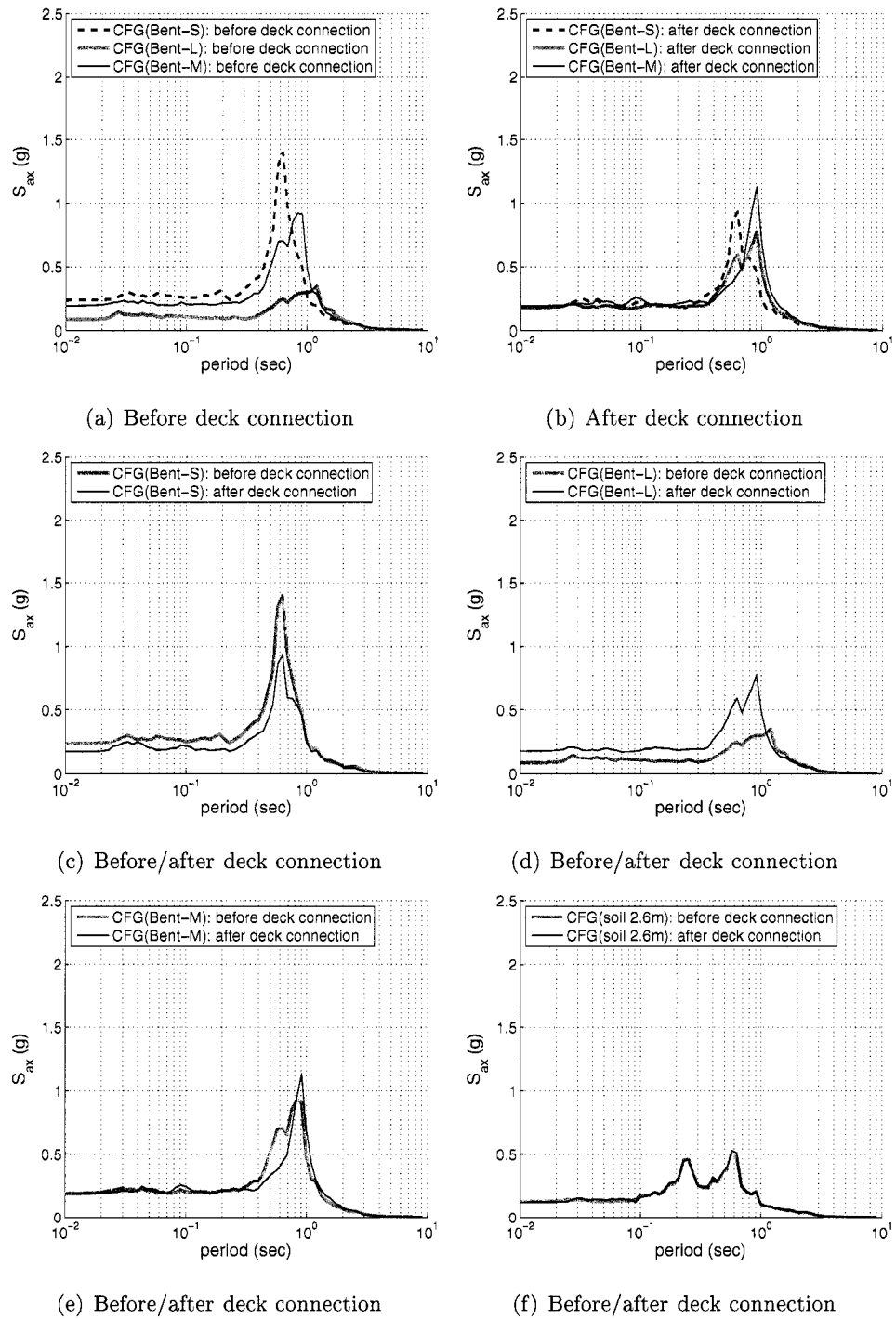


Figure 5.19: Acceleration response spectra of superstructure response before and after bridge deck connection for Northridge motion, $a_{max} = 0.10g$

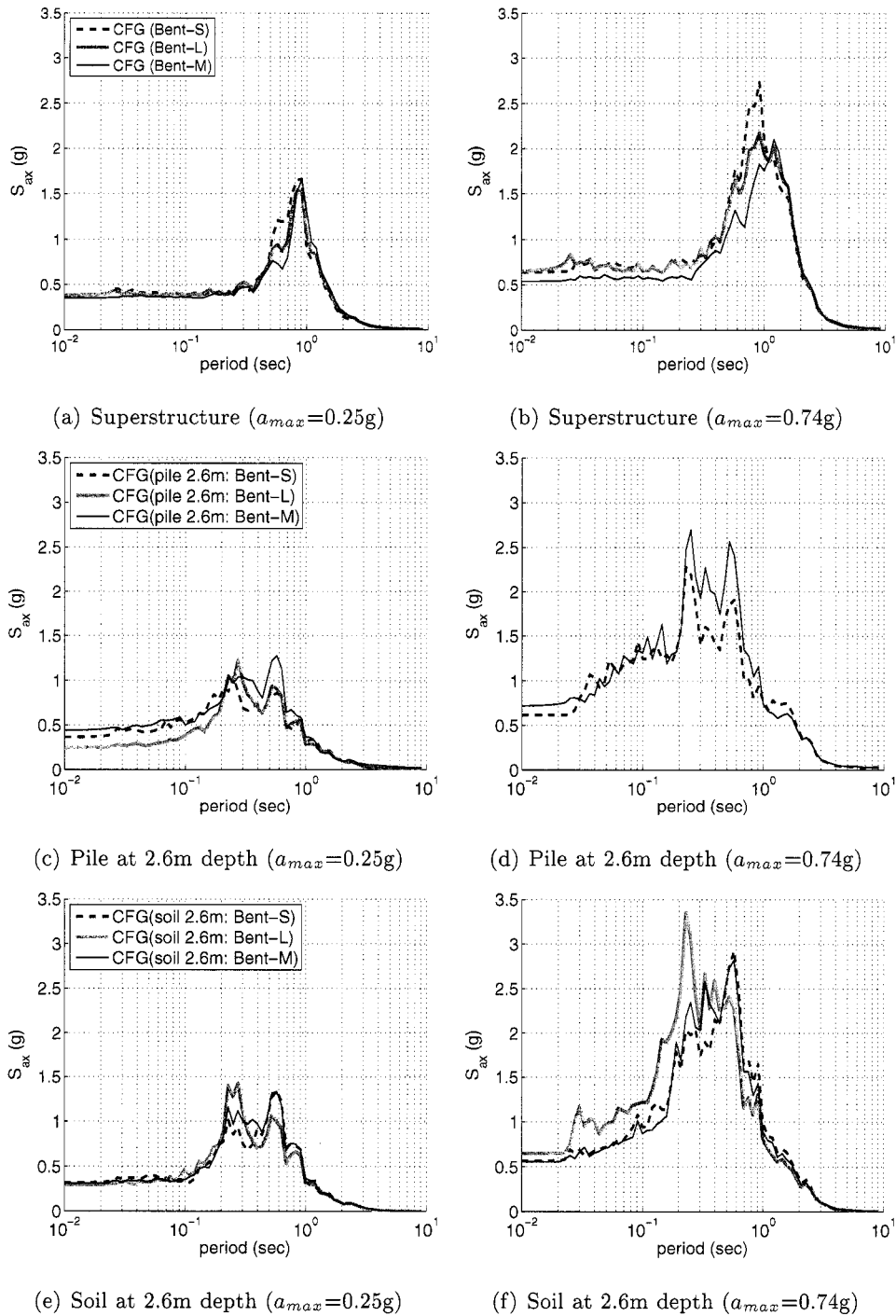


Figure 5.20: Response of superstructure, and pile and soil at 2.6m depth in centrifuge test (CFG1) for Northridge motion events ($a_{max} = 0.25g$ and $0.79g$)

5.4.3 Comparison of Centrifuge Test Results and OpenSees Simulations

Figures 5.21 through 5.23 show comparisons between the responses recorded in the centrifuge tests and those obtained from OpenSees simulations for each bent. The figures show that the superstructure response and maximum pile bending moments were well captured in OpenSees for moderate shaking. However, for strong shaking the OpenSees simulations showed shorter fundamental periods and slightly smaller maximum bending moments than those recorded in the centrifuge tests.

Figure 5.24 shows recorded and simulated maximum bending moments below the ground surface, and their corresponding depths, for each bent and for different shaking levels. The figure shows that each pile experienced different maximum bending moments at different depths for different motions. In the centrifuge tests, Bent-M showed the largest bending moment for small shaking events. However, Bent-S showed the largest bending moment for strong shaking events. This can be attributed to the fact that the bridge experienced twisting (in deck-plane) during the small and moderate shaking; increasing the demand on the medium bent. This rotational response was attributed to the incoherent soil response due to the differently elevated ground condition and different column clear-heights. The response observed in the simulation showed a similar pattern, especially for moderate shaking ($a_{max} = 0.25g$). However, the maximum bending moments were smaller than those recorded in the centrifuge test for strong shaking and the corresponding depths were deeper than those recorded in the experimental tests.

Figure 5.25 shows soil resistance distribution at the time of maximum shear force. Ilankatharan et al. (2006) back-calculated the centrifuge soil resistance from pile bending moment data. The OpenSees soil resistances were recorded at the p - y springs. It is clear that the centrifuge soil resistances are greater near the surface than Reese (1974)'s ultimate soil resistance values. The OpenSees soil resistance was smaller near the surface and greater at larger depths than those back-calculated from the centrifuge results. In the figure, it is shown that the maximum soil resistance mobilized in Bent-S increased with motion intensity and happened at deeper locations.

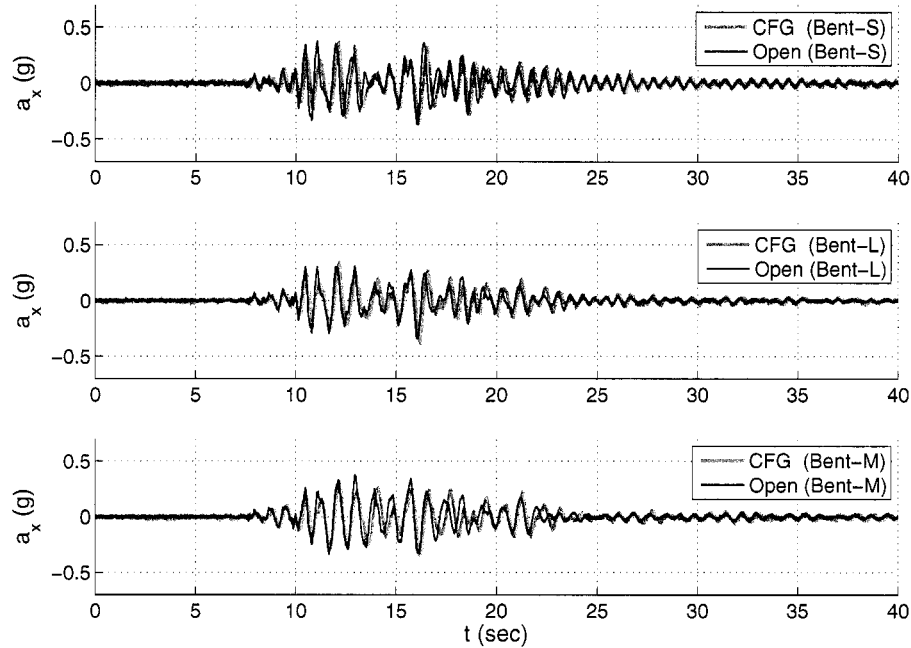


Figure 5.21: Centrifuge and OpenSees bridge deck acceleration time histories at three bent locations for Northridge event, $a_{max}=0.25g$

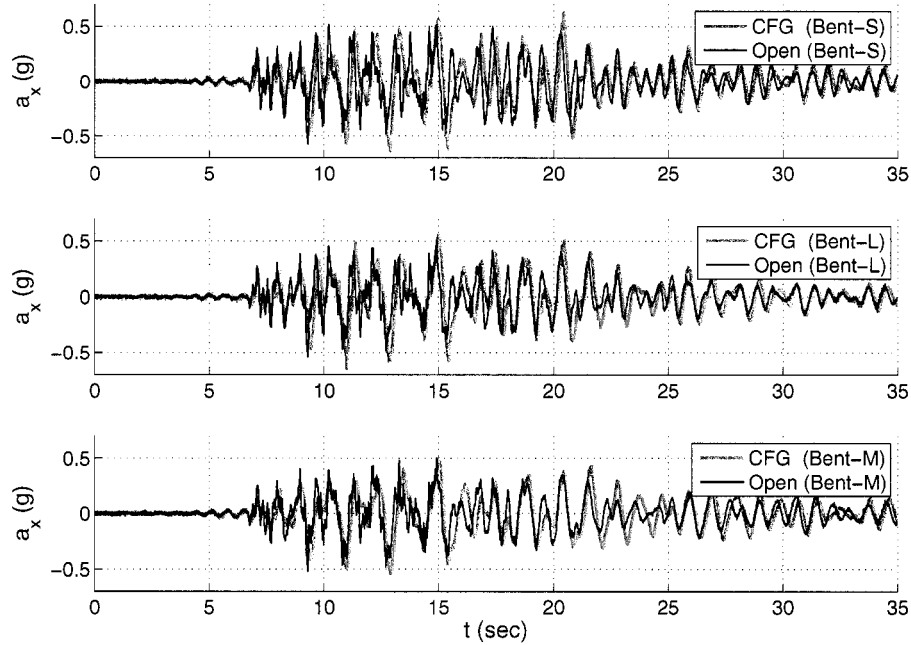


Figure 5.22: Centrifuge and OpenSees bridge deck acceleration time histories at three bent locations for Northridge event, $a_{max}=0.74g$

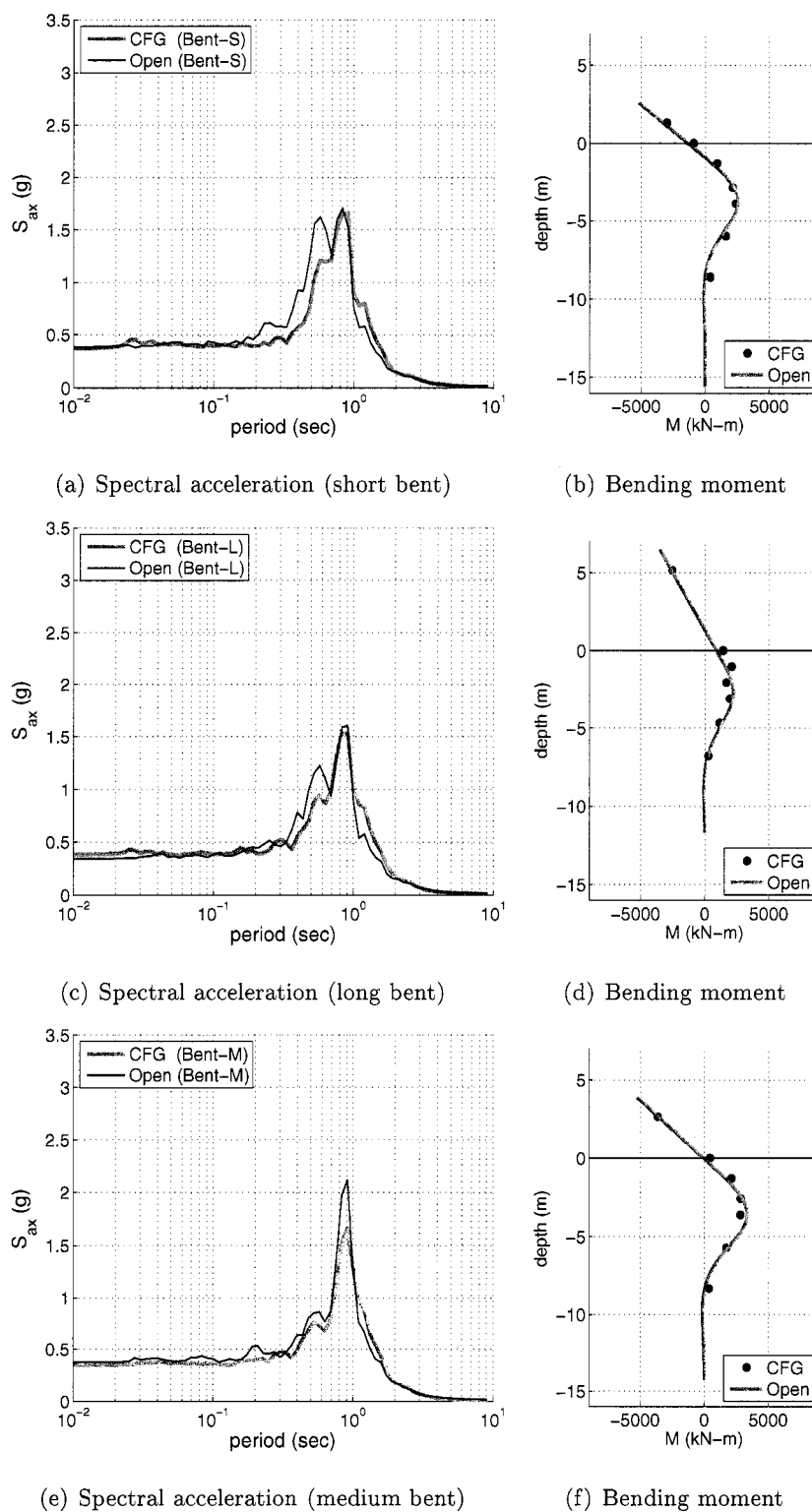


Figure 5.23: Centrifuge and OpenSees bridge superstructure response and pile bending moments for Northridge event, $a_{max}=0.25g$

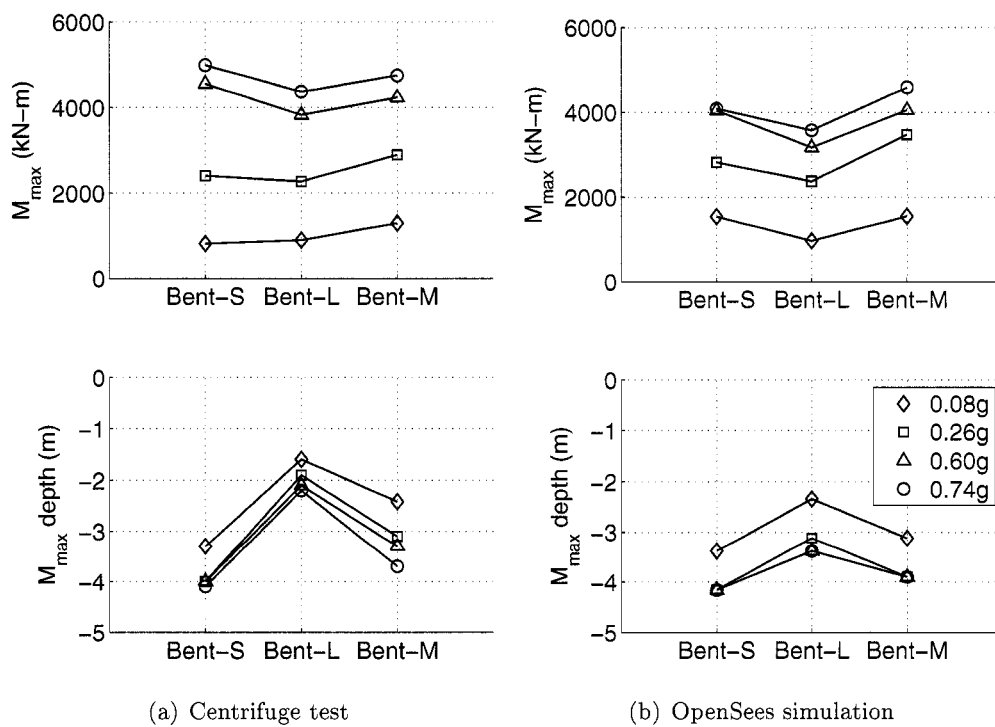


Figure 5.24: Centrifuge and OpenSees maximum bending moments below ground surface and the corresponding depths for a two-span bridge subjected to Northridge events with different intensities; $a_{max}=0.08g, 0.25g, 0.60g, \text{ and } 0.77g$

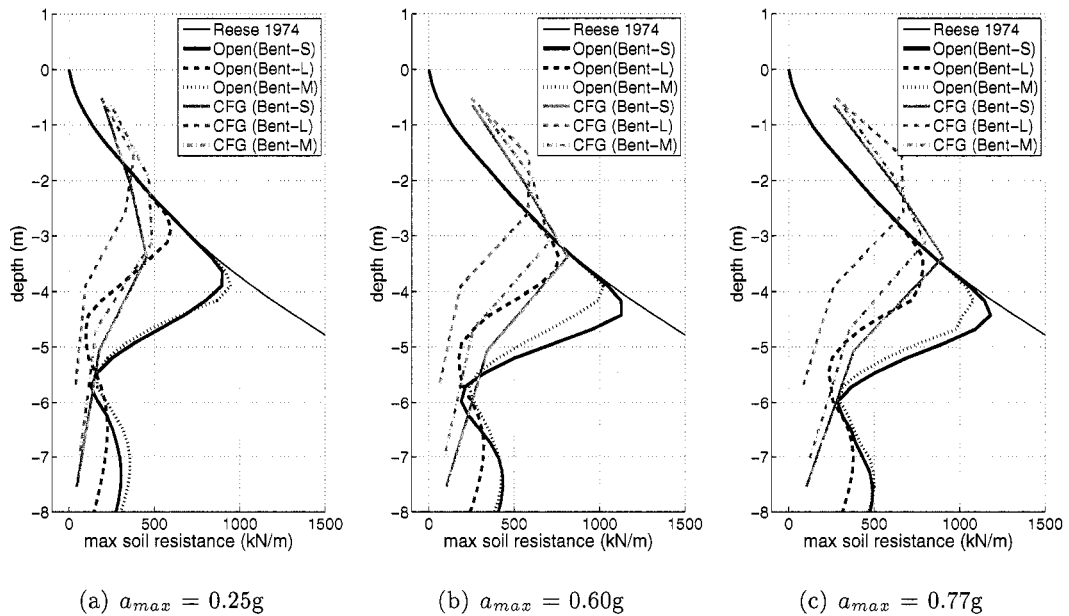


Figure 5.25: Centrifuge and OpenSees maximum soil resistance: Northridge events, $a_{max}=0.25g$, $0.60g$, and $0.77g$: the centrifuge back-calculated soil resistance data was provided by Ilankatharan (Ilankatharan et al., 2006)

5.5 Summary

The dynamic response of the soil and several drilled-shaft-supported structures (two-column bent, single-pile bent, and two-span bridge) in the centrifuge test was investigated using dynamic Beam-on-Nonlinear-Winkler-Foundation (BNWF) models in OpenSees numerical simulations. In this study, the physical response of bridge structures, especially the nonlinear soil-pile-structure interaction was investigated.

To better understand SPSI in these structures, parametric studies were performed for a bent and a single pile structure, focusing on the effects of different soil motions and $p-y$ parameters on the superstructure and pile response. In this study, the effect of the natural period of the soil-pile system on the structural response was investigated.

5.5.1 Centrifuge Experiments for Bridge Structures

In the centrifuge experiments, the two-span bridge, bents and single pile structures were supported by drilled shaft foundations installed in fairly good soil conditions (i.e, dry dense sand). The individual bents of the bridge structure had different clear heights above the ground surface due to varying ground surface elevation across the bridge.

5.5.2 Numerical Simulation of Centrifuge Experiments

The response of the bridge structures studied in the centrifuge experimental tests was simulated in OpenSees using dynamic BNWF models. For this purpose, 1-D shear beam soil models were coupled to two- or three-dimensional nonlinear structure models using interface p - y springs.

Soil Response

Using the Pressure-Dependent Multi-Yield (PDMY) elasto plastic material model available in OpenSees, the soil response in the centrifuge container was captured reasonably well for motions with various intensities. The 2-D soil model used to represent the centrifuge container dimension gave slightly better results than the 1-D soil model.

The natural period of the soil in the centrifuge container was investigated by evaluating the transfer function between the base and the soil at 2.6 m depth. It was also compared with simulations obtained using 1-D shear beam and 2-D centrifuge container soil models. The natural period of the soil in the centrifuge test (0.67 sec) was longer than that obtained from OpenSees eigenvalue analyses (0.52 sec for 2-D model and 0.48 sec for 1-D model based on elastic soil properties). In particular, the natural period of the 1-D shear beam soil model was shorter indicating a slightly stiffer soil system. Using the nonlinear PDMY soil model and the 2-D soil container model, the transfer function was captured very well in OpenSees.

Response of Bent, Single pile, and Two-span Bridge

The OpenSees two-column bent simulation results were in good agreement with the centrifuge results in terms of superstructure acceleration and pile bending moments. The response of the single pile structure was also well captured in OpenSees, especially in terms of superstructure accelerations. However, in the single pile, the maximum bending moments near the ground surface were underestimated for strong shaking and frequency sweeping shaking.

For the two-span bridge structure, the numerical model captured the centrifuge response reasonably well for various motions including bridge twisting due to varying ground surface elevation and maximum bending moment distribution.

Conclusion from Bridge Structure Simulations

From this simulation study, it is concluded that the dynamic BNWF models based on conventional p - y springs can capture the dynamic response of bridge structures supported by drilled shaft foundations installed in fairly good soil conditions (i.e, dry dense sand).

5.5.3 Sensitivity Studies for Bent and Single Pile Structures

To understand the effect of soil-pile-structure interaction in this bridge structure and to enhance user's confidence on interface spring parameter, parametric studies were performed using OpenSees, considering the effects of soil motion and p - y spring stiffness and ultimate resistance on the superstructure and pile response.

Soil Motion Effect on Structure Response

To change the soil motion, various soil masses and stiffness were used. The bent and single pile response seemed to be insensitive to the change in soil motion for moderate and strong shaking. The reason is that the frequency range affected by the changes in soil motion was far from the natural period of the soil-structure system. This observation was more evident in the single pile which had a longer natural period.

P-y Spring Parameter Effect on Superstructure and Pile Response

A p - y spring parametric study was conducted considering different p - y spring stiffness and ultimate resistances. Parameters were increased and decreased by 20% with respect to the base model parameters (Details on the parametric study are included in Appendix A).

To investigate the depths at which the p - y springs affect the superstructure response, several cases were considered: a near-surface region (from the surface to 3D depth), a deep region (below 3D depth), and full pile embedment depth. The change of both p - y parameters at deeper depths did not affect the superstructure and pile response. When the near-surface region and full depth region were considered, the superstructure response was very similar.

The p - y stiffness parameter change did not affect the bent and single pile superstructures response for moderate and strong shaking. However, the maximum bending moments and shear forces were slightly affected by the stiffness change, especially at large depths (e.g., greater than 3D). The change in p - y spring ultimate resistance did not affect the superstructure response at the bent and single pile structure for moderate and strong shaking. Especially, the peak superstructure acceleration was barely changed. However, the bending moment and shear force distributions were influenced. When the ultimate p - y resistance was decreased, the maximum bending moment (i.e, point of zero shear force) location moved deeper.

Natural Period of Soil-pile System

The natural period of the soil-foundation system was investigated by evaluating transfer functions between the soil and superstructure. From the study, it was found that the natural period of the soil-foundation system plays an important role in SPSI for bridges. The frequency content of the base, or soil, motion significantly affected the structural response (depending on the natural period of the soil-pile system).

One interesting observation in this study was that the natural periods of the soil-structure system varied due to the system nonlinearity associated with the motion characteristics and intensity. For example, the natural period of the bent and single pile subjected to moderate shaking were about 1.0 and 2.5 seconds, respectively. However, for the

frequency sweeping motion, the natural periods become 1.2 and 3.2 seconds (about 15% and 30% increase), respectively. To investigate the natural period variation during shaking, eigenvalue analyses were performed in OpenSees at every time step for a single pile structure. For moderate shaking, the natural period increased from 2.0 sec to 2.3 sec (15% increase). For strong shaking, the natural period increased from 2.0 sec to 2.7 sec (35% increase).

Conclusion from Sensitivity Study

From the sensitivity study, it is concluded that the bent and single pile superstructure response is insensitive to changes of soil ground motion and initial stiffness and ultimate resistance of p - y spring. The change of ultimate resistance slightly affects the bending moment distribution in the pile. One source of this insensitivity originates from the hyperbolic characteristics of the p - y curve envelope which shows a plateau after reaching ultimate resistance without any hardening.

Chapter 6

**RESPONSE OF BRIDGE BENTS WITH DIFFERENT PILE
EMBEDMENT LENGTHS AND SHAKING ORIENTATIONS****6.1 Introduction**

This chapter presents an investigation of different conditions that can be encountered in bridge structure design and analysis using motions of different intensities and frequency contents. The study included: i) bent structures subjected to different orientations of shaking, and ii) several bent and single pile structures with different pile embedment lengths. These scenarios were aimed at investigating higher nonlinear soil-pile-structure interaction with heavier superstructure mass and different pile embedment lengths.

6.2 Response of Two-column Bents Subjected To Various Orientation of Shaking

This section presents the results of response analyses of bent structures oriented at different angles with respect to the direction of shaking. Details of the models used in this study are presented in Section 4.4. The aim of this study was to understand the effect of shaking orientation on bent response. Simulation results for Bent-00, Bent-30, Bent-60, and Bent-90 were compared with centrifuge test results in terms of superstructure accelerations and pile bending moments in the transverse and longitudinal directions.

Figure 6.1 shows the superstructure response for the four oriented bents in two perpendicular directions. The superstructure response was well captured by the OpenSees simulations. The oriented bents showed relatively small twisting (θ_{zz}) - i.e., the translational response dominated.

At the top of the bent columns, Bent-00 and Bent-30 showed similar translational response in the transverse direction (i.e. x-direction) and Bent-60 and Bent-90 showed similar translational response (a_{y1} and a_{y2} in Figure 4.6) in the longitudinal direction with relatively small amplitudes. The high frequency content observed in Bent-60 and Bent-90 acceleration

time histories were associated with superstructure rotation (θ_{xx}) around the x-axis.

Figure 6.2 shows envelopes of maximum bending moment for the four oriented bents in two directions. The third column shows combined maximum bending moments calculated as the square root of sum of the squares (SRSS) using OpenSees simulation results. These values can be considered representative of the actual demand on the piles. The figure shows that the bending moments were well captured in OpenSees. The bending moment plots show that Bent-00 had the largest maximum bending moment at the top of the column.

The maximum acceleration in the transverse direction (a_x) correlated well with the peak transverse acceleration of Bent-00 multiplied by the cosine of the bent angle. The maximum accelerations in the longitudinal direction (a_{y1}) correlated well with the peak longitudinal acceleration of Bent-90 multiplied by the sine of the bent angle. Figure 6.3 shows these results. This relationship can be approximated by

$$a_{x,max}(\theta) = a_{x,max}(0^\circ) \times \cos(\theta) \quad (6.1)$$

$$a_{y,max}(\theta) = a_{y,max}(90^\circ) \times \sin(\theta) \quad (6.2)$$

where θ represents the bent structure orientation with respect to the shaking direction.

Figure 6.4 shows the rotational response of the superstructure. The superstructure rotation (θ_{yy}) around the y-axis was small for all structures while the rotation (θ_{xx}) around the x-axis was about 2 degrees for strong shaking events. The twisting rotation (θ_{zz}) was the largest in Bent-60. The rotation response (θ_{yy}) and (θ_{xx}) were well captured in OpenSees. The twisting rotation (θ_{zz}) could not be captured well in OpenSees.

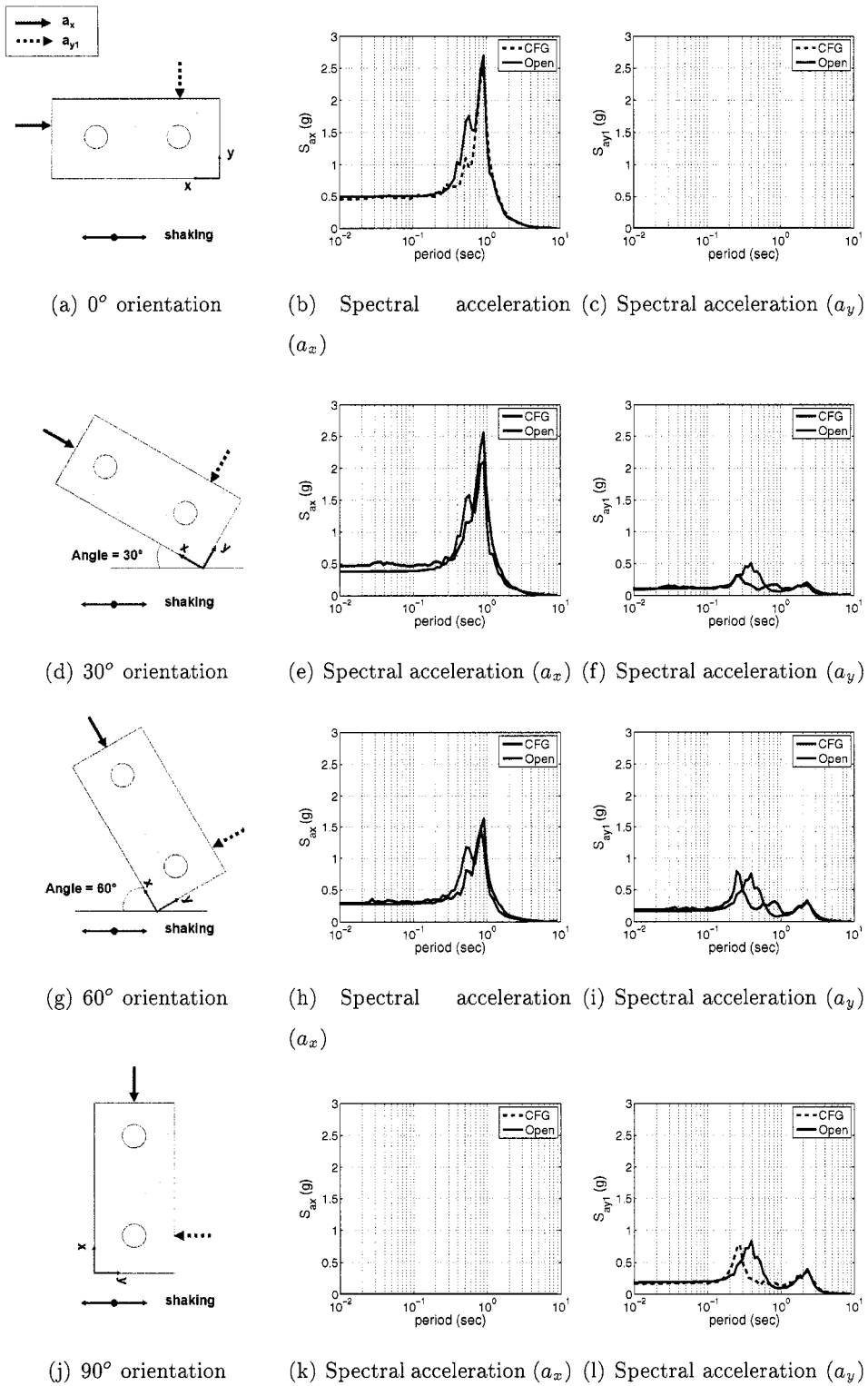


Figure 6.1: Centrifuge and OpenSees acceleration response spectra at bent top in bridge transverse and longitudinal direction - Northridge event, $a_{max}=0.25g$

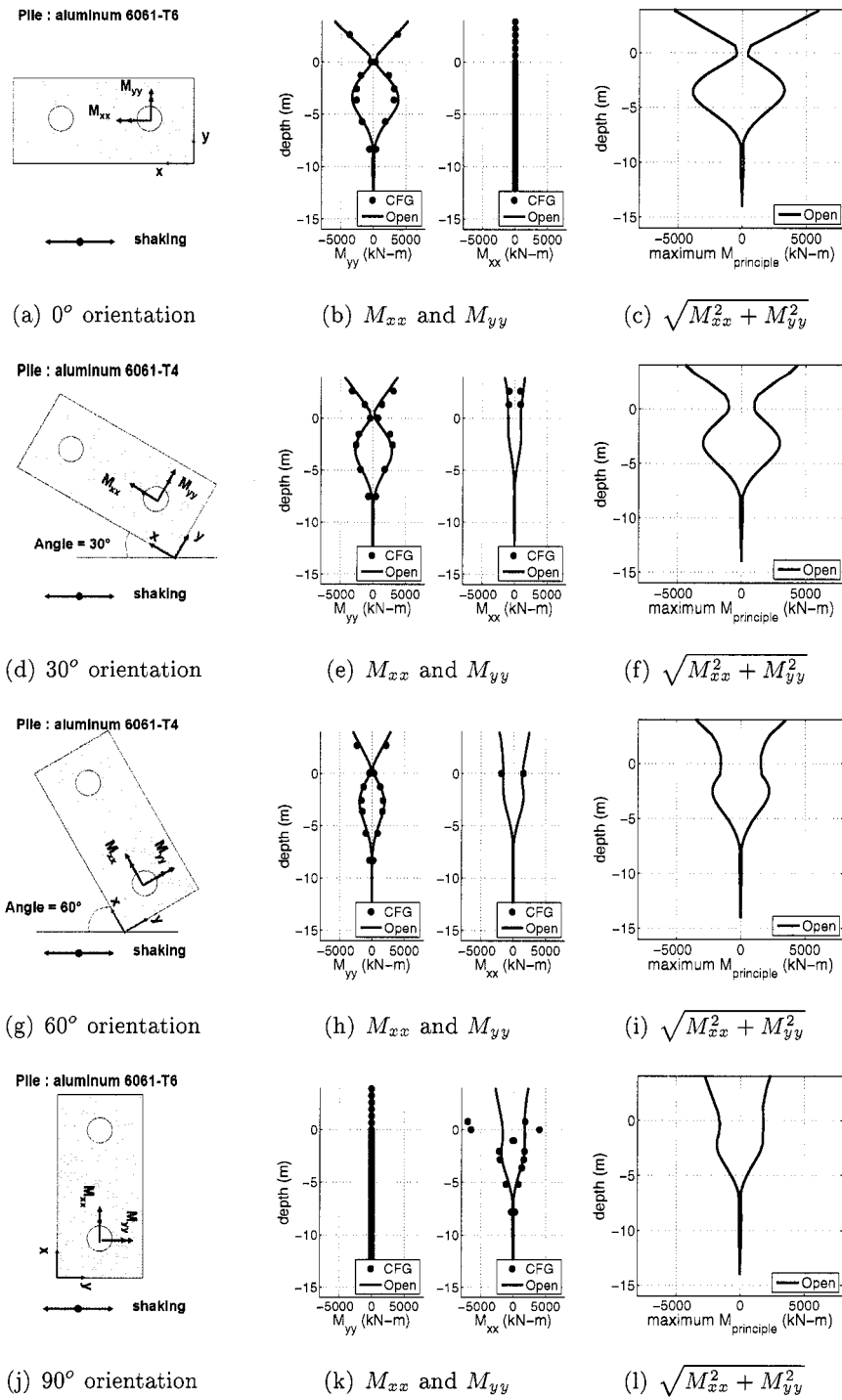
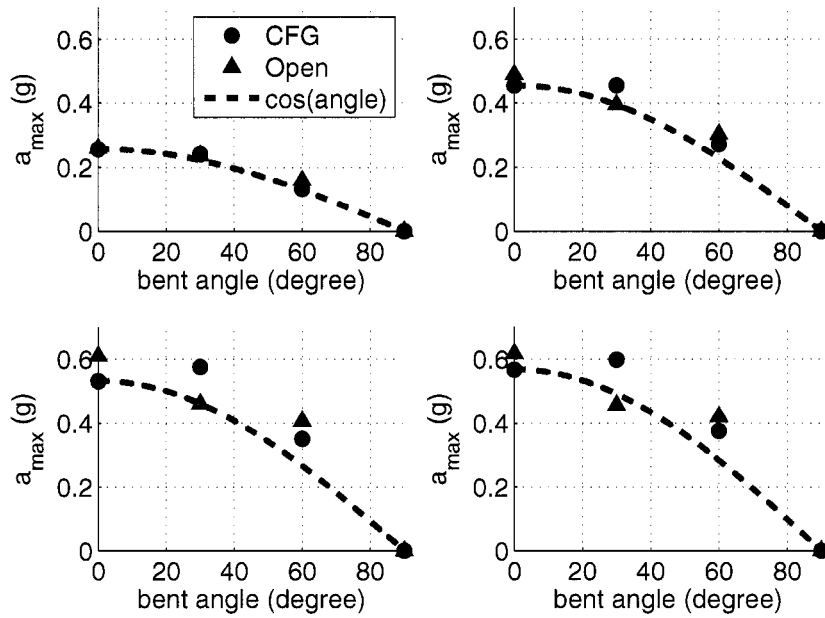
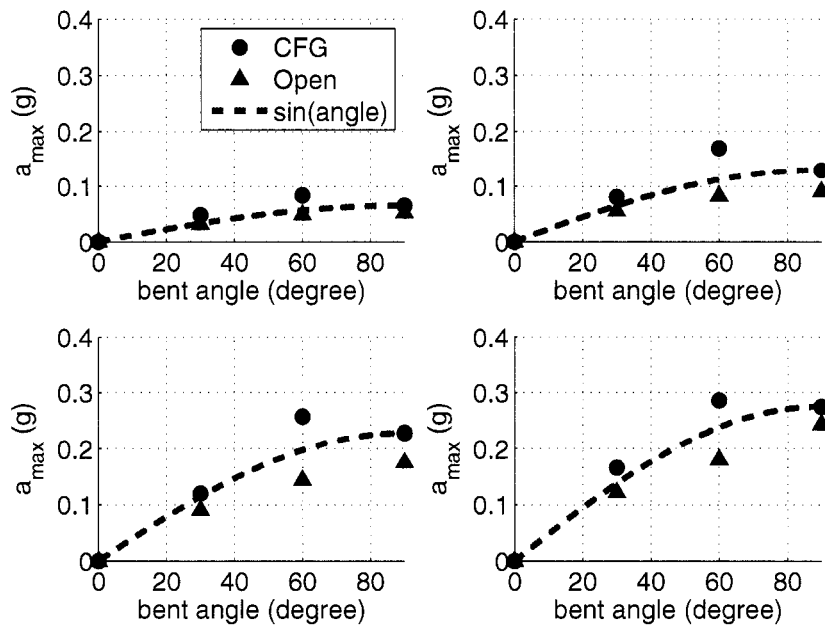


Figure 6.2: Centrifuge and OpenSees maximum pile bending moment envelopes (M_{xx} and M_{yy}) and maximum principal bending moments ($\sqrt{M_{xx}^2 + M_{yy}^2}$) in oriented bents - Northridge event, $a_{max}=0.25g$

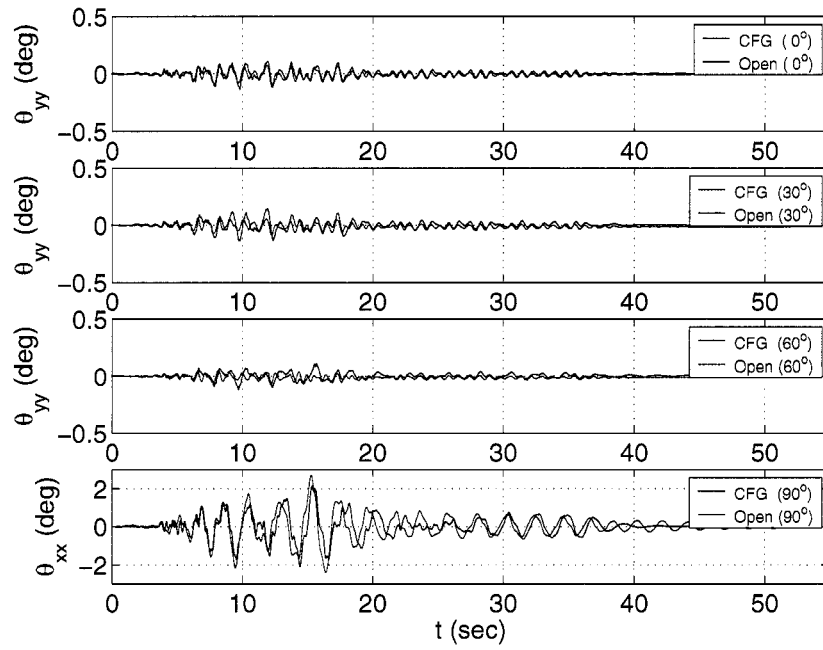


(a) Bent response in transverse direction

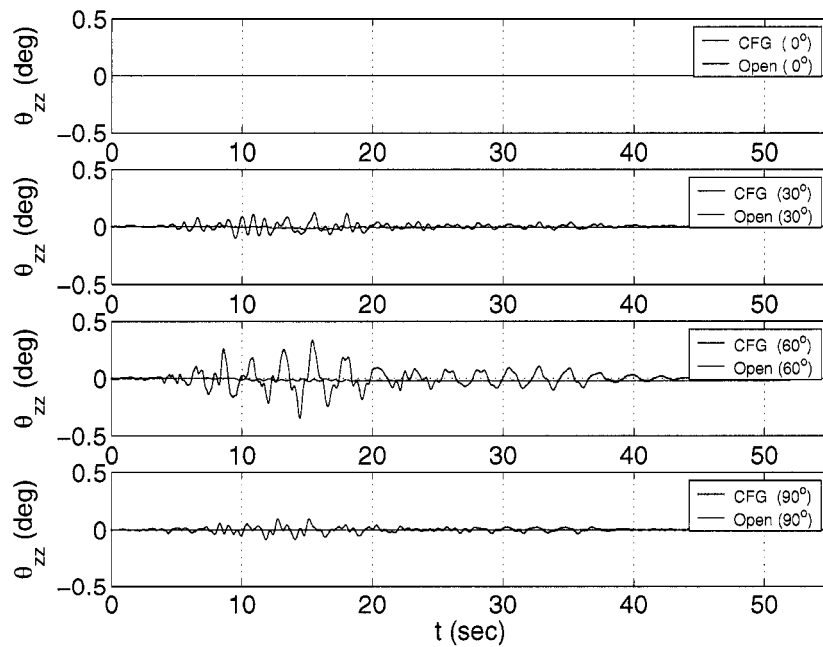


(b) Bent response in longitudinal direction

Figure 6.3: Bent orientation effect on recorded and simulated peak horizontal acceleration at the bent top in two local directions - Northridge event, $a_{max}=0.08g$, $0.25g$, $0.60g$, and $0.77g$



(a) Bent vertical rocking - θ_{xx} and θ_{yy}



(b) Bent horizontal twisting rotation - θ_{zz}

Figure 6.4: Rotation response of oriented bent superstructure - Northridge event, $a_{max}=0.77g$

6.3 Response of Bridge Structures with Various Pile Embedment Lengths

This section presents results corresponding to the response of bridge structures supported by one or two pile foundations with different pile embedment lengths and superstructure masses. The objective of this study was to understand the effect of pile embedment length on the structure response. For this purpose, several bridge structures were considered in the centrifuge (CFG3) and in corresponding numerical simulations:

- two heavy bents subjected to shaking in the transverse direction (Figure 4.4b) : Bent-LL-Hy with two long piles and Bent-SS-Hy with two short piles
- three single pile structures with different pile lengths (Figure 4.4b): sPile-L, sPile-M, and sPile-S
- heavy and light bents subjected to shaking in the longitudinal direction (Figure 4.4c): a heavy bent (Bent-LS-Hy) supported by one short and one long pile, and a light bent (Bent-LS-Lt) supported by one short and one long pile.

The centrifuge test results recorded in CFG3 were first compared to each other to understand the physical response. Then, the centrifuge test results were compared to OpenSees simulation results to show the capability of the dynamic BNWF model simplification for various structural conditions.

As a preliminary step, the theoretical pile embedment length (critical length) was evaluated using Equation 2.21 (Randolph, 1981). If pile embedment is greater than a critical length, the lateral response of the pile is not significantly affected by the additional pile length. The critical length for the single piles was found to be about 6D to 8D; depending on soil subgrade modulus. This means that Bent-SS-Hy and sPile-L would be considered as flexible piles.

6.3.1 Response of Heavy Bents Supported by Two Long Piles and Two Short Piles (Bent-LL-Hy and Bent-SS-Hy)

The effect of pile embedment length on the bent response was investigated for the heavy bents subjected to shaking in the transverse direction. Bent-LL-Hy had a 12D pile length

and Bent-SS-Hy had a 5D pile length. The superstructure mass was increased in both bents by 50% of the bent superstructure mass (e.g., Bent-M) to force higher nonlinear soil-pile-structure interaction effects.

Centrifuge Test Results

Figures 6.5 and 6.6 compare the centrifuge response of Bent-LL-Hy and Bent-SS-Hy in terms of superstructure acceleration time histories and response spectra in the transverse direction. The response of Bent-LL-Hy and Bent-SS-Hy were slightly different for different motions. For small shaking (Step-wave, $a_{max}=0.04g$), Bent-SS-Hy showed a shorter fundamental period and a slightly larger peak acceleration. For moderate shaking (Northridge, $a_{max}=0.25g$), Bent-LL-Hy and Bent-SS-Hy showed similar response. For strong shaking (frequency sweeping motion, $a_{max}=0.41g$), Bent-SS-Hy showed shorter fundamental period and a smaller peak acceleration. The acceleration time histories plots show that Bent-SS-Hy exhibited a shorter response period.

Comparison of Centrifuge Test Results and OpenSees Simulation Results

Figures 6.7 and 6.8 show comparisons between the simulated superstructure response and centrifuge results. For moderate Northridge shaking, the response of both structures was well captured in OpenSees. For Bent-LL-Hy, the frequency content in the 0.5 to 1.0 Hz range was underestimated and the frequency content in the 1.0 to 1.5 Hz range was overestimated by OpenSees, while for Bent-SS-Hy the frequency content in the 1.0 to 2.0 Hz range was overestimated by OpenSees. Figure 6.8 shows a similar effect for strong shaking (frequency sweeping, $a_{max}=0.41g$) and a large difference in peak acceleration and maximum bending moment is clearly noticeable. Since the structures were heavy, the underestimated peak superstructure acceleration was clearly reflected in the pile force. Figure 6.9a and 6.9b show that for small and moderate shaking events, the centrifuge maximum pile bending moments were well matched in OpenSees. However, it is shown in Figure 6.9c that for stronger events the OpenSees predictions were much smaller than the measured values.

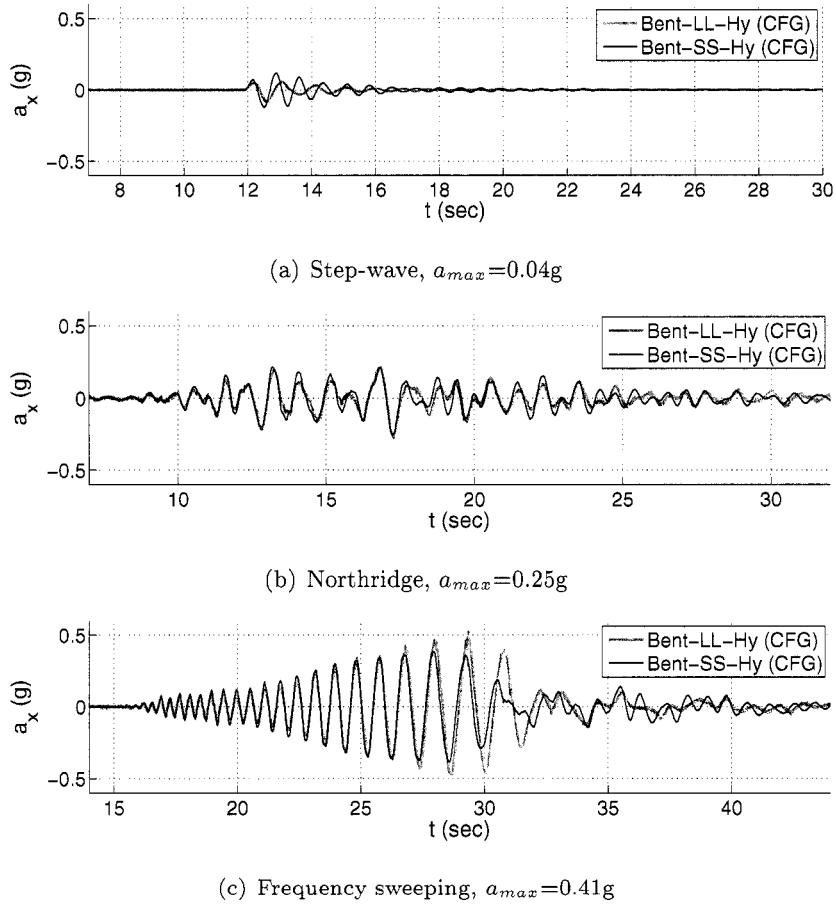


Figure 6.5: Comparison of superstructure acceleration time histories for Bent-LL-Hy (pile embedment length = 12.0 D) and Bent-SS-Hy (pile embedment length = 5.0D) in centrifuge test

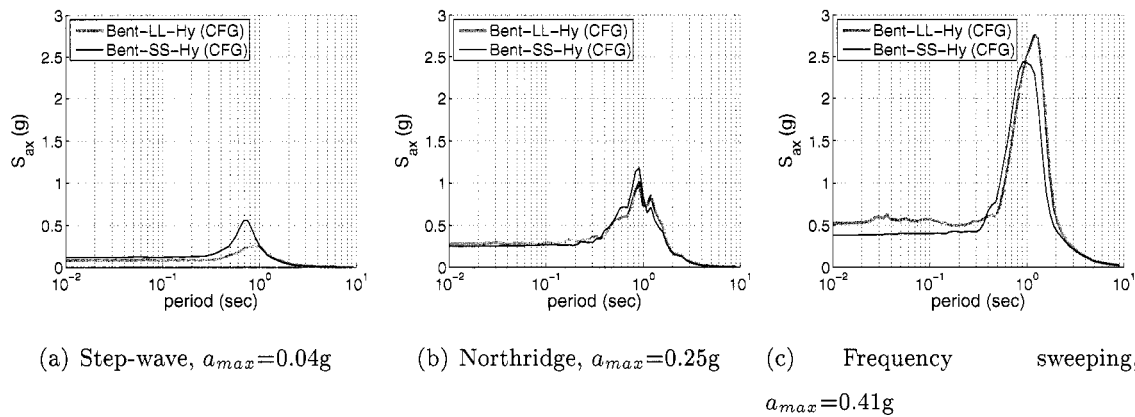
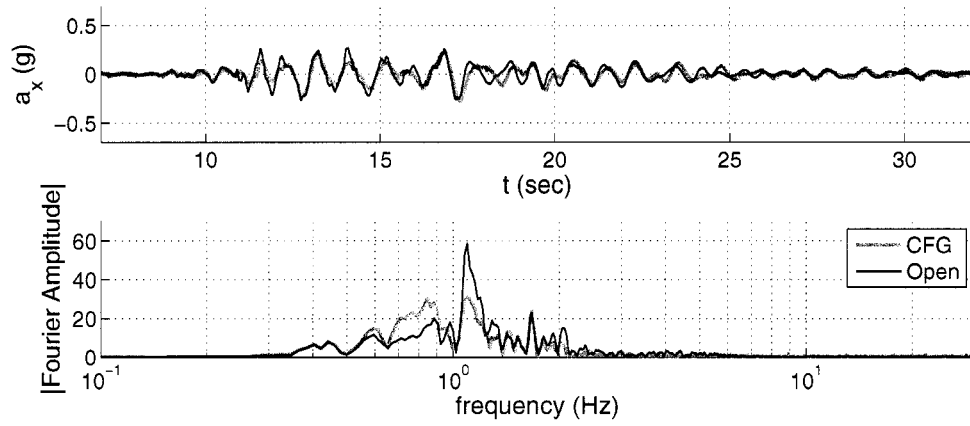
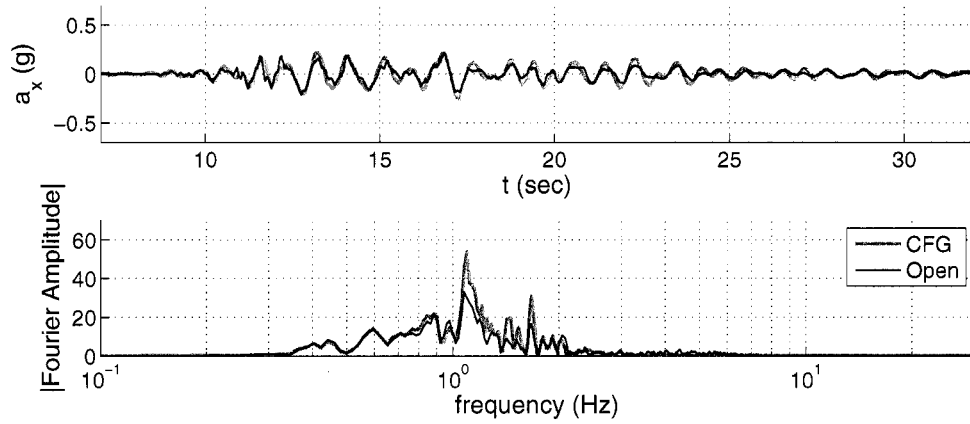


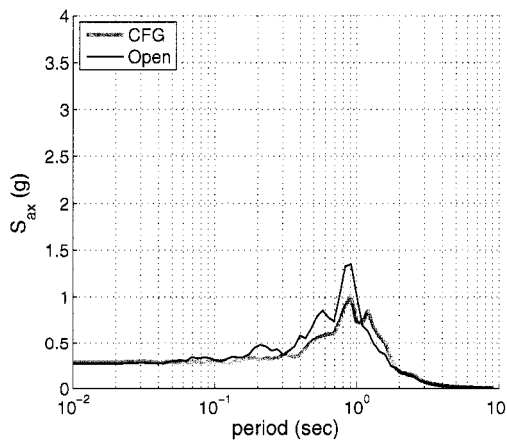
Figure 6.6: Comparison of superstructure response spectra for Bent-LL-Hy (pile embedment length = 12.0 D) and Bent-SS-Hy (pile embedment length = 5.0D) in centrifuge test



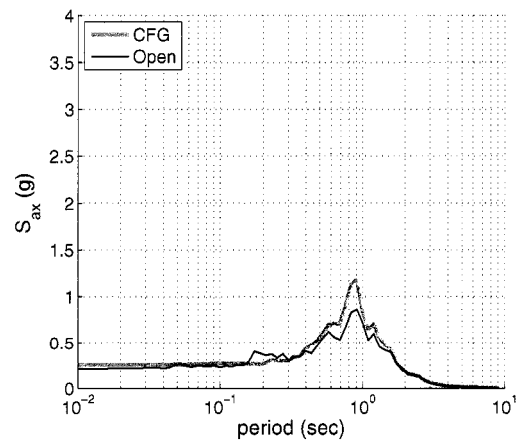
(a) superstructure acceleration (Bent-LL-Hy)



(b) superstructure acceleration (Bent-SS-Hy)

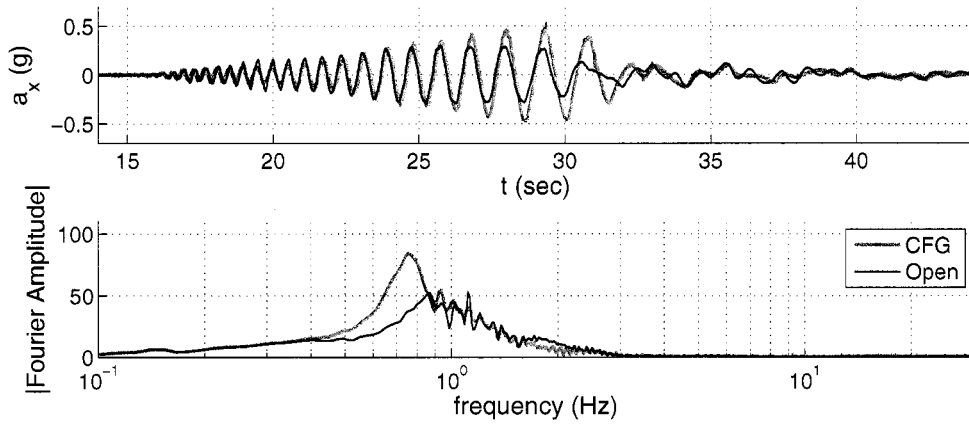


(c) Spectral acceleration (Bent-LL-Hy)

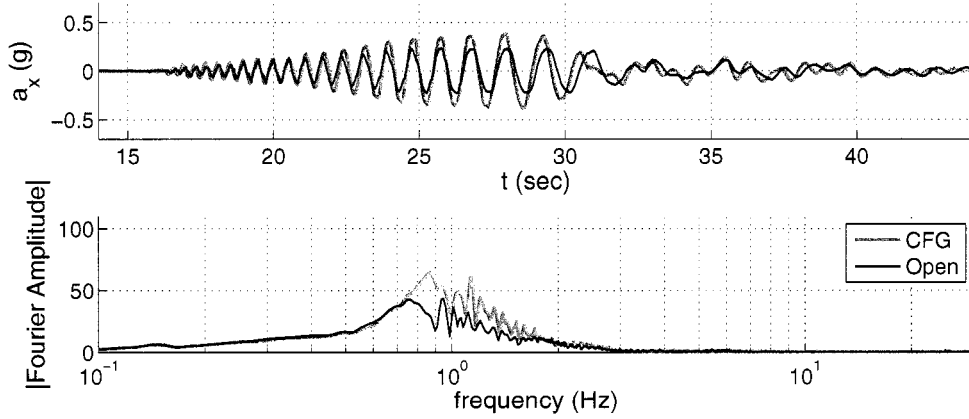


(d) Spectral acceleration (Bent-SS-Hy)

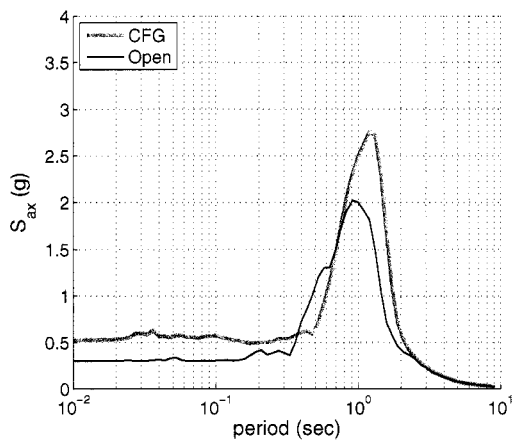
Figure 6.7: Centrifuge and OpenSees superstructure acceleration response for Bent-LL-Hy and Bent-SS-Hy subjected to Northridge motion, $a_{max} = 0.25g$



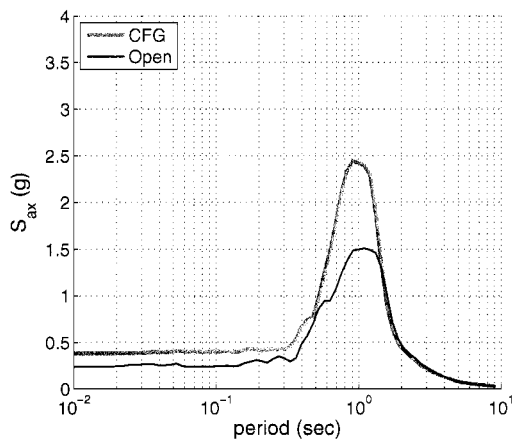
(a) superstructure acceleration (Bent-LL-Hy)



(b) superstructure acceleration (Bent-SS-Hy)



(c) Spectral acceleration (Bent-LL-Hy)



(d) Spectral acceleration (Bent-SS-Hy)

Figure 6.8: Centrifuge and OpenSees superstructure acceleration response for Bent-LL-Hy and Bent-SS-Hy subjected to sweeping motion, $a_{max}=0.41g$

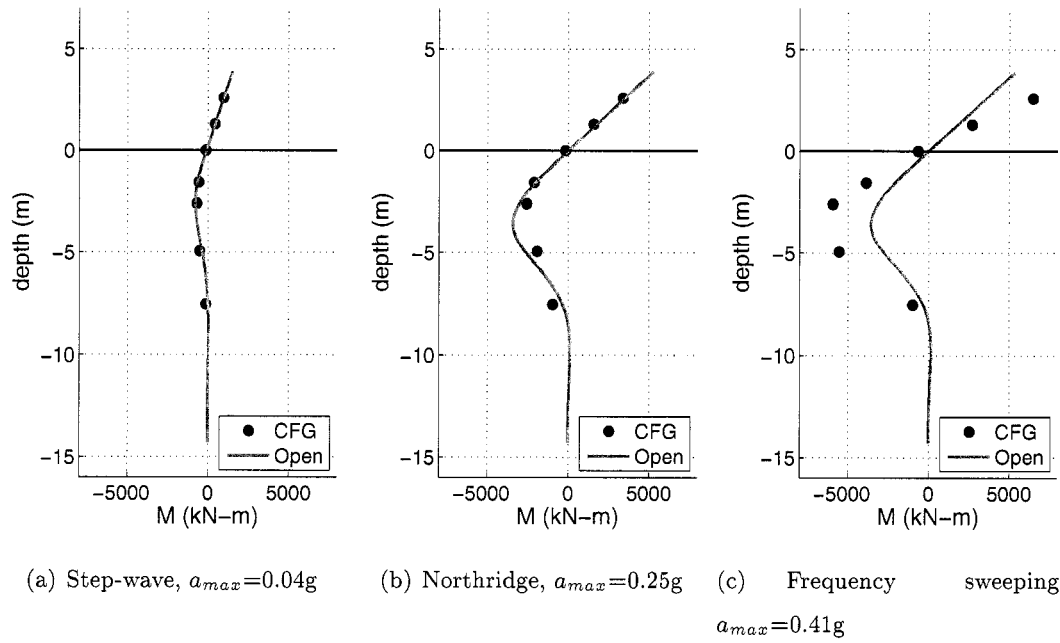


Figure 6.9: Centrifuge and OpenSees bending moments for Bent-LL-Hy (embedment length = 12.0D)

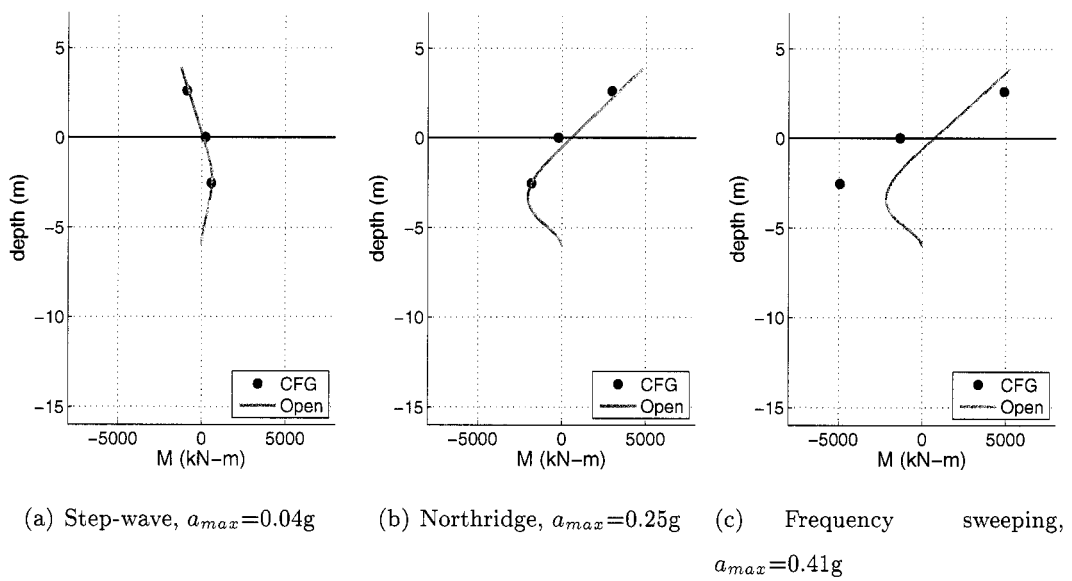


Figure 6.10: Centrifuge and OpenSees bending moments for Bent-SS-Hy (embedment length = 5.0D)

6.3.2 Response of Three Single Piles with Different Pile Length (*sPile-L*, *sPile-M*, and *sPile-S*)

To understand the effect of pile embedment length on the dynamic response of single piles, three different pile embedment lengths (12.1D, 7.5D, and 5.0D) were considered and the results recorded in centrifuge test and OpenSees simulations compared.

Centrifuge Test Results

The three single piles (*sPile-L*, *sPile-M*, *sPile-S*) tested in CFG3 had different embedment lengths (12.1D, 7.5D, and 5.0D) and the same clear-height above the ground surface. Figure 6.11 compares the centrifuge accelerations response spectra for the three structures and several motions. For the step-wave shaking, *sPile-S* showed a shorter fundamental period and larger peak acceleration than *sPile-L* and *sPile-M*. This is similar to what was observed in Bent-SS-Hy. For most shaking events, *sPile-L* and *sPile-M* showed similar response indicating the pile embedment length below the 7.5D depth did not affect the dynamic superstructure response. However, for strong shaking (frequency sweeping, $a_{max}=0.41g$), the peak acceleration of *sPile-S* was smaller than that recorded in the other two structures.

Comparison of Centrifuge Test Results and OpenSees Simulations

Figure 6.12 through 6.14 show comparisons between the centrifuge response and OpenSees numerical simulations for the three structures. Overall, the response of the three superstructures was well captured in OpenSees even though high frequency contents are slightly overestimated in OpenSees. For small and moderate shaking, pile bending moments were reasonably well predicted. For strong motions, however, the bending moments were underestimated in OpenSees.

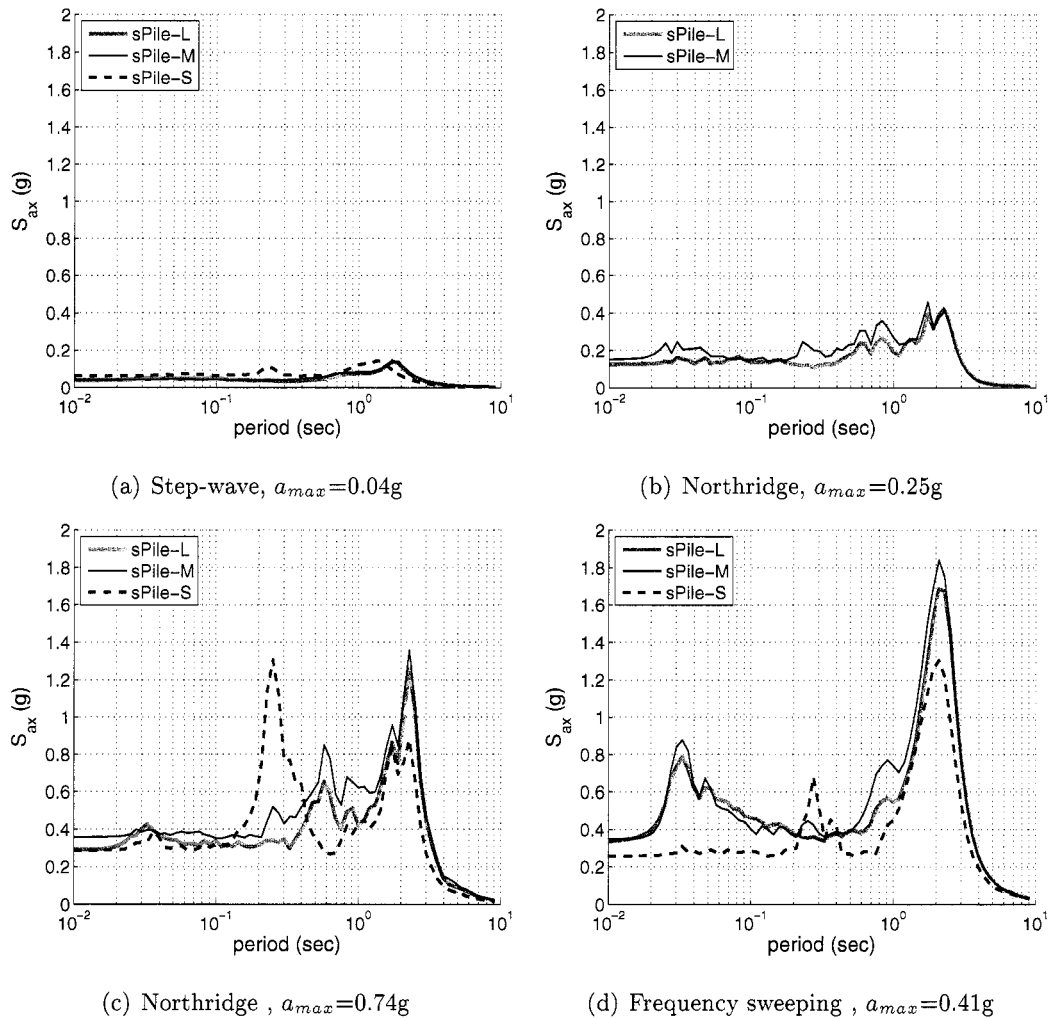
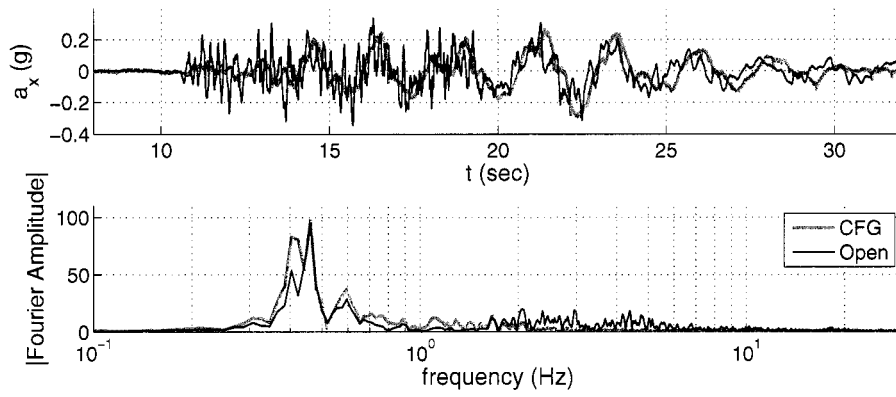
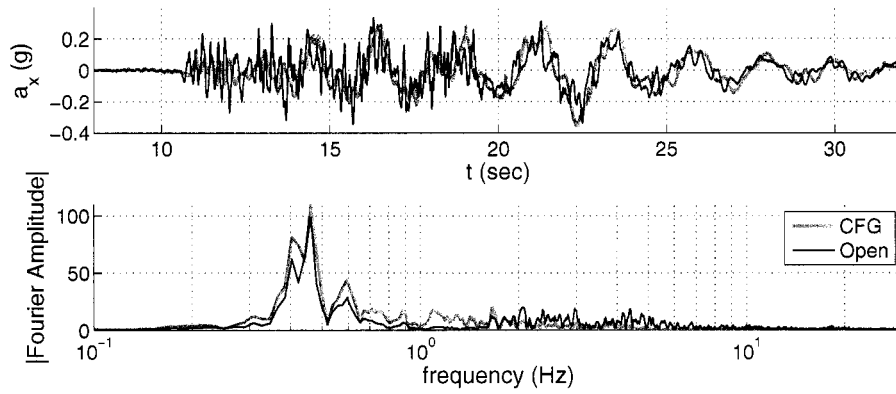


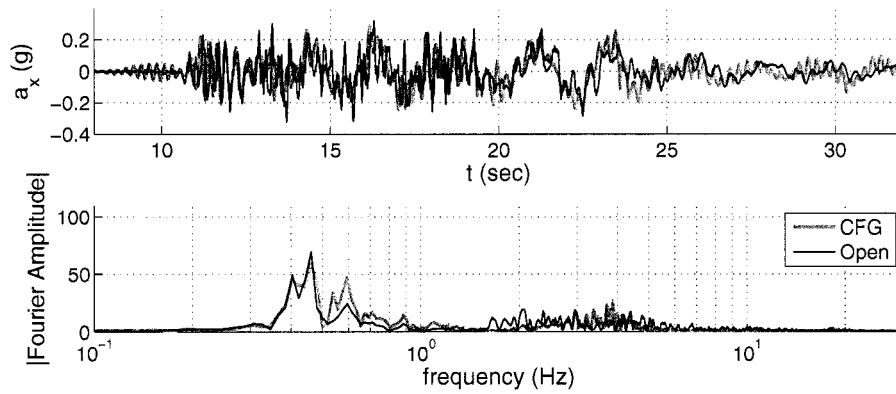
Figure 6.11: Structure response spectra for three single piles subjected to Northridge events ($a_{max} = 0.04g$, $0.25g$, and $0.74g$) and frequency sweeping event ($a_{max} = 0.41g$): pile embedment lengths = $12.0D$, $7.5D$, and $5.0D$. For the moderate Northridge motion ($a_{max} = 0.25g$), sPile-S superstructure response data could not be measured appropriately due to instrumentation malfunction.



(a) sPile-L



(b) sPile-M



(c) sPile-S

Figure 6.12: Centrifuge and OpenSees superstructure acceleration time histories for three single pile structures (embedment lengths = 12.0 D, 7.5 D, and 5.0 D) subjected to Northridge motion event, $a_{max} = 0.74g$

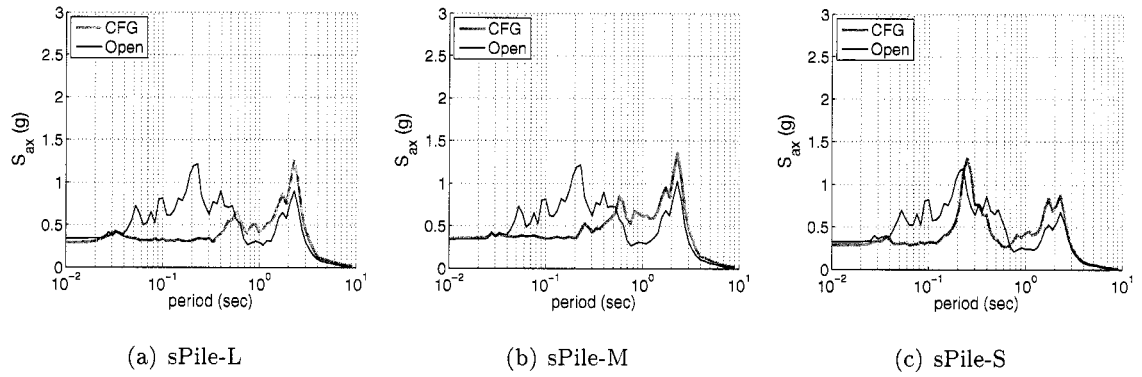


Figure 6.13: Centrifuge and OpenSees superstructure acceleration response spectra for three single pile structures (embedment lengths = 12.0 D, 7.5 D, and 5.0 D) subjected to Northridge motion event, $a_{max} = 0.74g$

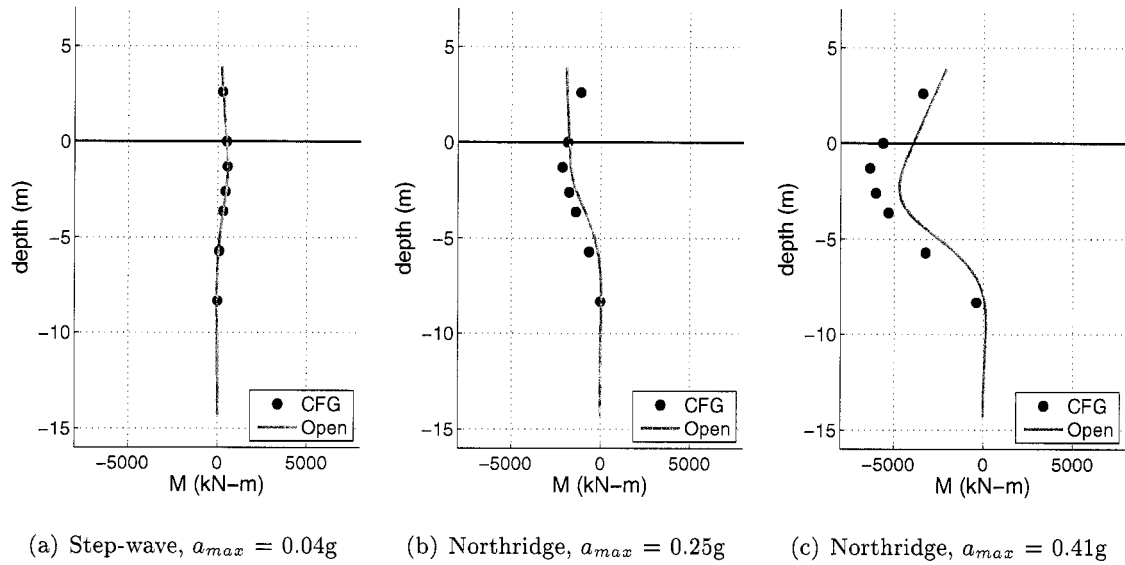


Figure 6.14: Centrifuge and OpenSees maximum bending moments for sPile-L (embedment length = 12.0D) subjected to varying intensity motions

6.3.3 Response of a Bent Structure with Long-Short-Pile-Embedment-Lengths

(Bent-LS-Hy and Bent-LS-Lt)

Bent-LS-Hy and Bent-LS-Lt were subjected to shaking in the longitudinal direction as in Bent-90. Therefore, their response was expected to be similar to that of a single pile structure. However, since Bent-LS-Hy and Bent-LS-Lt had different pile embedment lengths (12D and 5D), the response was expected to a combination of the response recorded in sPile-L and sPile-S, and rocking was also expected.

Centrifuge Test Results

Figure 6.15 shows a comparison between the centrifuge response of the superstructure at two locations, next to the long and short piles (a_{y1} and a_{y2} in Figure 4.6) for several motions. The figures in the left column of Figure 6.15 compare the superstructure response recorded in the heavy structure (Bent-LS-Hy). The figures in the right column of Figure 6.15 compare the superstructure response recorded in the light structure (Bent-LS-Lt). Bent-LS-Hy showed very similar accelerations at the two locations (a_{y1} and a_{y2}) indicating negligible twisting (θ_{zz}). However, Bent-LS-Lt showed higher amplitude at low periods (0.1 to 0.5 sec) at the short pile location.

Comparison of Centrifuge Test Results and OpenSees Simulations

Figures 6.16 and 6.17 show comparisons between centrifuge results with OpenSees simulations for Bent-LS-Hy and Bent-LS-Lt. The figures show recorded and simulated response at two locations of the superstructure. The OpenSees simulations for Bent-LS-Hy show that the low frequencies (0.2 to 0.8 Hz) were underestimated and higher frequencies (0.8 to 3.0 Hz) were overestimated at both long and short pile locations. In Bent-LS-Lt, the response of the short pile (a_{y2}) was well captured in OpenSees, but the long pile response (a_{y1}) was overestimated, especially at high frequencies. Figure 6.18 and 6.19 show recorded and simulated maximum bending moment for both structures' long piles. For small and moderate shaking, the bending moments were well captured in OpenSees. For strong shaking (frequency sweeping, $a_{max}=0.41g$), however, the OpenSees results were underestimated

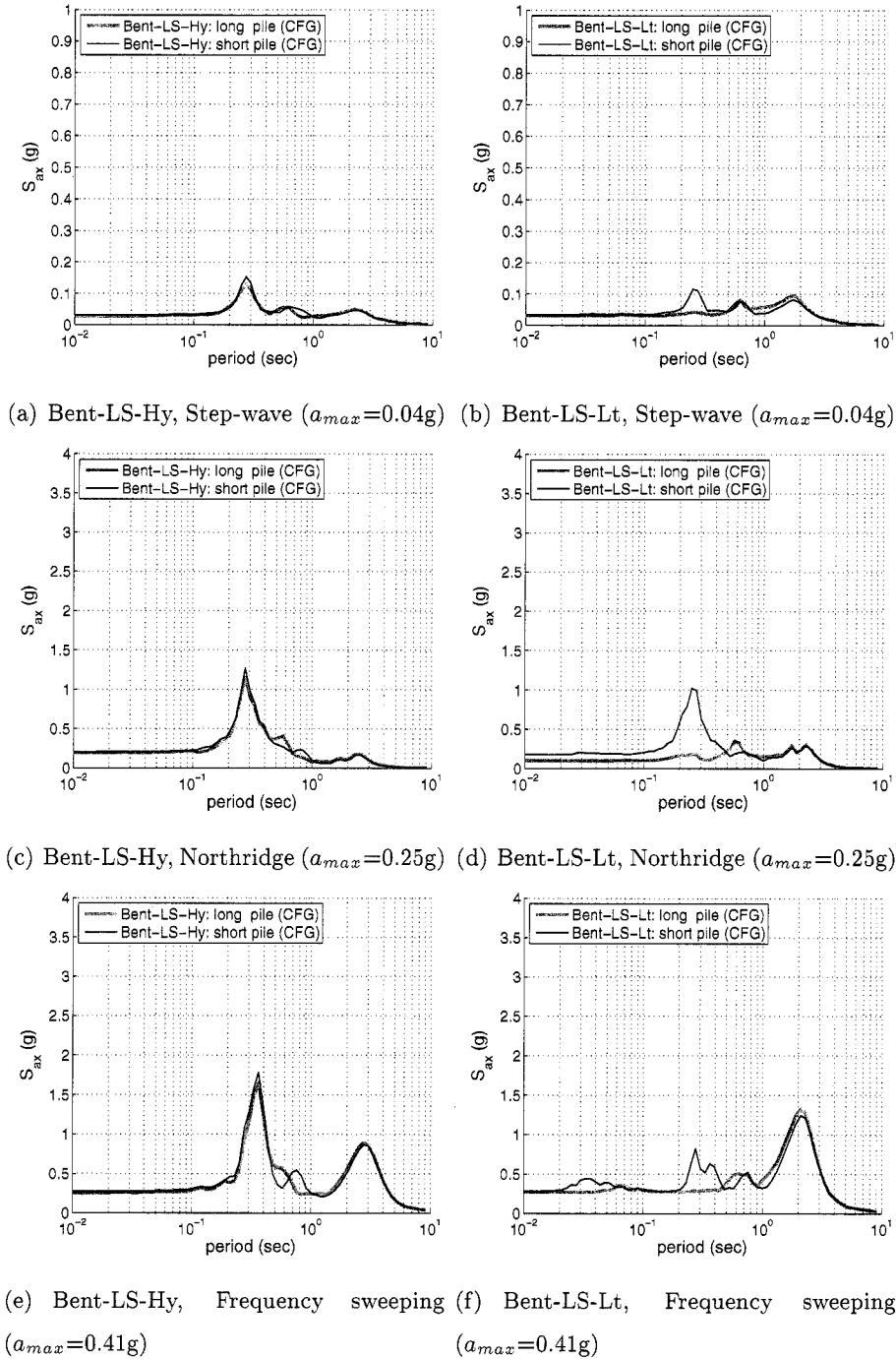


Figure 6.15: Comparison of centrifuge superstructure response spectra for Bent-LS-Hy and Bent-LS-Lt (with different pile embedment lengths = 12.0D and 5.0D) in CFG3

as observed in the single pile simulations.

6.4 Summary

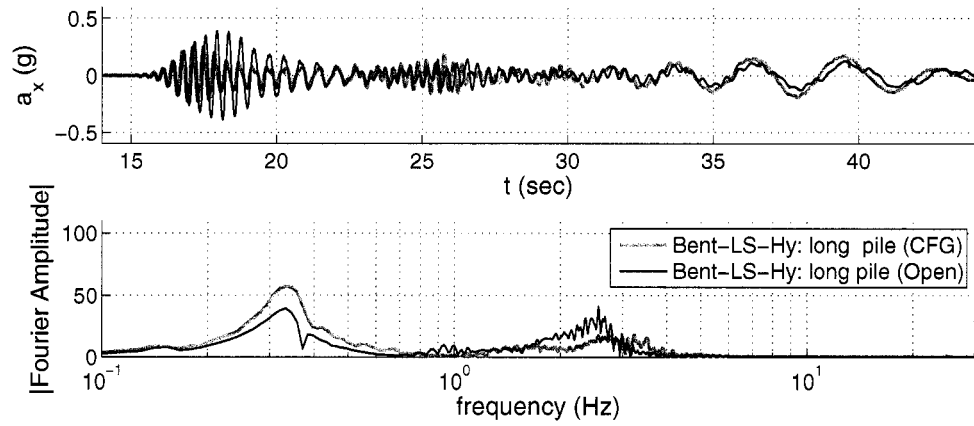
6.4.1 Centrifuge Experiments for Bridge Structures

The two-column bents subjected to shaking in different directions showed that the translation response of the structure dominated and twisting was minor. The bent at a 30-degree angle to the direction of shaking (Bent-30) showed a response similar to that observed in Bent-00. The bent with 60-degree angle to shaking (Bent-60) showed high frequency oscillations attributed to the superstructure rocking.

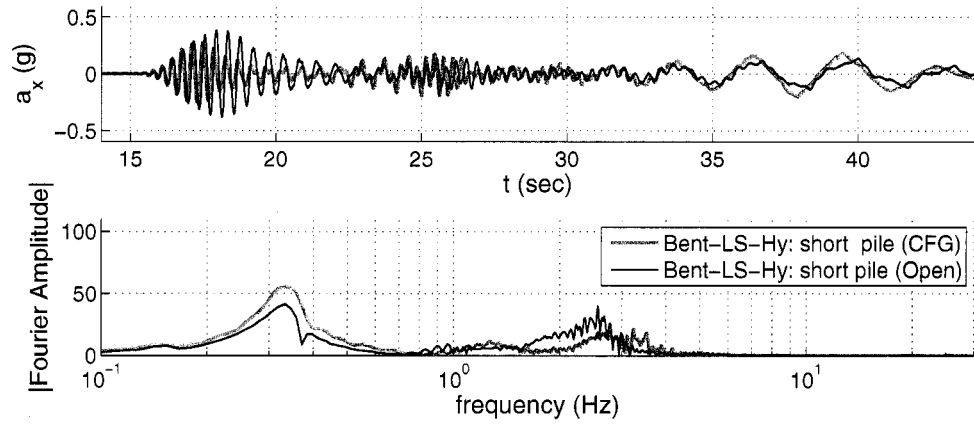
Three single piles were considered with different pile embedment lengths (12D, 7.5D, and 5D). The single piles with long and medium embedment lengths showed similar response indicating that the pile section below 8D did not affect the dynamic superstructure response for this particular soil conditions.

In two-column bents, long and short pile embedment lengths (12D and 5D) were considered and the superstructure mass was increased to force more nonlinear behavior. The superstructure response was slightly different depending on motion intensity. For moderate shaking, the two structures showed similar response. When strong shaking motions were applied, however, the bent with longer pile embedment (Bent-LL-Hy) showed larger peak acceleration with longer fundamental period than the bent with short pile embedment length (Bent-SS-Hy). This motion dependency indicated the effect of nonlinear soil-pile-structure interaction due to increased motion intensity and superstructure mass.

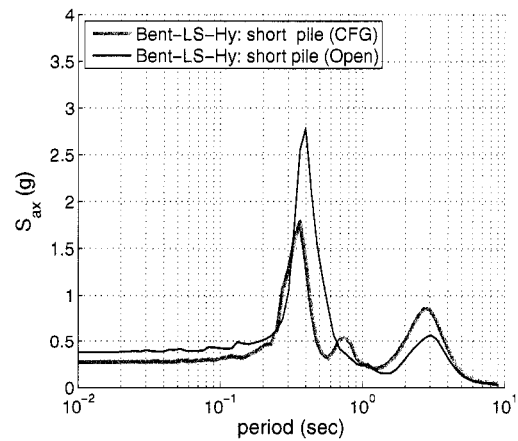
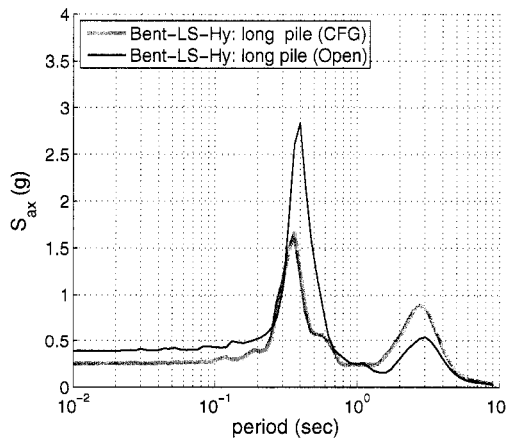
Targeting twisting and rocking, different pile embedment lengths (12D and 5D) were considered with two different superstructure masses. Even with different pile embedment lengths (Bent-LS-Hy and Bent-LS-Lt), the translational response of the superstructure dominated and the twisting response was small. The heavier structure (Bent-LS-Hy) showed very similar superstructure response at the long and short pile locations. The lighter bent (Bent-LS-Lt) showed high frequencies associated with superstructure rocking.



(a) superstructure acceleration (Bent-LS-Hy: long pile)

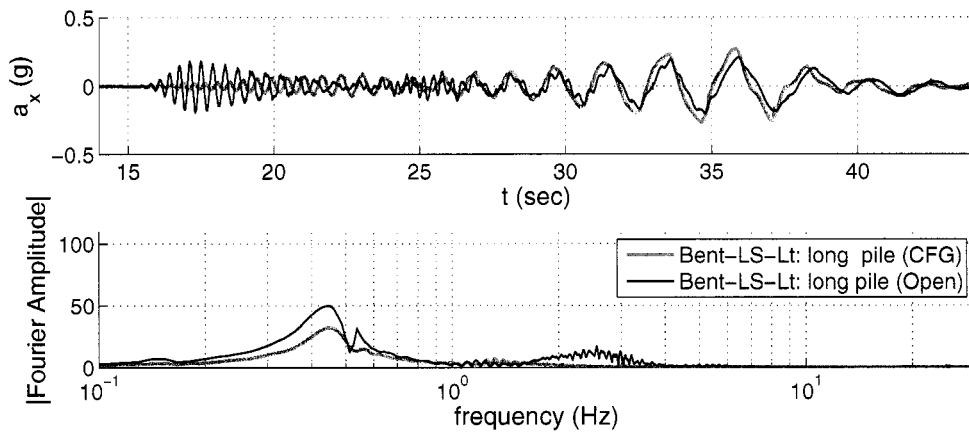


(b) superstructure acceleration (Bent-LS-Hy: short pile)

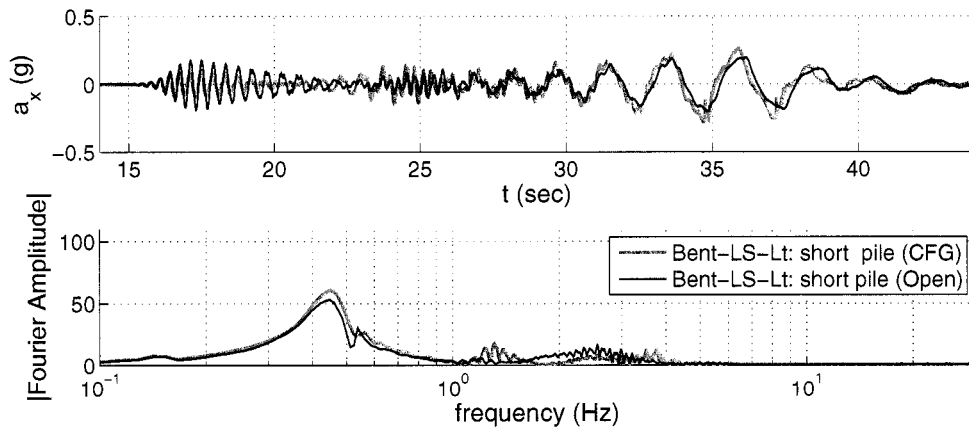


(c) Spectral acceleration (Bent-LS-Hy: long pile) (d) Spectral acceleration (Bent-LS-Hy: short pile)

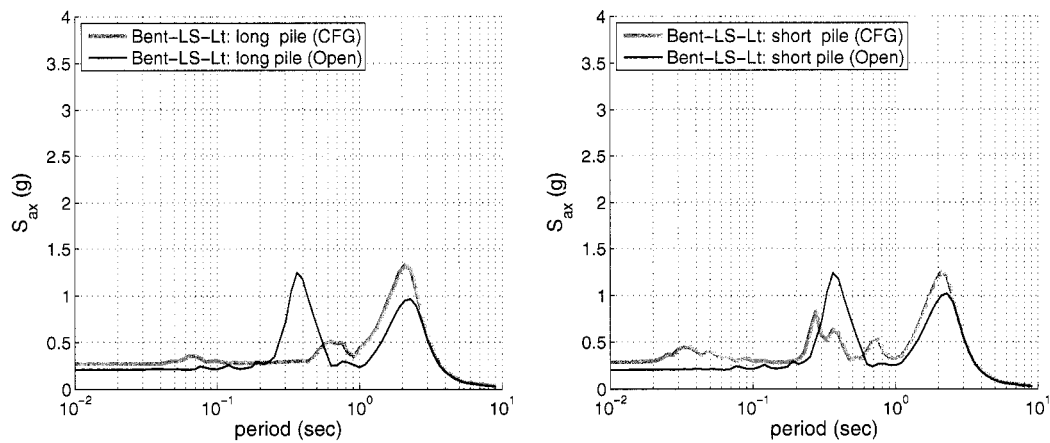
Figure 6.16: Comparison between centrifuge and OpenSees superstructure acceleration response for LS-Hy subjected to sweeping motion, $a_{max}=0.41g$



(a) superstructure acceleration (Bent-LS-Lt: long pile)



(b) superstructure acceleration (Bent-LS-Lt: short pile)



(c) Spectral acceleration (Bent-LS-Lt: long pile) (d) Spectral acceleration (Bent-LS-Lt: short pile)

Figure 6.17: Comparison between centrifuge and OpenSees superstructure acceleration response for Bent-LS-Lt subjected to sweeping motion, $a_{max}=0.41g$

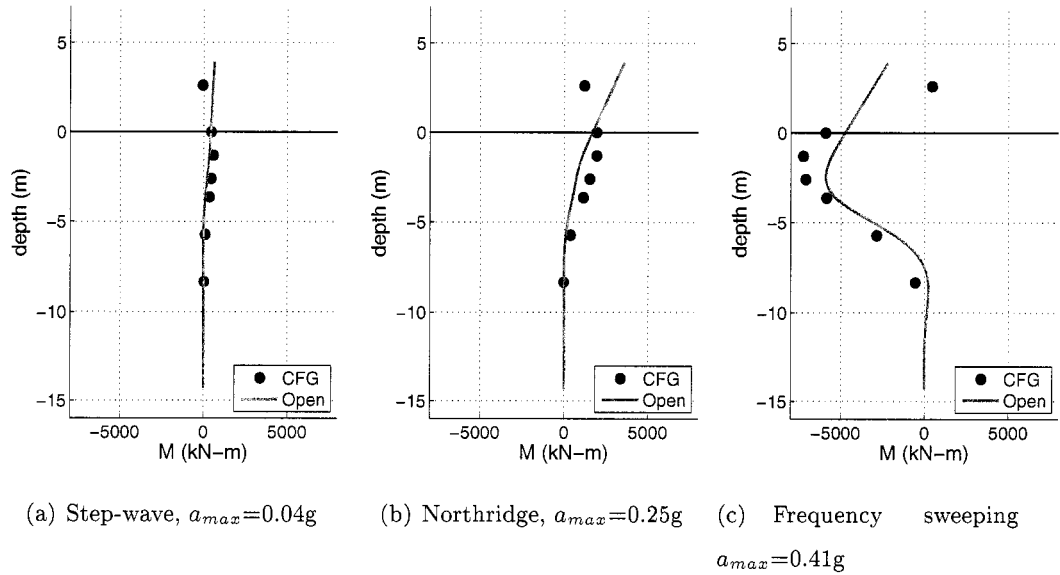


Figure 6.18: Comparison between centrifuge and OpenSees maximum bending moments for Bent-LS-Hy (embedment lengths = 12.0 D and 5.0 D) subjected to varying intensity motions

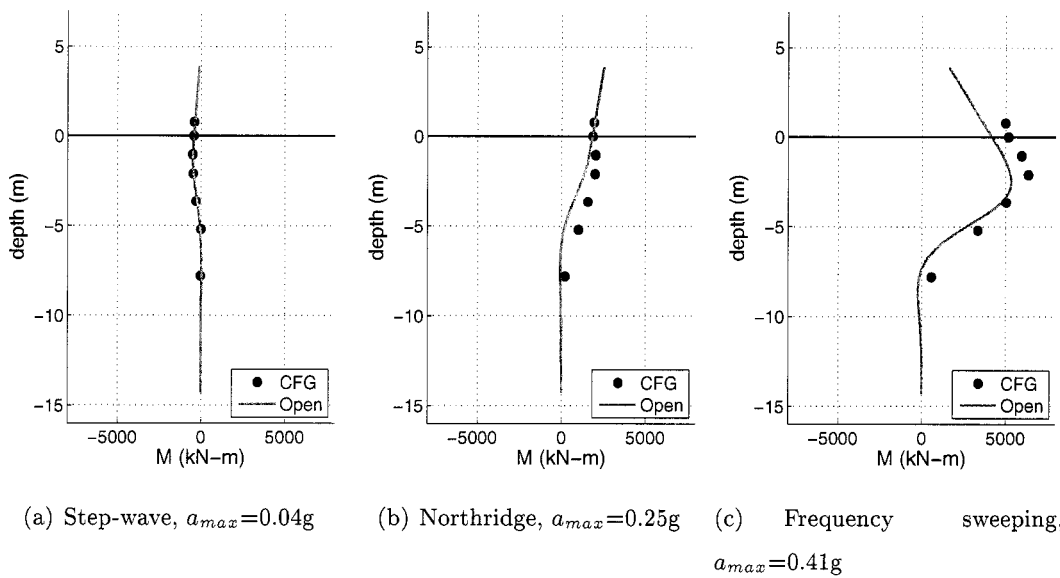


Figure 6.19: Comparison between centrifuge and OpenSees maximum bending moments for Bent-LS-Lt (embedment lengths = 12.0 D and 5.0 D) subjected to varying intensity motions

6.4.2 Numerical Simulation of Centrifuge Experiments

The numerical model could capture the oriented bent centrifuge response well, including rocking behavior of the bent superstructure due to the orientation of shaking, and maximum bending moment distribution. Similarly, the longitudinal peak acceleration of the oriented bents was well correlated to the sine of the bent angle.

The superstructure response and pile force of Bent-LL-Hy and Bent-SS-Lt was well captured in OpenSees for moderate shaking. However, for the sweeping motion ($a_{max}=0.41g$), both acceleration and bending moments were underestimated. The three single pile superstructure responses recorded in the centrifuge test were well captured in OpenSees for various motions. However, the maximum bending moments were underestimated. The results of the long-and-short-embedment-length bent structures (Bent-LS-Hy and Bent-LS-Lt) subjected to the longitudinal direction of shaking were well captured in the OpenSees simulations. However, the acceleration of the heavy superstructure (Bent-LS-Hy) was underestimated for the frequency sweeping motions resulting in smaller maximum pile bending moments.

Overall, the simulation results for the bent structures subjected to shaking in the longitudinal direction (Bent-LS-Hy and Bent-LS-Lt) and single piles (sPile-L, sPile-M, and sPile-S) showed similar response (i.e., good estimation of superstructure acceleration, but underestimation of pile force) for the Northridge motions. However, the peak accelerations and bending moments of the heavier structure (Bent-LS-Hy) were underestimated in OpenSees for the frequency sweeping motion. Similarly, the simulation results for the heavy bent structure subjected to shaking in the transverse direction (Bent-LL-Hy and Bent-SS-Hy) were underestimated in OpenSees for frequency sweeping motions; even though the simulation results were well predicted for the Northridge motion.

From the simulation results, it is concluded that the dynamic BNWF model captures the response of the structures i) subjected to various directions of shaking and ii) with heavier mass and different pile embedment length reasonably well especially for small and moderate shaking. However, the BNWF model underestimates the response of the heavier structures when they are subjected to a frequency sweeping motion.

Chapter 7

**SPSI APPROXIMATION USING EQUIVALENT-CANTILEVER
BRIDGE MODEL**

The structures used in the centrifuge experiments were made of aluminum since it was impractical to build small scale reinforced concrete structures. Even though the aluminum structures were designed to have stiffness similar to that of a target reinforced concrete structure, the ductility and nonlinear behavior of both structures were different; this especially affected the structures subjected to strong shaking. In this context, in order to investigate the response of more realistic nonlinear bridge structures, the aluminum bridge structural models were replaced by a reinforced concrete bridge model calibrated by Ranf (2007). Ranf calibrated the bridge model using experimental data from a large shaking table test (Johnson et al., 2006) and strong wall tests (Makido, 2007). In the shaking table test, a one-fourth scale model of a two-span reinforced concrete bridge was subjected to different motions by three individual shaking tables. The properties and dimensions of the bridge in the shaking table tests were consistent with those of the centrifuge bridge discussed in this dissertation except for the longer span lengths (since the two tests were aimed to target the same prototype bridge structure in their test designs).

The calibrated two-span bridge (including soil and p - y spring model verified in the centrifuge simulation study) was used in this study to investigate the applicability of the *equivalent cantilever* approach considering motions with various intensities.

For this purpose, the prototype and equivalent-cantilever model simulation results were compared to find optimal fixity depths. Then the optimal fixity depths were compared with the analytical solution of Chai (2002) for equivalent depth-to-fixity and depth-to-maximum-moment.

7.1 Equivalent Depth-to-Fixity Depth Approach for SPSI Simplification

Modeling drilled shaft foundation systems is usually approximated using several simplifications. One way is to use foundation springs that represent the entire soil and foundation system. In this approach, the spring parameters are obtained considering an elastic soil and fixed or free pile head conditions [e.g., Novak (1974)]. The simplest method is to model the structure above the ground surface without considering any soil and foundation.

Another simplified approach is to use an equivalent cantilever soil-pile system. In this approach, the structure columns are extended below the ground surface to a certain depth and the bottom of the extended columns are fixed so that the structure has an equivalent lateral stiffness similar to that of the drilled shaft embedded in the soil. This method is often referred to as the *equivalent depth-of-fixity* method.

The depth-to-fixity of the equivalent cantilever model is established by aiming for the same lateral stiffness of the soil-pile system considering elastic properties of a pile and soil springs (typically, a constant subgrade modulus for cohesive soil and a linearly increasing subgrade modulus for cohesionless soil). Chai (2002) derived expressions for equivalent depth-to-fixity for free-head piles embedded in cohesive and cohesionless soils, by equating the lateral stiffness of the equivalent cantilever to the lateral stiffness of the soil-pile system using known solutions for elastic piles embedded in an elastic Winkler foundation. To calculate the stiffness of the soil-pile system, he estimated the lateral displacement of the soil-pile system based on the flexural displacement of the pile above the ground (Δ_{L_a}), the lateral displacement (Δ_g) and rotation (θ_g) of the pile at the ground surface; as shown in Figure 7.1. The values of Δ_g and θ_g were obtained from the solutions by Poulos and Davis (1980). The equivalent depth-to-fixity (L_f) of a free-head pile in cohesive soil is expressed in Equation 7.1 as a function of the clear height (L_a) and characteristic length (R_c).

$$\frac{L_f}{R_c} = \sqrt[3]{4.24 + 6\left(\frac{L_a}{R_c}\right) + 3\sqrt{2}\left(\frac{L_a}{R_c}\right)^2 + \left(\frac{L_a}{R_c}\right)^3} \quad (7.1)$$

where the characteristic length (R_c) of a pile in cohesive soil is expressed as

$$R_c = \sqrt[4]{\frac{EI}{k_h}} \quad \text{for cohesive soil} \quad (7.2)$$

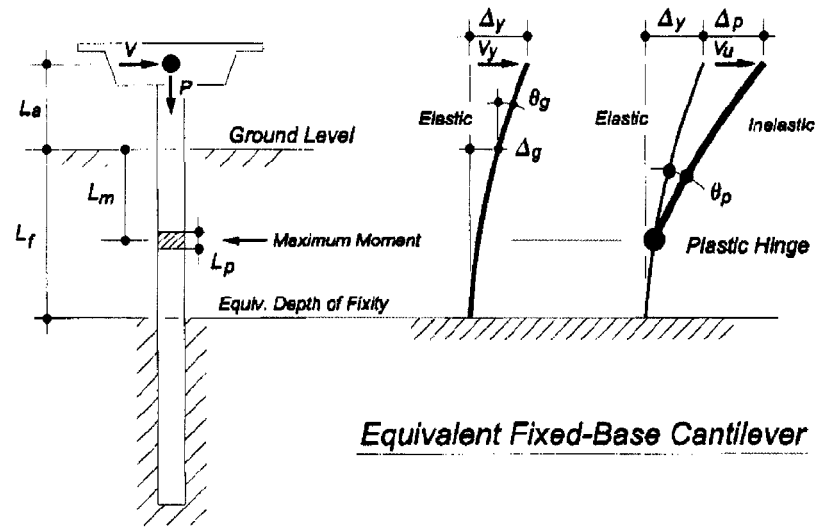


Figure 7.1: Representation of soil-pile system by equivalent fixed-based cantilever (after Chai 2002)

The equivalent depth-to-fixity (L_f) of a free-head pile in cohesionless soil is expressed in Equation 7.3 as a function of the clear height (L_a) and the characteristic length ($R_s = \sqrt[5]{\frac{EI}{n_h}}$) for cohesive soil as shown in Equation 7.4.

$$\frac{L_f}{R_s} = \sqrt[3]{7.2 + 9.6\left(\frac{L_a}{R_s}\right) + 5.22\left(\frac{L_a}{R_s}\right)^2 + \left(\frac{L_a}{R_s}\right)^3} - \left(\frac{L_a}{R_s}\right) \quad (7.3)$$

where the characteristic length (R_c) of a pile in cohesionless soil is expressed as

$$R_s = \sqrt[5]{\frac{EI}{n_h}} \quad \text{for cohesionless soil} \quad (7.4)$$

L_f vs. L_a relationships obtained using these equations show that the L_f of a free-head pile is not very sensitive to L_a , particularly for large L_a . For cohesive soil, L_f/R_c is 1.62 for $L_a = 0$ and 1.42 to 1.49 for $R_c < L_a < 6R_c$. For cohesionless soils, L_f/R_s is 1.93 for $L_a = 0$ and 1.77 to 1.81 for $2R_s < L_a < 6R_s$. These results are similar to the equivalent depth-to-fixity expressions shown in Equations 7.5 and 7.6 given by Scarlat (1996) for a free-head pile embedded in cohesive and cohesionless soils, respectively.

$$L_{f,cohesive} = \begin{cases} 1.6 R_c & \text{if } L_a/R_c < 2 \\ 1.4 R_c & \text{if } L_a/R_c \geq 2 \end{cases} \quad (7.5)$$

$$L_{f,cohesionless} = \begin{cases} 2.2 R_s & \text{if } L_a/R_s < 2 \\ 1.8 R_s & \text{if } L_a/R_s \geq 2 \end{cases} \quad (7.6)$$

Chai (2002) also investigated the depth-to-maximum-moment for free-head piles considering inelastic soil-pile systems. For cohesive soil, he derived the depth-to-maximum-moment (L_m) using equilibrium of horizontal forces and bending moment with a parabolic ultimate soil pressure distribution in the soil-pile system. The result of this analysis is expressed in Equation 7.7 in terms of a normalized pile flexural strength ($M_{max}^* = M_{max}/s_u D^3$), normalized aboveground height ($L_a^* = L_a/D$), and normalized depth-to-maximum-moment ($L_m^* = L_m/D$).

$$M_{max}^* = 2L_a^* L_m^* + (1 + \frac{19}{4} L_a^*) L_m^{*2} + \frac{7}{81} (12 - L_a^*) L_m^{*3} - \frac{7}{108} L_m^{*4} \quad \text{for } L_m^* \leq 6 \quad (7.7)$$

where s_u = undrained shear strength of clay, M_{max} = the ultimate pile bending moment, and D = pile diameter. In this equation, depths greater than 6D are not considered since the depth-to-maximum-moment is less than 6D for most cases except for very soft clays.

In a similar way, Chai derived the depth-to-maximum-moment for free-head piles in cohesionless soil using the ultimate soil pressure distribution proposed by Broms (1964b) and assuming fully mobilized ultimate soil resistance. The resulting normalized depth-to-maximum-moment (L_m^*) is expressed in Equation 7.8 in terms of normalized flexural strength ($M_{max}^* = M_{max}/K_p \gamma' D^4$) and normalized aboveground height (L_a^*).

$$L_m^* = \frac{1}{2} \left[\frac{(L_a^*)^2}{p} - L_a^* + p \right] \quad (7.8)$$

where

$$p = \sqrt[3]{\frac{12}{C}M_{max}^* - L_a^{*3}} + \sqrt{\frac{24}{C}M_{max}^* \left(\frac{6}{C}M_{max}^* - L_a^{*3}\right)}$$

and C is assumed to be 3 following the coefficient used in Broms (1964b) as shown in Figure 2.6.

The depth-to-maximum-moment is important in estimating the ductility capacity of a (yielded) pile since it defines the location of the in-ground plastic hinge and influences the lateral strength and ductility capacity of the pile. In soil-pile systems, the maximum bending moment in the pile occurs at a depth above the equivalent depth-to-fixity as illustrated in Figure 7.1.

In his study, Chai provided an example to estimate the equivalent depth-to-fixity and depth-to-maximum-moment for a bridge structure supported by drilled shafts and subjected to transverse loading considering cohesive and cohesionless soil. To emphasize the difference between the equivalent depth-to-fixity and depth-to-maximum-moment, the example calculation results are briefly introduced. Details on the example problem can be found in Chai (2002). A bridge structure with a circular reinforced column has a diameter (D) = 1.83 m, aboveground height (L_a) = 8.89 m, embedment length (L) = 19.8 m, $EI = 6.97 \times 10^5$ kN m², ultimate bending moment (M_{max}) = 21,320 kN m. For a soft clay soil (undrained shear strength, $s_u = 20$ kN/m²), the characteristic length of the pile (R_c) = 8.49 m, the normalized equivalent depth-to-fixity (L_f/D) = 6.9, and the normalized depth-to-maximum-moment (L_m/D) = 3.72. For a medium dry soil ($\phi = 33^\circ$), $R_s = 5.41$ m, $L_f/D = 5.38$, and $L_m/D = 1.87$. From these results, it is clear that the depth-to-maximum-moment is about 2 to 3 times shallower than the equivalent depth-to-fixity for this particular free-head pile structure embedded in two soil conditions.

7.2 Equivalent Depth-to-Fixity of Prototype Bridge

Equivalent depth-to-fixity and depth-to-maximum-moment for the prototype two-span bridge model embedded in dense sand soil were calculated using Equations 7.3 and 7.8. Even though these equations were derived for free-head pile structures, it was possible to

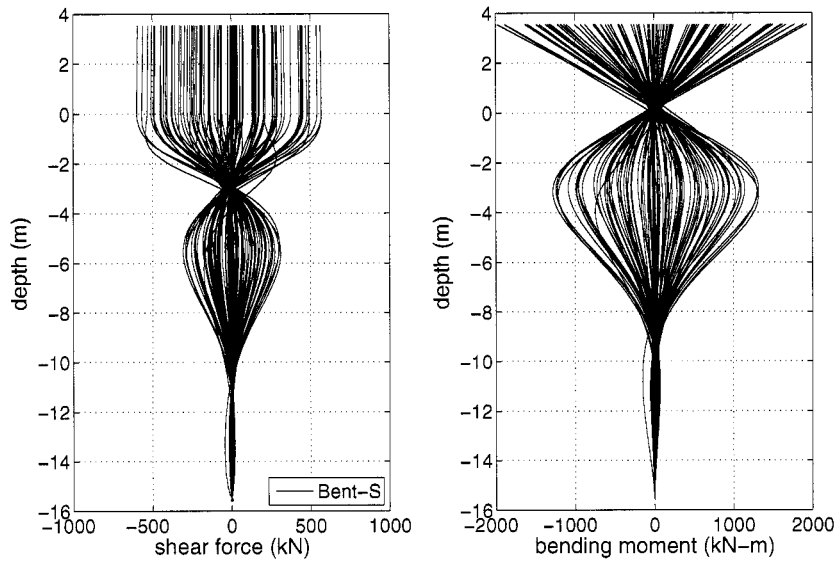


Figure 7.2: Prototype bridge shear force and bending moment distributions in Bent-S at different times during shaking (Coyote Lake 1979, Gilroy #6, $a_{max} = 0.167g$)

use the equations for the prototype bridge bent structure; since the bending moment near the ground surface was close to zero and the bent could be considered equivalent to a free-head pile with zero aboveground height. Examples of pile bending moment distributions with depth are shown in Figure 7.2.

The characteristic length (R_s) of the pile embedded in the dense dry sand ($\phi \approx 37^\circ$) was 2.247 using Equation 7.4 with EI_e of the pile = 8.5×10^5 kN m² and the rate of increase of horizontal subgrade reaction modulus (n_h) = 15000 kN/m³. Using $L_f = 1.93 \times R_s$ for $L_a = 0$, the equivalent depth-to-fixity was obtained as 4.34 m (3.6D). The value of n_h was obtained from API (1993)'s subgrade coefficients chart. Chai and Hutchinson (2002) found from their pile tests that n_h can be as low as 1/5 of API-based values since the API subgrade coefficient was estimated at the working loading level resulting in overestimation of soil stiffness when the pile is subjected to ultimate load. For that reason, another possible equivalent depth-to-fixity (L_f) was calculated as 5.72 m (4.8D) using $n_h = 15000/4$ kN/m³.

The depth-to-maximum-moment (L_m) was calculated as 4.06 m (3.4 D) using Equation 7.8 considering $L_a = 0$. In this analysis a passive soil pressure coefficient $K_p = (1 +$

Table 7.1: Equivalent depth-to-fixity and depth-to-maximum-moment of prototype bridge based on Chai(2002)'s method

	depth	soil conditions
equivalent depth-to-fixity (L_f)	4.43 m (3.6D)	using $n_h = 15000 \text{ kN/m}^3$
	5.72 m (4.8D)	using $n_h = 15000/4 \text{ kN/m}^3$
depth-to-maximum-moment (L_m)	4.06 m (3.4D)	

$\sin \phi)/(1 - \sin \phi) = (1 + \sin 37^\circ)/(1 - \sin 37^\circ) = 4.0$, soil unit weight $\gamma = 17.5 \text{ kN/m}^3$, and pile diameter $D = 1.2 \text{ m}$ were used to calculate the normalized flexural strength $M_{max}^* = M_{max}/(K_p \gamma D^4) = 38.7$.

The results for this particular dense soil condition shows that L_f is close to L_m when $n_h = 15000 \text{ kN/m}^3$ and L_f is about 1.4 times L_m when $n_h = 15000/4 \text{ kN/m}^3$. The equivalent depth-to-fixity and depth-to-maximum-moments obtained for the prototype bridge bent (Bent-S) are summarized in Table 7.1.

7.3 Dynamic Response of Equivalent Cantilever Bridge Model

The calibrated prototype bridge was simplified by removing the soil and p - y springs and fixing the bottom of the drilled shaft extended to a certain depth below ground surface. To investigate the response of the reinforced concrete bridge to motions with different intensities, both the prototype and equivalent bridge models were subjected to 40 motions corresponding to four hazard levels. These motions were also used in a performance based analysis of bridges that will be presented in Chapter 9. Each hazard includes 10 near-fault motions. More information on these motions is presented in Section 9.2.

7.3.1 Prototype Bridge Response

Maximum bending moments in the drilled shafts, and their corresponding depths, during shaking were investigated using the prototype bridge simulation results. Variation of maximum bending moment and corresponding depths for small shaking are presented in Figures 7.3a, 7.3c, and 7.3e. The bending moments greater than 2000 kN (dark circles in

the figures) occurred at about 2 to 4 seconds and the corresponding depths were about 2.5D to 3D. The pile in Bent-M showed larger maximum bending moment than the other bents indicating larger demand due to bridge twisting in the deck plane. The long bent in the middle of the bridge showed smaller values.

Figures 7.3b, 7.3d, and 7.3f show that, for strong shaking, depths of bending moment greater than 2000 kN were similar, or slightly deeper (2.5D to 4.0D), than those obtained using small shaking. The largest bending moment occurred at about 3.2D depth. For other strong motions, the maximum bending moment depths were about 3.0D to 3.5D, which is close to the depth-to-maximum-moment obtained using Chai's method. The maximum moments in Bent-S and Bent-M happened almost the same indicating large translation of bridge deck and a small effect of twisting.

7.3.2 Equivalent-Fixity-Depth Model Response

To investigate which fixity depths provide a response similar to that obtained using the prototype bridge model, the equivalent cantilever model was subjected to the same motions varying the fixity depth from ground surface to 5D depth with 0.26 m increment. The base motion used in each different equivalent cantilever model was obtained from prototype bridge model results at each fixity depth in the soil.

The results are presented in Figure 7.4 in terms of the maximum column shear force for Bent-M and Bent-S. In Figure 7.4a, each single line represents the variation of maximum column shear force for a single motion due to change of fixity depth from the surface to 5D with 0.26m increment (20 simulations per motion). For strong motions with return periods larger than 72 years, the maximum shear force vs. fixity-depth relationship showed an exponentially decaying pattern with increasing fixity depth. The figure also shows an upper bound of shear force when the motion intensity was very large. The exponentially decaying pattern of the maximum shear force vs. fixity-depth relationship showed the maximum shear force in the column can be affected by the choice of fixity depth. For example, when the fixity depth was small, larger shear force was obtained from an equivalent cantilever model. When the fixity depth was large, then the maximum shear force became smaller. Therefore,

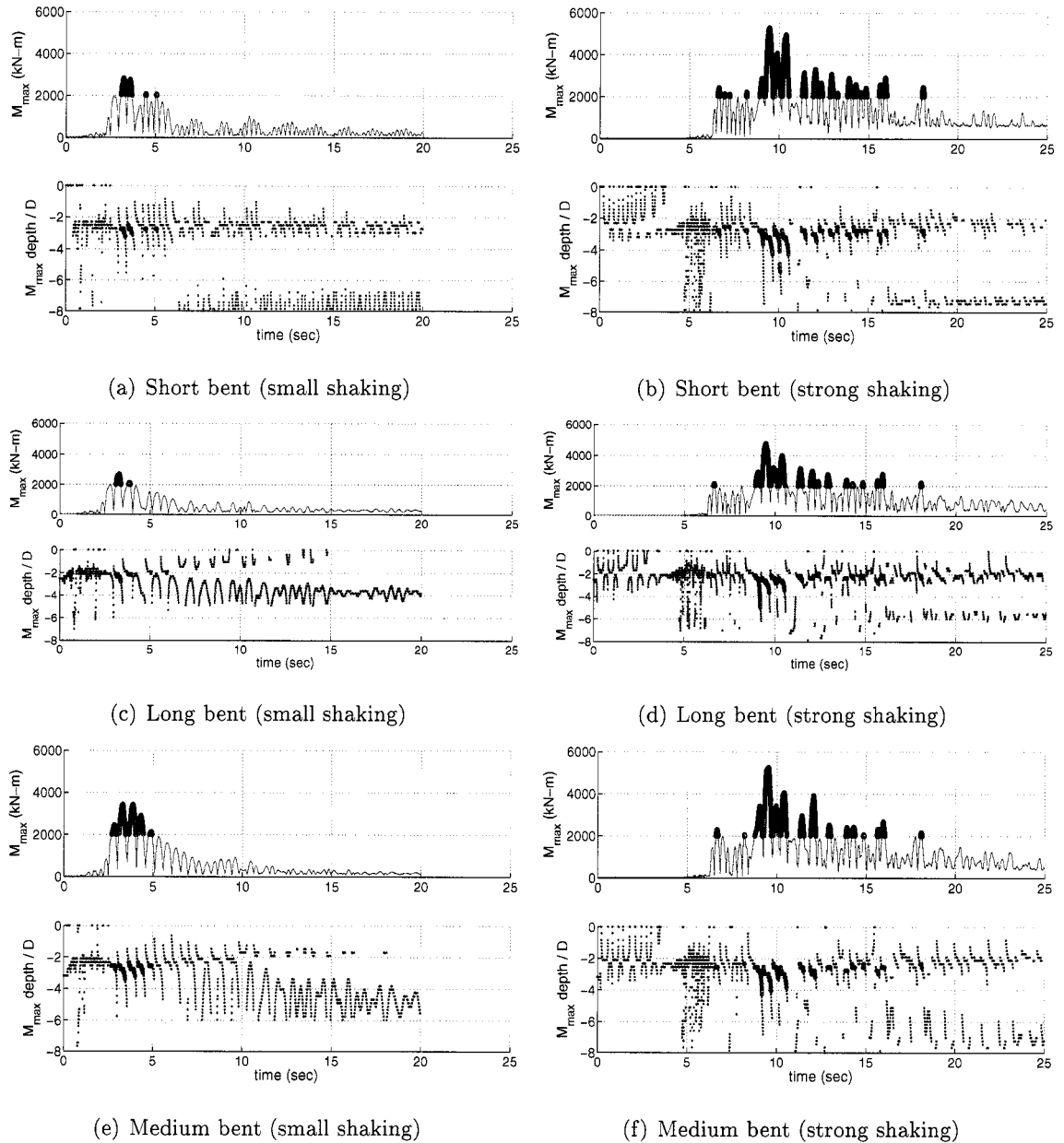
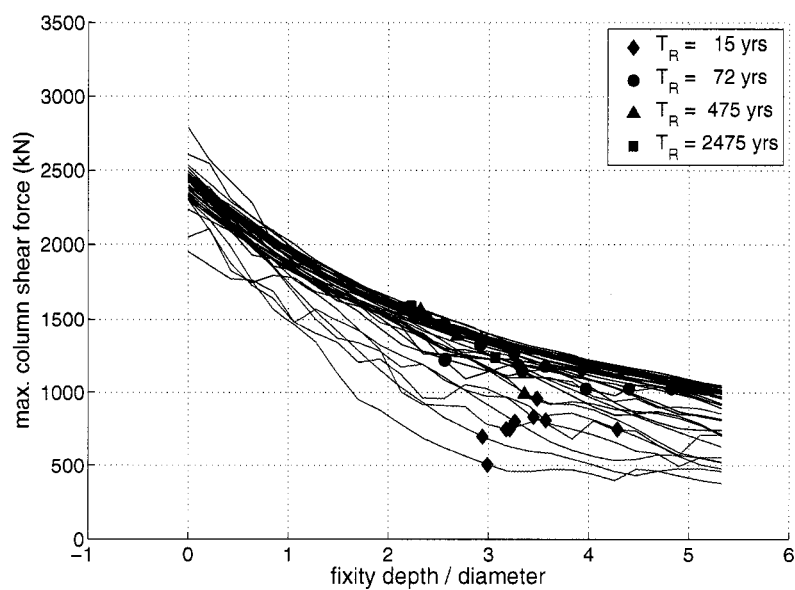


Figure 7.3: Locations of pile bending moments for different intensity shaking: small shaking = Coyote Lake 1979, Gilroy #6 ($a_{max} = 0.167g$) and strong shaking = Loma Prieta 1989, Gilroy Historic ($a_{max} = 0.691g$)

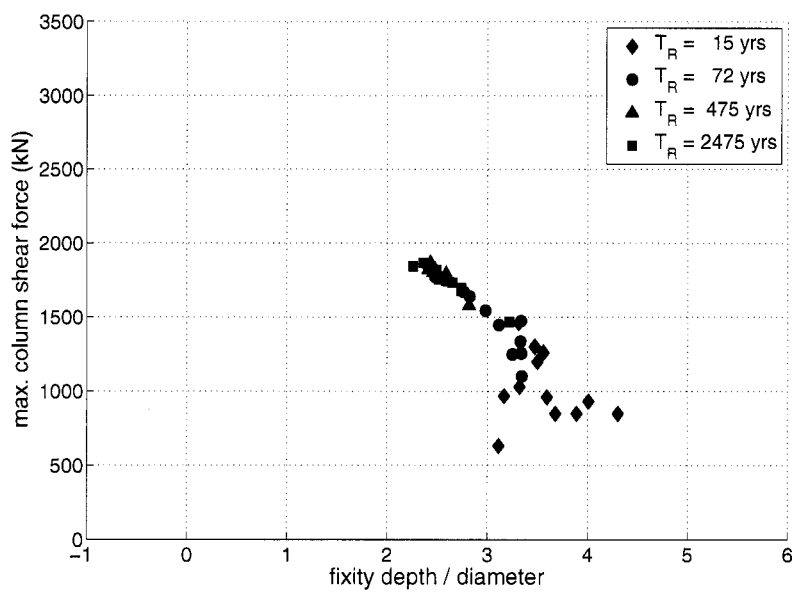
the choice of fixity depth can result in under- or over-estimation of bridge responses. In Figure 7.4a, the results of the prototype model are shown together with those corresponding to the equivalent cantilever models. The prototype bridge response data for each motion was interpolated with the equivalent cantilever model results to show which fixity depth was consistent to the prototype response. Figure 7.4b shows the prototype Bent-S maximum shear force results. Most of the prototype response was matched with fixity depths ranging from 2.2D to 4D. For short return period of shaking, the fixity depths that gave the prototype bridge response were 3D to 4D. For strong shaking, they were located at about 2.2D to 3.3D.

The fixity depth effect on bridge response was evaluated by comparing time histories of column shear force and relative bridge deck displacements obtained from prototype and equivalent cantilever models using different fixity depths (2.5D, 3.0D, and 3.5D) for different levels of shaking. In Figure 7.5a, 7.5c, and 7.5e, it is shown that for small shaking, the use of 3.5D fixity depth captured the maximum column shear force simulated in the prototype bridge model while the use of 2.5D fixity depth slightly overestimated the maximum shear force. However, Figures 7.5b, 7.5d, and 7.5f show that, for strong shaking, the use of 2.5D fixity depth gave a similar maximum shear force of prototype bridge and the use of a 3.5D fixity depth overestimated the maximum shear force. This pattern was not consistent with the bending moment at the top of the column. For both small and strong shaking, the column top bending moment was captured better when 3.5D fixity depth was used. Overall, the use of 3.0D fixity depth captured the maximum shear force and bending moment for small to strong shaking.

Figure 7.6 shows the relative bridge deck displacement to the base obtained from prototype and fixity-depth models. For small shaking, the use of fixity depths less than 3.0D resulted in underestimation of the superstructure lateral displacement while the use of 4.0D fixity depth resulted in displacement overestimation. For strong shaking, the use of 3.5D or 4.0D fixity depths captured the overall superstructure displacement better than other fixity depths. The motion intensity effect on the optimal fixity-depth for lateral displacement was attributed to the nonlinear soil response. For weak motions, the soil stiffness was close to the initial stiffness, and therefore, a shorter fixity depth was needed. However, for strong



(a) Maximum shear force without fixity model results (Bent-M)



(b) Maximum shear force without fixity model results (Bent-S)

Figure 7.4: Maximum shear force on prototype and fixed bridge models (I-880 four hazards, 40 motions)

shaking, soil stiffness was decreased, due to soil nonlinearity, and a longer fixity depth was required. This displacement prediction from fixity depth model was not always consistent for all motions.

To illustrate the effect of very short or long fixity depths on the structure response, 1D and 5D fixity depths were considered for small and strong shaking. Figure 7.7 shows that when a 1.0D fixity depth was used, the maximum shear force was overestimated and the time history of shear force had a higher frequency content (for both intensities). When 5.0D fixity depth was used, the maximum shear force was overestimated for strong shaking. Figure 7.8 shows that the superstructure displacement was clearly underestimated when 1.0D fixity depth was used. For small shaking, the displacement response period of the equivalent cantilever model was longer than that of the prototype model. For strong motion, the displacement time history was well captured.

7.4 Summary of Dynamic Response of Prototype and Equivalent Cantilever Bridge Model and Analytical Estimation of Fixity Depth

Following Chai (2002)'s method, the equivalent depth-to-fixity and depth-to-maximum-moment of the prototype bridge (Bent-S) were estimated as 3.6D considering the initial soil state stiffness (or 4.8D for ultimate soil stiffness state) and 3.4D, respectively. For the dense dry soil condition, the depth-to-maximum-moment was close to the equivalent depth-to-fixity even though there was a slight difference depending on the selected soil stiffness (i.e., initial soil stiffness or secant stiffness after ultimate pressure is mobilized).

From the two-span prototype bridge simulations, maximum moments were observed to be at 3.0D to 3.5D depth.

From the OpenSees cantilever model simulations, the use of 3.0D fixity depth provided good estimation of the maximum column shear force for small to strong shaking. The optimal fixity depth for the maximum column shear force was slightly different depending on motion intensity. For small shaking, the use of 3.5D fixity depth captured the maximum column shear force of the prototype bridge. For strong shaking, the use of 2.5D fixity depth gave a better estimation of the maximum shear force. The superstructure displacement was captured reasonably well when the fixity depth was between 3.5D to 5.0D depending on

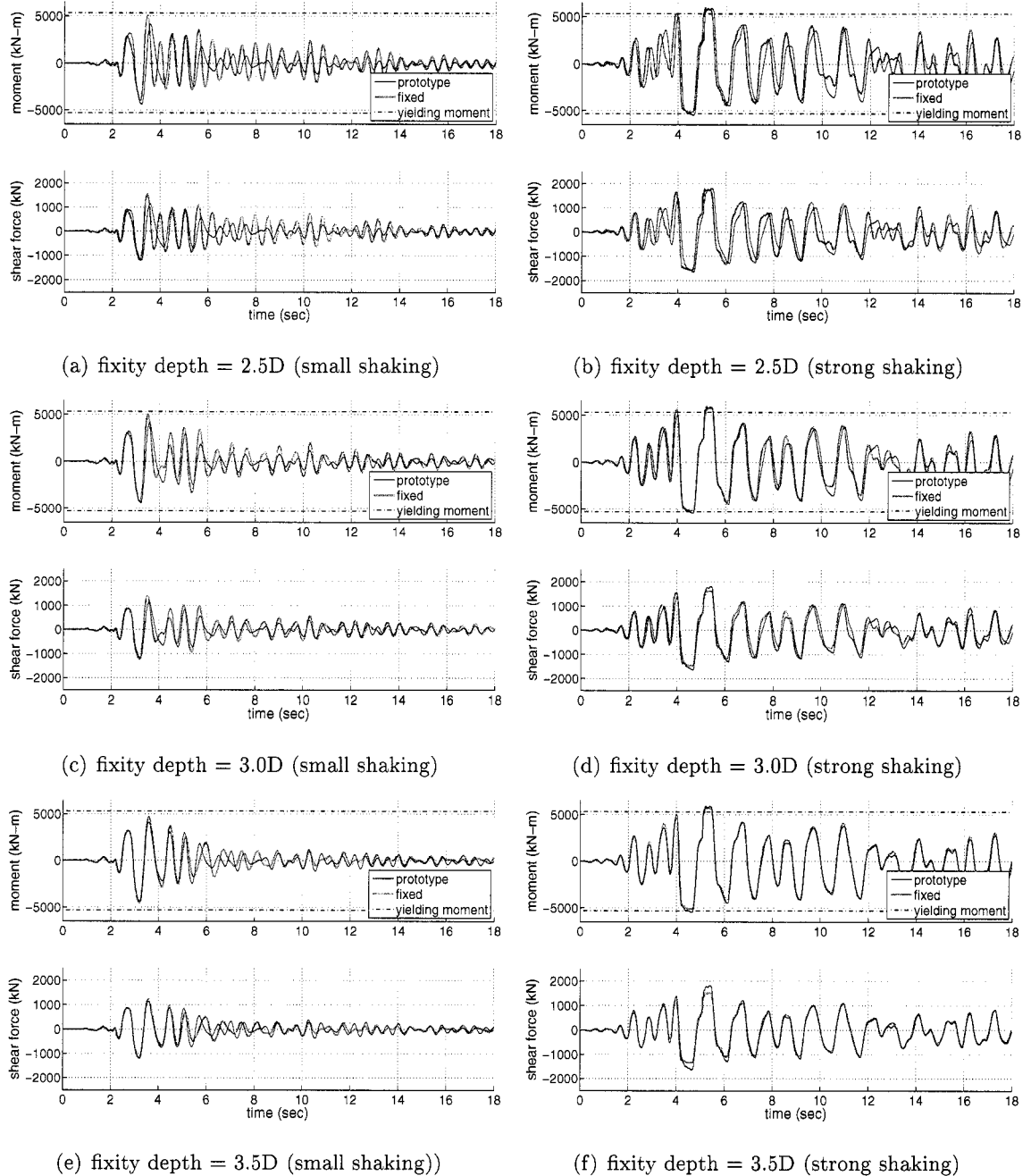
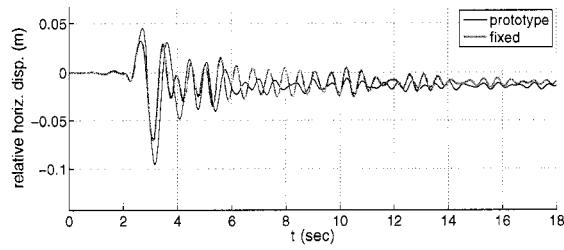
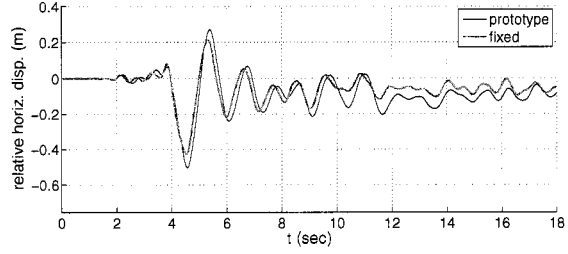


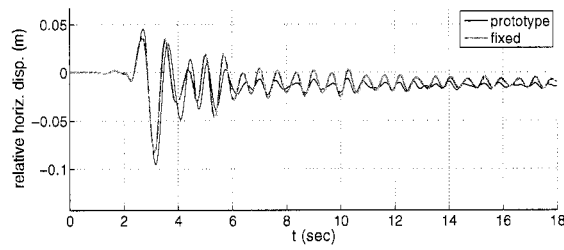
Figure 7.5: Time histories of bending moment and shear force at column top (Bent-S): small shaking = Coyote Lake 1979, Gilroy #6 ($a_{max} = 0.167g$) and strong shaking = Loma Prieta 1989, Gilroy Historic ($a_{max} = 0.691g$)



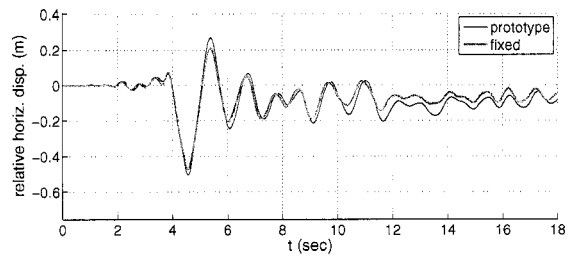
(a) fixity depth = 2.5D (small shaking)



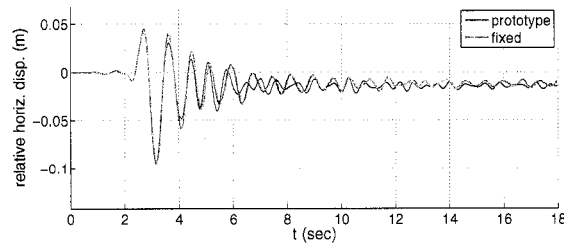
(b) fixity depth = 2.5D (strong shaking)



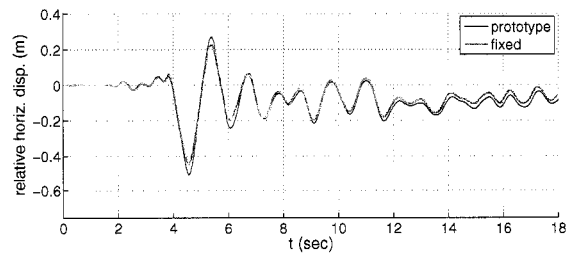
(c) fixity depth = 3.0D (small shaking)



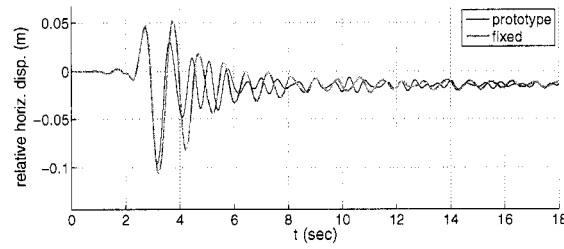
(d) fixity depth = 2.5D (strong shaking)



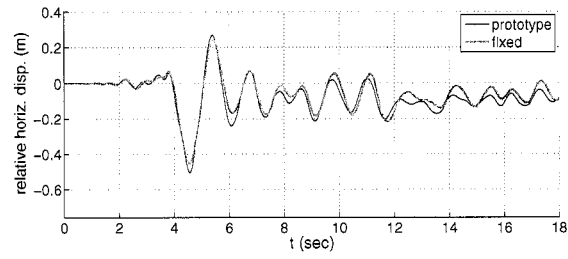
(e) fixity depth = 3.5D (small shaking)



(f) fixity depth = 3.5D (strong shaking)

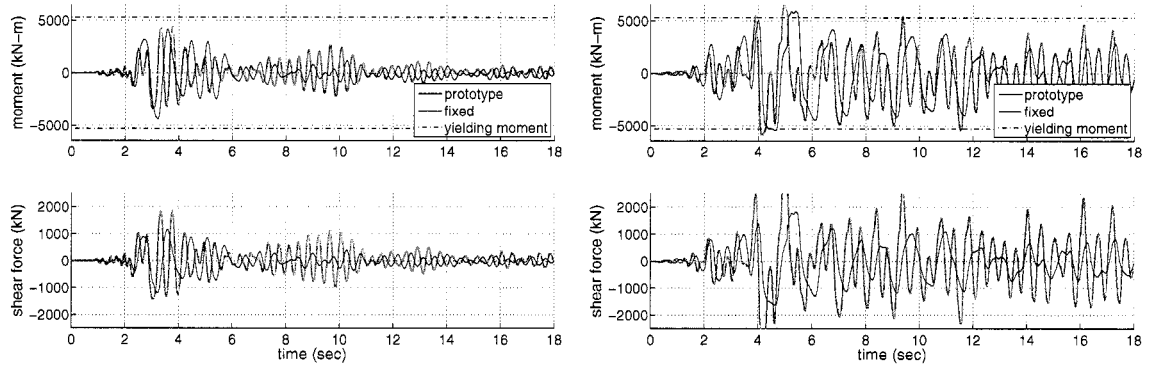


(g) fixity depth = 4.0D (small shaking)



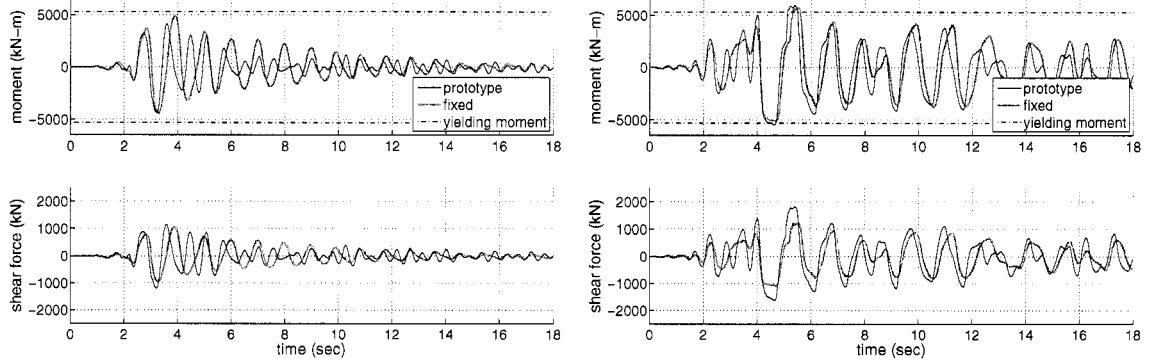
(h) fixity depth = 4.0D (strong shaking)

Figure 7.6: Time histories of displacement relative to base (Bent-S): small shaking = Coyote Lake 1979, Gilroy #6 ($a_{max} = 0.167g$) and strong shaking = Loma Prieta 1989, Gilroy Historic ($a_{max} = 0.691g$)



(a) fixity depth = 1.0D (small shaking)

(b) fixity depth = 1.0D (strong shaking)



(c) fixity depth = 5.0D (small shaking)

(d) fixity depth = 5.0D (strong shaking)

Figure 7.7: Bending moment and shear force at column top (Bent-S): small shaking = Coyote Lake 1979, Gilroy #6 ($a_{max} = 0.167g$) and strong shaking = Loma Prieta 1989, Gilroy Historic ($a_{max} = 0.691g$)

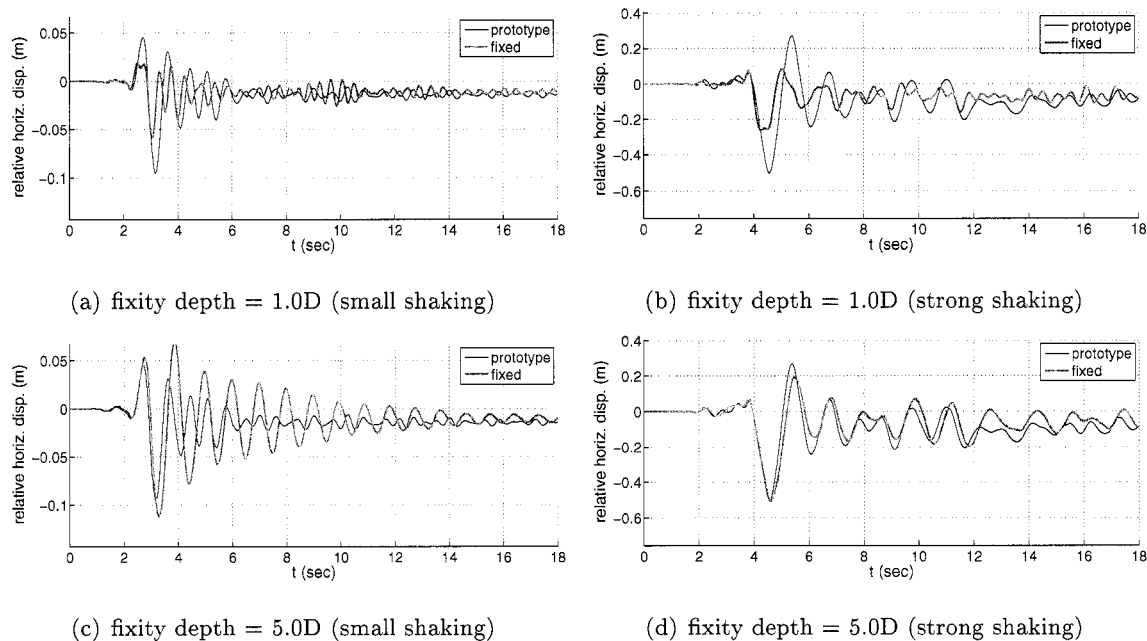


Figure 7.8: Time histories displacement relative to base (Bent-S): small shaking = Coyote Lake 1979, Gilroy #6 ($a_{max} = 0.167g$) and strong shaking = Loma Prieta 1989, Gilroy Historic ($a_{max} = 0.691g$)

motion intensity. For small shaking, shallow fixity depths (e.g., 2D or 3D) underestimated the superstructure lateral displacement, while a fixity depth greater than 4D gave slightly larger displacements. For strong shaking, deeper fixity depths (e.g., 5D) were required to capture the lateral displacement of the prototype bridge.

The dynamic simulation results of the calibrated prototype and fixed bridge model showed that the equivalent depth-to-fixity and depth-to-maximum-moment from Chai (2002)'s method were very similar to the optimal fixity depths that provided good estimation of maximum column shear force.

Chapter 8

SEISMIC RESPONSE OF A TYPICAL HIGHWAY BRIDGE IN LIQUEFIABLE SOIL**8.1 Introduction**

For reliable estimation of bridge performance especially when subjected to liquefaction and lateral spreading, appropriate modeling of soil-structure interaction and understanding of the global bridge behavior are essential. In practice, soil and foundation systems are often approximated using very simple foundation springs or unrealistic lateral spreading mechanisms that may not represent all important aspects of the global system behavior. In this context, a detailed bridge model in liquefiable soils was developed in this dissertation putting emphasis on an accurate characterization of the structural and soil behavior including various SPSI modeling strategies for several bridge system components such as pile, pile cap, and abutment wall structure. This model was used to apply the PEER Performance-Based Earthquake engineering (PBEE) framework described in Chapter 3.

8.2 Target Bridge System

This study considered a typical Caltrans highway bridge underlain by liquefiable soils susceptible to lateral spreading.

8.2.1 Bridge and Abutments

The configuration of the target bridge structure and abutment are shown in Figures 8.1 and 8.2. The bridge consists of a five-span reinforced concrete structure with a post-tensioned reinforced concrete box girder deck section and monolithic piers. The three middle spans are 45.7 m (150 ft) long and the two end spans are 36.6 m (120 ft) long. The deck is 1.83 m (6 ft) thick and the four piers are 6.71 m (22 ft) long. The pier columns are 1.2 m (4 ft) in diameter with a 2% longitudinal steel reinforcing ratio. The deck forces are transmitted

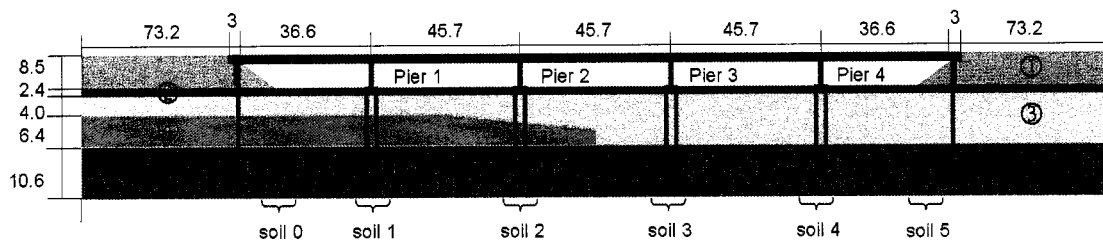


Figure 8.1: Target Bridge System (dimensions in meters)

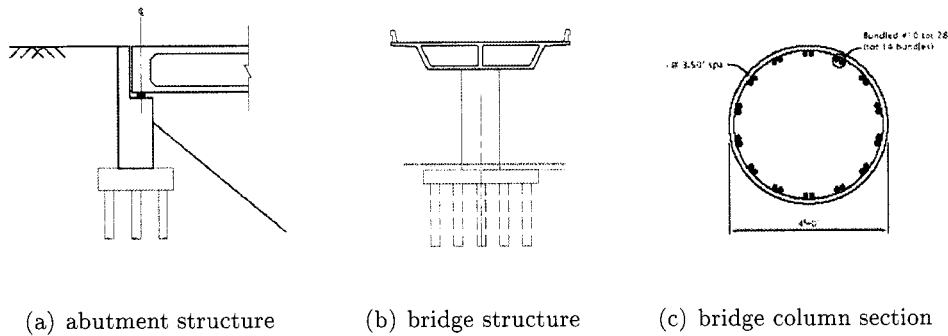


Figure 8.2: Structure configuration

through elastomeric bearing pads to seat wall abutments, and subsequently to piles and the backfill. The bearing pads were assumed to be 51 cm^2 (8 in^2) and 5 cm (2 in.) thick and to fail in shear before sliding with 15 cm (4 in.) displacement. Expansion joints between the deck and abutment walls were set to 10 cm (4 in.) initial gaps. The backwalls were designed to shear off when subjected to large longitudinal bridge forces based on Caltrans Seismic Design Criteria (SDC) (Caltrans, 2004). Details on the bridge structure design are presented by Ketchum et al. (2004) and the OpenSees structure modeling is described in more detail by Mackie and Stojadinovic (2003) and Mackie et al. (2004).

8.2.2 Pile Foundation

The bridge piers are supported by pile groups (3 by 2, center-to-center spacing = 1.83 m (6 ft)). The individual piles are open-ended steel pipe piles (diameter = 0.61 m (2 ft), wall thickness = 0.0127 m (0.5 in.), and yield stress = $413,700 \text{ kPa}$ (60 ksi)). The same

Table 8.1: Soil types and properties

Soil layer number	Soil type	Unit weight (kN/m^3)	Strength parameters
1	Dense sand	21.2	$\phi = 45^\circ$
2	Medium stiff clay	17.3	$c = 36 \sim 58$ kPa
3	loose sand	18.0 \sim 20.2	$\phi = 33^\circ \sim 36^\circ$
4	Medium stiff clay	17.3	$c = 40 \sim 58$ kPa
5	Dense sand	21.2	$\phi = 40^\circ$

pile type was used for the abutment foundations (6 by 1, center-to-center spacing = 2.44 m (8 ft)). Details on the pile design are presented by Ledzma and Bray (2006b) and Ledzma and Bray (2006a). The bridge piers and pile groups are labeled from the left abutment to the right as Pier 1, Pier 2, Pier 3, Pier 4, and Pile 1, Pile 2, Pile 3, Pile 4, respectively. The abutment pile groups in the left and right slopes are labeled as Pile 0 and Pile 5. The abutment piles were installed to the same depth as the other bridge piles.

8.2.3 Soils across Bridge

The soil below the left embankment consists of a medium stiff clay crust underlain by a thin, loose to medium dense sand, a layer of stiff clay, and a dense sand layer underlain by rock. The soil beneath the right embankment consists of the same clay crust underlain by a thicker layer of the loose sand, followed by a dense sand layer underlain by rock. The lower clay layer below the left abutment becomes thinner toward the center of the bridge and does not exist below the right embankment. The embankments are 8.53 m (28 ft) in height and have 2:1 slopes. The groundwater table is located at the bottom of the surface clay layer. The properties of the loose and medium sand layers across the bridge were aimed to induce liquefaction under moderate ground shaking so that lateral spreading, especially in the vicinity of the right abutment, triggered broad bridge damage. Soil types and properties are shown in Table 8.1. To define the model soil properties, the soil layers including embankment, sand and clay layers were divided into 49 sub-layers as schematically

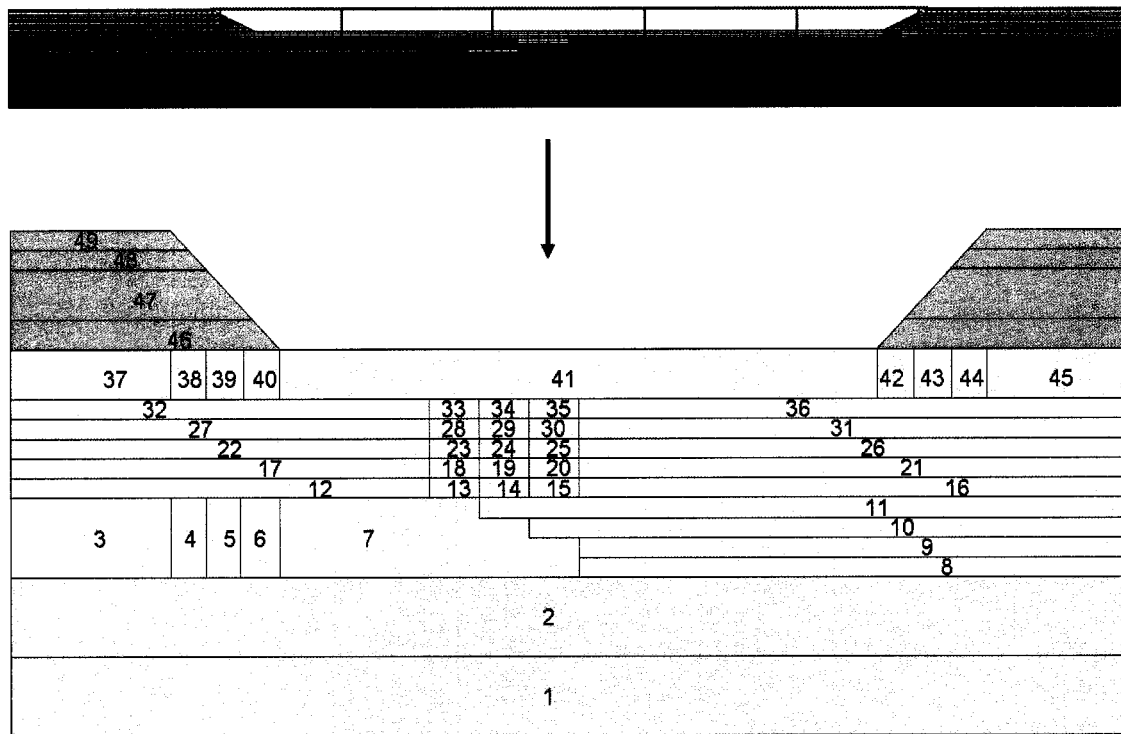


Figure 8.3: Layer definition and identification

shown in Figure 8.3. In Table 8.2, corrected Standard Penetration Test (SPT) blow counts ($N_{1,60}$) are shown for the sand layer below the left and right embankments together with the corresponding sub-layer number. SPT profiles at both locations are illustrated in Figure 8.4. The clay below the embankments were set to have higher strength, due to consolidation, than the clay located in the center bridge area. The variation of undrained shear strength of the clay layer is shown in Figure 8.5. These variable soil conditions along the bridge length contributed to the generation of incoherent motions at each bridge pier.

8.3 Numerical Modeling of the Target Bridge System

This section presents details on the numerical model created in OpenSees for the target bridge system.

Table 8.2: SPT profiles below embankments

below left embankment			below right embankment		
layer number	depth (m)	$N_{1,60}$	layer number	depth (m)	$N_{1,60}$
32	2.83	15	36	2.83	13
27	3.51	19	31	3.51	13
22	4.26	27	26	4.26	16
17	5.04	32	21	5.04	16
12	5.91	22	16	5.91	16
			11	7.08	18
			10	8.40	22
			9	9.75	25
			8	11.25	28

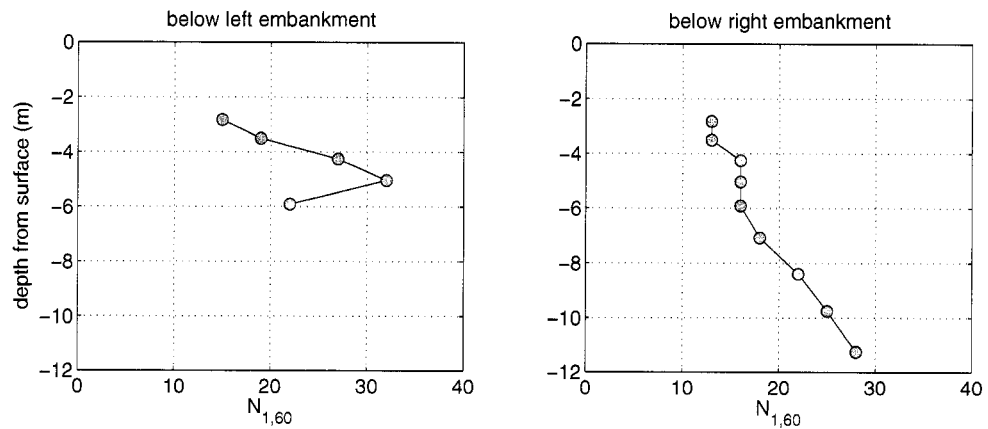


Figure 8.4: SPT profiles of loose sand layer below both embankments

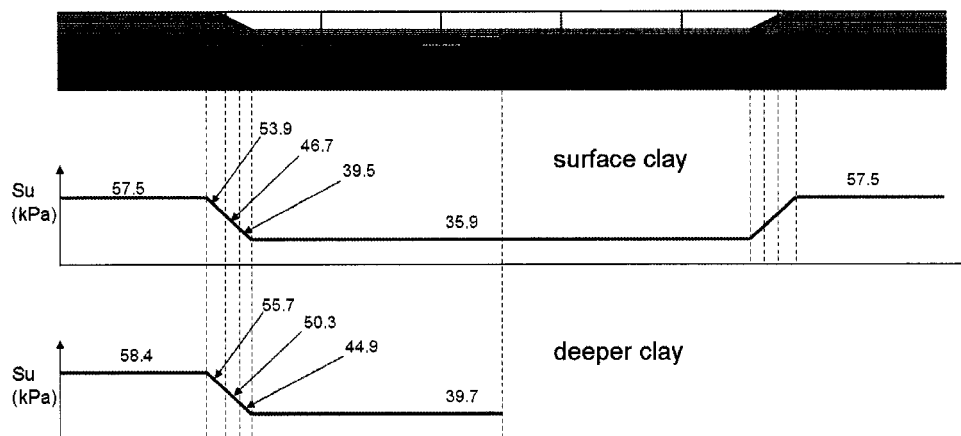


Figure 8.5: Variation of undrained shear strength of clay layer across bridge

8.3.1 Soils

Using the target soil profiles and foundation design, the soil-foundation system was modeled in OpenSees. The Pressure-Dependent Multi-Yield (PDMY) elasto-plastic material model developed by Yang et al. (2003) was used to model sandy soils. To account for saturated conditions, the PDMY material was coupled with a Fluid Solid Porous Material (FSPM) model. This material imposes an incompressibility condition that allows the generation of pore pressures. For the clay, the Pressure-Independent Multi-Yield (PIMY) material model was used. To capture these soil conditions in OpenSees, 49 sub-soil layers were used as shown in Figure 8.3. The soil parameters used in this study are based on recommendations provided by Yang and Elgamal (<http://cyclic.ucsd.edu/opensees/>) for typical soil conditions. Relative densities (D_r) for the sandy soils were determined based on the $N_{1,60}$ values selected for the target bridge soil conditions and Equation 8.1.

$$N_{1,60} = 60 (D_r)^2 \quad (8.1)$$

Then, using the recommended values, 16 PDMY material parameters for each sub-layer were obtained by interpolation of relative densities. The interpolation was performed in the 40 % to 75 % relative density range; where the model parameters show a linear relationship with relative density. Figure 8.6 shows the interpolated parameter values. The PIMY material

parameters for clay were interpolated in the same way using the selected undrained shear strength values. Soil parameter values for 49 sub-layers of sand and clay are tabulated with layer number in Tables 8.3 and 8.4. A total of 3874 quadrilateral finite elements and 4050 nodes were used to represent the soil domain.

The embankment side soil was extended 73.2 m (240 ft) outward from the slope crest. The outer-most soil column elements were modified to generate a free-field response by increasing their out-of-plane thicknesses and constraining the outer-most soil column element nodes at the same elevation to have the same horizontal movement.

8.3.2 Bridge structure

The OpenSees bridge structure model used in this study was originally developed and used for a PBEE investigation of a bridge on very competent soil by Mackie and Stojadinovic (2003). The original model used simple foundation springs at the bottom of the piers and abutment springs at the bridge deck-end to model soil compliance. To couple the bridge structure model with the soil-foundation model developed for this investigation, the simple foundation springs used by Mackie and Stojadinovic (2003) were removed and the pier columns were connected to pile groups. The abutment springs were also separated into bearing pad springs and passive earth pressure springs.

8.3.3 Pile Foundations

To model soil-structure interaction, several types of interface springs were used as shown in Figure 8.7. The chosen parameters for these interface elements reflect the complicated ground conditions and foundation types - different soil conditions and types, ground water conditions, pile group effects, and passive earth pressures in pile caps and abutments.

The 3×2 pile groups that support the piers were simplified using 1×2 pile group models by combining the three piles in each out-of-plane row to produce an equivalent single pile. In OpenSees, these equivalent pile is generated by patching three individual pile sections without changing the diameter or pile wall thickness. Each pile section was generated using nonlinear fiber beam elements.

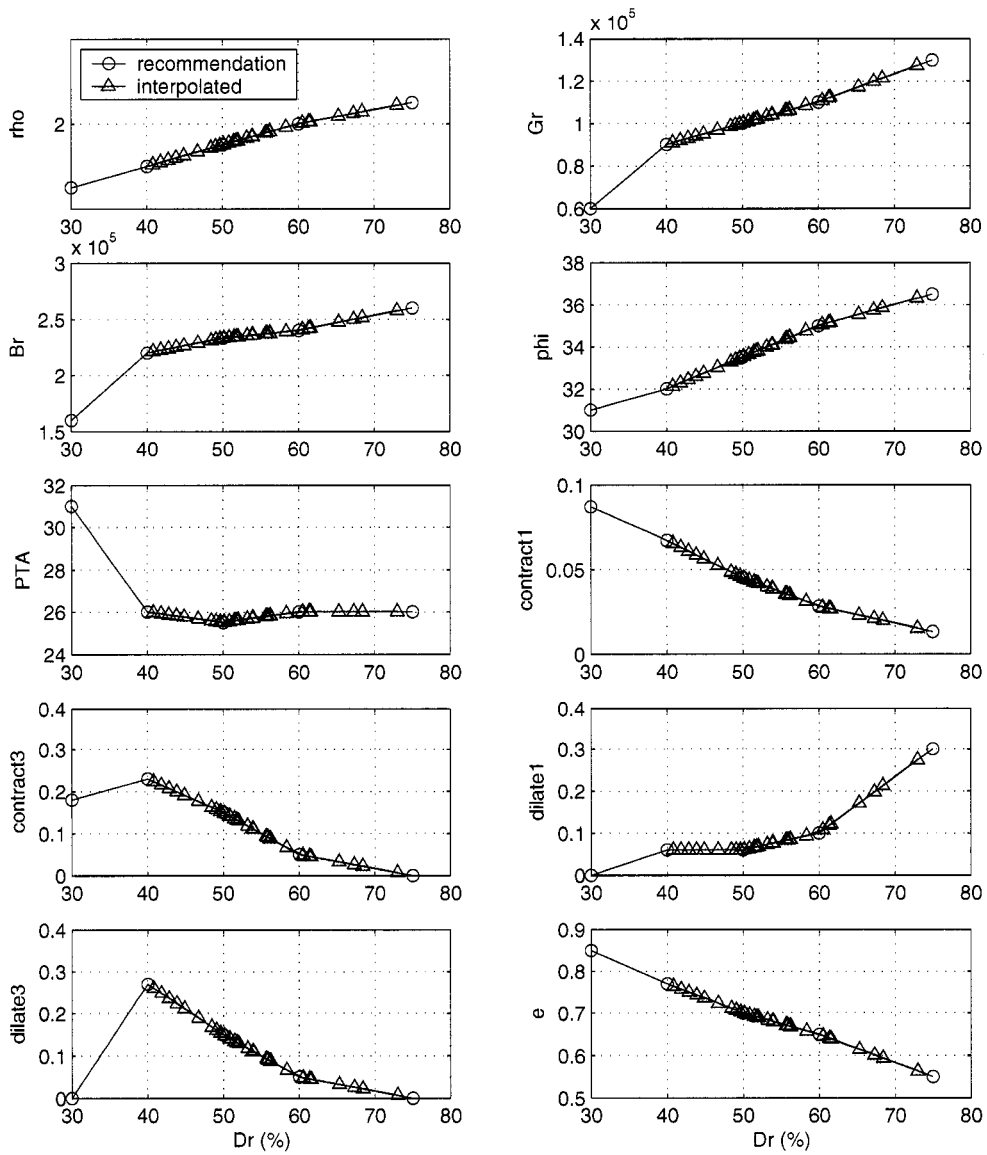


Figure 8.6: Recommended loose sand material parameters in OpenSees and interpolations

Table 8.3: Summary of PDMY material parameter values used for cohesionless soil

soil	layer number	$N_{1,60}$ (%)	Dr (%)	ρ_{ho} (Mg/m ³)	Gr (kPa)	Br (kPa)	ϕ (°)	PTA (°)	cnt1	cnt3	dill	die3	e
dense sand	1	40.0	99.0	2.292	159760	283040	39.9	26.0	0.002	0.000	0.617	0.000	0.406
	2	40.0	95.0	2.260	154800	279200	39.3	26.0	0.004	0.000	0.564	0.000	0.430
	8	28.0	68.3	2.055	121084	251084	35.8	26.0	0.020	0.022	0.211	0.022	0.595
	9	25.0	64.5	2.030	116066	246066	35.5	26.0	0.023	0.035	0.161	0.035	0.620
	10	22.0	60.6	2.004	110737	240737	35.1	26.0	0.027	0.048	0.107	0.048	0.646
	11	18.0	54.8	1.948	104772	236341	34.2	25.7	0.037	0.102	0.079	0.102	0.676
	12	22.0	60.6	2.004	110737	240737	35.1	26.0	0.027	0.048	0.107	0.048	0.646
	13	20.5	58.5	1.985	108452	238917	34.8	25.9	0.031	0.065	0.094	0.065	0.658
	14	19.0	56.3	1.963	106273	237391	34.4	25.8	0.034	0.087	0.085	0.087	0.669
	15	17.5	54.0	1.940	104006	235804	34.1	25.7	0.038	0.110	0.076	0.110	0.680
	16	16.0	51.6	1.916	101640	234148	33.7	25.6	0.042	0.134	0.067	0.134	0.692
loose sand	17	32.0	73.0	2.087	127373	257373	36.3	26.0	0.015	0.007	0.274	0.007	0.563
	18	28.0	68.3	2.055	121084	251084	35.8	26.0	0.020	0.022	0.211	0.022	0.595
	19	24.0	63.2	2.022	114327	244327	35.3	26.0	0.025	0.039	0.143	0.039	0.628
	20	20.0	57.7	1.977	107735	238415	34.7	25.9	0.032	0.073	0.091	0.073	0.661
	21	16.0	51.6	1.916	101640	234148	33.7	25.6	0.042	0.134	0.067	0.134	0.692
	22	27.0	67.1	2.047	119443	249443	35.7	26.0	0.021	0.026	0.194	0.026	0.603
	23	24.0	63.2	2.022	114327	244327	35.3	26.0	0.025	0.039	0.143	0.039	0.628
	24	21.5	59.9	1.999	109861	239903	35.0	26.0	0.028	0.051	0.099	0.051	0.651
	25	19.0	56.3	1.963	106273	237391	34.4	25.8	0.034	0.087	0.085	0.087	0.669
	26	16.0	51.6	1.916	101640	234148	33.7	25.6	0.042	0.134	0.067	0.134	0.692
	27	19.0	56.3	1.963	106273	237391	34.4	25.8	0.034	0.087	0.085	0.087	0.669
embankment	28	17.5	54.0	1.940	104006	235804	34.1	25.7	0.038	0.110	0.076	0.110	0.680
	29	16.0	51.6	1.916	101640	234148	33.7	25.6	0.042	0.134	0.067	0.134	0.692
	30	14.5	49.2	1.892	99160	231907	33.4	25.5	0.047	0.157	0.060	0.157	0.706
	31	13.0	46.5	1.865	96547	228512	33.0	25.7	0.053	0.178	0.060	0.178	0.724
	32	15.0	50.0	1.900	100000	233000	33.5	25.5	0.045	0.150	0.060	0.150	0.700
	33	14.5	49.2	1.892	99160	231907	33.4	25.5	0.047	0.157	0.060	0.157	0.706
	34	14.0	48.3	1.883	98305	230796	33.2	25.6	0.049	0.164	0.060	0.164	0.712
	35	13.5	47.4	1.874	97434	229664	33.1	25.6	0.051	0.171	0.060	0.171	0.718
	36	13.0	46.5	1.865	96547	228512	33.0	25.7	0.053	0.178	0.060	0.178	0.724
	46	40.0	95.0	2.260	154800	279200	39.3	26.0	0.004	0.000	0.564	0.000	0.430
	47	40.0	95.0	2.260	154800	279200	39.3	26.0	0.004	0.000	0.564	0.000	0.430
48	40.0	95.0	2.260	154800	279200	39.3	26.0	0.004	0.000	0.564	0.000	0.430	
49	40.0	95.0	2.260	154800	279200	39.3	26.0	0.004	0.000	0.564	0.000	0.430	

Table 8.4: Summary of PIMY material parameter values used for cohesive soil

soil	layer number	Su (kPa)	rho (Mg/m ³)	Gr (kPa)	Br (kPa)
deep clay	3	58.4	1.669	110684	553421
	4	55.7	1.648	104289	521447
	5	50.29	1.605	91476	457381
	6	44.89	1.562	78687	393434
	7	39.7	1.521	66395	331973
surface clay	37	57.5	1.662	108553	542763
	38	53.9	1.633	100026	500131
	39	46.7	1.577	82974	414868
	40	39.5	1.520	65921	329605
	41	35.9	1.488	57279	286394
	42	39.5	1.520	65921	329605
	43	46.7	1.577	82974	414868
	44	53.9	1.633	100026	500131
	45	57.5	1.662	108553	542763

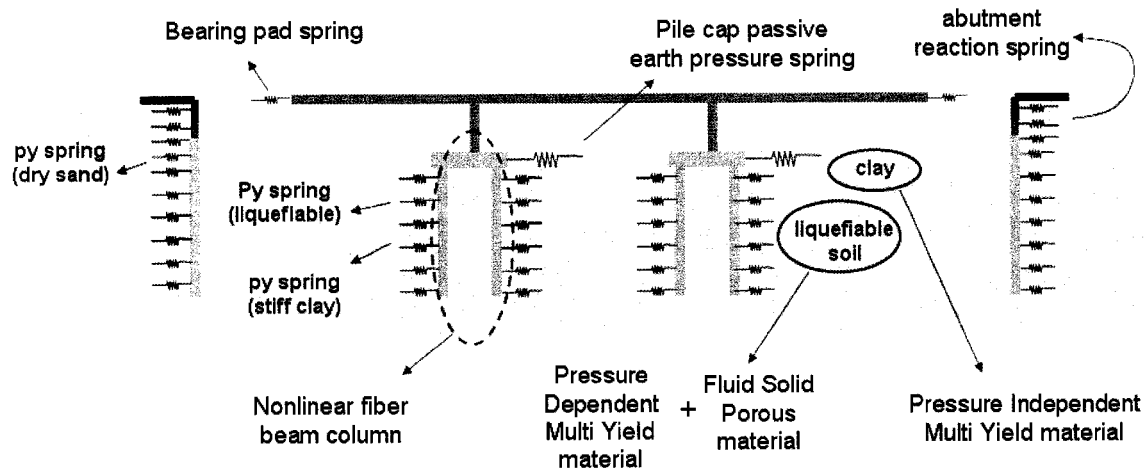


Figure 8.7: Modeling of soil-structure interaction in OpenSees

8.3.4 Pile p - y Springs

The p - y springs in the liquefiable soils were modeled using the *pyLiq1* model (Boulanger et al., 2004) available in OpenSees. The *pyLiq1* material was coupled with adjacent soil elements which provided porewater pressure ratio information; spring resistance forces based on API (1993) criteria were factored by the porewater pressure ratio to approximate the effect of liquefaction on soil-pile structure interaction. Residual strengths after liquefaction were calculated based on correlations to $N_{1,60}$ as proposed by Kramer (2006) (Equation 2.8). Figures 8.8 and 8.9 show p - y spring parameter distributions with depth for the six piles across the bridge (i.e., plots of ultimate lateral resistance, residual ultimate resistance ratio of liquefied soil, and y_{50}). These values correspond to individual springs in a single pile before group effects are considered. Residual ultimate lateral resistances ($p_{ult,res}$) for the case that all soils were fully liquefied were obtained using each soil's residual strength. Ratios of $p_{ult,res}$ to p_{ult} , here referred as residual ultimate resistance ratio, are shown in Figure 8.8b. The y_{50} values shown in Figure 8.9 represent the displacement that corresponds to resistances of 50% of p_{ult} in the p - y curve associated with the initial stiffness of the curve. These values were calculated by solving API p - y curve in Equation 8.2 for y using a 50% p_{ult} .

$$p = p_{ult} \tanh \left[\frac{k z}{p_{ult}} y \right] \quad (8.2)$$

where z is depth, k is a coefficient that can be determined from API (1993) charts based on density (or friction angle) and ground water condition.

To account for pile group effects, the strength spring parameters were factored using group efficiency factors, G_e , defined as the ratio of the average lateral capacity per pile in a group to the lateral capacity of a single pile. The group efficiency factor can also be expressed using Equation 8.3 as an average for the p -multipliers for each individual pile (i.e., the sum of the p -multipliers for all individual piles divided by pile number)

$$G_r = \sum_{i=1}^N \frac{f_{m_i}}{N} \quad (8.3)$$

where, N is the number of piles and f_m is an empirical reduction factor (i.e., p -multiplier) to adjust p - y curves for pile arrangement and pile spacing. To obtain the group efficiency

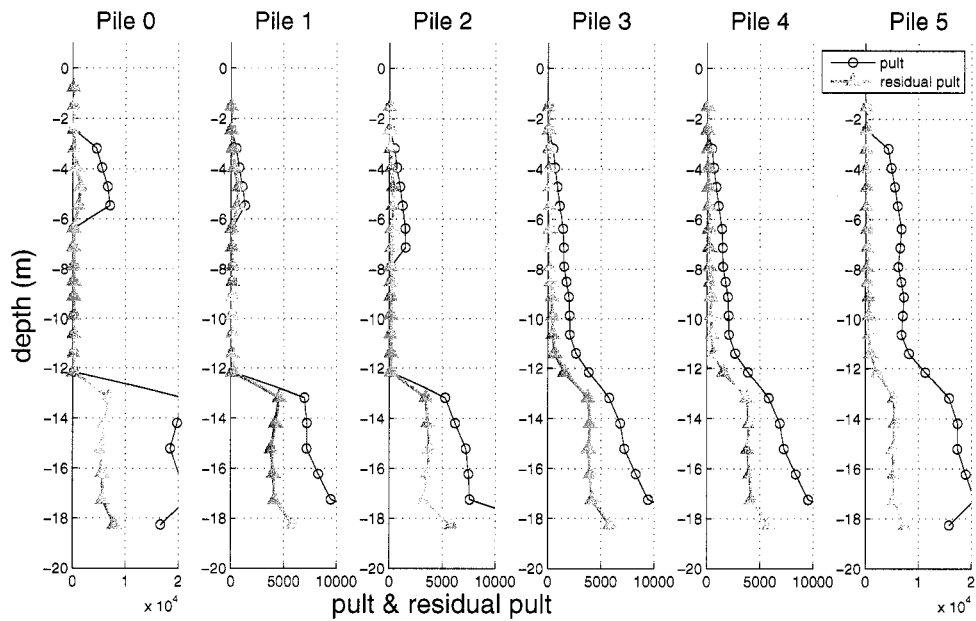
factor for the 3×2 pile groups in the target bridge, the p-multipliers for the leading and trailing piles were determined as 0.82 and 0.76 according to Figure 2.11. For the leading and trailing rows of piles in the out-of-plane direction, the p-multiplier values were set to 1.0; since the group effect can be ignored when the side-by-side pile spacing is greater or equal to $3D$. The resulting group efficiency for each pile group was 0.79. The capacity of each pile in the simplified 1×2 pile group was calculated as $3 \times$ the group efficiency times the capacity of the single pile. For the 1×6 pile groups under the abutments, no group effect was considered since they have a single row of piles and the side-by-side pile spacing ($4D$) is greater than $3D$. The skin resistance and pile tip resistance was modeled using t - z and q - z springs. These springs were assumed to have no group effects.

8.3.5 Pile Cap Passive Earth Pressure Springs

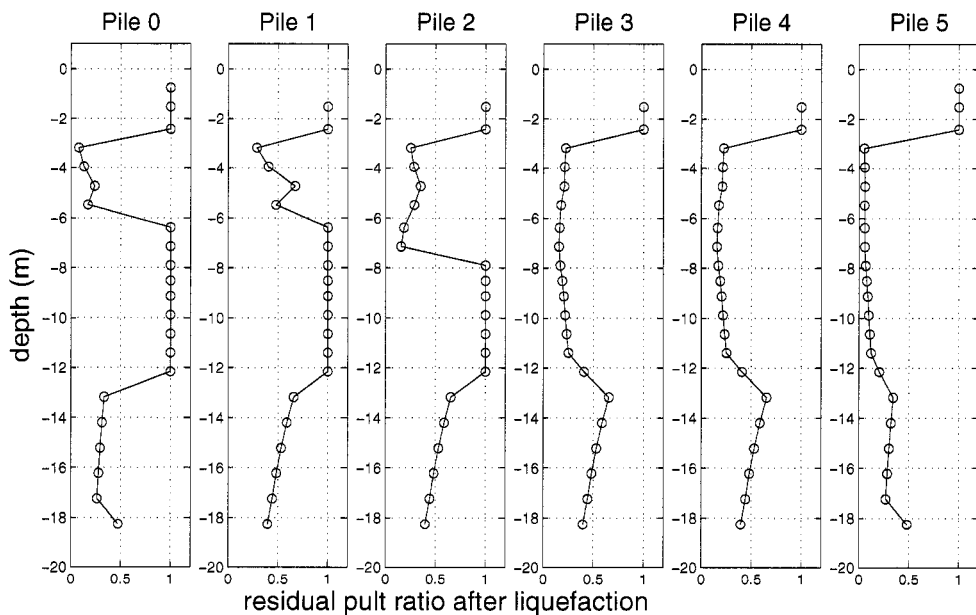
To capture the response of the pile caps, three passive earth pressure springs were used at the top, middle, and bottom of the cap. The clay passive earth pressure envelope of the pile cap was determined using the $\phi=0$ sliding wedge method (Equation 2.13) suggested by Mokwa (1999). It was assumed that the bridge longitudinal and transverse pile cap lengths were 3.6 m (12 ft) and 5.4 m (18 ft), respectively, and that the pile cap height was 1.5 m (5 ft). A cohesion factor (α) of 0.75 was used in the method for the medium stiff clay soil.

8.3.6 Abutment Interface Springs

The height of the backwall (break-off wall) was 1.8 m (6ft) and its width was 13.7 m (45 ft). The interaction between the bridge deck and abutment was decomposed into two interaction components. A schematic of the bridge deck-abutment interaction and its modeling are shown in Figures 2.19 and 8.10. The first component combined the bearing pad resistance and backwall resistance in a single spring model. This spring force was transferred to the stem wall and abutment pile foundation. The stem wall was connected to the soil without interface assuming its relative displacement was small. The second component included the expansion joint gap and backwall lateral soil resistance. In this case the force-displacement envelope was obtained combining a gap spring and a soil spring



(a) pult



(b) residual pult ratio

Figure 8.8: p - y spring parameters: ultimate lateral resistance (p_{ult})

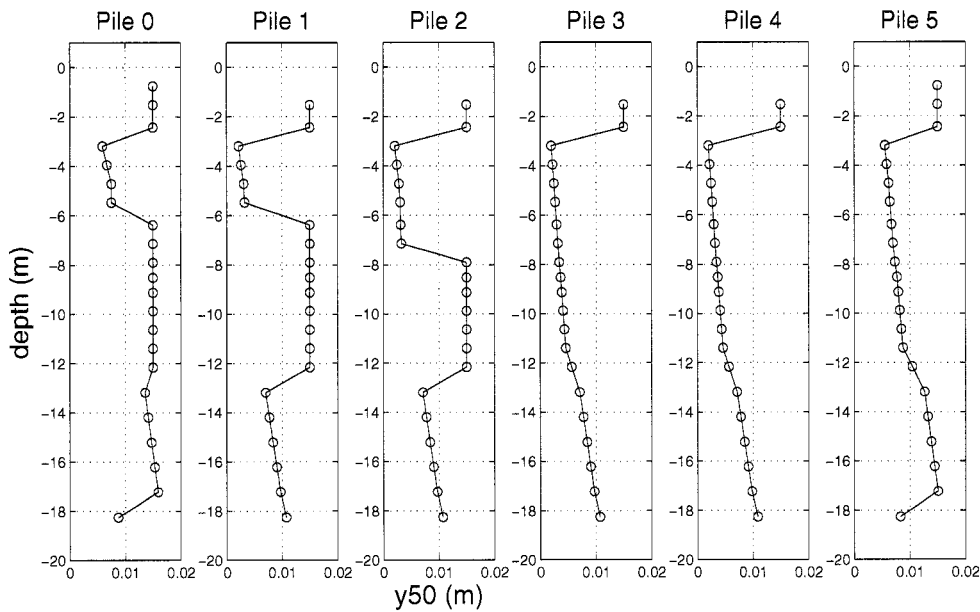


Figure 8.9: p - y spring parameters: y_{50}

whose parameters were obtained based on Caltrans' Seismic Design Criteria Caltrans (2004) in series. For the selected abutments, the initial stiffness and ultimate resistance used were 164,300 kN/m/m (20 kips/in/ft) and 6,258kN (1290 kips), respectively.

8.4 Seismic Response of Bridge System and Engineering Demand Parameters

Before using the PEER PBEE methodology, it was considered important to evaluate the global and local response of the selected bridge subjected to typical earthquake excitations. This section presents details of the global and local seismic bridge response characteristics for a moderate intensity motion (Northridge 1994 at Century city Lacc North, CMG Station 24389, $a_{max} = 0.25g$) and a strong motion with a 475-year return period (Erzincan, Turkey 1992, $a_{max} = 0.70g$). In this study, the soil lateral spreading response and its effect on the global bridge behavior was first investigated. Then, the local response of the bridge structure, abutment, piles, and interface springs was addressed. For the soil response, motions corresponding to four hazard levels were considered. More details on the motion characterization are presented in the next chapter (Section 9.2).

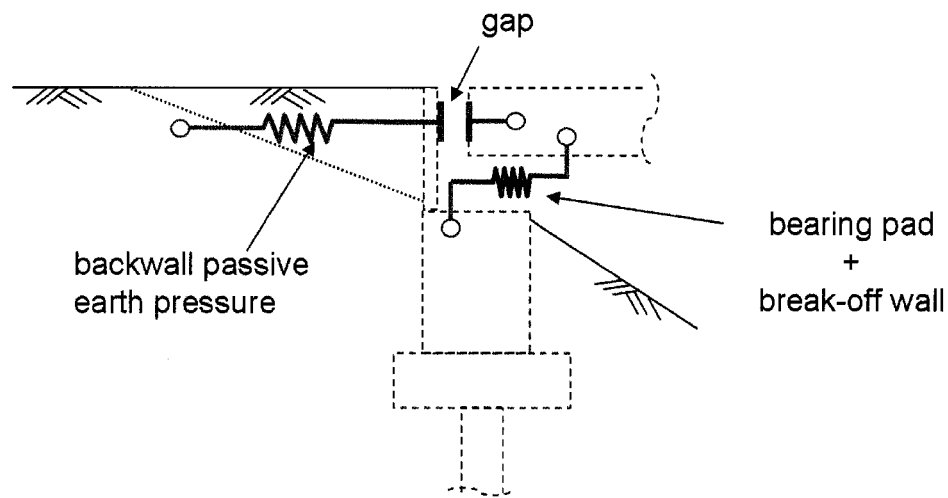


Figure 8.10: Modeling of bridge deck-abutment-soil interaction in OpenSees

8.4.1 Soil Response

The global bridge response was complicated due to the interaction between the bridge system components - i.e., bridge, free-field and sloping soil, and abutment structure. Lateral spreading can induce significant large demands on the bridge and pile structures. In addition, the presence of clay layers can make the soil displacement profile more complicated due to the possibility of slip displacements at the clay-sand layer boundaries. In Figures 8.11a and 8.12a, permanent displacement patterns of the bridge system for the Northridge and Erzincan motions are presented. These figures show that larger lateral deformation occurred in the vicinity of the right abutment. The deformed meshes show that the location of the shear plane in the left abutment, induced by the strong motion (Erzincan, Turkey 1992, $a_{max} = 0.70g$), was deeper than that produced by the moderate motion (Northridge 1994, $a_{max} = 0.25g$). This observation is more clearly illustrated in Figures 8.13 and 8.14 where the time variation of estimated horizontal shear strain distributions with depth below the left and right abutments is presented for both motions. For the moderate shaking, large shear strains below the left embankment were concentrated at the top of the loose sand layer. This was attributed to liquefaction of the sand layer. For the strong shaking, large

shear strains below the left abutment were accumulated at the interface between the clay layer and dense sand layer. Below the right abutment, shear strains were distributed more evenly over the thickness of the loose sand layer for both motions.

Figure 8.15 shows soil displacement profiles next to each pile foundation and at each slope toe (soil 0 to soil 5 in Figure 1) for three hazard levels. Lateral spreading is clearly observed in the right abutment. The permanent soil movement ranged from about 0.2 m to 1.3 m in the right abutment depending on the hazard level.

The loose sand layer across the bridge site liquefied over its full or partial thickness depending on the intensity of the input motion. Figures 8.11b and 8.12b illustrate the pore pressure ratio in the soil. For moderate shaking, most of the loose sand layer, except for the area below embankment, liquefied. For stronger shaking, the entire loose sand layer across the bridge liquefied.

To show the degree of liquefaction in the soil beneath the right abutment, pore pressure ratios are measured at several soil locations are shown in Figure 8.16a. The pore water pressure ratio time histories in the loose sand below the right abutment are shown in Figure 8.16b for the moderate shaking. The figure show that the upper layer of the loose sand was fully liquefied across the bridge. However, the bottom layer of the loose sand below the embankment had pore water pressure ratios less than 1.0. This was attributed to the fact that the soil at this location was slightly denser and had higher initial effective stress due to larger overburden from the embankment. Figure 8.17 shows the time variation of pore water pressure ratio with depth below the right abutment for the Northridge motion illustrating different degrees of pore water pressure generation with time.

8.4.2 Pinning Effect and Soil Element Out-of-plane Thickness

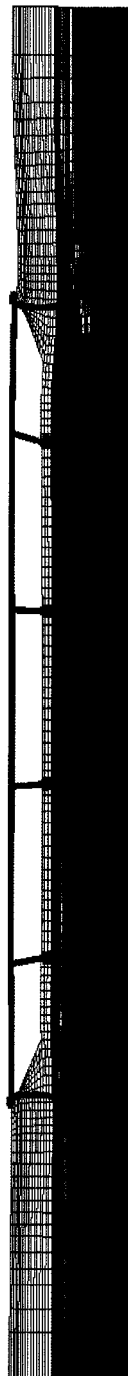
The embankment slope deformation is generally affected by the presence of the pile foundation which reduces the final soil deformations. This effect is often referred to as the *pinning effect*. Due to the pile foundation in the sloping soil, and its reinforcement effect, actual lateral and vertical displacements can be smaller than the displacements that occur in a case where no pile foundation exists (i.e., free-field case). This problem can be

Displacement
 0.30445
 0.27062
 0.2368
 0.20297
 0.16914
 0.13531
 0.10148
 0.067656
 0.033828
 0



(a) horizontal displacement

pwpratio
 1
 0.87556
 0.75111
 0.62667
 0.50222
 0.37778
 0.25333
 0.12889
 0.00444444
 -0.12



(b) pore water pressure ratio

Figure 8.11: Horizontal and vertical displacements of bridge and pore water pressure ratio in soil (after earthquake) - Northridge 1994, $a_{max} = 0.25g$; Magnification factor = 20

Displacement|
 0.934482
 0.830095
 0.72708
 -0.62321
 0.51934
 0.41547
 0.31161
 0.20774
 0.10387
 0



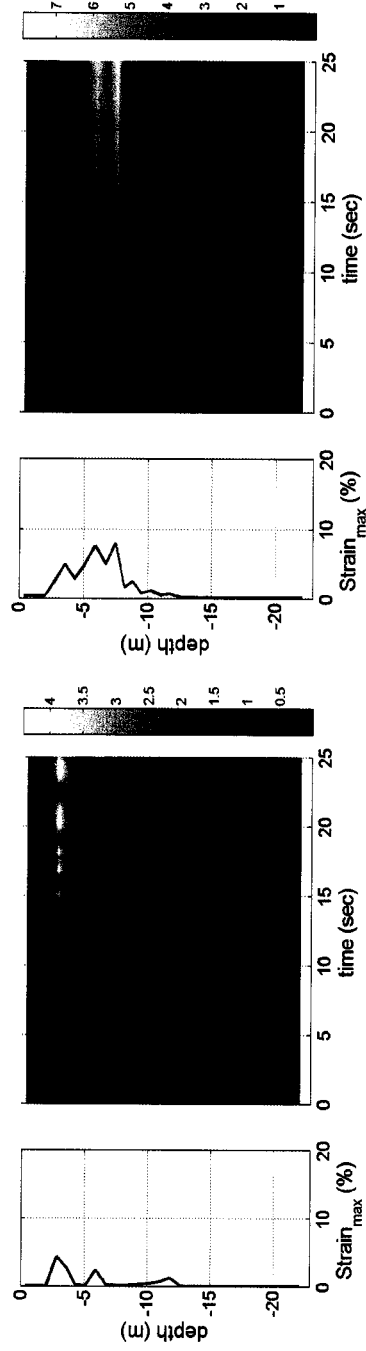
(a) horizontal displacement

pwpRatio
 1
 0.74667
 0.49333
 -0.24
 -0.013333
 -0.26667
 -0.52
 -0.77333
 -1.0267
 -1.28



(b) pore water pressure ratio

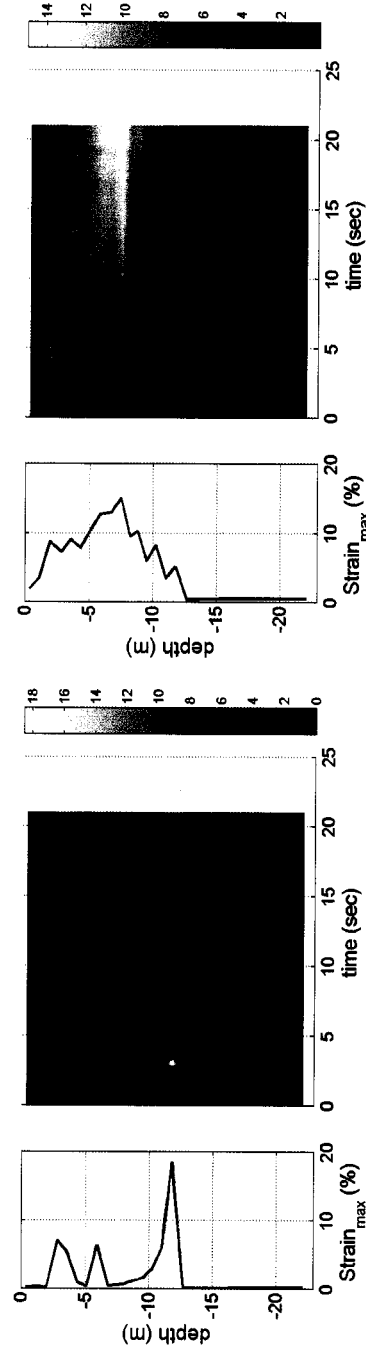
Figure 8.12: Horizontal and vertical displacements of bridge and pore water pressure ratio in soil (after earthquake) - Erzincan, Turkey 1992, $a_{max} = 0.70g$: Magnification factor = 20



(a) Below left abutment

(b) Below right abutment

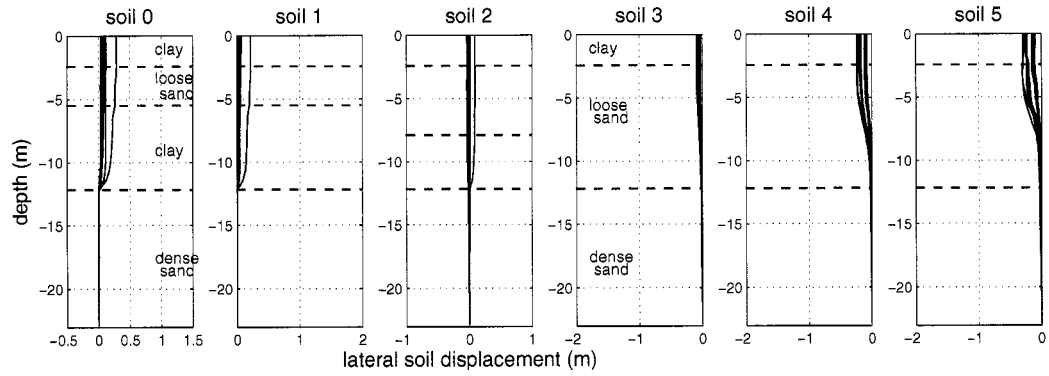
Figure 8.13: Time histories of shear strain profile below left and right abutment - Northridge 1994, $a_{max} = 0.25g$



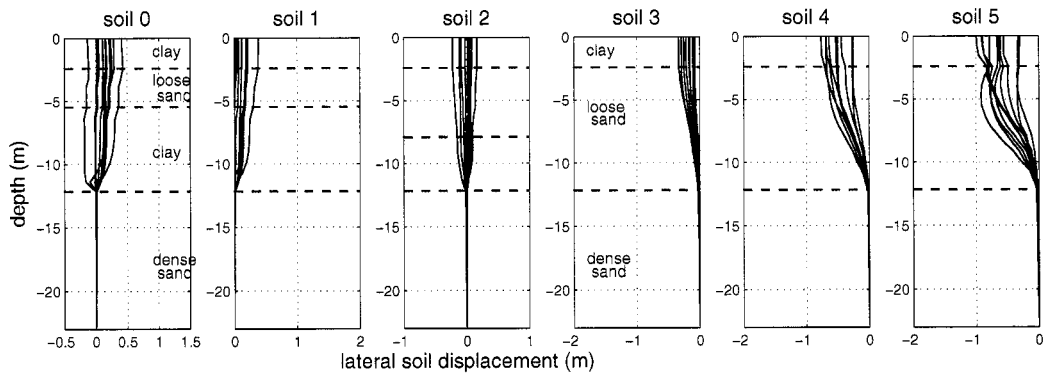
(a) Below left abutment

(b) Below right abutment

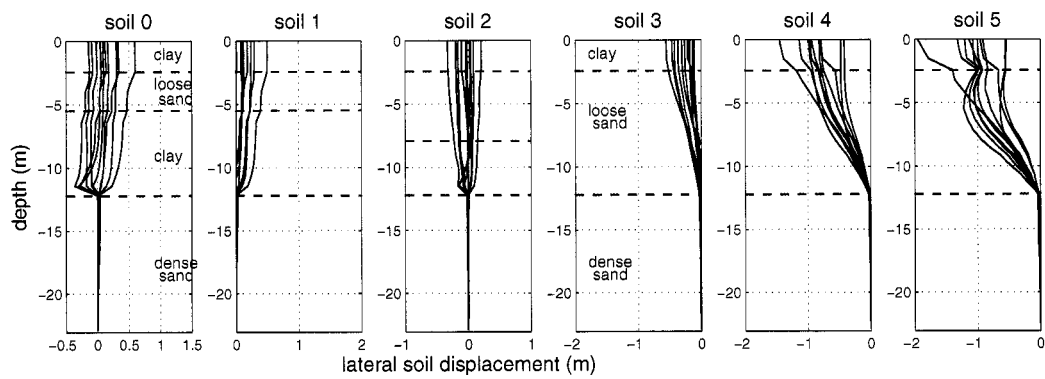
Figure 8.14: Time histories of shear strain profile below left and right abutment - Erzincan, Turkey 1992, $a_{max} = 0.70g$



(a) $T_R = 72$ years

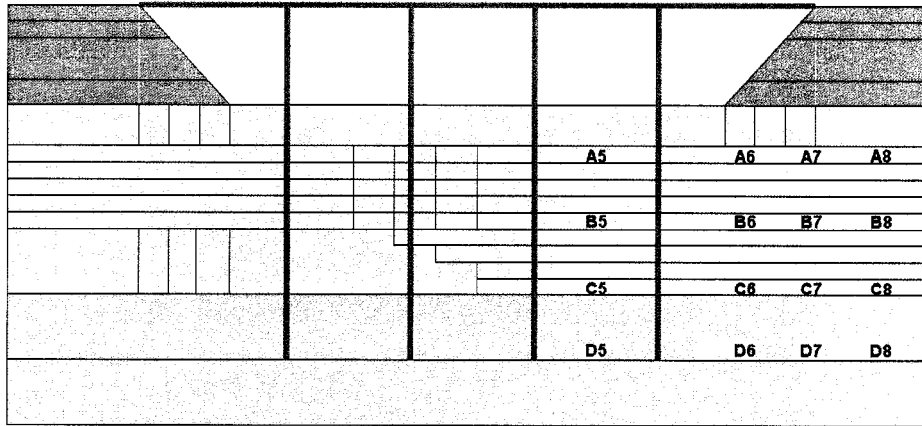


(b) $T_R = 475$ years

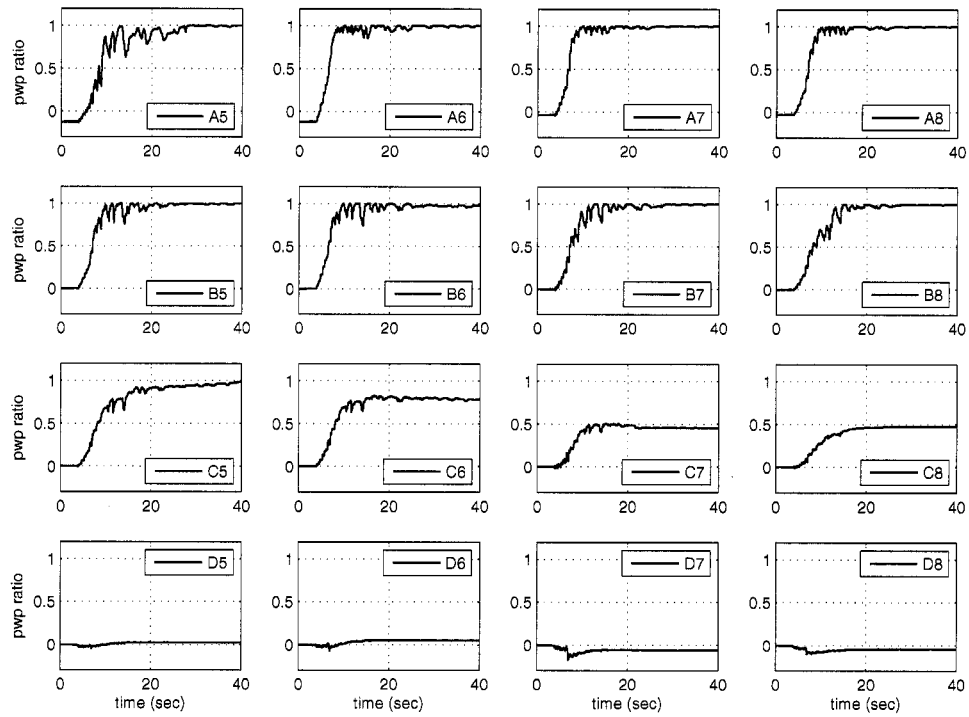


(c) $T_R = 2475$ years

Figure 8.15: Permanent soil displacement profiles at pile foundation and slope toe locations for 10 motions



(a) Location of pore pressure measurements



(b) Pore pressure ratio in soil below right abutment (Northridge 1994, $a_{max} = 0.25g$)

Figure 8.16: Pore pressure ratio time histories in liquefiable soil

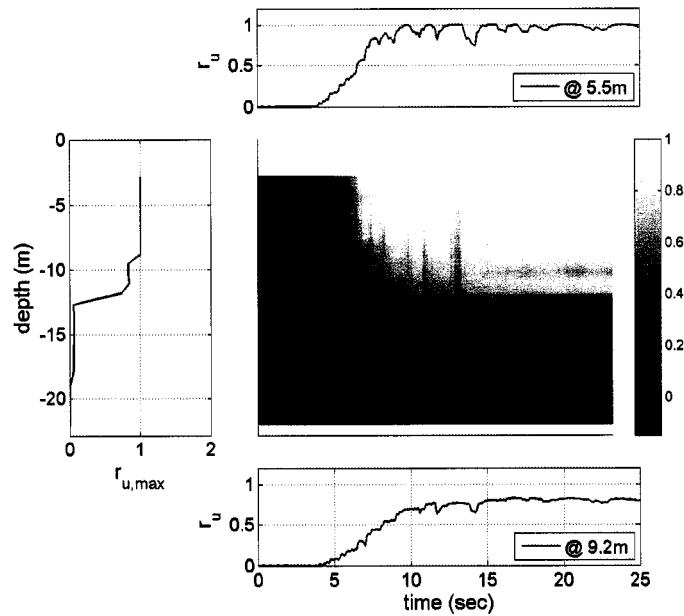


Figure 8.17: Spatial and temporal variation of pore pressure profile below right abutment in liquefiable soil - Northridge 1994, $a_{max} = 0.25g$

approximately simulated by adjusting the soil element out-of-plane thickness in a 2-D plane strain model assuming the pinning effect is the same in the upper embankment and lower soil. If the soil element out-of-plane thickness is very small, the slope displacements would be underestimated. If the thickness is very large, the slope displacements would be close to those of a slope without pile foundation. To understand the effect of the out-of-plane thickness on the slope deformation and pile cap movement for this bridge system, several thicknesses were considered in the simulations. The results are shown in Figure 8.18. The use of a thickness smaller than 5 m gave very small soil displacement relative to the other cases. When the thickness was greater than 75 m, the displacements converged to a limiting value beyond which they were insensitive to the out-of-plane thickness. This pattern was also observed in the pile cap lateral displacement near the slope. Therefore, soil element out-of-plane thicknesses between 5 m and 75 m were considered necessary to avoid the two extreme cases (i.e., too much pinning effect or no pinning effect).

An appropriate thickness to mimic the pinning effect can be determined considering

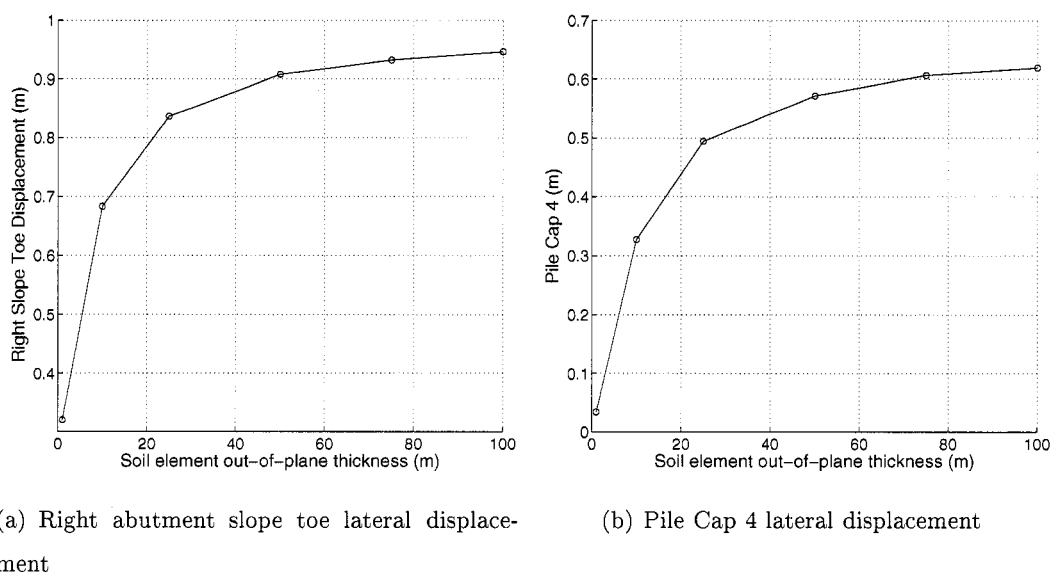


Figure 8.18: Effect of soil element out-of-plane thickness on slope toe and pile cap lateral displacement - Erzincan, Turkey 1992, $a_{max} = 0.70g$

several aspects that contribute to the pinning effect, such as ground motion intensity, 3-D embankment configuration and deformation pattern, actual demand on adjacent structures, and tributary width of embankment. First, the pinning effect can be slightly different when different intensities of motions are used. Second, even though it is only affected by a longitudinal direction of shaking, the slope may have deformation in the longitudinal and transverse directions; as schematically shown in Figure 8.19, resulting in larger displacements than what would be simulated in a 2-D FEM analysis. Third, structural demands due to possibly larger ground deformation can be reduced by the nonlinear behavior of the interface springs, (e.g., a simulation where the pile cap passive earth pressure springs reach ultimate resistance after which it shows a constant resistance with continued soil displacement). Another factor is the tributary width of the embankment. In the case under consideration, the width of the pile foundation at the abutment is about 30 m, which is similar to the tributary width based on the trapezoidal shape of sloping embankment (Boulangier et al., 2005). For these reasons, 50 m soil element out-of-plane thickness was chosen for the analysis. For improved estimation of out-of-plane thickness effect, 3-D model

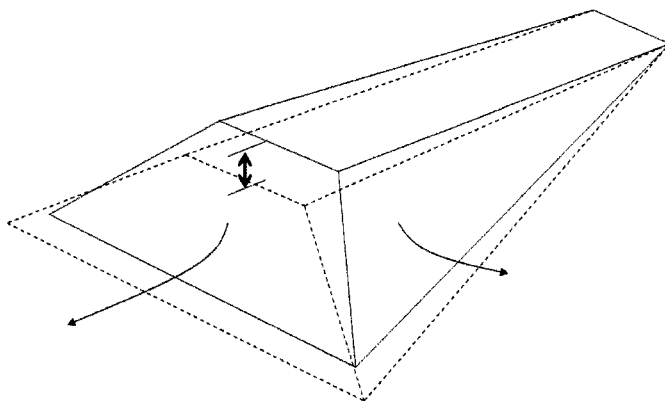


Figure 8.19: Schematic drawing of 3-D embankment deformation

studies are required.

This is certainly a limitation of 2-D analysis (performed in this study). However, 2-D analysis brings the possibility to evaluate the influence of the complete structure in a logical way, keeping the computational time at reasonable levels.

8.4.3 Global Behavior of Bridge System

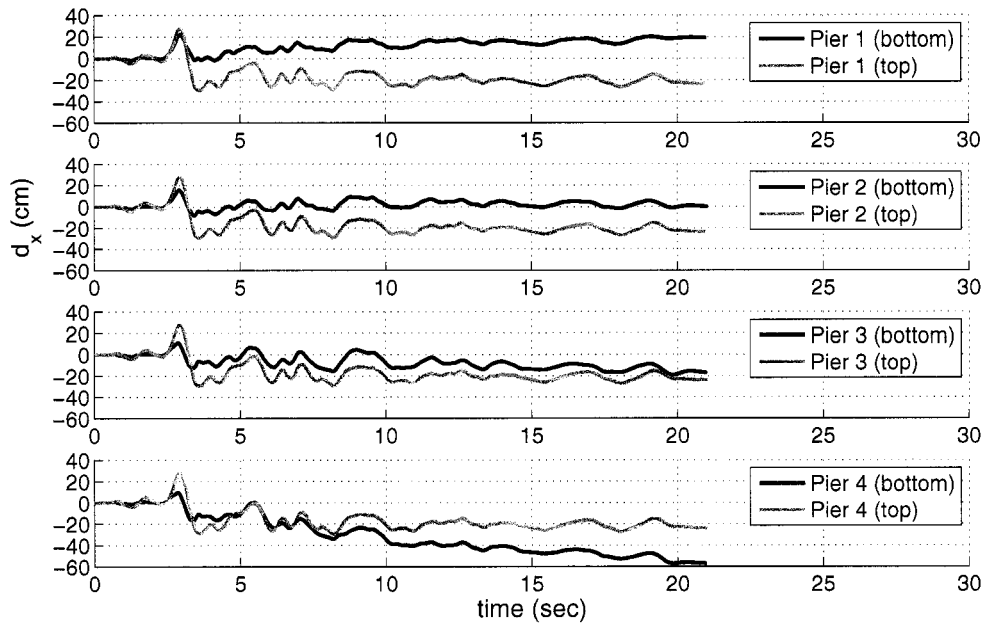
The expansion joints between the bridge deck and backwall closed when lateral spreading occurred. Since the amount of lateral spreading in the right abutment was considerably larger than that in the left abutment, the entire bridge deck tended to move towards the left. At the same time, lateral spreading also pushed the pile cap of Pier 4 to the left resulting in relatively small drift in that column. On the other hand, Pier 1 was subjected to very large column drifts because the bridge deck moved the upper end of the column to the left and lateral spreading moved the pile cap at the bottom of the column to the right. This global bridge behavior, which would likely not be anticipated by typical analyses that model only individual parts of the bridge, greatly affected the local response. Details of the local response of bridge piers, abutments and piles are discussed in the following sections.

8.4.4 *Bridge Pier Response*

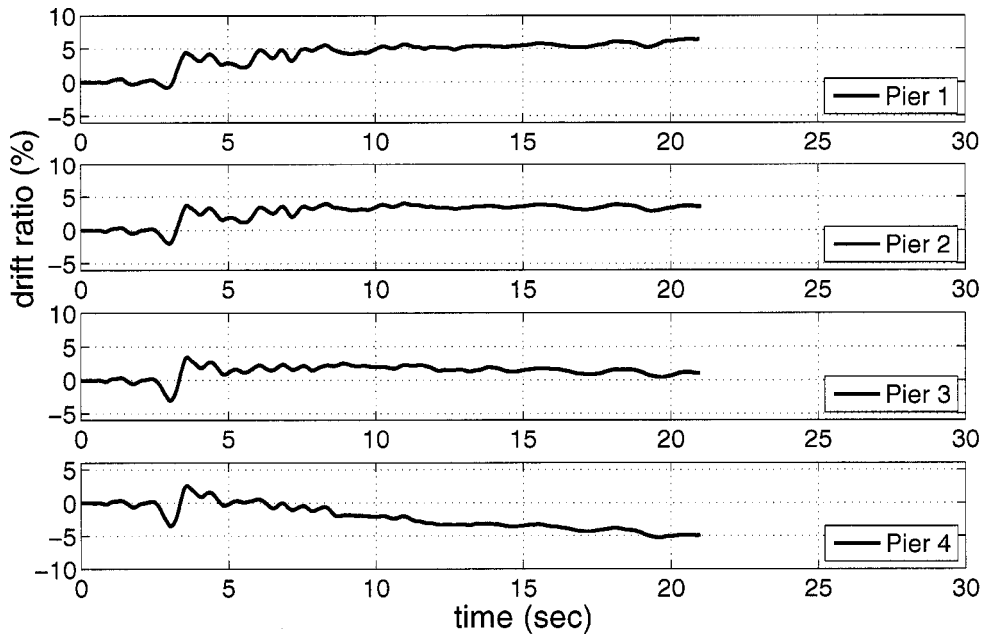
The bridge pier response was investigated using the displacements of the bridge deck and pile cap. Figure 8.20 shows drift ratios obtained by the displacement difference between top and bottom of piers. The bottoms of the four piers (pile caps) moved towards the center of the bridge and the amount of each pier base displacement varied due to different levels of lateral spreading. As shown in Figure 8.20a, Pier 1 base residual lateral displacement was about 20 cm after shaking and Pier 4 base residual lateral displacement was about 60 cm. In the meantime, the top of all piers moved together to the left as the larger lateral spreading beneath the right abutment pushed the entire bridge deck to the left. This bridge deck movement increased Pier 1 drift and decreased Pier 4 drift. Due to this global response, similar drift ratios were observed in Pier 1 and Pier 4 for this particular motion even though the base residual lateral displacement of Pier 4 was greater than that of Pier 1. This demonstrates that lateral spreading in an abutment slope can affect the column drift in the other side of bridge.

Actual input motions at the bottom of each bridge pier are presented in Figure 8.21 in terms of acceleration response spectra and acceleration time histories. Due to non-uniform soil conditions (i.e., different soil profile below the left and right abutments) and liquefaction induced lateral spreading, the bottom of each pier was subjected to different acceleration time histories and peak accelerations.

The horizontal slope movements significantly influenced the pile and pier bending moments. In particular, the bending moments in Pier 4 appear to be closely correlated to horizontal slope movements. For small to moderate shaking events, the maximum bending moments at each bridge pier were greater than the residual bending moments after shaking, indicating that inertial forces controlled the maximum bending moments. For strong shaking events, however, the residual bending moment at each bridge pier or deck was greater than the transient maximum bending moment, indicating that the kinematic forces associated with lateral spreading controlled the maximum bending moment.

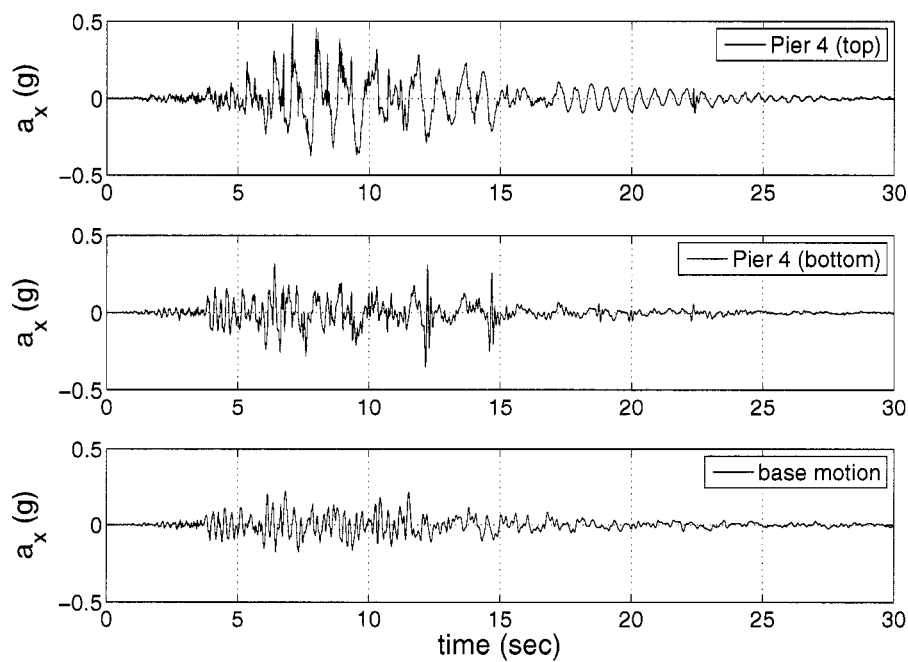


(a) Column displacement

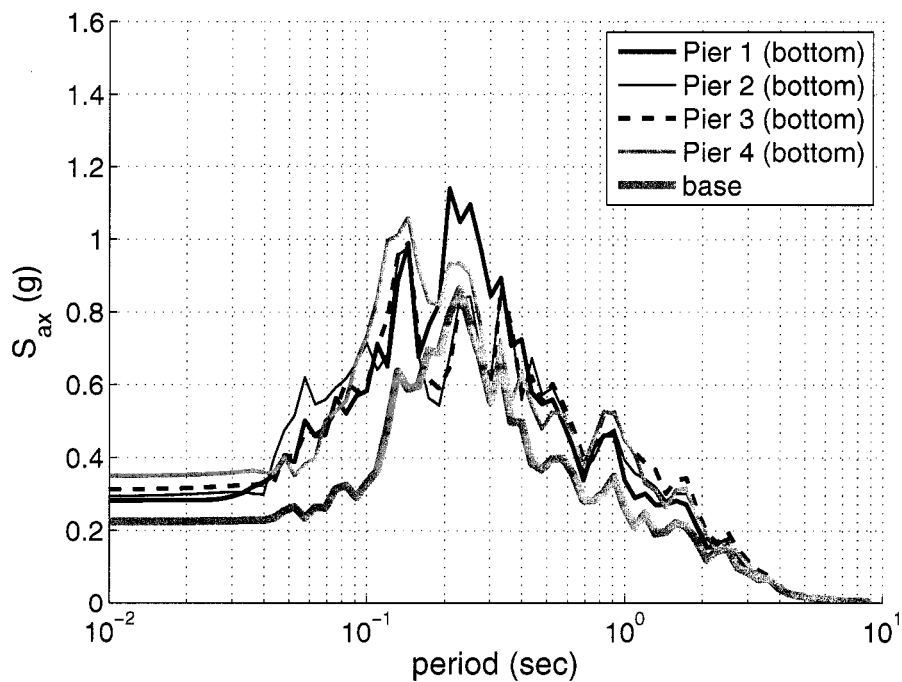


(b) Drift ratio

Figure 8.20: Displacement of each bridge column at top and bottom and drift ratios (column height = 6.7m) - Erzincan motion, Turkey 1992, $a_{max} = 0.70g$



(a) Acceleration time histories



(b) Acceleration response spectra

Figure 8.21: Acceleration time histories and response spectra at soil base and pile cap - Northridge motion 1994, $a_{max} = 0.25g$

8.4.5 Abutment response

The bridge deck and abutment structure interaction was investigated by looking at relative displacements between the bridge deck and abutment and interaction forces in the bearing pad, break-off wall, and backfill. Figure 8.22 shows the horizontal and vertical positions of the bridge deck and abutment during shaking. Each abutment was set to have 10 cm initial expansion joint gaps. The abutments (black line in the figure) moved toward the center of the bridge with increasing vertical displacement. For the Northridge motion ($a_{max} = 0.25g$), the expansion joint gap was closed at the end of shaking, but the backwall did not break. For the Erzincan motion ($a_{max} = 0.70g$), the left abutment showed about 25 cm of permanent lateral movement while the right abutment showed approximately 90 cm of permanent lateral movement with slightly more vertical displacement. Figure 8.22b shows that during strong shaking the bridge deck moved to the left abutment due to the large ground deformation in the right abutment, thereby indicating abutment-abutment interaction through the bridge deck. Moreover, the relative position of the deck-end and backwall, which overcomes the initial gap, indicates shearing failure of the back wall and bridge deck penetration into the backfill soil. At the end of the shaking, the permanent penetration of the left and right bridge-deck-ends into the soil were around 30 cm and 60 cm, respectively.

Bridge deck and abutment interaction is illustrated in Figure 8.23 in terms of spring force-displacement response for strong shaking motion. Figure 8.23a and 8.23b show lateral resistance in the bearing pad and backwall. After 10 cm of displacement, where bearing pad resistance develops, large lateral resistance was mobilized in the break-off wall. This wall resistance disappeared after the wall break-off. This interaction force was delivered to the stem wall of the abutment. Figures 8.23c and 8.23d show that passive earth pressure resistance in the backfill soil was mobilized with the broken portion of the wall after closing the gap. Figure 8.23e and 8.23f show the total lateral resistance transmitted from the abutment system to the bridge deck.

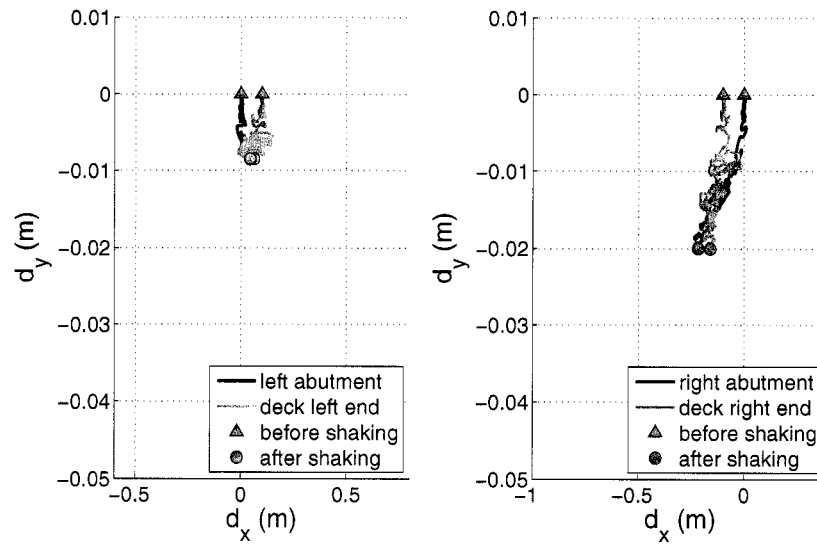
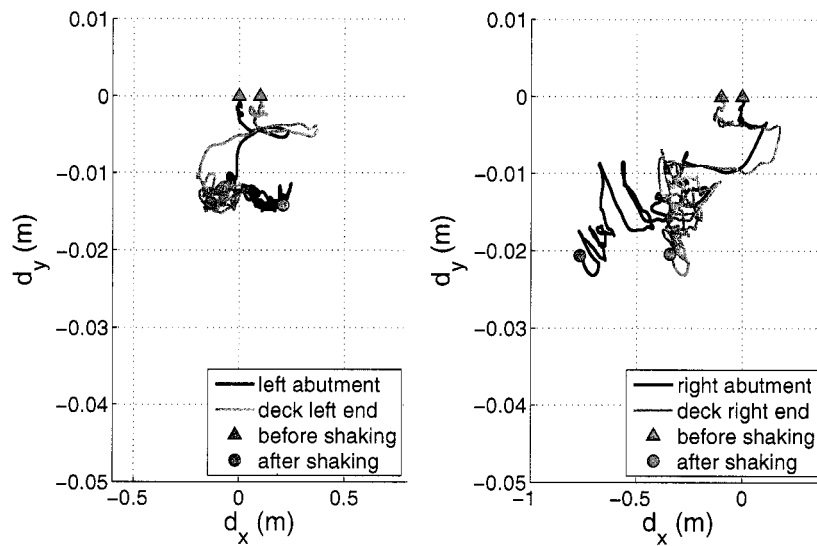
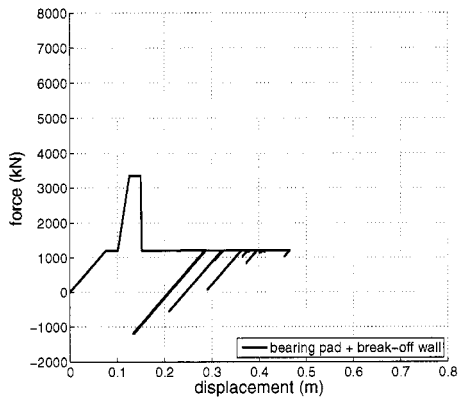
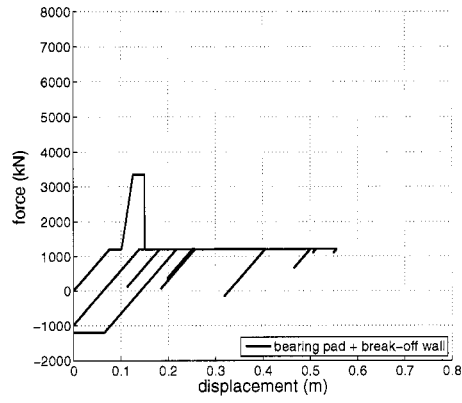
(a) Northridge 1994, $a_{max} = 0.25g$ (b) Erzincan, Turkey 1992, $a_{max} = 0.70g$

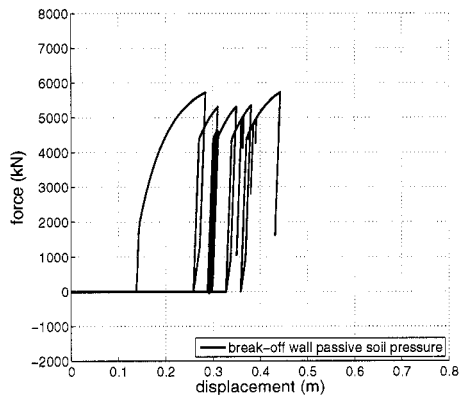
Figure 8.22: Abutment and bridge deck movements



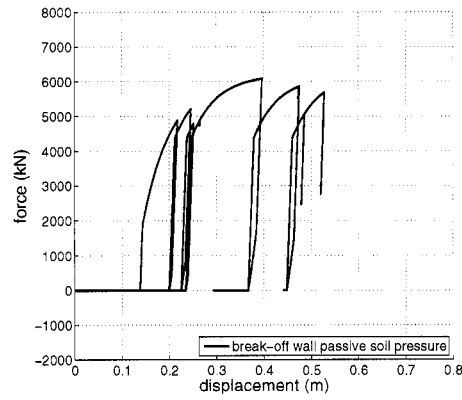
(a) Left bearing pad spring



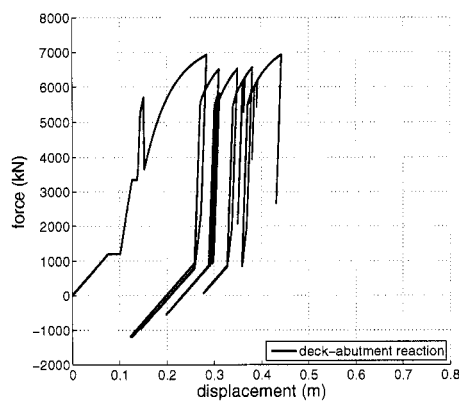
(b) Right bearing pad spring



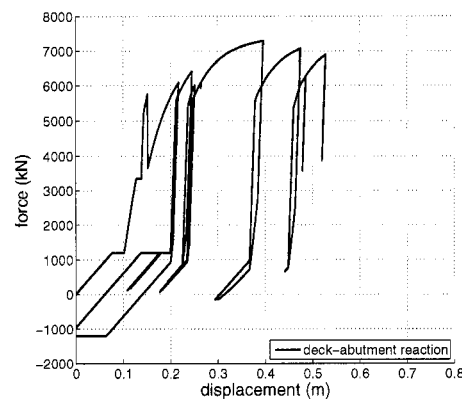
(c) Left backwall soil spring



(d) Right backwall soil spring



(e) Left abutment composite spring



(f) Right abutment composite spring

Figure 8.23: Bridge deck and abutment interaction force-displacement - Erzincan motion, Turkey 1992, $a_{max} = 0.70g$

8.4.6 Pile and p - y spring Response

The pile force distribution and pile cap movement were significantly influenced by lateral spreading and the pattern of soil displacement with depth. This effect varied with ground motion intensity. Figures 8.24 and 8.25 show maximum bending moments and their locations for motions corresponding to all four hazard levels in Pile 0 at the left abutment, and Piles 4 and 5 at the right abutment. In Pile 0, maximum bending moments occurred for most motions at the interface between the clay and dense sand layers. In Pile 4, the maximum pile moment occurred, for small and moderate shaking, below the pile cap or at the interface between the surface clay and lower loose sand layers. However, for higher intensities, the maximum bending moment location moved down to the interface between the loose and dense sand layers (around 12 m depth). Similar patterns were observed in Pile 5. However, for moderate shaking (72-year return period, Motions 11 to 20 in Figure 8.25b), the maximum bending moments occurred in the middle of the loose sand layer. This can be related to the fact that the upper portion of the loose sand layer was liquefied while the lower portion was not fully liquefied for these strong motions. For stronger motions (i.e., 475- and 2475-year return periods, Motions 21 to 40 in Figure 8.25b), the maximum pile bending moment reached the ultimate bending moment capacity.

Figure 8.26 shows residual pile bending moments after shaking and the distribution of kinematic lateral force on the soil due to lateral spreading for the Erzincan motion ($a_{max} = 0.70g$). The figure shows that, for this motion, the maximum bending moment occurred at the interface between the loose and dense sand (around 12 m depth) in all piles. Since most of the loose sand layer was liquefied and the lateral soil resistance of the clay layer was relatively small, the overall mobilized soil resistance was small except for the non-liquefied soil at 5 m depth near Pile 1 and the dense sand layer below 12 m depth. The kinematic p - y spring force at depths from 2 m to 6 m in Pile 4 reached the ultimate residual lateral soil resistance of the fully liquefied soil. In Figure 8.27, the p - y spring response in Pile 4 at 5.5 m is plotted together with the corresponding pore pressure ratio (r_u) time history of an adjacent soil element. API-based soil resistance time history mobilized by the same displacement is also presented in the figure. After 5 seconds, when the soil was liquefied,

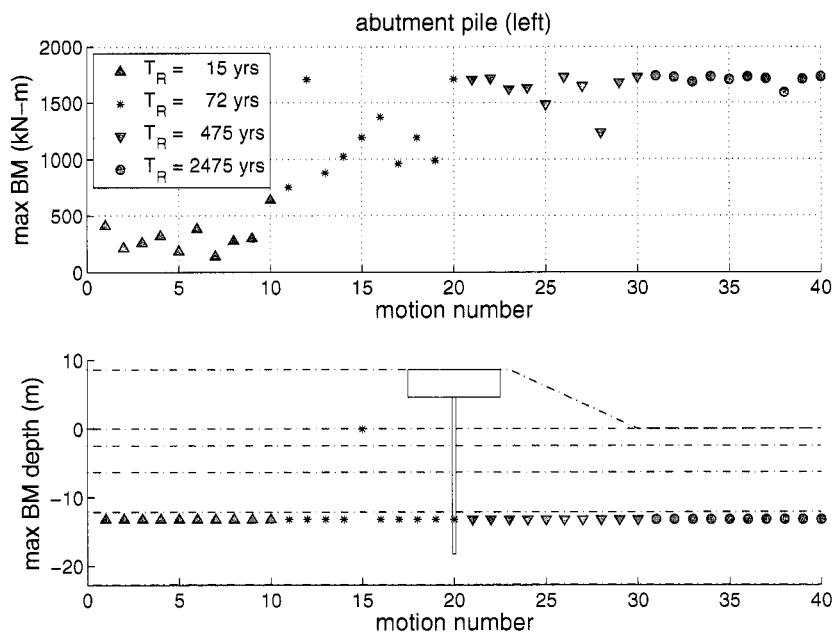
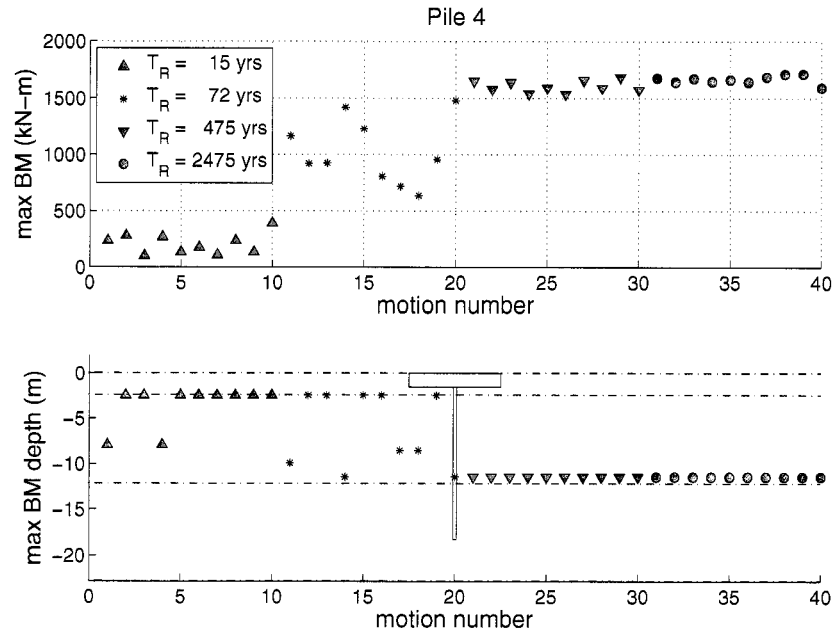


Figure 8.24: Location of maximum pile bending moment in Pile 0 at the left abutment

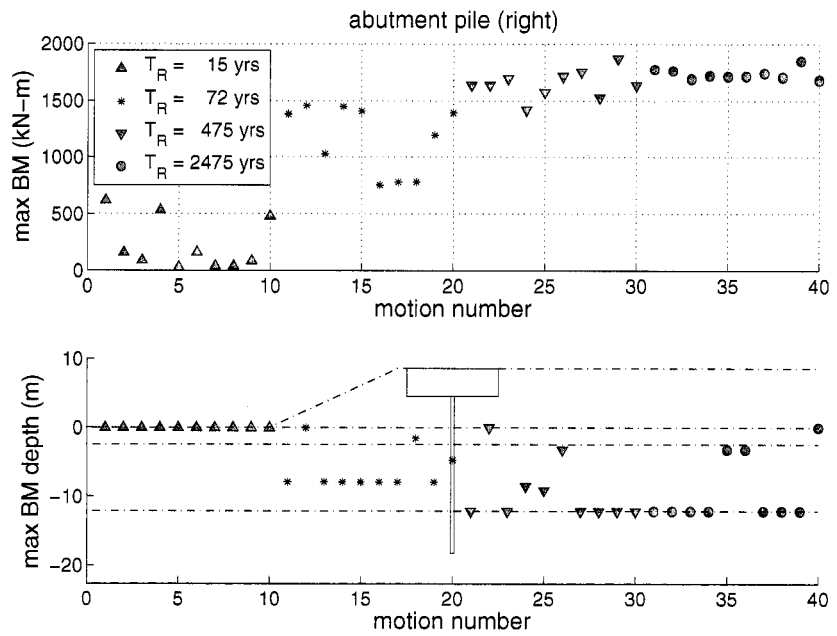
the lateral soil resistance reached an ultimate residual lateral resistance with increasing p - y spring displacement. The figure shows the clear effect of liquefaction on lateral soil resistance by comparison with a possible API-based resistance. The liquefaction effect is also observed in Figure 8.28 which shows p - y curves for Pile 3 and Pile 4 at two locations in the liquefiable layer. Finally, Figure 8.29 shows pile cap lateral passive earth pressure spring force-displacement curves for four pile caps during the strong motion. Pile cap 4 interface spring reached ultimate resistance with lateral-spreading-induced large soil displacements.

8.5 Summary and Conclusions

A complete geotechnical bridge system model including pile foundations embedded in realistic soil conditions and abutment structures was developed and coupled to a bridge structure model (Mackie and Stojadinovic, 2003). Appropriate modeling of soil-pile-structure interaction and soil-abutment-bridge interaction under lateral spreading soil conditions allowed the bridge structure to capture realistic force boundary conditions at the pier base

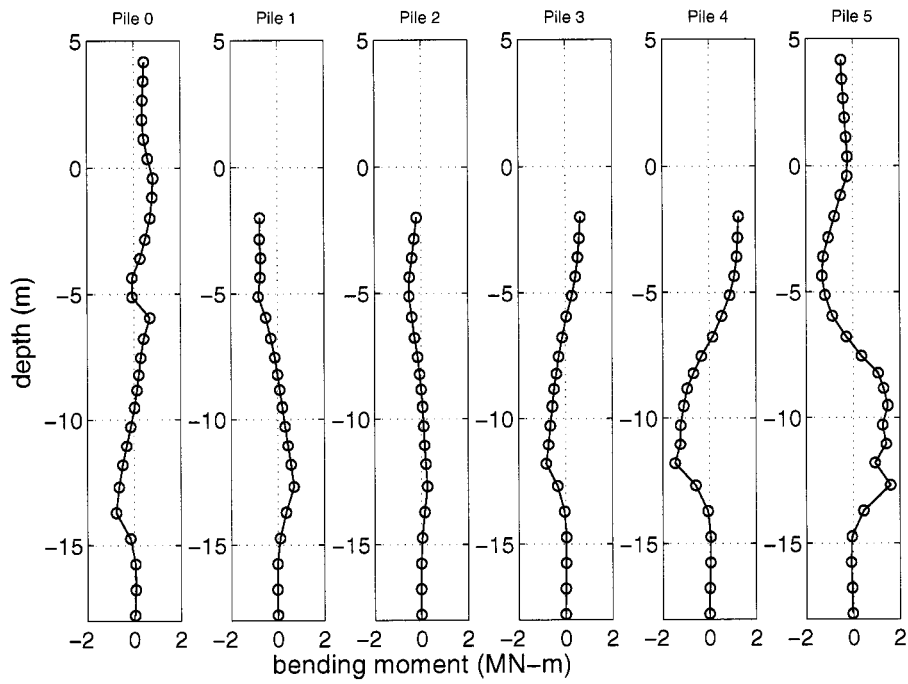


(a) Pile 4

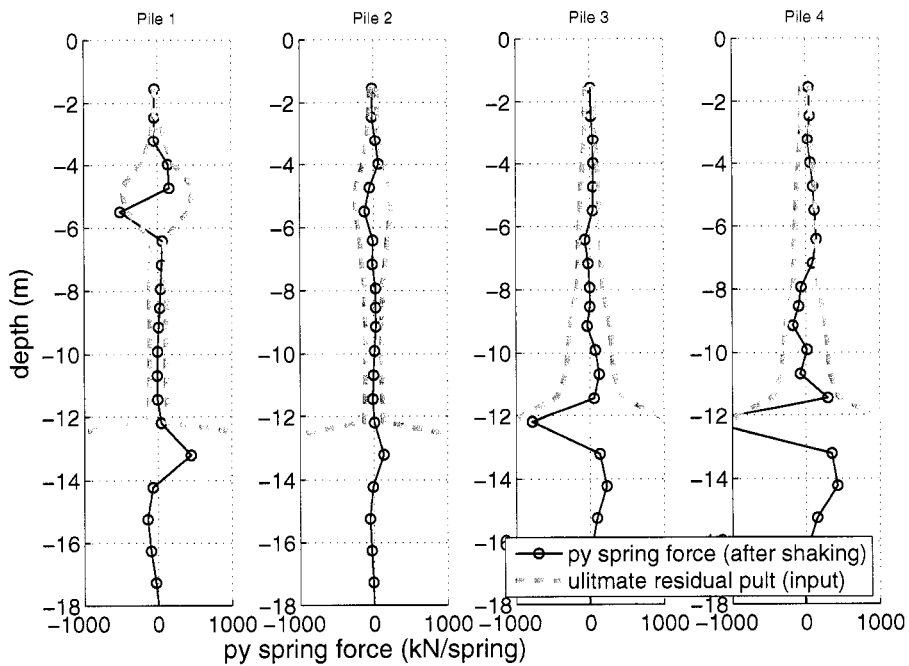


(b) Pile 5

Figure 8.25: Location of maximum pile curvatures in Pile 4 and Pile 5 at the right abutment



(a) Bending moment distribution



(b) Soil pressure on pile

Figure 8.26: Maximum pile bending moments and lateral soil resistance during earthquake - Erzincan motion, Turkey, $a_{max} = 0.70g$

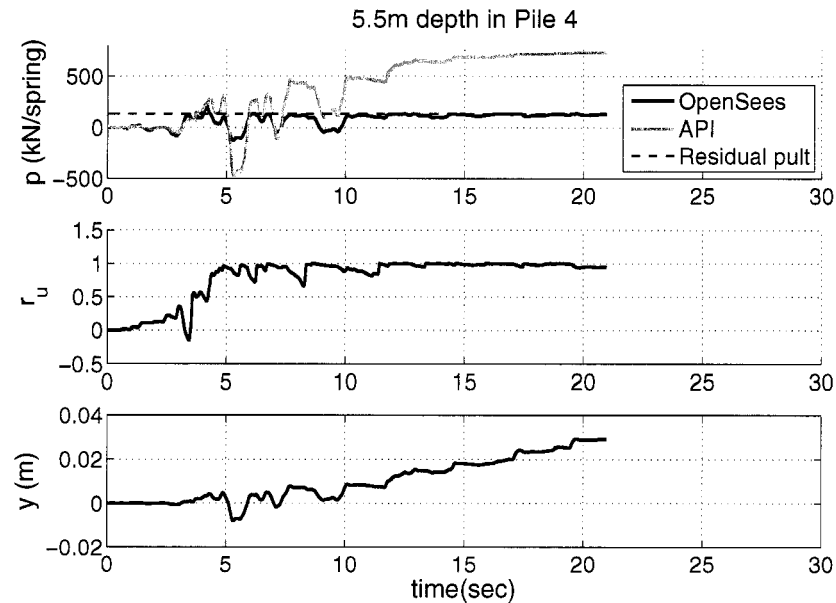


Figure 8.27: p - y time histories during earthquake excitation - Erzincan motion, Turkey, $a_{max} = 0.70g$

and bridge deck ends. Using this coupled model, the global behavior of the bridge system could be better understood and important bridge performance variable (i.e., Engineering Demand Parameters), could be identified. This study shows that the global response of a soil-foundation-bridge system was quite complex, particularly when soft and/or liquefiable soils are present. The use of OpenSees simulations provided improved understanding of the global response, and allowed identification of damage mechanisms that would not be captured by simplified analyses commonly used in contemporary practice.

8.5.1 Lateral Spreading Effects on Global Bridge Behavior

One of the important components to the global bridge response was the abutment-to-abutment interaction caused by different level of lateral spreading and its effect on the bridge pier drift near slopes. Since the amount of the right abutment lateral spreading in the simulation was considerably greater than that in the left abutment, the entire bridge deck moved toward to the left. At the same time, lateral spreading also pushed the pile cap

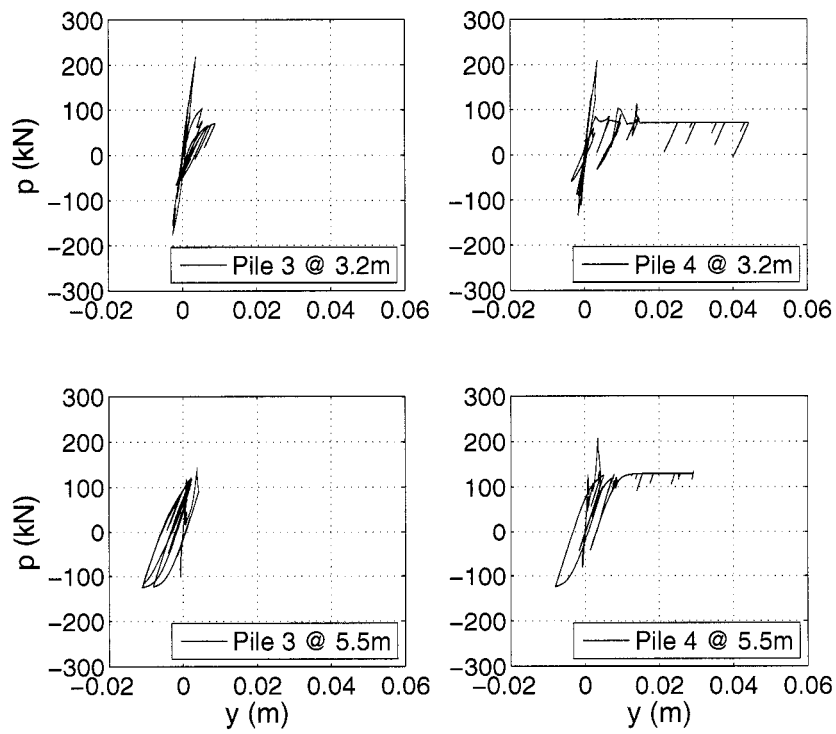


Figure 8.28: p - y curves during earthquake excitation - Erzincan motion, Turkey, $a_{max} = 0.70g$

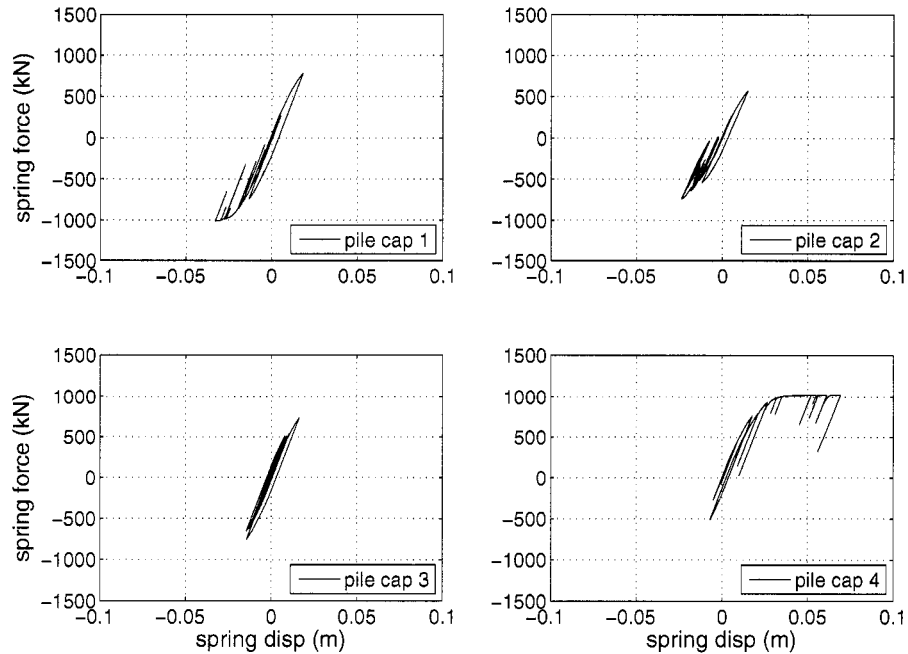


Figure 8.29: Pile cap resistance curves - Erzincan motion, Turkey, $a_{max} = 0.70g$

of the pier near the right slope to the left, so the column drift became smaller. On the other hand, the pier near the left slope was subjected to large column drift because the bridge deck moved to the left and the pile cap at the bottom of the column moved to the right due to lateral spreading of the left abutment. This type of response can only be obtained using advanced numerical models.

8.5.2 Local Bridge Behavior

The soil behavior, including lateral soil displacement and soil liquefaction, were investigated for different intensity motions. At most hazard levels except the lowest hazard level, most of the loose sand layer was liquefied, which resulted in lateral spreading beneath the embankments on both sides of the bridge. The clay layer between the loose sand and dense sand layers in the left abutment area caused complicated soil deformation patterns. The shear strain in the soil below the right embankment was distributed over the thickness of the liquefied area.

Lateral soil displacement patterns strongly affected the location of maximum bending moment. The piles were subjected to relatively low kinematic soil pressure due to soil liquefaction. The soil pressure (interface spring forces) on the pile were investigated in several locations and the pore water pressure generation effect on the p - y spring force were reflected in the OpenSees model.

The bridge pier response was investigated with respect to displacement at the top and bottom of the piers and it was found that drifts at all piers were strongly affected by lateral spreading. The relative position between bridge deck and abutment during the shaking, and corresponding interaction forces, were described to show abutment-bridge-soil interaction.

Chapter 9

APPLICATION OF PBEE TO A TYPICAL HIGHWAY BRIDGE IN LIQUEFIABLE SOIL**9.1 Introduction**

Estimation of the seismic performance of bridges is an important part of evaluating the potential costs of earthquake damage and identification of appropriate retrofit strategies. The Pacific Earthquake Engineering Research Center (PEER) has developed a probabilistic framework for performance-based earthquake engineering (PBEE) to evaluate the risk associated with earthquake shaking at a particular site (Cornell and Krawinkler, 2000; Krawinkler, 2002; Deierlein et al., 2003) The risk, expressed in terms of economic loss, fatalities or other measures, is computed as a function of ground shaking through a series of intermediate steps: i) seismic hazard, ii) demand hazard, and iii) damage hazard. The seismic hazard is characterized in terms of an Intensity Measure, IM which describes the level of ground shaking. The demand hazard is some form of response, characterized in terms of an Engineering Demand Parameter, EDP, at the site of interest. The damage hazard that results from this EDP contributes to the overall risk.

For the PBEE analysis performed in this study, four different hazard levels of near-fault motions were considered in OpenSees simulations using the bridge system model described in Chapter 8. Measures of structural and geotechnical response relevant to bridge damage were identified. Using OpenSees results, record-to-record uncertainties were estimated. In this estimation, the relative efficiencies of several IMs were investigated to reduce the demand model uncertainties. Besides the record-to-record uncertainty, model parameter uncertainty and spatial variability uncertainty were considered. To demonstrate the effect of parametric uncertainty, controlling parameters were first identified by conducting sensitivity analyses and using Tornado diagrams. Using the sensitivity results, parametric uncertainties were estimated from an FOSM analysis. To determine the spatial variability

uncertainty, Gaussian stochastic fields were generated for the liquefiable and clay soil layers. The three uncertainties were combined and used to develop EDP hazard curves.

9.2 Input Motions and Intensity Measures

To apply the PEER PBEE methodology, four sets of input motions corresponding to return periods of 15, 72, 475, and 2475 years (i.e., 97 %, 50 %, 10 %, and 2 % in 50 years) at the site of an I-880 bridge study (Somerville, 2000) were used together with the proposed bridge model. In the I-880 bridge study (Somerville, 2000), near-fault ground motions were used. Near-fault ground motions are different from ordinary ground motions since they are often dominated by strong, long period pulses, which result from rupture directivity effects. Details of the characteristics of the selected near-fault ground motions are described by Somerville (2000). Figure 9.1 shows acceleration and displacement time histories for one of these motions with a return period of 275 years. In the simulations performed in this study, the bridge was assumed to be subjected to fault-normal motions - i.e., the longitudinal direction of the target bridge was assumed perpendicular to the strike-slip.

Somerville (2000) provided soft rock uniform hazard spectra for three hazard levels (50 %, 10 %, and 2 % in 50 years) for the I-880 site. The target modal magnitudes for these three hazards were obtained from deaggregation data as 6.6, 6.8, and 7.0, respectively. The corresponding target peak acceleration values were 0.453g, 0.871g, and 1.228g, respectively. In this study, to minimize dispersion in the EDP vs. IM relationships, particularly for the case where lateral spreading affects the bridge response, motions for each hazard level were scaled to a constant value, target magnitude-corrected PGA (PGA_M), expressed as

$$PGA_M = \frac{PGA}{MSF} \quad (9.1)$$

where PGA is the mean PGA for the hazard level of interest and MSF is the magnitude scaling factor corresponding to the modal magnitude for that hazard level. Magnitude scaling factors can be calculated using NCEER's recommendations as

$$MSF = \begin{cases} \left(\frac{7.5}{M_w}\right)^{2.95} & M_w \leq 7.5 \\ \left(\frac{7.5}{M_w}\right)^{2.56} & M_w < 7.5 \end{cases} \quad (9.2)$$

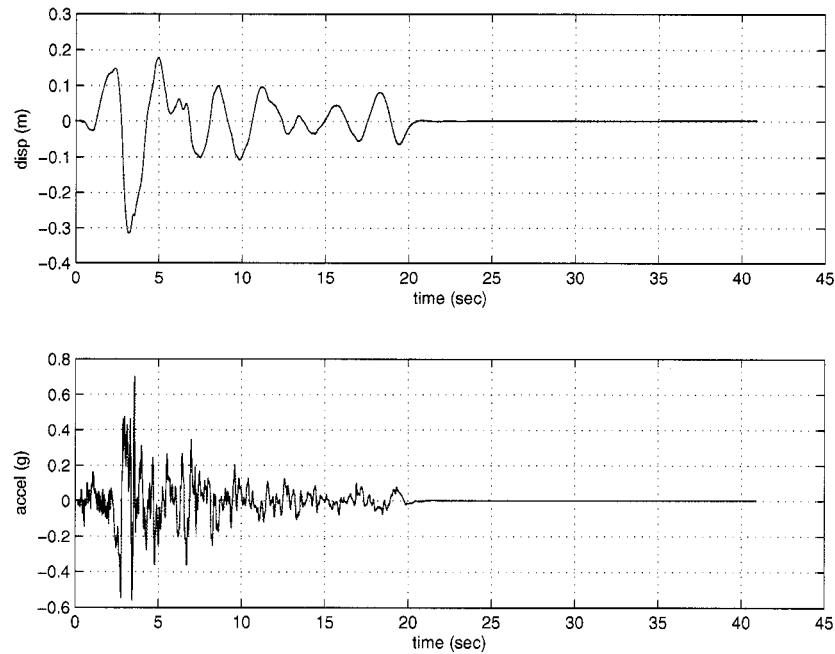


Figure 9.1: Example of an input motion used in the comprehensive bridge study (Erzincan, Turkey 1992, $a_{max} = 0.70g$)

where M_w is modal magnitude. Using the target modal magnitudes and their corresponding MSF, magnitude-corrected PGAs (PGA_M) for each hazard were computed and are presented in Table 9.1. To include a hazard which does not cause liquefaction, the motions used for 50% in 50 years were scaled for a target magnitude-corrected peak acceleration of 0.094 g, which results in a 97% in 50 years hazard. Ten motions were selected for each hazard. Individual motions were scaled to have the target magnitude-corrected peak acceleration in each hazard. The values are presented in the 7th column (i.e., PGA_M) in Table 9.2.

Since the scaled motions were based on rock outcrop conditions, the motions were corrected using the computer program *Proshake* to remove free surface effects prior to their use as rigid base input motions in OpenSees. Information for the 40 motions is summarized in Table 9.2. Figure 9.2 shows the range of PGAs for each hazard level and the corresponding PGA hazard curve.

The uncertainties in the estimated EDP vs. IM relationships are different for different

Table 9.1: Magnitude-corrected PGA

Hazard Level	a_{max} (g)	modal magnitude	MSF	$PGA_M = \frac{a_{max}}{MSF}$
50 % in 50 years	0.453	6.6	1.516	0.299
10 % in 50 years	0.871	6.8	1.335	0.652
2 % in 50 years	1.228	7.0	1.226	1.002

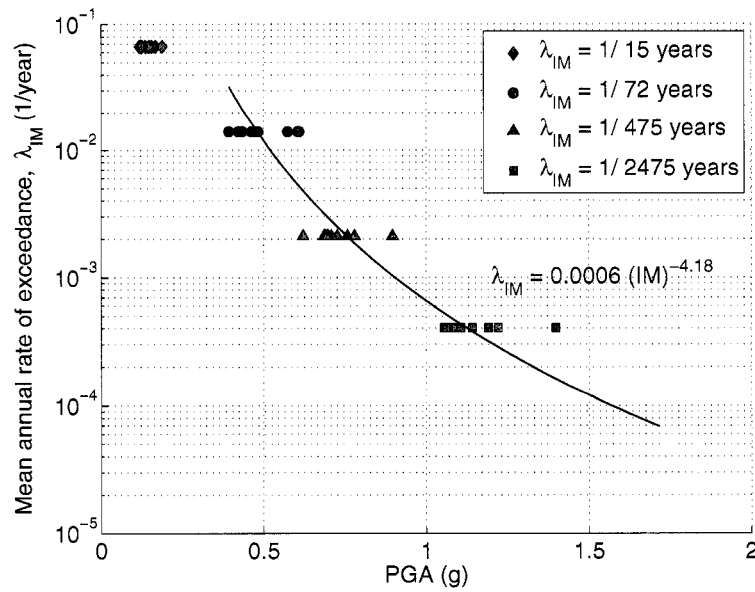


Figure 9.2: PGA hazard curve used in OpenSees simulations

Table 9.2: I-880 Input motion characteristics (four hazards)

hazard	Record (station)	File	Earthquake	Magnitude	MSF	PGA_M	dt	PGA	duration
return period 72 yrs target PGA_M = 0.299g	Coyote Lake Dam abutment	A01	Coyote Lake	5.7	2.247	0.672	0.005	0.574	40.96
	Gilroy #6	A02	(6/ 8/1979)				0.005	0.610	40.96
	Temblor	A03	Parkfield	6.0	1.931	0.578	0.010	0.469	40.96
	Array #5	A04	(6/27/1966)				0.010	0.470	81.92
	Array #8	A05					0.010	0.394	40.96
	Fagundes Ranch	A06	Livermore	5.5	2.497	0.747	0.005	0.606	20.48
	Morgan Territory Park	A07	(6/27/1980)				0.005	0.483	40.96
	Coyote Lake Dam abutment	A08	Morgan Hill	6.2	1.753	0.524	0.005	0.423	40.96
	Anderson Dam DS	A09	(4/24/1984)				0.005	0.435	40.96
	Halls Valley	A10					0.005	0.464	40.96
return period 475 yrs target PGA_M = 0.652g	Los Gatos Presentation Ctr	B01	Loma Prieta	7.0	1.226	0.799	0.005	0.687	40.96
	Saratoga Aloha Avenue	B02	(10/17/1989)				0.005	0.728	40.96
	Corralitos	B03					0.005	0.709	40.96
	Gavilan College	B04					0.005	0.699	40.96
	Gilroy Historic	B05					0.005	0.691	40.96
	Lexington Dam abutment	B06					0.020	0.759	40.96
	Kobe JMA	B07	Kobe, Japan (1/17/1995)	6.9	1.279	0.834	0.020	0.781	81.92
	Kofu	B08	Tottori, Japan	6.6	1.458	0.951	0.010	0.622	40.96
	Hino	B09	(10/6/2000)				0.005	0.897	81.92
	Erzincan	B10	Erzincan (3/13/1992)	6.7	1.395	0.909	0.005	0.696	40.96
return period 2475 yrs target PGA_M = 1.002g	Los Gatos Presentation Ctr	C01	Loma Prieta	7.0	1.226	1.228	0.005	1.101	40.96
	Saratoga Aloha Avenue	C02	(10/17/1989)				0.005	1.141	40.96
	Corralitos	C03					0.005	1.078	40.96
	Gavilan College	C04					0.005	1.055	40.96
	Gilroy Historic	C05					0.005	1.063	40.96
	Lexington Dam abutment	C06					0.020	1.191	40.96
	Kobe JMA	C07	Kobe, Japan (1/17/1995)	6.9	1.279	1.282	0.020	1.221	81.92
	Kofu	C08	Tottori, Japan	6.6	1.458	1.461	0.010	1.092	40.96
	Hino	C09	(10/6/2000)				0.005	1.399	81.92
	Erzincan	C10	Erzincan,Turkey (3/13/1992)	6.7	1.395	1.398	0.005	1.107	40.96
return period 15 yrs target PGA_M = 0.094g	Coyote Lake Dam abutment	D01	Coyote Lake	5.7	2.247	0.211	0.005	0.168	40.96
	Gilroy #6	D02	(6/ 8/1979)				0.005	0.167	40.96
	Temblor	D03	Parkfield	6.0	1.931	0.182	0.010	0.157	40.96
	Array #5	D04	(6/27/1966)				0.010	0.137	81.92
	Array #8	D05					0.010	0.119	40.96
	Fagundes Ranch	D06	Livermore	5.5	2.497	0.235	0.005	0.189	20.48
	Morgan Territory Park	D07	(6/27/1980)				0.005	0.148	40.96
	Coyote Lake Dam abutment	D08	Morgan Hill	6.2	1.753	0.165	0.005	0.122	40.96
	Anderson Dam DS	D09	(4/24/1984)				0.005	0.126	40.96
	Halls Valley	D10					0.005	0.124	40.96

Table 9.3: Intensity Measures

IM name	Definition	Units
Peak ground acceleration	$PGA = \max a(t) $	g
Peak ground velocity	$PGV = \max v(t) $	m/s
Arias intensity	$I_a = \frac{\pi}{2g} \int_0^{T_d} [a(t)]^2 dt$	cm/s
Cumulative absolute velocity	$CAV_5 = \int_0^{T_d} \langle \chi \rangle a(t) dt$ where $T_d =$ earthquake duration $\langle \chi \rangle = 0$, if $ a(t) < 5 \text{ cm/s}^2$ $\langle \chi \rangle = 1$, if $ a(t) \geq 5 \text{ cm/s}^2$	cm/s
Spectral acceleration	$Sa(T_1) = Sa(T_1)$	g
Cordova predictor	$Sa^*(T_1) = Sa(T_1) \sqrt{\frac{Sa(2T_1)}{Sa(T_1)}}$	g

EDPs and IMs. An efficient IM is one for which an EDP of interest is closely related; i.e. one for which a plot of EDP vs. IM exhibits little scatter. The use of efficient IMs leads to more accurate and less conservative performance estimation in PBEE evaluation procedures. For example, to capture the inertial structural response, spectral acceleration and Cordova (2000) predictor (Table 9.3) are generally recognized as efficient IMs. For a situation influenced by the occurrence of liquefaction, however, the response should be more closely related to an IM that reflects the liquefaction response, e.g., PGA , I_a , or CAV_5 . For example, Kramer and Mitchell (2006) have shown that excess pore pressure generation in potentially liquefiable soils is considerably more closely related to CAV_5 than to other intensity measures. In this study, several IMs are considered and their definitions are summarized in Table 9.3.

IM hazard curves are usually obtained from Probabilistic Seismic Hazard Analyses (PSHA) as described in Section 3.2.1. Since IM hazard curves often follow power laws, the hazard curve can be expressed as

$$\lambda_{IM} = k_0 (IM)^{-k} \quad (9.3)$$

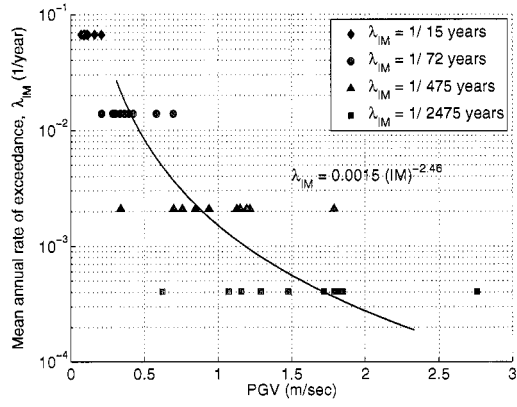
Table 9.4: IM hazard curve coefficients for I-880 input motions

IM	coefficient k_0	coefficient k
Peak ground acceleration (<i>PGA</i>)	6.578e-04	-4.1808
Peak ground velocity (<i>PGV</i>)	1.520e-03	-2.4645
Arias Intensity (I_a)	1.586e+01	-1.4230
Cumulative absolute velocity (CAV_5)	7.881e+04	-2.3859
Spectral acceleration (Sa(T=0.5 sec))	9.455e-03	-3.5338
Spectral acceleration (Sa(T=1.0 sec))	1.675e-03	-2.0630
Cordova predictor (Cordova(T=0.5 sec))	2.799e-03	-2.6514

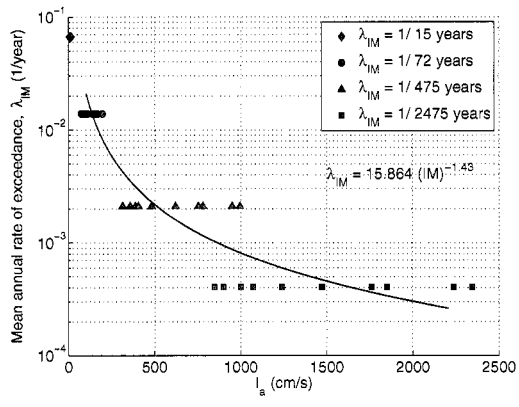
where the two unknown coefficients, k_0 and k , can be obtained solving Equation 9.3 by substituting two hazard levels - e.g., (IM_1, λ_1) and (IM_2, λ_2) . In this research, the mean annual rates of exceedance for the four hazard levels were based on *PGA*. The mean annual rates of exceedance for the other IMs should have been obtained from PSHAs performed using attenuation relationships corresponding to each IM. As an approximate estimation of each IM hazard curve, the IM value of each individual motion was calculated based on the definitions shown in Table 9.3 considering the same mean annual rate of exceedance obtained for *PGA*. The generated IM hazard curves for different IMs are shown in Figure 9.3. The figure shows a large scatter for some IMs. Therefore, if a set of motions obtained from a PSHA analysis for a particular IM is used for other IM hazard curve construction, the IM hazard curve should be used with care. The power law coefficients for several IM hazard curves are summarized in Table 9.4. The IM hazard curve for *PGA* is also shown in Figure 9.2.

9.3 EDPs of Bridge System

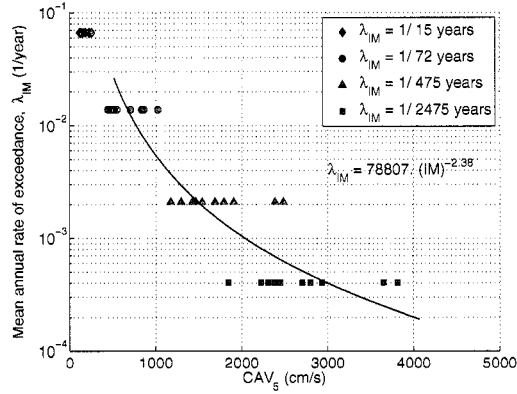
By examining the bridge behavior from multiple numerical analyses, important EDPs (such as maximum and residual values of bridge pier drift, horizontal slope movement, embankment settlement, relative displacement between bridge deck and abutment approach, pile cap movement, and pile curvature) were identified. A list of possible EDPs for the bridge system is shown in Table 9.5.



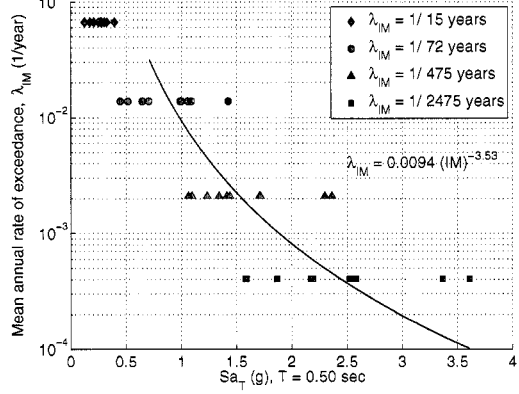
(a) $IM = PGV$



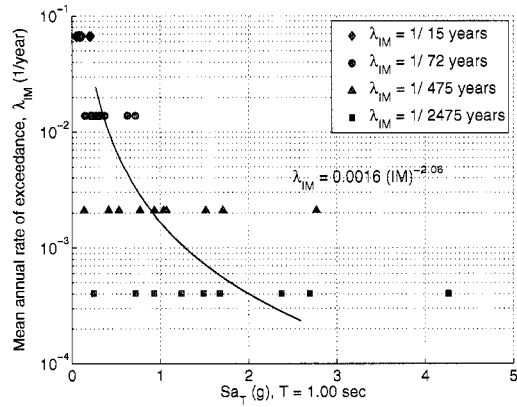
(b) $IM = I_a$



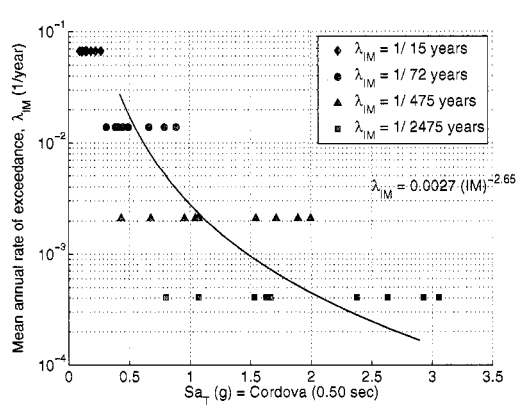
(c) $IM = CAV_5$



(d) $IM = S_a(T = 0.5sec)$



(e) $IM = S_a(T = 1.0sec)$



(f) $IM = Cordova predictor (T=0.5sec)$

Figure 9.3: IM hazard curves

The list classifies EDPs into several EDP groups that can be associated with structural and geotechnical damage and cost estimation. The structural EDP groups include column drift, expansion joint displacement, bridge approach vertical off-set, break-off wall displacement, and bearing pad shear strain. The structural EDPs were selected to be consistent to the EDPs used by Mackie et al. (2004), who performed similar analyses using the same bridge model on competent soil. Abutment slope deformation and pile cap displacement were included as new geotechnical EDP groups. Even though the actual damage to a pile is most closely related to pile bending moment or curvature, these EDPs may not be practical for estimation of damage because they represent response measures that cannot be easily observed following an earthquake. Therefore, the correlation between pile cap and pile curvature was investigated. Figure 9.4 shows that the residual pile cap displacement after shaking and maximum pile curvature were reasonably well correlated, especially for large pile cap displacements.

9.4 Uncertainties in EDP Estimation

There are several sources of uncertainty in EDP estimation as illustrated in Figure 9.5. One of the major sources of uncertainty is the record-to-record uncertainty that originates from the different characteristics of the earthquake motions. Any structural or geotechnical system response is affected by ground motion characteristics such as peak acceleration, frequency content, duration, number of cycles, etc. For example, two motions that have the same peak acceleration could result in significantly different responses if they have different frequency content, number of cycles, and duration. For that reason, to estimate performance uncertainty due to earthquake motion uncertainty, it is required to subject the model to various motions that reflect a range of earthquake source and path characteristics similar to those affecting the site of interest. In situations like this with multiple simulations, it is important to identify efficient IMs to reduce the performance uncertainty (less dispersion in EDP-IM relationship) as well as to reduce the number of simulations required to achieve a given level of confidence in the EDP-IM relationship.

The second source of uncertainty is the parametric uncertainty that results from inherent material property uncertainties. This uncertainty is comprised of aleatory uncertainty

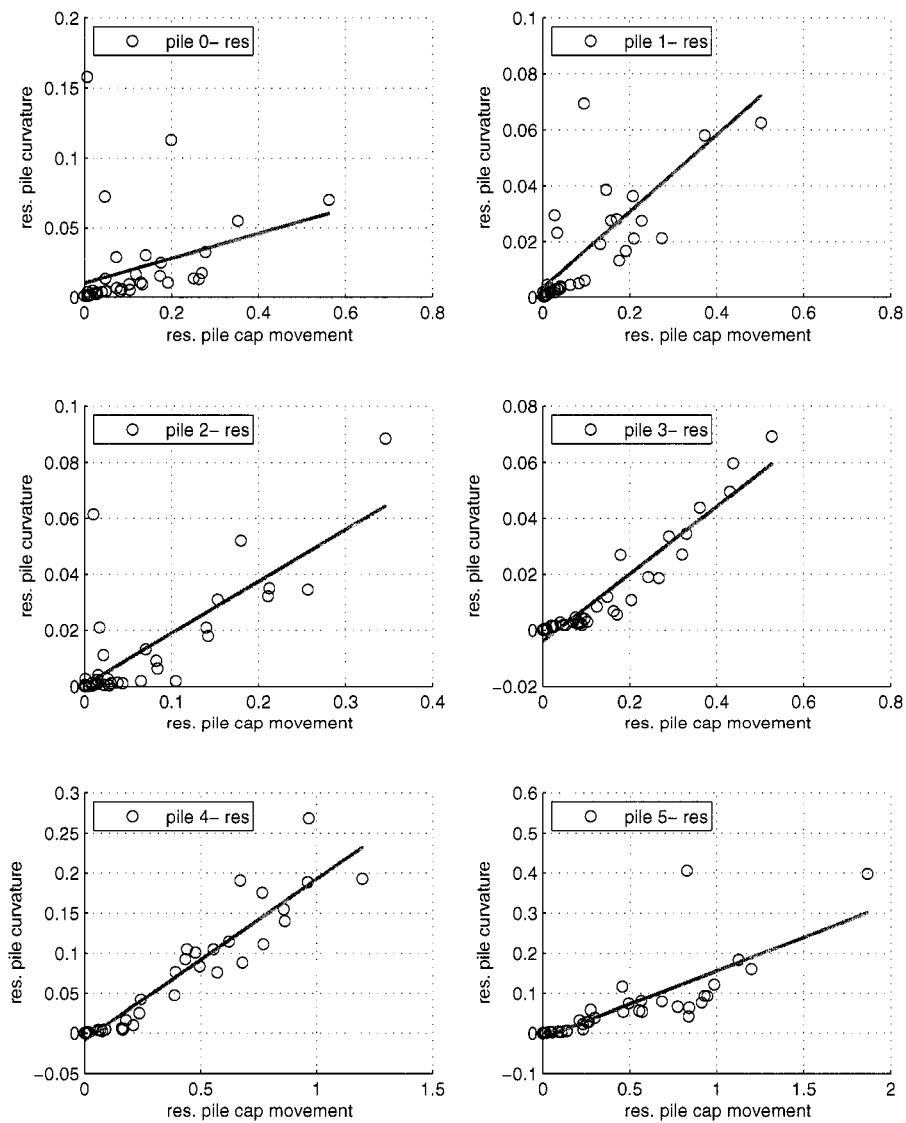


Figure 9.4: Correlation between lateral pile cap displacement and curvature from simulations for Northridge 1994, 0.2557g: unit of curvature = 1/m

Table 9.5: EDP list

EDP group	EDP description	EDP symbol	Definition
column	drift ratio	$C1_{[drift,max]}$ $C2_{[drift,max]}$ $C3_{[drift,max]}$ $C4_{[drift,max]}$	maximum drift ratio = maximum drift/column height
pile cap	pile cap drift (displacement)	$P0_{[drift,res]}$ $P1_{[drift,res]}$ $P2_{[drift,res]}$ $P3_{[drift,res]}$ $P4_{[drift,res]}$ $P5_{[drift,res]}$	permanent lateral displacement of pile cap
abutment exp. joint	gap between deck and abutment	$EJ1_{[gap,res]}$ $EJ2_{[gap,res]}$	relative distance between deck end and break-off wall
abutment backwall	backwall displacement	$BW1_{[dx,max]}$ $BW2_{[dx,max]}$	break-off wall displacement = disp. of bearing pad spring - initial gap
abutment approach	bridge approach vert. off-set	$BA1_{[dy,res]}$ $BA2_{[dy,res]}$	relative vertical displacement between abutment top and adjacent backfill soil
bearing pad	bearing pad displacement	$BP1_{[dx,max]}$ $BP2_{[dx,max]}$	maximum relative lateral displacement between deck and stem wall
embankment slope	lateral disp.	$E1_{[dx,res]}$ $E2_{[dx,res]}$	average lateral displacement of slope top and toe
	settlement	$E1_{[dy,res]}$ $E2_{[dy,res]}$	average vertical displacement of slope top and toe

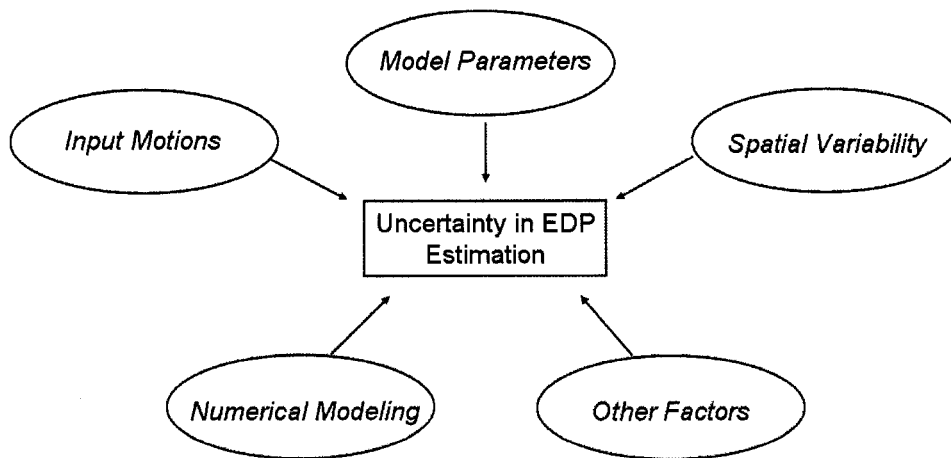


Figure 9.5: Components of total uncertainty in EDP estimation

which represents the natural randomness of a property and epistemic uncertainty which results from the lack of information or knowledge and shortcomings in measurements and calculations.

The third source of uncertainty originates from spatial variability. Soil physical properties vary from place to place within a soil deposit due to depositional factors such as sedimentation, erosion, transportation, and weathering processes and loading history.

A final source of uncertainty originates from the numerical modeling. Since the OpenSees bridge model uses model components where assumptions, approximations and simplifications are made, especially for a complete bridge including several interfacing components, the simulated response cannot be free from model uncertainty even though the uncertainty can be reduced using advanced and verified analysis methods and tools that can handle the simulation properly. This is why the global and local response evaluation performed in Chapter 8 is so important.

In this study, the first three uncertainties were included in the EDP estimation procedure. To estimate the record-to-record uncertainty, motions for four hazards levels were used in the simulations. To estimate parametric uncertainty, 16 model parameters were varied and results from the simulations were used in First-Order-Second-Moment (FOSM) analysis. To

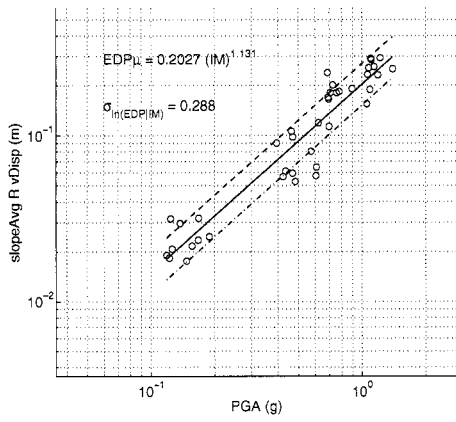
evaluate the spatial variability uncertainty, stochastic fields were generated using Gaussian random fields. The numerical modeling uncertainty was not explicitly evaluated in this study.

9.5 Record-to-record Uncertainty

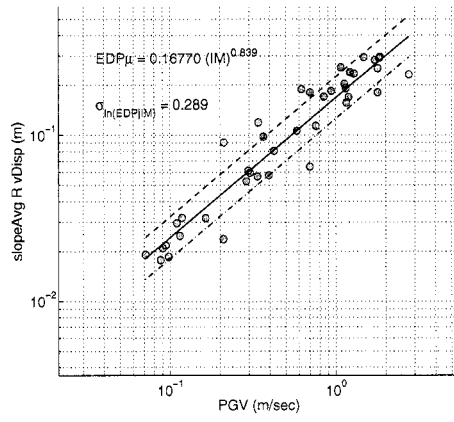
Using simulation results for all four hazard levels, several EDP-IM relationships and uncertainty parameters were obtained for different IMs using a *cloud analysis* approach. From the EDP-IM relationships linear regressions in log-log space were obtained to estimate record-to-record uncertainties assuming a constant lognormal probability distribution of EDP conditional upon IM.

Based on these results, efficient IMs were identified for different EDPs. For example, Figure 9.6 shows residual settlements in the right abutment slope as a function of six different IMs. This figure also shows the standard deviation of $\ln EDP$ residual and median relationship with median \pm standard deviation lines. Figure 9.7 shows the same information for maximum drift ratio in Pier 4. For the right abutment settlement, CAV_5 appears to be the most efficient IM (least dispersion in EDP-IM) among the IMs considered in Table 9.3. For Pier 4 drift ratio, the Cordova parameter at the fundamental structural period appears to be the most efficient IM. Figure 9.8 compares the efficiency of IMs for the two EDPs. These results show that the most efficient IMs depends on the EDP being considered.

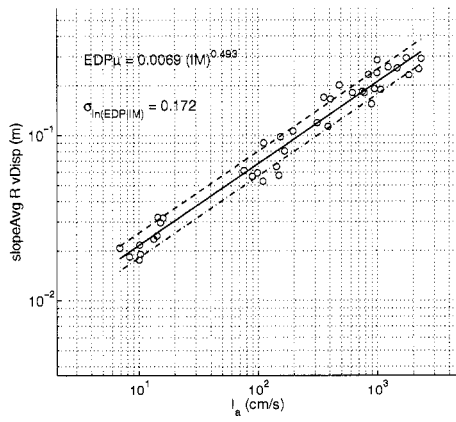
Using EDP-IM results, record-to-record uncertainties and median EDP-IM relationships were obtained for several EDP groups. The results are summarized in Table 9.6 where the corresponding efficient IMs are indicated. This summary table shows that CAV_5 is one of the most efficient IMs for the EDPs affected by lateral spreading such as slope deformation, abutment expansion joint movement, and pile cap lateral movement near slopes, while spectral acceleration or PGV is more efficient for structural related EDPs such as bridge pier drift ratio. Overall, residual EDPs obtained at the end of shaking showed higher uncertainty than maximum EDPs. Pile cap displacements also showed higher uncertainty than bridge pier drifts.



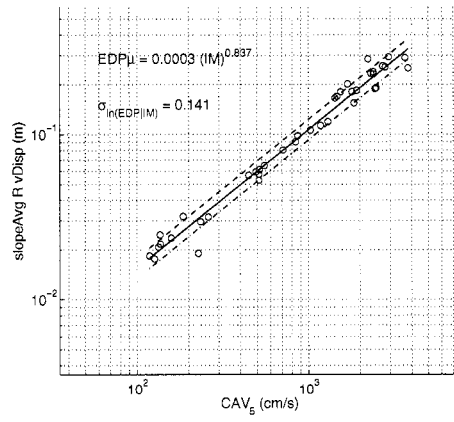
(a) IM = PGA



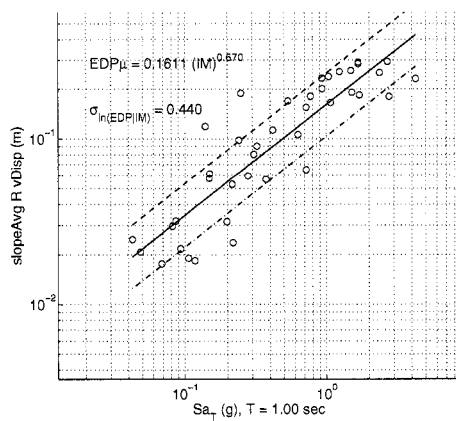
(b) IM = PGV



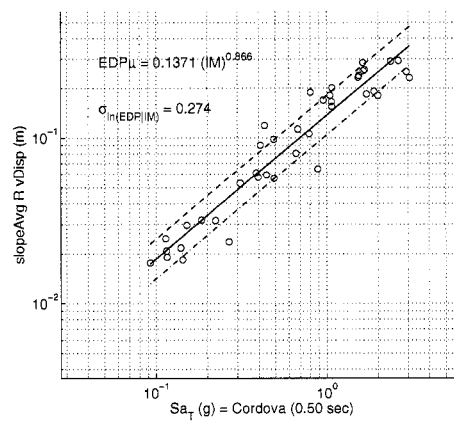
(c) IM = I_a



(d) IM = CAV₅

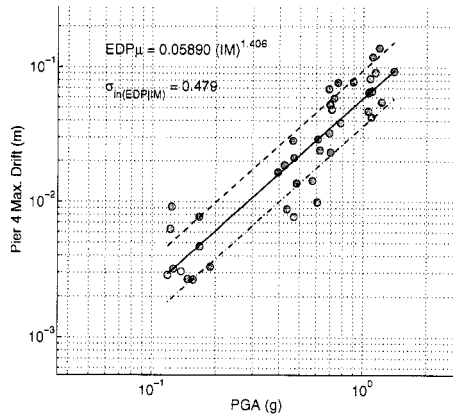


(e) IM = S_a(T)

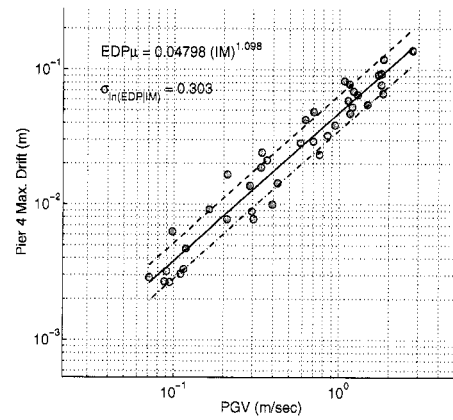


(f) IM = Cordova predictor

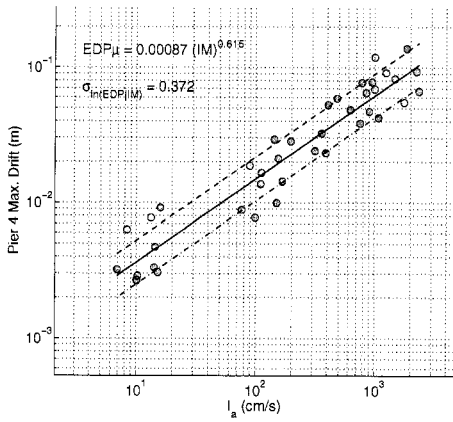
Figure 9.6: EDP-IM relationships for right abutment slope residual vertical settlement



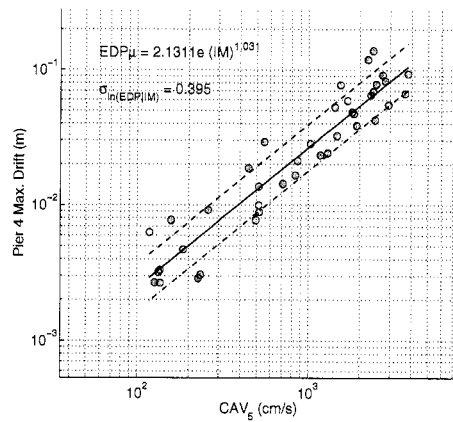
(a) $IM = PGA$



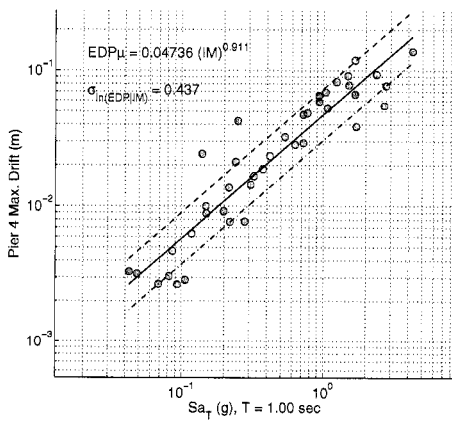
(b) $IM = PGV$



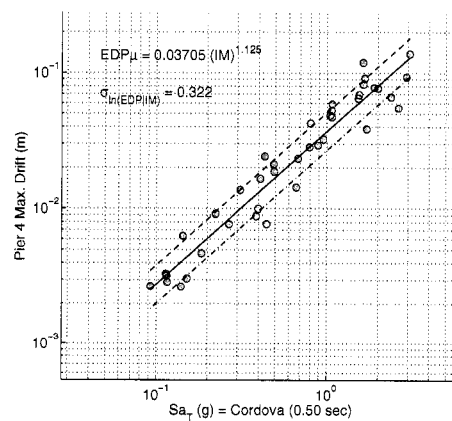
(c) $IM = I_a$



(d) $IM = CAV_5$

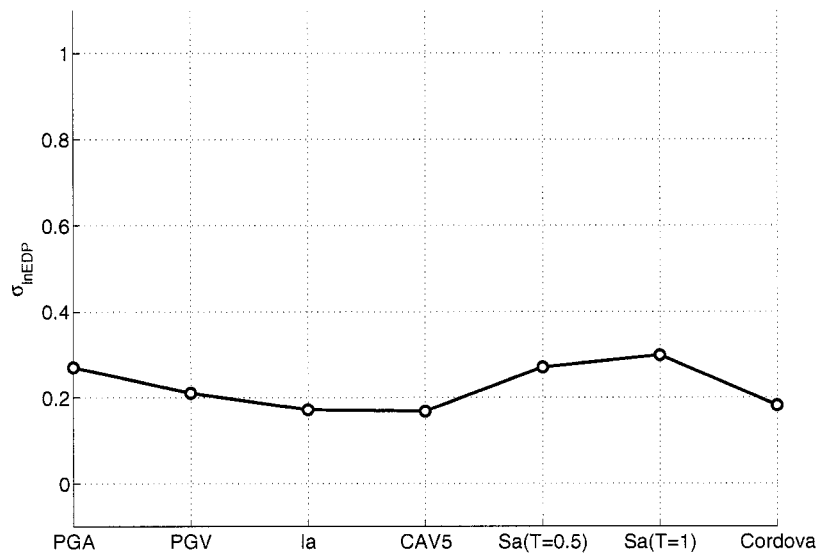


(e) $IM = S_a(T)$

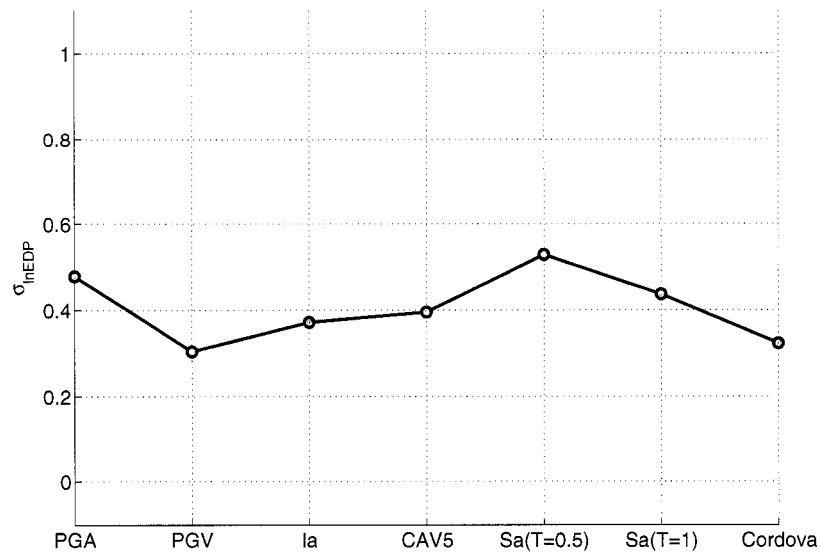


(f) $IM = \text{Cordova predictor}$

Figure 9.7: EDP-IM relationships for Pier 4 maximum drift



(a) Right abutment slope residual settlement



(b) Pier 4 maximum drift ratio

Figure 9.8: IM Efficiency

Table 9.6: Summary of EDP median coefficients and record-to-record uncertainty for power-law median response model, $EDP = a IM^b$.

EDP group	EDP description	EDP symbol	efficient IM	EDP median coef. (a,b)	$\sigma_{\ln(EDP IM)}$
column	drift ratio	$C1_{[drift,max]}$	Cordova(T=0.5)	3.520e-2, 1.0318	0.327
		$C2_{[drift,max]}$	PGV	3.080e-2, 0.9867	0.401
		$C3_{[drift,max]}$	Sa(T=1.0)	3.194e-2, 0.9230	0.432
		$C4_{[drift,max]}$	PGV	4.799e-2, 1.0983	0.304
pile cap	pile cap drift (displacement)	$P0_{[drift,res]}$	CAV_5	5.567e-5, 0.9996	1.275
		$P1_{[drift,res]}$	I_a	9.908e-4, 0.6818	1.026
		$P2_{[drift,res]}$	Sa(T=0.5)	1.930e-2, 1.6540	1.266
		$P3_{[drift,res]}$	CAV_5	7.943e-7, 1.6357	0.673
		$P4_{[drift,res]}$	I_a	2.526e-4, 1.1586	0.761
		$P5_{[drift,res]}$	CAV_5	2.464e-6, 1.6554	0.687
abutment exp. joint	gap between deck and abutment	$EJ1_{[gap,max]}$	Sa(T=1.0)	7.475e-2, 0.7899	0.737
		$EJ2_{[gap,max]}$	Sa(T=1.0)	6.153e-2, 0.6047	0.715
abutment backwall	backwall displacement	$BW1_{[dx,max]}$	PGV	3.899e-1, 0.4383	0.197
		$BW2_{[dx,max]}$	PGV	5.205e-1, 0.5915	0.195
abutment approach	bridge approach vert. off-set	$BA1_{[dy,max]}$	CAV_5	5.373e-4, 0.6521	1.173
		$BA2_{[dy,max]}$	CAV_5	2.259e-4, 0.8635	0.176
bearing pad	bearing pad displacement	$BP1_{[dx,max]}$	PGV	2.874e-1, 0.8228	0.340
		$BP2_{[dx,max]}$	PGV	3.683e-1, 0.9540	0.288
embankment slope	lateral disp.	$E1_{[dx,res]}$	CAV_5	1.915e-4, 0.8484	0.874
		$E1_{[dy,res]}$	CAV_5	6.488e-4, 1.6115	0.601
	settlement	$E2_{[dx,res]}$	CAV_5	3.480e-6, 0.6601	0.168
		$E2_{[dy,res]}$	CAV_5	3.279e-4, 0.8396	0.142

9.6 Model Parameter Uncertainty

As mentioned before, an important source of uncertainty in the bridge response originates from uncertainties in the evaluation of material input parameters. The main material properties used in these analyses, such as soil shear modulus, density, friction angle, and undrained shear strength, have uncertainties that originate from several sources including: i) spatial variation of soil deposit and testing error due to randomness of test sample or location (e.g., an erratic boulder) and ii) measurement procedures and statistical error due to insufficient data. The first source is categorized as aleatory uncertainty associated with the natural randomness of the property. The second source is categorized as epistemic uncertainty related to the lack of information and shortcomings in measurement and calculation.

In this study, a list of material model parameters was considered to evaluate this uncertainty. Input parameter uncertainties was estimated based on literature reviews and judgement. Using the values of the mean \pm half of a standard deviation for each input parameter, a sensitivity study was performed, and Tornado diagrams were generated to identify the most influencing parameters. Then, First-Order Second-Moment (FOSM) analyses were conducted to estimate the parametric uncertainty of bridge system for different EDPs.

9.6.1 List of Model Parameters

Several bridge model input parameters were considered to estimate the parametric uncertainty. Shear modulus, friction angle, and undrained shear strength were considered for all soils. To evaluate the liquefaction sensitivity, one of the contraction parameters related to pore pressure generation in the PDMY material, was considered. For the various types of interface springs, initial stiffness and ultimate resistance were considered including the break-off wall capacity and bearing pad stiffness. Table 9.7 summarizes the selected parameters and their coefficient of variance (COV). The COV represents a relative measure of dispersion and is expressed for a variable, X , as

$$COV = \frac{\sigma_X}{\mu_X} \quad (9.4)$$

Table 9.7: Input Parameter Uncertainties

Parameters	used COV	Related materials or models	Comments
Shear modulus, G	0.4	embankment, clay, loose sand	geotechnical
undrained shear strength, c	0.3	upper and lower clay layer	
friction angle, ϕ	0.1	embankment, loose sand	
contraction parameter, contrac1	0.2	loose sand	constitutive
py spring (stiffness, K_1)	0.4	pile, pile cap, abutment wall	interaction spring
py spring (pult): clay	0.3	pile, pile cap	
py spring (pult): sand	0.1	pile, pile cap	
abutment earth spring (stiffness, K_2)	0.4	abutment wall	
break-off wall capacity	0.1	break-off wall in abutment	structural
bearing pad (stiffness, K_3)	0.05	bearing pad	
Shear wave velocity, V_s	0.2		indirect parameters
SPT resistance	0.3		
density	0.08		

where, σ_X is the standard deviation and μ_X is the mean. The COV values shown in the table were determined based on literature reviews and judgement. Jones et al. (2002) compiled COV values for several soil properties measured from laboratory and field tests based on studies by Harr (1987), Kulhawy (1992), Lacasse and Nadim (1996), Phoon and Kulhawy (1999), and Duncan (2000).

9.6.2 Tornado Diagrams

Relevant input parameters that can strongly influence the bridge behavior can be identified from sensitivity studies using Tornado diagrams. The parameter values described in Tables 8.3 and 8.4 for the target bridge model represent the mean values used here as base parameters. These input values were also used in the simulations performed to evaluate record-to-record uncertainty. To account for the effect of parameter uncertainty on the bridge response, each input parameter, X , was varied independently according to its own uncertainty, σ_X , while the other parameters were kept constant (i.e., mean values). For example, for a particular parameter, three values ($X_{\mu-\sigma/2}$, X_μ , and $X_{\mu+\sigma/2}$) corresponding to the mean and mean \pm half of the standard deviation were used in the numerical simulations,

while the other parameters were held at their mean values. These simulations gave three responses, $g(X_{\mu-\sigma/2})$, $g(X_\mu)$, and $g(X_{\mu+\sigma/2})$. The total number of simulations was $2N + 1$ (including the base simulation), where N is the number of considered input parameters. In a tornado diagram, the considered parameters are ordered from top to bottom by decreasing swing, which is calculated by the absolute value of the difference in two outputs, $g(X_{\mu-\sigma/2})$ and $g(X_{\mu+\sigma/2})$, for an input parameter. The response values, $g(X_{\mu-\sigma/2})$ and $g(X_{\mu+\sigma/2})$, corresponding to each parameter variation, $X_{\mu-\sigma/2}$ and $X_{\mu+\sigma/2}$, are often normalized by $g(X_\mu)$ value, which allows them to be presented as a percentage of $g(X_\mu)$. In this study, the function $g(X)$ represents the EDPs of interest. Even though the motion dependency was considered in record-to-record uncertainty, a couple of motions were used for additional simulations. This was done to account for the effect of motion characteristics and intensities on the input parameter sensitivities. The motions were selected to be close to the average response spectra for each hazard. Additionally, the Northridge 1994 motion described in section 4.3 was considered as a non-near-fault motion and its PGA was scaled to different values.

Figure 9.9 shows tornado diagrams for the horizontal slope displacements and pile curvatures for the Temblor 1966 motion at Parkfield ($a_{max} = 0.47g$, $T_R = 72$ years). The horizontal axis represents normalized maximum EDP ($g(X_{\mu-\sigma/2})/g(X_\mu)$ and $g(X_{\mu+\sigma/2})/g(X_\mu)$). The vertical axis represents the parameters ordered by swing. The figure shows that the horizontal slope displacement in the left abutment is sensitive to the variation of undrained shear strength of the clay, while the horizontal slope displacement in the right abutment is sensitive to the friction angle, clay undrained shear strength, and sand soil contraction parameter. Figures 9.9c and 9.9d show that the clay undrained shear strength controls the maximum curvatures of Pile 1 near the left slope, while the maximum curvature of Pile 4 near the right slope is sensitive to sand friction angle, clay undrained shear strength and ultimate resistance of pile cap. Overall, the clay undrained shear strength is one of the controlling parameters for most of the piles that extend through the clay. This was attributed to the fact that large shear strains were concentrated in the clay soil interface resulting in large pile curvatures. In addition, the drift of Pier 1 near the left abutment is sensitive to clay undrained shear strength and loose sand friction angle. The drift of Pier 4 next to the

right abutment slope is similarly sensitive to several parameters such as shear modulus of embankment soil and clay and ultimate resistance of pile cap.

Tornado diagrams are helpful in identifying the input parameters that control bridge response. Friction angle for the loose sand and undrained shear strength for the clay affect dominantly the bridge responses associated with lateral spreading and slope displacement. The secondary influencing parameters are soil shear modulus and pile/pile cap interface spring parameters.

9.6.3 First Order Second Moment (FOSM) Analysis

Tornado diagrams give an insight on the response sensitivity to variation of individual parameters and help engineers determine where they must put their efforts when deciding testing and exploration programs. However, Tornado diagrams do not provide quantitative estimates of uncertainty caused by parameter variation. To estimate the effect of parametric uncertainties, First-Order Second-Moment (FOSM) analyses were used. The Second-Moment represents the second central moment for a random variable, X. The First-Order represents the first order term in a Taylor series approximation used to define the relationship between an output response and input parameters. This relationship can be expressed as

$$Y = g(X_1, X_2, \dots, X_N) \quad (9.5)$$

where Y is the output response variable and X_i are the input parameters (for $i = 1$ to N).

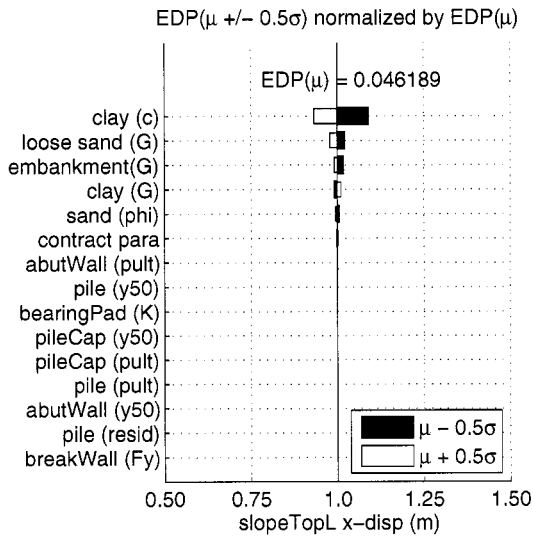
This relationship can be expanded using a Taylor series of the form

$$Y = g(\mu_{X_1}, \mu_{X_2}, \dots, \mu_{X_N}) + \frac{1}{1!} \sum_{i=1}^N (X_i - \mu_{X_i}) \frac{\partial g}{\partial X_i} + \frac{1}{2!} \sum_{i=1}^N \sum_{j=1}^N (X_i - \mu_{X_i})(X_j - \mu_{X_j}) \frac{\partial^2 g}{\partial X_i \partial X_j} + \dots \quad (9.6)$$

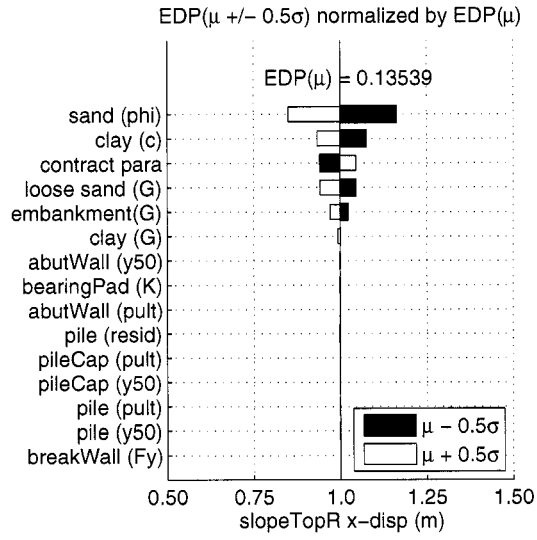
where μ_{X_i} is the mean value of i-th input parameter. Considering only the first order terms, the series can be approximated as

$$Y \approx g(\mu_{X_1}, \mu_{X_2}, \dots, \mu_{X_N}) + \sum_{i=1}^N (X_i - \mu_{X_i}) \frac{\partial g}{\partial X_i} \quad (9.7)$$

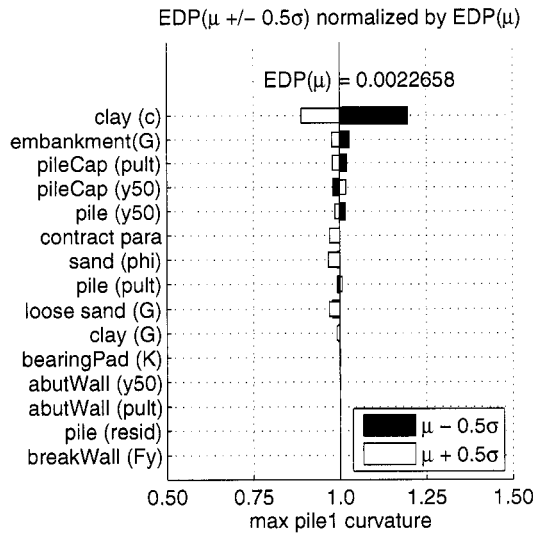
where the value of $g(\mu_{X_1}, \mu_{X_2}, \dots, \mu_{X_N})$ is the mean response (μ_Y). The mean response is obtained from the simulation where all the input parameters are set to the mean (base)



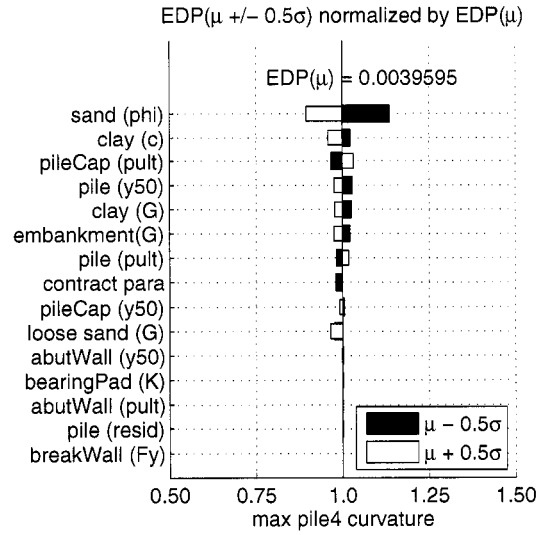
(a) Left slope horiz. displacement



(b) Right slope horiz. displacement



(c) Pile 1 max curvature



(d) Pile 4 max curvature

Figure 9.9: Tornado diagrams for four maximum EDPs: Temblor 1966 motion at Parkfield ($a_{max} = 0.47g$)

values. The variance of the output variable can be expressed as

$$\sigma_Y^2 \approx \sum_{i=1}^N \sum_{j=1}^N \text{cov}(X_i, X_j) \frac{\partial g}{\partial X_i} \frac{\partial g}{\partial X_j} \quad (9.8)$$

where $\text{cov}(X_i, X_j)$ is the covariance of X_i and X_j which can be expressed as

$$\text{cov}(X_i, X_j) = \rho_{X_i, X_j} \sigma_{X_i} \sigma_{X_j} \quad (9.9)$$

The correlation coefficient, ρ_{X_i, X_j} , varies from -1 to 1. When two variables are correlated in a positive linear relationship, the value of ρ is close to 1. For instance, if two variables are the same, $\rho = 1$ and $\text{cov}(X_i, X_i)$ becomes $\sigma_{X_i}^2$. When two variables are correlated in a negative linear relationship, then the ρ value is close to -1. If there is no correlation between two variables, ρ is zero. Therefore, Equation 9.8 can be expressed as

$$\sigma_Y^2 \approx \sum_{i=1}^N \sigma_{X_i}^2 \left(\frac{\partial g}{\partial X_i} \right)^2 + \sum_{i=1}^N \sum_{j \neq i}^N \rho_{X_i, X_j} \sigma_{X_i} \sigma_{X_j} \frac{\partial g}{\partial X_i} \frac{\partial g}{\partial X_j} \quad (9.10)$$

Using simulation results, Equation 9.10 can be used and parametric uncertainties can be evaluated. From the simulations, the mean \pm half of standard deviation of the input parameters can be expressed in terms of the COV

$$x_i^- = \mu_{x_i} - \sigma_{x_i}/2 = (1 - COV/2)\mu_{x_i} \quad (9.11)$$

$$x_i^+ = \mu_{x_i} + \sigma_{x_i}/2 = (1 + COV/2)\mu_{x_i} \quad (9.12)$$

Assuming a linear relationship between x_i^- and x_i^+ , $\frac{\partial g}{\partial X_i}$ can be approximated by a central difference equation as

$$\frac{\partial g}{\partial X_i} = \frac{g(x_i^+) - g(x_i^-)}{x_i^+ - x_i^-} = \frac{g(x_i^+) - g(x_i^-)}{COV \mu_{x_i}} = \frac{g(x_i^+) - g(x_i^-)}{\sigma_{x_i}} \quad (9.13)$$

Therefore, Equation 9.10 can be expressed as

$$\sigma_Y^2 \approx \sum_{i=1}^N \left[\frac{g(x_i^+) - g(x_i^-)}{x_i^+ - x_i^-} \right]^2 \sigma_{X_i}^2 + \sum_{i=1}^N \sum_{j \neq i}^N \left[\frac{g(x_i^+) - g(x_i^-)}{x_i^+ - x_i^-} \right] \left[\frac{g(x_j^+) - g(x_j^-)}{x_j^+ - x_j^-} \right] \rho_{X_i, X_j} \sigma_{X_i} \sigma_{X_j} \quad (9.14)$$

Since the value of $x_i^+ - x_i^-$ is equal to σ_{x_i} , this equation can be simplified as

$$\sigma_Y^2 \approx \sum_{i=1}^N [g(x_i^+) - g(x_i^-)]^2 + \sum_{i=1}^N \sum_{j \neq i}^N [g(x_i^+) - g(x_i^-)] [g(x_j^+) - g(x_j^-)] \rho_{X_i, X_j} \quad (9.15)$$

In this study, the values of the correlation coefficients (ρ_{x_i, x_j}) between input parameters were approximated as shown in Table 9.8. These values were determined approximately considering possible correlations with judgment. Most of the correlation coefficients between soil and structural parameters were set to zero.

Parametric uncertainties were obtained based on Equation 9.15 using the simulation results, $g(x_i^+)$ and $g(x_i^-)$, obtained for two variations (x_i^+ and x_i^-) of each input parameter. Since there was some variation in parametric uncertainties due to variability in the input motions, the uncertainty values were averaged. The parametric uncertainties for each EDP are presented in Table 9.9.

In this study, the sensitivity results were obtained using mean \pm half of a standard deviation input parameters. When simulation results from a sensitivity study are used in a FOSM analysis using Equation 9.14 or Equation 9.15, the response gradient over the input parameter variation ($\frac{\partial g}{\partial X_i}$) can be sometimes incorrect. This is because the tangent of the response function at the mean input parameter value sometimes is not close to the gradient based on two variations, x_i^+ and x_i^- ; especially when one value is located in the left of the peak response and the other value is located in the right of the peak values. This problem is illustrated in Figure 9.10. Therefore, for more accurate estimation of the effect of parametric uncertainties, Monte Carlo simulation can be used.

9.7 Spatial Variability Uncertainty of Soil

To investigate the spatial variability uncertainty, Gaussian stochastic random fields were generated for the clay and liquefiable soil layers by randomizing the assigned soil strength parameter over the soil layers with a certain spatial probability density. This section briefly describes the method used to prepare the stochastic fields and presents the estimated bridge response uncertainty values due to spatial variability. For this purpose 10 random field simulations for several earthquake motions were performed.

9.7.1 Spatial Variability within Homogeneous Soil Deposits

Physical properties of soils vary from place to place within a soil deposit due to varying geologic formation and loading histories such as sedimentation, erosion, transportation,

Table 9.9: Summary of parametric uncertainty

EDP symbol	Northridge (0.1g)	Northridge (0.25g)	A03 (0.46g)	B10 (0.70g)	average
$C1_{\text{[drift,max]}}$	0.018	0.040	0.401	0.075	0.134
$C2_{\text{[drift,max]}}$	0.023	0.025	0.024	0.044	0.031
$C3_{\text{[drift,max]}}$	0.013	0.042	0.029	0.042	0.031
$C4_{\text{[drift,max]}}$	0.008	0.052	0.042	0.076	0.045
$P0_{\text{[drift,res]}}$	0.062	0.064	0.090	0.056	0.068
$P1_{\text{[drift,res]}}$	0.118	0.344	0.588	0.082	0.283
$P2_{\text{[drift,res]}}$	0.784	0.060	0.041	0.653	0.384
$P3_{\text{[drift,res]}}$	0.288	0.051	0.042	0.095	0.119
$P4_{\text{[drift,res]}}$	0.219	0.035	0.029	0.065	0.087
$P5_{\text{[drift,res]}}$	0.236	0.086	0.047	0.049	0.105
$EJ1_{\text{[gap,max]}}$	0.346	0.031	0.070	0.074	0.130
$EJ2_{\text{[gap,max]}}$	0.695	0.121	0.075	0.100	0.248
$BW1_{\text{[dx,max]}}$	0.016	0.027	0.022	0.051	0.029
$BW2_{\text{[dx,max]}}$	0.010	0.012	0.018	0.056	0.024
$BA1_{\text{[dy,max]}}$	0.020	0.039	0.025	0.055	0.035
$BA2_{\text{[dy,max]}}$	0.040	0.066	0.043	0.084	0.058
$BP1_{\text{[dx,max]}}$	0.346	0.031	0.070	0.074	0.130
$BP2_{\text{[dx,max]}}$	0.695	0.121	0.075	0.100	0.248
$E1_{\text{[dx,res]}}$	0.059	0.067	0.081	0.054	0.065
$E2_{\text{[dx,res]}}$	0.019	0.034	0.022	0.049	0.031
$E1_{\text{[dy,res]}}$	0.227	0.080	0.047	0.048	0.101
$E2_{\text{[dy,res]}}$	0.035	0.063	0.039	0.080	0.054

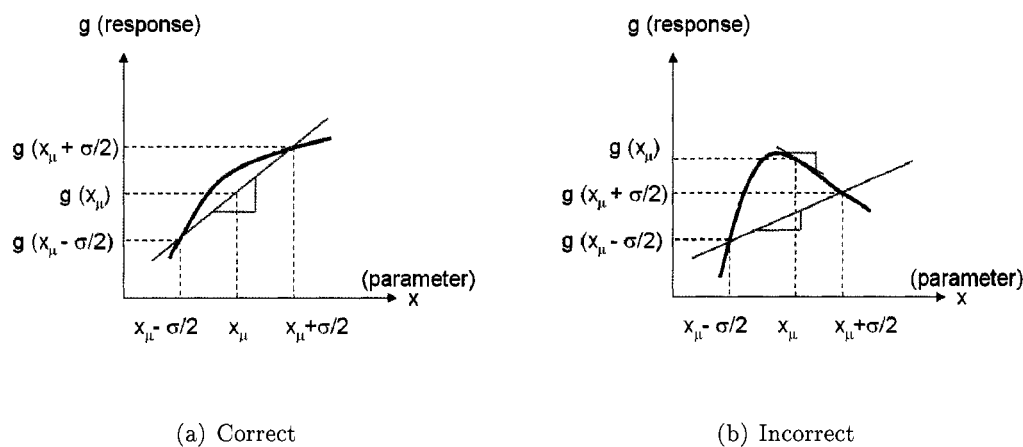


Figure 9.10: Gradient of a response over variation of a input parameter ($\frac{\partial g}{\partial X_i}$)

and weathering processes. This spatial variability in the soil properties cannot be simply described by a mean and variance since the estimation of the two statistic values does not account for the spatial variation of the soil property data in the soil profile.

Spatial variability is often modeled using two separated components: a known deterministic trend and a residual variability about the trend. These components are illustrated in Figure 9.11. The simplified spatial variability (Phoon and Kulhawy, 1999) can be expressed as

$$\xi(z) = t(z) + w(z) \quad (9.16)$$

where $\xi(z)$ = soil property at location z , $t(z)$ = deterministic trend at z , and $w(z)$ = residual variation. The trend is a smooth deterministic function that can be obtained from a regression analysis of measured data. The residuals are characterized statistically as random variables, usually with zero mean and non-zero variance. The pattern of the residuals depends on the local spatial variability of a property. The residual about a trend does not change erratically in a probabilistically independent way. Rather, similar property values (positive or negative residuals around a trend) occur together in adjacent locations characterizing the scale of fluctuation (or wave length of a residual along the trend) as shown in Figure 9.11. This spatial distribution can be described by a spatial correlation,

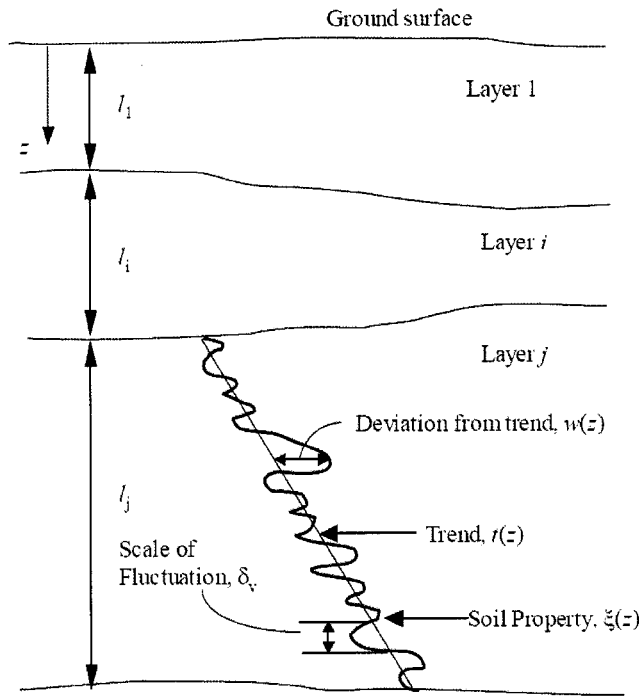


Figure 9.11: Inherent soil variability - after Phoon and Kulhawy (1999)

referred to as *autocorrelation*, which represents the correlation of an individual variable with itself over space. The autocorrelation is the property to show that residuals have a degree of association among the residual values. This degree of association can be measured by a correlation coefficient, taken as a function of separation distance. For two values of a soil property (e.g., ϕ , c , or SPT) at two locations, the correlation coefficient is defined as

$$\rho = \frac{Cov[\xi(z_1), \xi(z_2)]}{\sqrt{Var[\xi(z_1)] Var[\xi(z_2)]}} \quad (9.17)$$

where, z_1 and z_2 are two locations, $Cov[\xi(z_1), \xi(z_2)]$ is the covariance, $Var[\xi(z_1)]$ and $Var[\xi(z_2)]$ are the variances of $\xi(z_1)$ and $\xi(z_2)$, respectively. The autocorrelation of geotechnical data usually falls monotonically from 1.0 to zero with increasing separation distance. Figure 9.12 illustrates the effect of correlation on residual variation by comparing four cases with different variance and autocorrelation (Baecher and Christian, 2003). The figure shows a high variance leads to large residual magnitudes and a large autocorrelation results in long residual wave lengths.

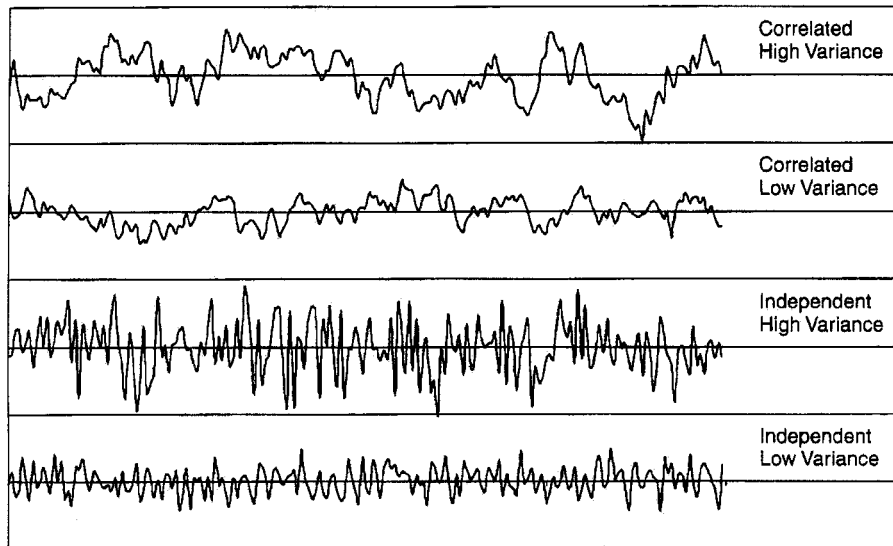


Figure 9.12: Illustration of autocorrelation effect on residual variation - after Baecher and Christian (2003)

The mathematical function that describes autocorrelation, called *autocorrelation function* is expressed as a function of separation distance, δ , as

$$R(\delta) = \frac{1}{\text{Var}[w(z)]} E[w(z_i) w(z_{i+\delta})] \quad (9.18)$$

where, $\text{Var}[w(z)]$ is the variance of the residuals across the site, and $E[w(z_i) w(z_{i+\delta})] = \text{Cov}[w(z_i) w(z_{i+\delta})]$ is the covariance of the residuals spaced at a separation distance δ . If the autocorrelation function is multiplied by the variance of the residuals, $\text{Var}[w(z)]$, the autocovariance function, $C(\delta)$, is obtained as

$$C(\delta) = E[w(z_i) w(z_{i+\delta})] \quad (9.19)$$

9.7.2 Generation of Gaussian Random Fields

This subsection introduces a procedure for generating stochastic random field based on the method outlined in Yamazaki and Shinozuka (1988) and considering uncertainties in soil properties. As explained earlier, the stochastic random field for a soil property consists

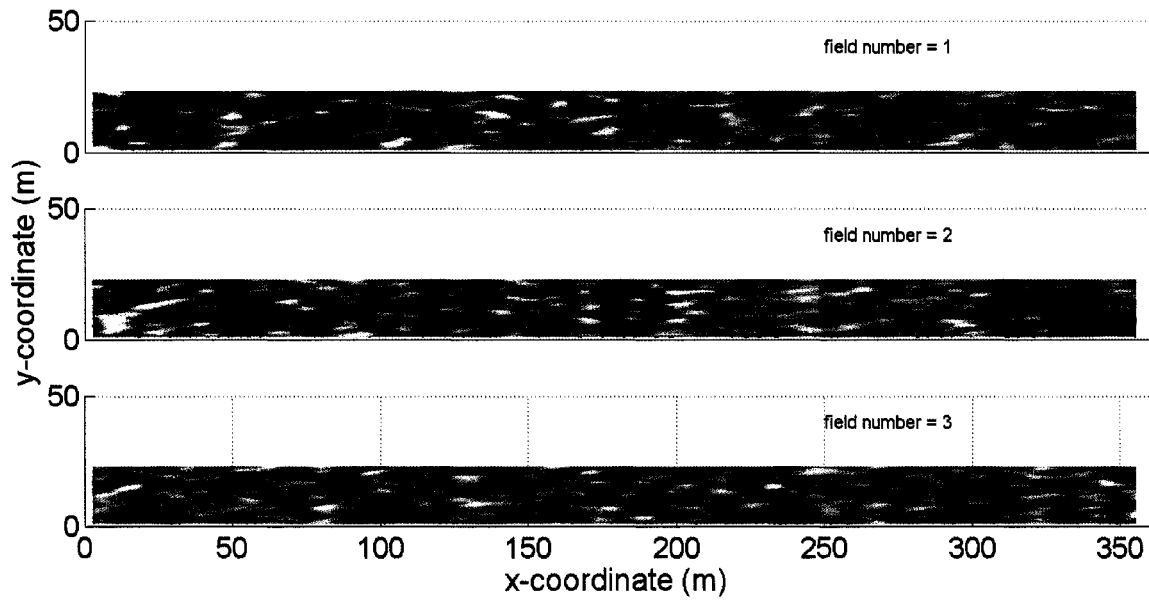


Figure 9.13: Example of generated Gaussian fields

of a trend (or mean) field and a residual field.

$$F_{stochastic} = F_{trend} + F_{residual} \quad (9.20)$$

The trend field represents the deterministic mean field shown in Tables 8.3 and 8.4. To obtain the residual field, a Gaussian random field was generated using the generation algorithm used by Yamazaki and Shinozuka (1988).

In the Gaussian field generation used in this study, the standard deviation of spectral density function was set to 1.0 and the correlation decay coefficients were set to 1.0. The wave number increment (Δk_x) in the x-direction was determined considering the ratio of the length and height of the space. Several samples of the generated Gaussian field are shown in Figure 9.13. In the numerical simulation, since individual soil elements had different soil properties, the stochastic random field was expressed in matrix form as

$$F_{stochastic}(i, j) = F_{mean}(i, j) + F_{residual}(i, j) = F_{mean}(i, j) + COV F_{mean}(i, j) F_{Gaussian}(i, j) \quad (9.21)$$

where i and j represent the element position in the horizontal and vertical directions. $F_{stochastic}$ is a matrix of stochastic random fields for a soil property, F_{mean} is a matrix of

deterministic mean fields, COV is the coefficient of variance of the considered soil property, and $F_{Gaussian}$ represents the residual Gaussian field in matrix form. The dimension of the generated field matrix was the same as that of the soil mesh used in the numerical simulations: the rectangular soil domain that includes loose sand and clay layers below ground surface and above the dense sand layer (i.e., layer 2, 3, and 4 in Figure 8.1). The generated Gaussian field could not be directly used in the simulation since values in the field were calculated for uniform incremental positions in the horizontal and vertical direction, whereas the soil mesh in the OpenSees model did not have uniform element size. Therefore, the values obtained using Yamazaki and Shinozuka (1988)'s method were interpolated according to the soil element center locations. A summary of the random field preparation procedure for the bridge FEM analysis is described below:

1. Generate mean field using mean target soil properties
2. Generate Gaussian random (autocorrelated) field for ϕ and c in loose sand and clay layers (layer numbers 2, 3, and 4 in Figure 8.1) with mean = 0.0 and $\sigma = 1.0$: Yamazaki and Shinozuka (1988)
3. Normalize the Gaussian Field by the maximum value
4. Interpolate Gaussian field to FEM mesh
5. Determine COV values for ϕ and c
6. Combine the mean field and Gaussian field to obtain a stochastic field using Equation 9.21

To illustrate the difference between deterministic and stochastic fields, a stochastic field friction angle was considered for the loose sand layer. Figure 9.14 compares the mean friction angle parameter field (F_{mean}) to the Gaussian friction angle parameter field ($F_{Gaussian}$).

9.7.3 Spatial Variability Uncertainty

To estimate the spatial variability uncertainty, 10 gaussian fields were generated following Yamazaki and Shinozuka (1988)'s method and the uncertainties of the controlling parameters found from the sensitivity study were considered, i.e., strength parameters in

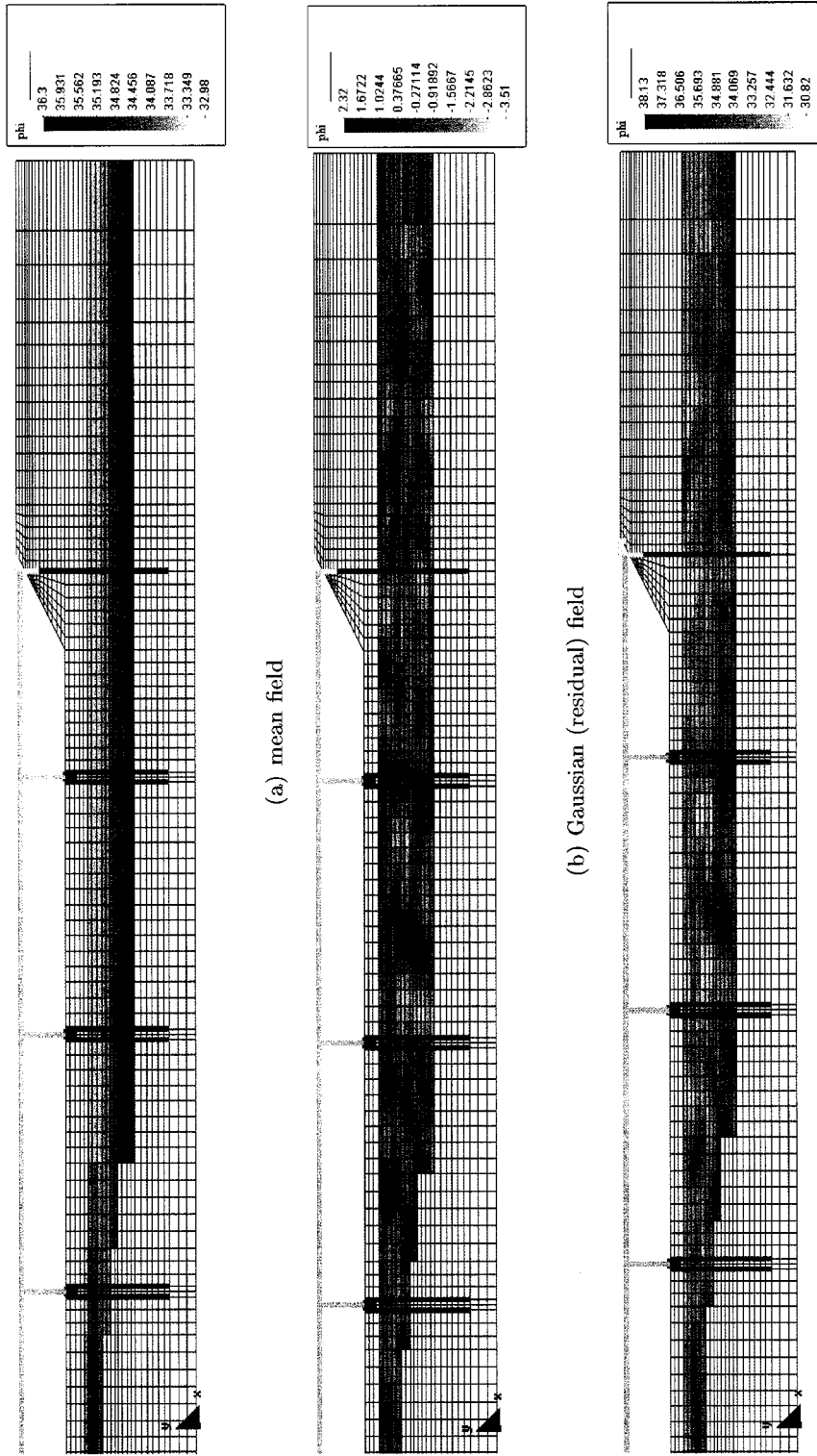


Figure 9.14: Stochastic friction angle field in loose sand layer

loose sand and clay soil. The COV values used in Equation 9.21 were 0.1 and 0.3 for loose sand friction angle and undrained shear strength of clay, respectively. When only loose sand was considered in the Gaussian field, the value of COV in the clay soil element field was set to zero so that the clay layer was assigned by the mean property values without random variation. Similarly, when only the clay soil was considered in the Gaussian field generation, the value of COV for the sand soil element field was set to zero. Using several motions corresponding to different hazard levels, the response of the bridge model based on 10 stochastic fields was obtained and the resulting spatial variability uncertainties were investigated for three cases: i) loose sand and clay, ii) only loose sand, and iii) only clay. Since there was some variation in the spatial uncertainty values due to input motions, the uncertainty values were averaged. The results are summarized in Table 9.10 to 9.12. Overall, the estimated uncertainties that originated from considering spatial variability of strength parameters in the loose sand and clay soil were small compared to record-to-record uncertainty and parametric uncertainty.

9.8 EDP Hazard Curves

This section summarizes the total EDP uncertainties obtained from record-to-record, parametric, and spatial variability uncertainties. These uncertainties were used together with IM hazard curves to obtain EDP hazard curves for several EDP groups.

9.8.1 Total Uncertainty

The total EDP uncertainties for several EDP groups were calculated using Equation 9.22 considering the uncertainties discussed in the preceding sections. These results are summarized in Table 9.13. It is observed in the table that for this case the record-to-record uncertainty dominantly contributes to the total uncertainty with an almost 90 to 95 % of ratio. The parametric and spatial variability uncertainties were about 5 to 10 % of the total uncertainty even though the spatial variability uncertainty was smaller than the parametric uncertainty.

$$\sigma_{\ln EDP|IM,total} = \sqrt{\sigma_{\ln EDP|IM,record}^2 + \sigma_{\ln EDP|IM,parameter}^2 + \sigma_{\ln EDP|IM,spatial}^2} \quad (9.22)$$

Table 9.10: Summary of spatial variability uncertainty (loose sand + clay)

EDP symbol	Northridge (0.1g)	Northridge (0.25g)	A03 (0.46g)	B10 (0.70g)	average
$C1_{[drift,max]}$	0.008	0.096	0.020	0.066	0.048
$C2_{[drift,max]}$	0.004	0.118	0.018	0.035	0.044
$C3_{[drift,max]}$	0.005	0.012	0.009	0.048	0.018
$C4_{[drift,max]}$	0.004	0.071	0.053	0.072	0.050
$P0_{[drift,res]}$	0.053	0.059	0.052	0.085	0.062
$P1_{[drift,res]}$	0.209	0.189	0.094	0.073	0.141
$P2_{[drift,res]}$	0.108	0.188	0.067	0.488	0.213
$P3_{[drift,res]}$	0.102	0.108	0.048	0.089	0.087
$P4_{[drift,res]}$	0.098	0.075	0.049	0.032	0.064
$P5_{[drift,res]}$	0.080	0.062	0.039	0.044	0.056
$EJ1_{[gap,max]}$	0.016	0.018	0.027	0.070	0.033
$EJ2_{[gap,max]}$	0.004	0.004	0.008	0.008	0.006
$BW1_{[dx,max]}$	0.002	0.005	0.005	0.019	0.008
$BW2_{[dx,max]}$	0.001	0.001	0.002	0.001	0.001
$BA1_{[dy,max]}$	0.009	0.029	0.010	0.096	0.036
$BA2_{[dy,max]}$	0.024	0.041	0.027	0.055	0.037
$BP1_{[dx,max]}$	0.012	0.079	0.016	0.040	0.037
$BP2_{[dx,max]}$	0.004	0.071	0.018	0.050	0.036
$E1_{[dx,res]}$	0.043	0.058	0.044	0.080	0.057
$E2_{[dx,res]}$	0.010	0.025	0.006	0.088	0.032
$E1_{[dy,res]}$	0.067	0.062	0.038	0.040	0.051
$E2_{[dy,res]}$	0.019	0.045	0.029	0.053	0.036

Table 9.11: Summary of spatial variability uncertainty (loose sand)

EDP symbol	Northridge (0.1g)	Northridge (0.25g)	A03 (0.46g)	B10 (0.70g)	average
$C1_{\text{[drift,max]}}$	0.003	0.019	0.015	0.026	0.016
$C2_{\text{[drift,max]}}$	0.002	0.013	0.014	0.019	0.012
$C3_{\text{[drift,max]}}$	0.003	0.008	0.007	0.011	0.007
$C4_{\text{[drift,max]}}$	0.002	0.056	0.054	0.057	0.042
$P0_{\text{[drift,res]}}$	0.005	0.040	0.027	0.044	0.029
$P1_{\text{[drift,res]}}$	0.123	0.070	0.081	0.036	0.077
$P2_{\text{[drift,res]}}$	0.095	0.083	0.058	0.233	0.117
$P3_{\text{[drift,res]}}$	0.094	0.045	0.042	0.075	0.064
$P4_{\text{[drift,res]}}$	0.089	0.049	0.046	0.036	0.055
$P5_{\text{[drift,res]}}$	0.076	0.056	0.043	0.019	0.048
$EJ1_{\text{[gap,max]}}$	0.003	0.004	0.030	0.002	0.010
$EJ2_{\text{[gap,max]}}$	0.001	0.002	0.005	0.002	0.002
$BW1_{\text{[dx,max]}}$	0.000	0.001	0.005	0.001	0.002
$BW2_{\text{[dx,max]}}$	0.000	0.000	0.001	0.000	0.000
$BA1_{\text{[dy,max]}}$	0.002	0.029	0.005	0.040	0.019
$BA2_{\text{[dy,max]}}$	0.023	0.035	0.029	0.046	0.033
$BP1_{\text{[dx,max]}}$	0.002	0.034	0.018	0.029	0.021
$BP2_{\text{[dx,max]}}$	0.001	0.064	0.022	0.023	0.028
$E1_{\text{[dx,res]}}$	0.005	0.037	0.024	0.041	0.027
$E2_{\text{[dx,res]}}$	0.002	0.024	0.004	0.031	0.015
$E1_{\text{[dy,res]}}$	0.063	0.055	0.041	0.019	0.045
$E2_{\text{[dy,res]}}$	0.017	0.038	0.030	0.045	0.033

Table 9.12: Summary of spatial variability uncertainty (clay)

EDP symbol	Northridge (0.1g)	Northridge (0.25g)	A03 (0.46g)	B10 (0.70g)	average
$C1_{[\text{drift,max}]}$	0.008	0.025	0.019	0.221	0.068
$C2_{[\text{drift,max}]}$	0.003	0.006	0.017	0.299	0.081
$C3_{[\text{drift,max}]}$	0.003	0.006	0.008	0.071	0.047
$C4_{[\text{drift,max}]}$	0.003	0.020	0.060	0.205	0.072
$P0_{[\text{drift,res}]}$	0.051	0.071	0.036	0.063	0.055
$P1_{[\text{drift,res}]}$	0.130	0.106	0.078	0.065	0.095
$P2_{[\text{drift,res}]}$	0.023	0.101	0.046	0.637	0.202
$P3_{[\text{drift,res}]}$	0.018	0.051	0.026	0.159	0.063
$P4_{[\text{drift,res}]}$	0.018	0.022	0.047	0.041	0.032
$P5_{[\text{drift,res}]}$	0.017	0.034	0.013	0.050	0.028
$EJ1_{[\text{gap,max}]}$	0.014	0.015	0.028	0.069	0.032
$EJ2_{[\text{gap,max}]}$	0.003	0.004	0.007	0.007	0.005
$BW1_{[\text{dx,max}]}$	0.002	0.004	0.005	0.018	0.007
$BW2_{[\text{dx,max}]}$	0.000	0.001	0.001	0.001	0.001
$BA1_{[\text{dy,max}]}$	0.009	0.023	0.009	0.098	0.035
$BA2_{[\text{dy,max}]}$	0.006	0.018	0.006	0.029	0.015
$BP1_{[\text{dx,max}]}$	0.012	0.036	0.010	0.219	0.069
$BP2_{[\text{dx,max}]}$	0.003	0.042	0.005	0.199	0.062
$E1_{[\text{dx,res}]}$	0.042	0.069	0.030	0.060	0.050
$E2_{[\text{dx,res}]}$	0.010	0.018	0.006	0.090	0.031
$E1_{[\text{dy,res}]}$	0.015	0.032	0.012	0.044	0.026
$E2_{[\text{dy,res}]}$	0.005	0.014	0.007	0.025	0.013

Table 9.13: Summary of total EDP uncertainty - percentage is calculated by the ratio of individual uncertainty to total uncertainty

EDP symbol	efficient IM	record-to-record uncertainty	parametric uncertainty	spatial uncertainty	total EDP uncertainty
$C1_{[drift,max]}$	Cordova(T=0.5)	0.327 (84%)	0.134 (14%)	0.048 (2%)	0.356
$C2_{[drift,max]}$	PGV	0.401 (98%)	0.031 (1%)	0.044 (1%)	0.404
$C3_{[drift,max]}$	Sa(T=1.0)	0.432 (99%)	0.123 (1%)	0.018 (0%)	0.434
$C4_{[drift,max]}$	PGV	0.311 (95%)	0.104 (2%)	0.050 (3%)	0.311
$P0_{[dx,res]}$	CAV_5	1.275 (99%)	0.068 (1%)	0.062 (0%)	1.278
$P1_{[dx,res]}$	I_a	1.026 (91%)	0.283 (7%)	0.141 (8%)	1.073
$P2_{[dx,res]}$	Sa(T=0.5)	1.266 (89%)	0.384 (8%)	0.213 (3%)	1.340
$P3_{[dx,res]}$	CAV_5	0.673 (95%)	0.119 (4%)	0.087 (1%)	0.689
$P4_{[dx,res]}$	I_a	0.761 (98%)	0.087 (1%)	0.064 (1%)	0.769
$P5_{[dx,res]}$	CAV_5	0.687 (97%)	0.105 (2%)	0.056 (1%)	0.697
$EJ1_{[gap,max]}$	Sa(T=1.0)	1.043 (97%)	0.130 (3%)	0.033 (0%)	0.749
$EJ2_{[gap,max]}$	Sa(T=1.0)	0.348 (89%)	0.248 (11%)	0.006 (0%)	0.756
$BW1_{[dx,max]}$	PGV	0.197 (97%)	0.029 (2%)	0.008 (2%)	0.199
$BW2_{[dx,max]}$	PGV	0.195 (98%)	0.024 (1%)	0.001 (0%)	0.196
$BA1_{[dy,max]}$	CAV_5	0.173 (92%)	0.035 (4%)	0.036 (4%)	0.180
$BA2_{[dy,max]}$	CAV_5	0.176 (86%)	0.058 (10%)	0.037 (4%)	0.189
$BP1_{[dx,max]}$	PGV	0.340 (86%)	0.130 (13%)	0.037 (1%)	0.365
$BP2_{[dx,max]}$	PGV	0.288 (57%)	0.248 (42%)	0.036 (1%)	0.381
$E1_{[dx,res]}$	CAV_5	0.874 (84%)	0.065 (14%)	0.057 (2%)	0.878
$E2_{[dx,res]}$	CAV_5	0.601 (98%)	0.031 (1%)	0.032 (1%)	0.603
$E1_{[dy,res]}$	CAV_5	0.168 (99%)	0.101 (1%)	0.051 (0%)	0.203
$E2_{[dy,res]}$	CAV_5	0.142 (95%)	0.054 (2%)	0.036 (3%)	0.156

9.8.2 EDP Hazard Estimation Using a Closed Form

Using the IM hazard curves and the estimated total EDP uncertainties, EDP hazard curves were obtained using the PEER PBEE framework; either using numerical integration or the previously described assumptions in closed form. Since the uncertainties in EDP estimation were based on assumptions of a constant lognormal probability distribution of EDP residual to median along IMs, the EDP hazard curve could be obtained in closed

form (Jalayer 2003). To do this it was additionally assumed: i) the IM hazard curve followed a power law as expressed in Equation 3.14 and ii) the EDP-IM relationship can be approximated by a power law relationship as expressed in Equation 3.12. The closed form can be expressed as

$$\lambda_{EDP} = k_0 \left[\frac{EDP}{a} \right]^{-k/b} \exp\left[\frac{1}{2} \frac{k^2}{b^2} \sigma_{\ln EDP|IM, total}^2 \right] \quad (9.23)$$

or

$$\lambda_{EDP} = c (EDP)^d \quad (9.24)$$

where the coefficient $c = k_0 a^{k/b} \exp\left[\frac{1}{2} \frac{k^2}{b^2} \sigma_{\ln EDP|IM, total}^2 \right]$ and $d = -\frac{k}{b}$. The coefficients k_0 and k are the coefficient and exponent of the power law that defines the IM hazard curve. Looking more closely at Equation 9.23, the first term can be seen to represent the median relationship between IM and EDP (in the inverted form $IM = \left(\frac{EDP}{a}\right)^{1/b}$) and the second represents an *uncertainty-based amplification* function. This exponential term takes on a value of 1.0 when the uncertainty in EDP|IM is zero, and values greater than 1.0 when uncertainty in EDP|IM exists. For the hazards under consideration, the corresponding values for several IMs are presented in Table 9.4. The coefficients a and b represent the coefficient and exponent of the power law that defines the median EDP-IM relationship. Corresponding values for the EDPs under consideration in this study are presented in Table 9.6. Total uncertainties in EDP estimation for several EDPs are presented in Table 9.13. Values for the coefficients c and d are presented in Table 9.14 with the EDP range obtained from the simulations.

Figure 9.15 presents EDP hazard curves for maximum Pier 4 drift and residual Pile Cap 4 lateral displacement. From the EDP hazard curve, for example, it is expected that Pier 4 and Pile Cap 4 can have 4.6 % of drift ratio and 50 cm of residual lateral displacement every 475 years, respectively. The EDP values that correspond to each return period (75, 475, and 2475 years) are summarized in Table 9.15. In the figure, EDP hazard curves based on zero uncertainty in EDP estimation are plotted together with those obtained using the total EDP uncertainties showing the uncertainties from earthquake and soil result in larger EDP values for a return period. For example, the Pile Cap 4 lateral displacement is expected to

Table 9.14: Summary of EDP hazard curve: exponential coefficients

EDP symbol	coefficient c	coefficient d	EDP range
$C1_{[drift,max]}$	7.8354e-07	-2.5698	0.2 - 9.7 (%)
$C2_{[drift,max]}$	4.2444e-07	-2.4978	0.2 - 8.8 (%)
$C3_{[drift,max]}$	1.2170e-06	-2.2352	0.2 - 13.1 (%)
$C4_{[drift,max]}$	2.1292e-06	-2.2439	0.3 - 13.8 (%)
$P0_{[drift,res]}$	5.7960e-04	-2.3869	0.000 - 0.562 (m)
$P1_{[drift,res]}$	1.0018e-04	-2.0973	0.001 - 0.502 (m)
$P2_{[drift,res]}$	1.2409e-04	-2.1365	0.000 - 0.346 (m)
$P3_{[drift,res]}$	1.6531e-04	-1.4586	0.001 - 0.527 (m)
$P4_{[drift,res]}$	9.0295e-04	-1.2342	0.000 - 1.198 (m)
$P5_{[drift,res]}$	1.0782e-03	-1.4413	0.001 - 1.866 (m)
$EJ1_{[gap,max]}$	1.2992e-05	-2.6119	0.004 - 0.567 (m)
$EJ2_{[gap,max]}$	3.4581e-06	-3.4115	0.004 - 0.217 (m)
$BW1_{[dx,max]}$	8.4257e-08	-8.0652	0.000 - 0.667 (m)
$BW2_{[dx,max]}$	1.1128e-10	-11.382	0.000 - 0.317 (m)
$BA1_{[dy,max]}$	1.0650e-07	-3.6588	0.013 - 0.125 (m)
$BA2_{[dy,max]}$	7.6176e-06	-2.7629	0.015 - 0.274 (m)
$BP1_{[dx,max]}$	2.2324e-04	-1.8777	0.004 - 0.589 (m)
$BP2_{[dx,max]}$	4.8268e-04	-1.7349	0.003 - 0.997 (m)
$E1_{[dx,res]}$	5.8392e-05	-2.8123	0.003 - 0.563 (m)
$E2_{[dx,res]}$	9.7270e-04	-1.4806	0.002 - 1.840 (m)
$E1_{[dy,res]}$	3.1000e-07	-3.6142	0.015 - 0.178 (m)
$E2_{[dy,res]}$	1.0355e-05	-2.8483	0.018 - 0.293 (m)

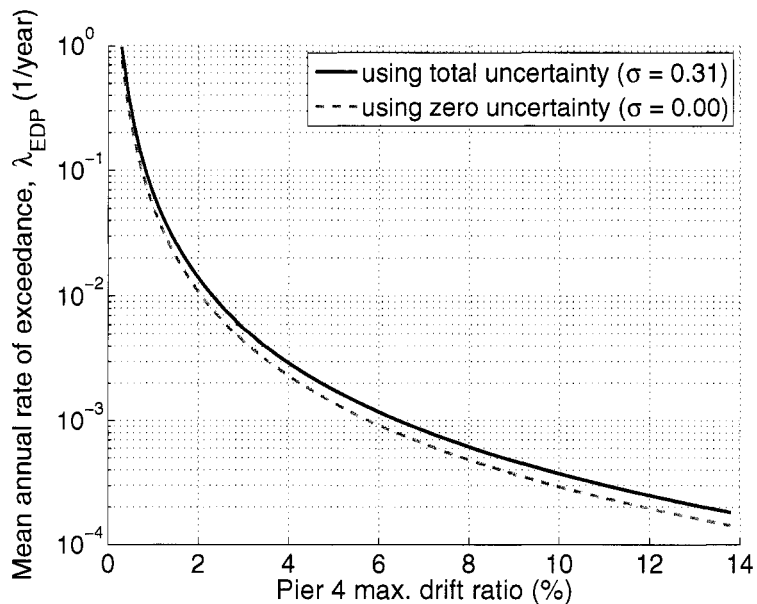
Table 9.15: Summary of EDP at different return periods

EDP symbol	T_R = 75 years	T_R = 475 years	T_R = 2475 years
$C1_{[drift,max]}$	2.2217 (%)	4.6296 (%)	8.8005 (%)
$C2_{[drift,max]}$	1.5576 (%)	3.3150 (%)	6.4194 (%)
$C3_{[drift,max]}$	1.5303 (%)	3.5592 (%)	7.4486 (%)
$C4_{[drift,max]}$	1.9955 (%)	4.6260 (%)	9.6536 (%)
$P0_{[drift,res]}$	0.2643 (m)	0.5825 (m)	1.1632 (m)
$P1_{[drift,res]}$	0.0952 (m)	0.2341 (m)	0.5143 (m)
$P2_{[drift,res]}$	0.1099 (m)	0.2658 (m)	0.5755 (m)
$P3_{[drift,res]}$	0.0479 (m)	0.1748 (m)	0.5419 (m)
$P4_{[drift,res]}$	0.1092 (m)	0.5037 (m)	1.9185 (m)
$P5_{[drift,res]}$	0.1698 (m)	0.6286 (m)	1.9758 (m)
$EJ1_{[gap,max]}$	0.0692 (m)	0.1426 (m)	0.2682 (m)
$EJ2_{[gap,max]}$	0.0878 (m)	0.1527 (m)	0.2477 (m)
$BA1_{[dy,max]}$	0.0400 (m)	0.0670 (m)	0.1051 (m)
$BA2_{[dy,max]}$	0.0660 (m)	0.1307 (m)	0.2376 (m)
$BP1_{[dx,max]}$	0.1108 (m)	0.3027 (m)	0.7291 (m)
$BP2_{[dx,max]}$	0.1442 (m)	0.4279 (m)	1.1079 (m)
$E1_{[dx,res]}$	0.1429 (m)	0.2795 (m)	0.5027 (m)
$E2_{[dx,res]}$	0.1660 (m)	0.5936 (m)	1.8101 (m)
$E1_{[dy,res]}$	0.0516 (m)	0.0870 (m)	0.1374 (m)
$E2_{[dy,res]}$	0.0798 (m)	0.1548 (m)	0.2763 (m)

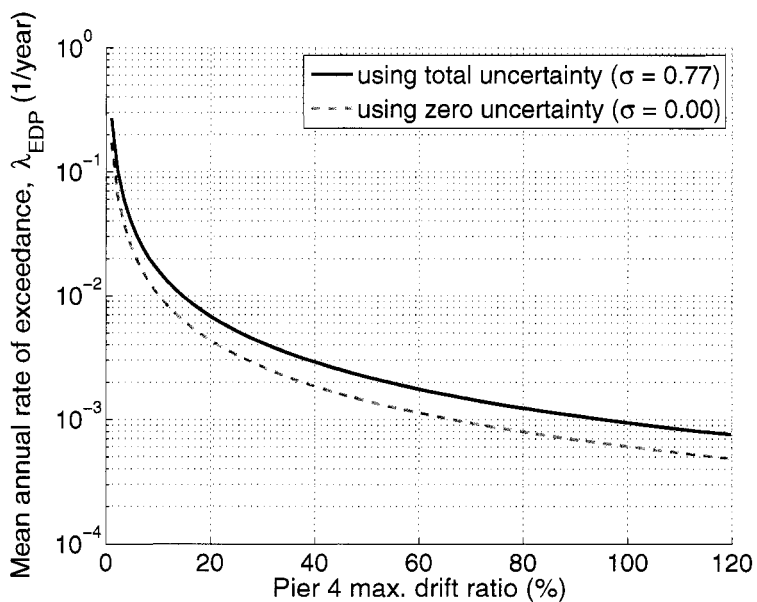
be 50 cm and 35 cm for 475 years of return period resulting in more conservative design due to the uncertainty. This also represents the importance of efficient IM.

9.8.3 IM Efficiency and EDP Hazard Curve

The uncertainty in EDP estimation and its efficiency are reflected in the mean annual rate of the EDP exceedance in EDP hazard curves. Equation 9.23 shows that the term including the uncertainty ($\sigma_{\ln EDP|IM}$) amplifies the mean annual rate of EDP exceedance. To illustrate this effect, Figure 9.16 shows EDP hazard curves for the maximum drift ratio in Pier 4 and the lateral residual displacement in Pile Cap 4 with different IMs. For the maximum drift in Pier 4, *PGV* gives the lowest mean annual rate of exceedance and



(a) Maximum Pier 4 drift



(b) Residual Pile Cap 4 lateral displacement

Figure 9.15: EDP hazard curves for maximum Pier 4 drift and residual Pile Cap 4 lateral displacement

is the most efficient IM for this case. For the lateral residual displacement in Pile Cap 4, CAV_5 gives the lowest mean annual rate of exceedance. The mean annual rate of exceedance of each EDP hazard curve is consistent with IM efficiency. For example, the Pier 4 maximum drift ratio hazard curves presented in the Figure 9.16 shows lower mean annual rate of exceedance in the order such as PGV , Cordova($T=0.5\text{sec}$), I_a , CAV_5 , $Sa(T=1.0\text{sec})$, PGA , and $Sa(T=0.5\text{sec})$. This order is consistent with the efficiency order shown in Figure 9.8b. The plot demonstrates that an efficient IM produces equally conservative performance estimations (at given mean annual rates of occurrence) at lower EDP levels. Since designs are generally based on EDPs, the use of efficient IMs allows more economical designs without any reduction in safety. This study shows the importance of evaluating IM efficiency.

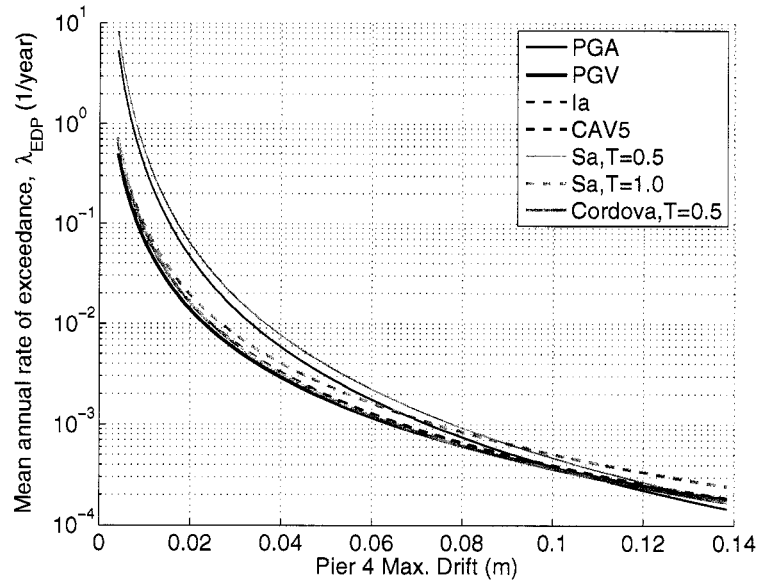
9.9 Summary and Conclusions

The PEER Performance Based Earthquake Engineering (PBEE) methodology was applied to a typical Caltrans highway bridge founded on liquefiable soil and subjected to lateral spreading. The model was subjected to 40 earthquake motions representing four different hazard levels.

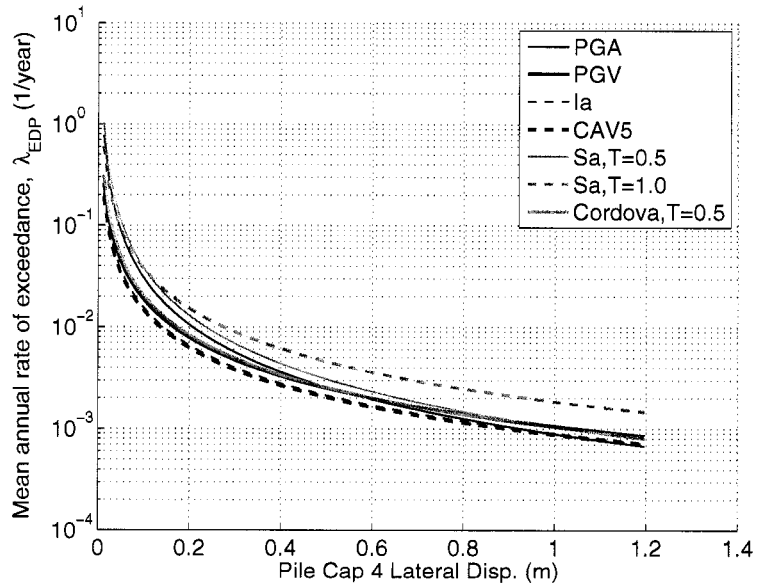
9.9.1 Uncertainties in EDP Estimation

In the process of EDP hazard curve estimation, several sources of uncertainties were addressed including: record-to-record uncertainties, parametric uncertainties, and spatial variability uncertainties. To estimate the record-to-record uncertainty, the bridge model was subjected to 40 near-fault motions corresponding to four hazard levels in a cloud analysis approach. The record-to-record uncertainty was obtained from the residuals obtained from EDP-IM regression relationships. In the uncertainty estimation, the efficiency of several IMs was investigated with respect to structural and geotechnical EDPs. CAV_5 was found to be an efficient IMs for lateral spreading related EDPs such as slope displacement or movement of pile caps near slopes.

To estimate the parametric uncertainty, variation of 16 input parameters were considered in a sensitivity analysis. Tornado diagrams showed that strength parameters such as sand friction angle and clay undrained shear strength were the most influential parameters.



(a) Maximum Pier 4 drift



(b) Residual Pile Cap 4

Figure 9.16: Effect of IM efficiency on EDP hazard curves

Initial stiffness and ultimate resistance of interface spring belonged to a secondary group of influencing parameters. The parametric uncertainty was obtained using First-Order Second-Moment analysis as an approximate estimation. Finally, to estimate the spatial variability uncertainty, stochastic fields for the clay and loose sand layers were generated considering strength parameter variability.

By combining the uncertainties, total uncertainties for several EDPs were obtained. Record-to-record uncertainty appeared to be the most dominant uncertainty among the three uncertainties (about 90 to 95 % of the total uncertainty). The parametric and spatial variability uncertainties were secondary contributors (accounting for about 5 to 10 % of the total uncertainty).

9.9.2 Integration of Uncertainty through PEER PBEE Framework

In this dissertation, EDP hazard curves were developed for several bridge EDPs integrating the (total) uncertainties in bridge performance estimation with the seismic hazard curve. The integration was performed in closed form assuming: i) the lognormal probability distribution of EDP residual to median is constant along the IMs, ii) the IM hazard curve follows a power law, and iii) the EDP-IM relationship can be approximated by a power law relationship.

The IM hazard curves and EDP hazard curves corresponding to the most efficient IMs for each EDP were expressed in an exponential form. The results of the hazard curves, EDP-IM median relationship, EDP uncertainties, range of EDP values for each EDP were summarized.

Chapter 10

**SUMMARY, CONCLUSIONS AND RECOMMENDATIONS FOR
FUTURE RESEARCH****10.1 Introduction**

Many bridges are subjected to damage during earthquakes. The pattern and severity of this damage varies from column failures and bridge deck collapse due to joint unseating to pile and abutment foundation failure due to lateral spreading. In these problems, soil-pile-structure interaction (SPSI) plays an important role. SPSI is affected by soil conditions (e.g., competent soil and liquefiable soil) and loading conditions (e.g., earthquake intensity, motion characteristics, and shaking direction).

In this context, two bridges with different soil conditions and loading conditions were considered in this research focusing on key aspects of SPSI. One is a two-span portion of a bridge supported by drilled shafts embedded in a competent soil (dry dense sand). The other represents a typical five-span highway bridge system supported by pile groups embedded in liquefiable soils and subjected to lateral spreading.

To better understand SPSI in soil-bridge systems, numerical simulations were performed in OpenSees to capture the response recorded in centrifuge experiments and the Beam-on-Nonlinear-Winkler-Foundation (BNWF) modeling approach was validated as a tractable model to capture the dynamic response of soil-structure systems. Further, an approximate SPSI method, here referred as *Equivalent Cantilever Method*, was investigated and used for the analysis of a calibrated reinforced concrete bridge.

A numerical model of a complete bridge system was developed to understand the global behavior of bridges subjected to lateral spreading. Using a comprehensive numerical model,

bridge performance hazards were estimated considering several sources of uncertainties in a Performance Based Earthquake Engineering (PBEE) framework.

10.2 Summary and Conclusions

The results and findings that emerge from this research on the seismic response of bridges are summarized considering various SPSI aspects and applications; including: i) understanding of dynamic SPSI of bridge structures embedded in a competent soil and validation of BNWF models, and ii) evaluation of the seismic response of a complete bridge subjected to lateral spreading and estimation of bridge performance hazards considering several sources of uncertainties using the PEER PBEE framework.

10.2.1 Understanding of Dynamic SPSI of Bridge Structures in a Competent Soil and Validation of BNWF Models

Soil-pile-structure interaction of drilled-shaft-supported bridge structures were investigated by performing three centrifuge tests and numerical simulations using OpenSees. In this study, conditions that can be encountered in a bridge structure design, or analysis, were considered using various motions with varying intensity and frequency contents. The study included: i) a two-span bridge embedded in soil with varying ground surface elevation, ii) bent structures subjected to different orientations of shaking, and iii) several bent and single pile structures with different pile embedment lengths. These scenarios were aimed to investigate the effect of higher nonlinear soil-pile-structure interaction or the superstructure response.

Centrifuge Experiments of Bridge Structures

The centrifuge two-span bridge, bents and single piles were supported by drilled shaft foundations installed in fairly good soil conditions (i.e, dry dense sand). The individual bents had different clear heights above the ground surface due to varying ground surface elevation across the bridge. When earthquakes motions were applied in the transverse di-

rection, this soil configuration mobilized different lateral stiffness at each column resulting in twisting of the bridge structure. This mode of deformation increased the demand on the outmost drilled shafts.

When the two-column bents were subjected to shaking with various orientations, the translation mode dominated the structural response and twisting had a minor effect. The bent with a 30-degree angle with respect to the direction of shaking (Bent-30) had a similar response as the bent with 0 degree angle (Bent-00). Bent-60 showed high frequency components in the superstructure response that were associated with superstructure rocking.

Three single piles with varying pile embedment lengths (12D, 7.5D, and 5D) were shaken with different motions. The piles with long and medium embedment lengths showed similar response indicating that the existence of the pile below 8D did not contribute to the dynamic superstructure response for this particular soil condition.

Two-column bents (Bent-LL-Hy and Bent-SS-Hy) with long and short pile embedment lengths (12D and 5D) were considered. In these structures, the superstructure mass was increased to induce larger nonlinear response. The superstructure response was slightly different depending on motion intensity indicating more nonlinear effects due to increased motion and superstructure mass.

With the idea of generating more twisting, different pile embedment lengths (12D and 5D) were considered with two different superstructure masses (Bent-LS-Hy and Bent-LS-Lt). Even with different pile embedment lengths, the translational mode of the superstructure dominated and twisting was small. The heavier structure showed very similar response in both pile locations. The lighter bent showed high frequencies in the response associated with superstructure rocking.

Numerical Simulation of Centrifuge Experiments

The bridge structures studied in the centrifuge experiments were simulated using OpenSees BNWF models. To capture the six degrees-of-freedom response, three-dimensional (3-D) nonlinear models were used together with transverse and longitudinal p - y springs. For these cases, 1-D shear beam soil models were coupled to the structure through p - y springs.

Using the Pressure Dependent Multi-Yield elasto-plastic material model available in OpenSees, the soil response in the centrifuge container could be captured reasonably well for motions with various intensities. The 2-D soil model used to represent the centrifuge container gave slightly better results than the 1-D soil model. The natural period of soil in the centrifuge container was investigated by evaluating the transfer function between the base and soil at 2.6 m depth. The centrifuge test transfer function was compared with the transfer functions obtained using 1-D shear beam and 2-D soil container models. The natural period of the soil in the centrifuge test (0.67 sec) was longer than that obtained from the OpenSees eigenvalue analysis (0.52 sec for 2-D model and 0.48 sec for 1-D model based on the soil condition before shaking). Particularly, the natural period of the 1-D shear beam soil model was shorter indicating a slightly stiffer soil system. The transfer function obtained using the 2-D soil model captured very well the recorded centrifuge response.

The OpenSees bent simulation results were in good agreement with the centrifuge results in terms of superstructure acceleration and pile bending moments. The response of the single pile structure was also well captured, especially in terms of superstructure acceleration. However, the simulated single pile maximum bending moments near the ground surface were underestimated for strong shaking and frequency sweeping shaking.

The numerical model developed for the two-span bridge structure and the oriented bents captured well the centrifuge response for various motions, including bridge twisting and superstructure rocking, and maximum bending moment distribution.

The superstructure response and pile force of Bent-LL-Hy and Bent-SS-Lt were well captured in OpenSees for moderate shaking. However, for the sweeping frequency motion ($a_{max}=0.41g$), both responses were underestimated. The three single pile superstructure centrifuge responses were well captured in OpenSees. However, the maximum bending moments were overall underestimated. The results of the long-and-short-embedment-length bent structures subjected to longitudinal shaking were well captured in OpenSees. However, the acceleration of the heavy superstructure was underestimated for the frequency sweeping motions resulting in smaller maximum pile bending moments.

Overall, the simulation results for the bent structures subjected to the longitudinal direction of shaking (Bent-LS-Hy and Bent-LS-Lt) and single piles (sPile-L, sPile-M, and sPile-S) showed similar response (i.e., good estimation of superstructure acceleration, but underestimation of pile force for Northridge motions). However, the heavier structure (Bent-LS-Hy) response subjected to a sweeping motion was underestimated with OpenSees. Similarly, the simulation results for the heavy bent structure subjected to the transverse direction of shaking (Bent-LL-Hy and Bent-SS-Hy) was underestimated for frequency sweeping motion; even though the simulation results were well predicted for the Northridge motion.

From the comparison of centrifuge and simulation results, it was concluded that the BNWF models are capable of providing reasonably good estimation of the seismic behavior of a bridge structure supported by drill shaft foundations embedded in good soil conditions (i.e., uniform dry dense sand) and for earthquake motions with various intensity levels.

Sensitivity Studies on Bent and Single Pile

To understand the effect of soil-pile-structure interaction in this bridge structure and to obtain more confidence on the use of conventional p - y spring parameter assignments, parametric studies were performed using OpenSees considering the effect of soil motion and p - y spring stiffness and ultimate resistance on superstructure and pile response. Two pile

bents and single pile structure were considered in this study.

The natural period of the soil-foundation system was investigated by evaluating the transfer function between the soil and superstructure motions. From the study, it was found that the natural period of the soil-foundation system plays an important role on SPSI in bridge structures. The frequency content of the soil motion was founded to be significantly related to the structure response depending on the natural period of the soil-pile system. One interesting aspect obtained from this study was that the natural period of the soil-structure system varied with the mobilized system nonlinearity ; which was affected by motion characteristics and intensity. For example, the natural periods of the bent and single pile subjected to moderate shaking ($a_{max} = 0.25g$) were about 1.0 second and 2.5 second, respectively. However, for the frequency sweeping motion ($a_{max} = 0.41g$), the natural periods became 1.2 second and 3.2 second (about 15% and 30% increase), respectively. To investigate the natural period variation during shaking, eigenvalue analyses were performed in OpenSees at every time step for a single pile structure. For moderate shaking, the natural period increased from 2.0 sec to 2.3 sec (15% increase) during shaking. For strong shaking, the natural period increased from 2.0 sec to 2.7 sec (35% increase).

To change the soil motion, various soil masses and stiffness were used. The bent and single pile response was insensitive to the change of soil motion for moderate and strong shaking. This is because the frequency range that was affected by the changed in soil motion was not close to natural period of the soil-structure system. This observation was more evident in the single pile structure whose natural period was longer.

The p - y spring parametric study was conducted considering different p - y spring stiffness and ultimate resistances. Parameters were increased and decreased by 20 % with respect to the base model parameters. To investigate the depth at which p - y springs plays an important role on the superstructure response, several cases were considered, including: near-surface region (from the surface to 3D depth), deep region (below 3D depth), and full pile embedment depth. The change of p - y spring parameters at larger depths did not affect the superstructure and pile response. When the near-surface and full depth regions were

considered, the superstructure response was very similar.

The p - y stiffness parameter change did not affect the superstructure accelerations for moderate and strong shaking. However, the maximum bending moments and shear forces were slightly affected by the stiffness change. For the single pile cases, the effect of the p - y initial stiffness was less sensitive than for the bent structure. The change in p - y spring ultimate resistance did not affect the superstructure response at the bent and single pile structure for moderate and strong shaking. Particularly, the peak superstructure acceleration was only slightly changed. However, the bending moment and shear force distributions were influenced. When the ultimate resistance was decreased, the maximum bending moment (i.e, zero shear force) location moved deeper.

From the sensitivity study, it was concluded that the bent and single pile superstructure response was insensitive to changes of soil ground motion and initial stiffness and ultimate resistance of p - y spring. The change of ultimate resistance slightly affected the bending moment distribution in the pile. Therefore, conventional p - y spring parameters for this particular structure and soil condition (uniform dry dense sand) can be used with less concern. A source for this insensitivity was found to be the hyperbolic characteristics of the p - y curve envelope which shows a plateau after reaching ultimate resistance without any hardening. Another conclusion from the study was that the frequency content of the base or soil motion was significantly related to the structure response depending on the natural period of the soil-pile system. The natural period of the bridge system became longer due to soil (or p - y spring) nonlinearity.

Evaluation of Equivalent Cantilever Approach Using a Calibrated Prototype Bridge

A prototype bridge model was developed coupling i) the soil and p - y spring models verified in the centrifuge test study and ii) a reinforced concrete bridge structure model

calibrated by Ranf (2007) using experimental data from large shaking table tests (Johnson et al., 2006) and strong wall tests (Makido, 2007). Using the prototype reinforced concrete bridge model, the *equivalent cantilever* approach was evaluated and the location of the fixity depth was investigated considering four hazard motions. From the simulation of the two-span prototype bridge subjected to shaking with various intensities, maximum bending moments were observed at 3.0D to 3.5D depth. From the equivalent cantilever model simulations, it was observed that for weak shaking, the fixity depths that give accurate prototype bridge response (maximum shear force) were about 3D to 3.5D. For strong shaking, the optimal fixity depths were located at around 2.5D to 3D. From the study, it was concluded that reasonable dynamic SPSI results can be obtained using 2.5D to 3.5D fixity depths for uniform dry dense sand conditions. In addition, dynamic simulations using the calibrated prototype and fixed bridge model showed that the equivalent depth-to-fixity and depth-to-maximum-moment evaluated from Chai (2002)'s method were very similar to the optimal fixity depths and provide a good estimation of maximum column shear force.

10.2.2 Evaluation of Seismic Soil-Pile-Bridge-Abutment Interaction of a Complete Bridge Subjected to Lateral Spreading and Estimation of Bridge Performance Hazards Using the PBEE Framework

The PEER Performance-Based Earthquake Engineering (PBEE) methodology was applied to a typical Caltrans highway bridge founded on liquefiable soil and subjected to lateral spreading. A complete geotechnical bridge system finite element model, including abutment structures and pile foundations embedded in realistic soils was developed and coupled to a well-defined bridge structural model (Mackie and Stojadinovic 2003). The model was subjected to 40 earthquake motions representing four hazard levels.

The study showed the importance of understanding the global bridge behavior. In addition, by including several sources of uncertainties in the PBEE framework, the seismic bridge performance could be evaluated using a probabilistic approach demonstrating a logical and useful way to be considered in conventional design and analysis of earthquake problems.

Importance of Global Bridge Behavior

Appropriate modeling of soil-pile-structure interaction and soil-abutment-bridge interaction under lateral spreading helped identify realistic force boundary conditions at the pier base and bridge deck ends. Using this model, the global behavior of the bridge system could be better understood and important EDPs could be identified. This study showed that the global response of a soil-foundation-bridge system is quite complex, particularly when soft and/or liquefiable soils are present. The use of a detailed OpenSees model provided improved understanding of the global response, and allowed the identification of damage mechanisms that would not be captured using the simplified analyses commonly used in contemporary practice.

Effect of Lateral Spreading on Global Bridge Behavior

An important global bridge behavior identified in this study was the abutment-to-abutment interaction through the bridge deck caused by different levels of lateral spreading and its effect on the drift of the bridge piers near slopes. Since the amount of lateral spreading in the right abutment was considerably greater than that in the left abutment, the entire bridge deck moved towards to the left abutment. At the same time, lateral spreading pushed the pile cap of the pier near the right slope to the left, so the column drift was smaller. On the other hand, the pier near the left slope was subjected to large column drifts because the bridge deck moved to the left and the pile cap at the bottom of the column moved to the right due to lateral spreading of the left abutment.

Uncertainties in EDP Estimation

In the process of EDP estimation, several sources of uncertainties were considered including: record-to-record uncertainty, parametric uncertainty, and spatial variability uncertainty. For the record-to-record uncertainty, the bridge model was subjected to 40 near-fault motions corresponding to four hazard levels using a cloud analysis approach. The record-to-record uncertainty was obtained using EDP residuals with respect to the linear median which was obtained from EDP-IM relationships in log-log space; assuming a constant log-

normal probability distribution of EDP residual to median along IMs. In the uncertainty estimation, the efficiency of several IMs was investigated for structural and geotechnical EDPs. CAV_5 was found to be an efficient IM for lateral spreading related EDPs, such as slope displacement or movement of pile caps near slopes.

To evaluate the parametric uncertainty, sensitivity analyses were performed considering the variation of 16 input parameters and Tornado diagram were generated. The Tornado diagrams showed that strength parameters, such as friction angle and undrained shear strength, were the most influencing parameters. Soil stiffness and interface spring ultimate resistance appeared to be secondary influencing parameters. The parametric uncertainty was obtained using First-Order Second-Moment analyses. Finally, for the spatial variability uncertainty, stochastic fields for the clay and loose sand strength parameters were generated using Yamasaki and Shinozuka (1988)'s method.

By combining the uncertainties, total uncertainties for the EDPs were obtained. Record-to-record uncertainty appeared to be the most dominant uncertainty among the three uncertainties considered (about 90 % to 95 % of the total uncertainty). The parametric uncertainty showed a secondary effect (about 5 to 10 % of the total uncertainty) and the spatial variability uncertainty was found to be a minor contributor to total uncertainty.

Integration of Uncertainty through PEER PBEE Framework

EDP hazard curves were developed for several bridge EDPs integrating the (total) EDP uncertainties and the seismic hazard curve. The integration was performed in closed form. The IM hazard curves and EDP hazard curves for the most efficient IMs for each EDP were expressed in an exponential form. The results of the hazard curves, EDP-IM median relationship, uncertainties, range of EDP values for each EDP were summarized.

10.3 Recommendations for Future Research

The centrifuge experiments and their numerical simulations have provided many important conclusions for bridge soil-pile-structure interaction and validated the BNWF model for dynamic bridge structure response estimation. The study of a complete bridge on liquefiable soil has also helped us understand the global bridge behavior and allowed us to estimate bridge performance hazards following the PEER PBEE framework.

Besides these achievements, this research has also challenged us to consider the potential use of these validated and comprehensive numerical tools to better understand SPSI in bridges. Nevertheless, there are still some limitations and challenges to improve and overcome in bridge numerical modeling. In this context, the author suggests several recommendations for future research on these topics.

10.3.1 Recommendations for SPSI Study of Soil-Bridge System in Competent Soil Conditions

The use of the dynamic Beam-on-Nonlinear-Foundation simplification (BNWF) with conventional p - y spring has been verified for the seismic Soil-Pile-Structure Interaction (SPSI) of a bridge structure founded in good soil conditions. The study has improved the confidence on using this approach for dynamic bridge structure response estimation and p - y parameter assignment. The following ideas can be considered as an extension of this research:

1. The laterally loaded pile often shows gapping between pile and soil. This phenomenon may influence SPSI since the near-surface soil resistance can strongly affect the superstructure response and pile force. In this context, the BNWF approach can be used to investigate the dynamic response of the bridge system where gapping between pile and soil is developed. The gapping effect can be modeled using the p - y spring material available in OpenSees.

2. The location of fixity depths for two-column bents, that provide reasonable SPSI simplifications, have been evaluated using the *equivalent cantilever* method for various intensity motions. This study can be considered for bent and single pile structures which have different aboveground heights and different soil conditions.
3. The two-span bridge model can be expanded to a full bridge that includes abutment structures that could be used to understand the response of bridges in the transverse direction.

10.3.2 Recommendations for Complete Soil-Bridge System Modeling and Its Use in PBEE Applications

The study on seismic bridge performance has shown the usefulness of the PEER PBEE approach, especially for bridges subjected to lateral spreading. The results have encouraged to move forward to a complete demonstration of the PEER PBEE methodology including damage and repair cost evaluation. Further, a more practical application of the PBEE methodology to bring decision makers and stakeholder to various decision options is needed to demonstrate the benefits of the PEER PBEE methodology.

1. The bridge damage mechanism observed in the comprehensive numerical simulation has shown that lateral spreading is one of the most influencing factors on seismic bridge behavior. However, the amount of lateral spreading can be affected by pinning due to the existence of the pile foundation in the embankment slopes. In this context, more research is required to better understand the foundation pinning effect and to reduce the numerical uncertainty. For example, appropriate choice of soil element out-of-plane thickness in 2-D finite element analysis can be obtained from experimental tests and 3-D embankment slope simulations.
2. A complete application of the full PEER PBEE framework, from the seismic hazard to the cost risk, is necessary to demonstrate the applicability of the PBEE methodology. In this context, the repair cost of the structural and geotechnical damage should

be evaluated for a total bridge repair cost. To evaluate the structural damage and repair cost, the bridge structure damage/repair cost evaluation procedure proposed by Mackie et al. (2006) can be followed; since the same bridge model was used in both their study and this research. This will allow us to compare the damage cost of a bridge embedded in good soil and in liquefiable soil. To evaluate geotechnical damage/repair costs, especially for the pile foundation, reasonable damage and repair cost fragility curves should be established based on professional judgement and surveys to experts.

3. The most important product of a PEER PBEE analysis is the risk curve. To bring decision makers and stakeholder decision options for a planned or existing bridge design, a practical PBEE methodology should be established to demonstrate the benefits of the PBEE approach. One good example could be to use the PBEE framework to evaluate retrofitting options for an existing bridge susceptible to lateral spreading, so that decision makers are informed of the cost-effective retrofit strategies or the need for a new structure.

BIBLIOGRAPHY

- Abdoun T., Dobry R., O'Rourke T.O., and Goh S.H. (2003). Pile response to lateral spreads: Centrifuge modeling. *Journal of Geotechnical and Geoenvironmental Engineering, ASCE*, Vol. 129(No. 10):869–878.
- API (1993). Recommended practice for planning, designing and constructing offshore platforms. API Recommended Practice 2A (RP 2A), 20th Edition, Washington, D.C.
- Arulanandan R., Boulanger R.W., Kutter B.L., and Sluis W.K. (2000). New tool for shear wave velocity measurements in model tests. *Geotechnical testing journal*, Vol. 23(No. 4): 444–453.
- Baecher G.B. and Christian J.T. (2003). *Reliability and Statistics in Geotechnical Engineering*. Prentice-Hall.
- Barton Y.O. and Finn W.D.L. (1983). Lateral pile response and p-y curves from centrifuge tests. *Proceedings of the 15th Annual Offshore Technology Conference, Houston, Texas*, (Paper 4502):503–508.
- Berber T.M. and Rollins K.M. (2005). Lateral subgrade moduli for liquefied sand under cyclic loading. *Seismic Performance and Simulation of Pile Foundations in Liquefied and Laterally Spreading Ground, Geotechnical Special Publication*, (No. 145):149–160.
- Berry M.P. and Eberhard M.O. (2003). Performance models for flexural damage in reinforced concrete columns. PEER Report No. 2003/18. Pacific Earthquake Engineering Research Center, University of California, Berkeley.
- Boulanger R.W., Chang D., Gulerce U., Brandenburg S.J., and Kutter B.L. (2005). Evaluation pile pinning effects on abutments over liquified ground. *Seismic Performance and Simulation of Pile Foundations in Liquefied and Laterally Spreading Ground, Geotechnical Special Publication*, (No. 145):306–318.
- Boulanger R.W., Curras C.J., Kutter B.L., D.W. Wilson, and A. Abghari (1999). Seismic soil-pile-structure interaction experiments and analysis. *Journal of Geotechnical and Geoenvironmental Engineering, ASCE*, Vol. 125(No. 9):750 – 759.
- Boulanger R.W., Wilson D.W., Kutter B.L., Brandenburg S.J., and Chang D. (2004). Non-linear fe analysis of soil-pile-interaction liquefying sand. *Proceedings, Geotechnical Engineering for Transportation Projects, Geotechnical Special Publication*, (No. 126):470–478.
- Brandenber S.J., Boulanger R.W., Kutter B.L., and Chang D. (2005). Behavior of pile foundations in laterally spreading ground during centrifuge tests. *Journal of Geotechnical and Geoenvironmental Engineering, ASCE*, Vol. 131(No. 11):1378–1391.

- Brandenberg S.J. (2005). *Behavior of Pile Foundations in Liquefied and Laterally Spreading Ground*. PhD thesis, University of California, Davis.
- Briaud J.-L. and Smith T.D. (1983). Using the pressuremeter curve to design laterally loaded piles. *Proceedings of the 15th Annual Offshore Technology Conference, Houston, Texas*, (Paper 4502):495–502.
- Broms B.B. (1964). Lateral resistance of piles in cohesionless soils. *Journal of Soil Mechanics and Foundations Division*, Vol. 90(SM3):123–156.
- Broms B.B. (1964). Lateral resistance of piles in cohesive soils. *Journal of Soil Mechanics and Foundations Division*, Vol. 90(SM2):27–63.
- Brown D.A., Morrison C., and Reese L.C (1988). Lateral load behavior of pile group in sand. *Journal of Geotechnical and Geoenvironmental Engineering, ASCE*, Vol. 114(No. 11):1261–1276.
- Caltrans (2004). Caltrans seismic design criteria.
- Castello R.R. (1980). *Bearing Capacity of Driven Piles in Sand*. PhD thesis, Texas AM University, College Station, Texas.
- Chai Y.H. (2002). Flexural strength and ductility of extended pile-shafts. i: Analytical model. *Journal of Structural Engineering*, Vol. 128(No. 5):586 – 594.
- Chai Y.H. and Hutchinson T.C. (2002). Flexural strength and ductility of extended pile-shafts. ii: Experimental study. *Journal of Structural Engineering*, Vol. 128(No. 5):595 – 602.
- Cordova P. (2000). Development of a two-parameter seismic intensity measure and probabilistic seismic assessment procedure. PEER Report No.2000/10, 195-214. Pacific Earthquake Engineering Research Center, University of California, Berkeley.
- Cornell C. A. and Krawinkler H. (2000). Progress and challenges in seismic performance assessment. *PEER News, April*, pages 1 – 3.
- Coyle H. and Castello R. (1981). New design correlations for piles in sand. *Journal of Geotechnical Engineering Division, ASCE*, Vol. 107(No. GT7).
- Coyle H.M and Sulaiman I.H. (1967). Skin friction for steel piles in sand. *Journal of the Soil Mechanics and Foundation Division, ASCE*, Vol. 93(No. Sm-6).
- Curras C.J., Boulanger R.W., Kutter B.L., and Wilson D.W. (2001). Dynamic experiences and analysis of a pile-group-supported structure. *Journal of Geotechnical and Geoenvironmental Engineering, ASCE*, Vol. 127(No. 7):585–596.
- Deierlein G.G., Krawinkler H., and Cornell C.A. (2003). A framework for performance-based earthquake engineering. *Proceedings, 2003 Pacific Conference on Earthquake Engineering*.

- Dobry R., Taboada V., and Liu L. (1995). Centrifuge modeling of liquefaction effects during earthquakes. *Proc. 1st Intl. Conf. on Earthquake Geotechnical Engineering*, K. Ishihara, ed., Tokyo, Japan, Vol 3:1291–1324.
- Duncan J.M. (2000). Factors of safety and reliability in geotechnical engineering. *Journal of Geotechnical and Geoenvironmental Engineering*, ASCE, Vol. 126(No. 4):307–316.
- Fleming W.G.K., Weltman A.J., and Randolph M.F. (1992). *Piling engineering*. Surrey University Press, London.
- Gazetas G. and Mylonakis G. (1998). Seismic soil-structure interaction: New evidence and emergin issues. *Geotechnical Earthquake Engineering and Soil Dynamics III, Geotechnical Special Publication*, Vol 2(No. 75):1119–1174.
- Gerolymos N. and Gazetas G. (2005). Phenomenological model applied to inelastic response of soil-pile interaction systems. *Soil and Foundations*, Vol. 45(No. 4):119–132.
- Hamada M. (1992). Large ground deformatons and their effects on lifelines: 1964 niigata earthquake. *Case Studies of Liquefaction and Lifeline Performance During Past Earthquakes, Japanese Case Studies*. Technical Report NCEER-92-0001, NCEER, Buffalo, NY, USA., Vol (1), 3.1-3.123.
- Harr M.E. (1987). *Reliability-Based Design in Civil Engineering*. McGraw-Hill.
- He L., Elgamal A., Abdoun T., Dobry R., Meneses J., Sato M., and Tokimatsu K. (2006). Lateral load on piles due to liquefaction-induced lateral spreading during one-g shake table experiments. *Proceedings of 8th National Conference on Earthquake Engineering, San Francisco, August 2006*.
- Hose Y., Silva P., and Seible F. (2000). Development of a performance evaluation database for concrete bridge components and systems under simulated seismic loads. *Earthquake Spectra*, Vol. 16(No. 2):413 – 442.
- Ilnkatharan M., Kutter B., Shin H., Arduino P., and Kramer S.L. (2007). A demonstration of nees system for studying soil-foundation-structure interaction: Centrifuge data report for test series mil02. and Enviromental Engineering, University of California, Davis, California.
- Ilnkatharan M., Kutter B., Shin H., Arduino P., and Kramer S.L. (2007). A demonstration of nees system for studying soil-foundation-structure interaction: Centrifuge data report for test series mil03. and Enviromental Engineering, University of California, Davis, California.
- Ilnkatharan M., Kutter B.L., Shin H., Arduino P., Kramer S.L., Johnson N., and Sasaki T. (2006). Comparison of centrifuge and 1g shake table models of a pile supported bridge structure. *Proceedings of the International Conference on Physical Modeling in Geotechnics, August*.

- Ilankatharan M., Sasaki T., Shin H., Kutter B., Arduino P., and Kramer S.L. (2005). A demonstration of nees system for studying soil-foundation-structure interaction: Centrifuge data report for test series mil01. Rep. No. UCD/CGMDR-05/05, Ctr. for Geotech. Modeling, Dept. of civil and Enviromental Engineering, University of California, Davis, California.
- Jalayer F. (2003). *Direct probabilistic Seismic Analysis: Implementating non-linear dynamic assessments*. PhD thesis, Stanford University, Stanford, California.
- Johnson N., Saiidi M., and Sanders D. (2006). Large-scale experimental and analytical seismic studies of a two-span reinforced concrete bridge system. Technical Report CCEER-06-02, University of Nevada, Reno.
- Jones A.L., Kramer S.L., and Arduino P. (2002). Estimation of uncertainty in geotechnical properties for performance-base earthquake engineering. PEER Report No.2002/16, Pacific Earthquake Engineering Research Center, University of California, Berkeley.
- JRA (2002). Specifications for highway bridges. Japan Road Association, Preliminary English Version, prepared by Public Works Research Institute (PWRI) and Civil Engineering Research Laboratory (CRL), Japan, November.
- Juirnarongrit T. and Ashford S.A. (2004). Analyses of pile responses based on results from full-scale lateral spreading test: Tokachi blast experiment. *Proceedings of 13th World Conference on Earthquake Engineering, Vancouver, Canada, August 1-6*.
- Kawamata Y., Ashford S.A., and Juirnarongrit T. (2006). Numerical simulation of deep foundations subjected to lateral spreading for tokachi blast test. *Proceedings of 8th National Conference on Earthquake Engineering, San Francisco, August 2006*.
- Kerisel J. (1964). Deep foundations, basic experimental facts. Proceedings, Conference on Deep Foundations, Mexican Society of Soil Mechanis, Mexico City, Mexico, Vol.1, p.5.
- Ketchum M., Chang V., and Shantz T. (2004). Influence of design ground motion level on highway bridge cost. PEER Lifelines Project Number 6D01 Report, Pacific Earthquake Engineering Research Center, University of California, Berkeley.
- Kramer S.L. (1996). *Geotechnical Earthquake Engineering*. Prentice-Hall.
- Kramer S.L. (2006). Personal communications.
- Kramer S.L. and Mitchell R.A. (2006). Ground motion intensity measures for liquefaction hazard evaluation. *Earthquake Spectra*, Vol. 22(No. 2).
- Krawinkler H. (2002). A general approach to seismic performance assessment. *Proceedings, International Conference on Advances and New Challenges in Earthquake Engineering Research (ICANCEER), Hong Kong*.
- Krawinkler H. and Miranda E. (2004). Performance-based eathquake engineering. In Bozorgnia Y. and Bertero V., editors, *Earthquake Engineering from Engineering Seismology to Performance-Based Earthquake Engineering*. CRC Press.

- Kulhawy F.H. (1992). On the evaluation of static soil properties. *ASCE Geotechnical Special Publication*, (No. 31):95–115.
- Lacasse S. and Nadim F. (1996). Uncertainties in characterizing soil properties (plenary), uncertainty in the geologic environment, from theory to practice. *Proceeding of Uncertainty '96, Geotechnical Special Publication No.58*.
- Ledzma C.A. and Bray J.D. (2006). Peer bridge design of piles under the abutment.
- Ledzma C.A. and Bray J.D. (2006). Peer bridge pile design report.
- Luco N. and Cornell C.A. (2001). Structure-specific scalar intensity measures for near-source and ordinary earthquake ground motions. *Earthquake Spectra*. Submitted for publication.
- Mackie K and Stojadinovic B. (2003). Seismic demands for performance-based design of bridges. PEER Report No. 2003/16. Pacific Earthquake Engineering Research Center, University of California, Berkeley.
- Mackie K and Stojadinovic B. (2005). Simplified application of the peer methodology. <http://dodo.ce.berkeley.edu/mackie/Yr8/>.
- Mackie K., Wong J-M., and Stojadinovic B. (2004). Method for post-earthquake highway bridge repair cost estimation. *Proceedings of 5th National Seismic Conference on Bridges and Highways, San Mateo, CA*.
- Mackie K.R. and Stojadinovic B. (2005). Comparison of incremental dynamic, cloud, and stripe methods for computing probabilistic seismic demand models. *In Proceedings of the 2005 ASCE Structures Congress, April 20-24, New York, NY*.
- Makido A. (2007). *Behavior of Spirally Reinforced Concrete Columns under Load Reversals*. PhD thesis, Purdue University.
- Maroney B.H. (1995). *Large scale bridge abutment tests to determine stiffness and ultimate strength under seismic loading*. PhD thesis, University of California, Davis, CA.
- Matlock H (1970). Correlations for design of laterally loaded piles in soft clay. *Proceedings of the II Annual Offshore Technology Conference, Houston, Texas*, (OTC 1204):577–594.
- Mokwa R.L. (1999). *Investigation of the Resistance of Pile Caps to Lateral Loading*. PhD thesis, Virginia Polytechnic Institute.
- Mosher R.L (1984). Load transfer criteria for numerical analysis of axially loaded piles in sand. US Army Engineering Waterways Experimental Station, Automatic Data Processing Center, Vicksburg, Mississippi.
- NAVFAC (1982). Foundations and earth structures design manual 7.2. Department of the Navy, Naval Facilities Engineering Command, Alexandria, VA.
- Novak M. (1974). Dynamic stiffness and damping of piles. *Canadian Geotechnical Journal, ASCE*, Vol. 11:574–598.

- O'Neill M.W. and Reese L.C (1999). Drilled shafts: construction procedures and design methods. Report FHWA-HI-88-042, US Department of Transportation, Federal Highway Administration, Office of Implementation, McLean, Virginia.
- Ovesen N.K. (1964). Anchor slabs, calculation methods and model tests. *Bulletin No. 16*. The Danish Geotechnical Institute, Copenhagen.
- Parker Jr., Fl and Reese L.C. (1969). Experimental and analytical studies of behavior of single piles in sand under lateral and axial loading. Research Report 117-2, Center for Highway Research, University of Texas, Austin, TX.
- Peck R.B., Hanson W.E., and Thornburn T.H. (1974). *Foundation engineering, 2nd Edn.* New York, Wiley.
- Petek K.A. (2006). *Development and Application of Mixed Beam-Solid Models for Analysis of Soil-Pile Interaction Problems*. PhD thesis, University of Washington.
- Phoon K. and Kulhawy F.H. (1999). Characterization of geotechnical variability. *Canadian Geotechnical Journal, ASCE*, Vol. 36:625–639.
- Poulos H.G. and Davis E.H. (1980). *Pile foundation analysis and design*. Wiley, New York.
- Randolph M.F. (1981). The response of flexible piles to lateral loading. *Geotechnique*, Vol. 31(No. 2):247–259.
- Ranf R.T. (2007). *Model Selection for Performance-Based Earthquake Engineering*. PhD thesis, University of Washington.
- Reese L.C., Allen J.D., and Hargrove J.Q. (1981). Laterally loaded piles in layered soils. *Proceedings of the tenth international conference on soil mechanics and foundation engineering, Stockholm, Vol 2, 819-822, 15-19 June*.
- Reese L.C., Cox W.R., and Koop F.D. (1974). Analysis of laterally loaded piles in sand. *Proceedings of the 6th Offshore Technology Conference, Houston, Texas, (2(OTC2080))*: 473–485.
- Reese L.C., Cox W.R., and Koop F.D. (1975). Field testing and analysis of laterally loaded piles in stiff clay. *Proceedings of the 7th Offshore Technology Conference, Houston, Texas, (2(OTC2312))*:672–690.
- Reese L.C. and Van Impe W.F. (2001). *Single Piles and Pile Groups Under Lateral Loading*. A. A. Balkema, Rotterdam.
- Rollins K.M., T.M. Gerber, Lane D., and Ashford S.A. (2005). Lateral resistance of a full-scale pile group in liquefied sand. *Journal of Geotechnical and Geoenvironmental Engineering, ASCE*, Vol. 131(No. 1):115–125.
- SDC (2004). Caltrans seismic design criteria.
http://www.dot.ca.gov/hq/esc/earthquake_engineering/SDC/SDCPage.html.

- Seed H.B. (1986). Design problems in soil liquefaction. *Journal of Geotechnical Engineering, ASCE*, Vol. 113(No. 8):827–845.
- Seed H.B. and Harder L.F. (1990). Spt-based analysis of cyclic pore pressure generation and undrained residual strength. *Proceedings, H. Bolton Seed Memorial Symposium*, University of California, Berkeley, Vol. 2, pp 351-376.
- Seed H.B and Idriss I.M. (1970). Soil moduli and damping factors for dynamic response analyses. Report EERC 70-10, Earthquake Engineering Research Center, University of California, Berkeley.
- Somerville P. G. (2000). Characterizing near fault ground motion for the design and evaluation of bridges. *Proceedings of the Third National Seismic Conference and Workshop on Bridges and Highways*.
- Stark T.D. and Mesri G. (1992). Undrained shear strength of sands for stability analysis. *Journal of Geotechnical Engineering, ASCE*, Vol. 118(No. 11):1727–1747.
- Suzuki H., Tokimatsu K., and Ozawa G. (2006). Evaluation of group pile effects in non-liquefied and liquefied ground based on centrifuge model tests. *Proceedings of 8th National Conference on Earthquake Engineering, San Francisco, August 2006*.
- Tokimatsu K., Suzuki H., and Suzuki Y. (2001). Back-calculated p-y relation of liquefied soils from large shaking table tests. *Fourth International Conference on Recent Advances in Geotechnical Earthquake Engineering and Soil Dynamics*, (Paper No. 6.24):672–690. S. Prakash ed.
- Vesic A.S. (1970). Tests on instrumented piles, ogeechee river site. *Journal of the Soil Mechanics and Foundations Division, ASCE*, Vol. 96(SM2):pp 561– 584.
- Vijayvergiya V.N (1997). Load-movement characteristics of piles. Proceedings of the Ports 77 Conference, Long Beach, California, ASCE.
- Wang S.-T. and Reese L.C. (1998). Design of pile foundation in liquefied soils. *Geotechnical Earthquake Engineering and Soil Dynamics III, Geotechnical Special Publication*, Vol 2 (No. 75):1331–1343.
- Weaver T.J., Ashford S.A., and Rollins K.M. (2005). Response of 0.6 m cast-in-steel-shell pile in liquefied soil under lateral loading. *Journal of Geotechnical and Geoenvironmental Engineering, ASCE*, Vol. 131(No. 1):94–102.
- Wilson D.W. (1998). *Soil-Pile-Superstructure Interaction in Liquefying Sand and Soft Clay*. PhD thesis, University of California, Davis.
- Wilson D.W., Boulanger R.W., and Kutter B.L. (2000). Observed seismic lateral resistance of liquefying sand. *Journal of Geotechnical and Geoenvironmental Engineering, ASCE*, Vol. 126(No. 10):898–906.
- Wood D.M. (2004). *Geotechnical Modeling, Applied Geotechnis Volume 1*. Spon Press.

- Wood S.L., Anagnos T., Eberhard M.O., Fenves G.L., Finholt T.A., Futrelle B., J.M. Jeremic, Kramer S.L., Kutter B.L., Matamoros A.B., McMullin K.M., Ramirez E.M., J.A. Rathje, Saiidi Sanders D.H. Stokoe K.H., M., and Wilson D.W. (2004). Using nees to investigate soil-foundation-structure interaction. *Proceedings of 13th World Conference on Earthquake Engineering, Vancouver, Canada, August 1-6.*
- Yamazaki F. and Shinozuka M. (1988). Digital generation of non-gaussian stochastic fields. *Journal of Engineering Mechanics, ASCE*, Vol. 114(No. 7):1183–1197.
- Yang Z., Elgamal A., and Parra E. (2003). Computational model for cyclic mobility and associated shear deformation. *Journal of Geotechnical and Geoenvironmental Engineering, ASCE*, Vol. 129(No. 12):1119–1127.
- Zhang L., Silva F., and Grismala R. (2005). Ultimate lateral resistance to piles in cohesionless soils. *Journal of Geotechnical and Geoenvironmental Engineering*, Vol. 131(No. 1):78 – 83.

Appendix A

SENSITIVITY OF TWO-COLUMN BENT AND SINGLE PILE STRUCTURES

The response of the bridge components in the centrifuge was well captured in OpenSees using the BNWF models based on conventional p - y springs and 1-D shear beam soil columns. The reasonably well predicted global response results from the combination of several model components including: i) soil model which generates the correct free-field motion, ii) soil-pile interface spring model, and iii) the structural model which captures the nonlinear structural behavior. To gain confidence on this simplified modeling approach, a sensitivity study on the response of each component is necessary. In this context several questions were addressed to better understand soil-pile-structure interaction in bridge structures. Among them are:

- How sensitive is the superstructure response to the ground soil response?
- Is the sensitivity the same for bents and single piles?
- How much is the structure response influenced by p - y parameters (stiffness and ultimate resistance)?
- How much does the p - y parameter variation with depth affect the superstructure response?
- How much is the structure and soil response affected by motion intensity and nonlinearity?
- The sPile-1 simulations captured well the superstructure response but underestimated the the maximum bending moment near the surface. The two-span bridge simulations also captured well the superstructure response but failed to reproduce the soil resistance distributions back-calculated from experimental data (Figure 5.25). How can we explain then these discrepancies?

To find answers to these questions a sensitivity study was performed considering various values of soil and p - y parameters for bents and single piles.

A.0.3 Base Model

To perform the sensitivity study a base model was considered. The soil properties of the base model were the same as the parameters used in the centrifuge simulations presented in earlier chapters. The reference shear modulus of the soil was estimated to be 910,000 kPa using impulse shear wave velocity measurements as shown in Figure 5.1. The soil (inertial) mass was increased by 30 % of the original soil density (1.66 Mg/m^3) to account for the presence of the centrifuge flexible container ring mass. In OpenSees, the p - y spring elements use API recommendations. The main parameters required to define the p - y curve are the initial stiffness and ultimate resistance. To define the initial stiffness, y_{50} , (i.e., the displacement that corresponds to half of the ultimate soil resistance) was used. The ultimate resistances (p_{ult}) at different depths is determined following Reese's (1974) method and the y_{50} values are obtained solving API's hyperbolic tangent expression as shown in Equation 4.1 at each corresponding depth. In OpenSees, about 5 % of numerical damping associated with Rayleigh damping and Newmark integration parameters ($\alpha = 0.6$ and $\beta = 0.3$) was used to match the centrifuge test results. The soil element out-of-plane thickness was determined as 40 times the pile diameter (40D) to ensure the generation of freefield motions and to avoid a large vertical stress discontinuity in the soil column; which occurs at the pile tip location due to the vertical weight of the structure. The base model parameters are summarized in Table A.1 together with structure types and input motions. In the sensitivity study, the bent and single pile models used in CFG2 were considered. Various motions with different intensity and frequency content were used in the analysis.

A.0.4 Parameter Variation

The purpose of this sensitivity study was mainly to investigate the effect of the variation in soil motion and p - y parameters on the bridge bent response. To modify the soil motion, several soil shear moduli and densities were considered in the simulations. In this study,

Table A.1: Structures, motions, and base variable values used in sensitivity study

Structure type	Single pile Two-column bent
Input motion	Moderate Northridge (peak 0.25g, ID = MIL02-11) Strong Northridge (peak 0.74g, ID = MIL02-13) Frequency sweeping (peak 0.41g, ID = MIL02-16)
Base model parameters	Reference soil shear modulus (G_r) = 910,000 kPa (Inertial) Soil density (ρ) = $1.66 + 0.3 \times 1.66$ p - y curves (y_{50} and p_{ult}) based on API (1993) Numerical damping: around 5 % Soil element out-of-plane thickness: 40 D

three cases that generated different soil motions were analyzed, including: i) base soil model, ii) a soil model with increased density, and iii) a soil model with increased density and shear modulus. In the second model, a $1.5 \times 1.66 \text{ Mg/m}^3$ soil mass was used (15 % increased base density) keeping the same base shear modulus. The soil parameters used in the third soil model were a 130,000 kPa reference shear modulus and $2.0 \times 1.66 \text{ Mg/m}^3$ soil mass. This was done in an effort to find soil properties that provided a soil response closest to that recorded in the centrifuge, even though these values were not physically close to those corresponding to the centrifuge soil. In this study, the soil properties were changed independently of the p - y spring parameters.

The p - y parameters (initial stiffness and ultimate soil resistance) were varied considering 80 % and 120 % of the base p - y parameters. When varying these parameters, the soil properties followed the base model properties. Since conventional p - y parameters were developed from push-over field tests, there is not sufficient information on the effect of p - y parameters on the response of piles, particularly the effect of p - y parameters at large depths. For this reason, three different p - y spring regions, shown in Figure A.1, were considered in the study. All the variables and conditions used in the sensitivity study are summarized in Table A.2. The table also lists the figure where the results are presented.

In the following section, the sensitivity study results are summarized showing the influence of the variation in soil motion, p - y spring stiffness, and p - y spring ultimate resistance.

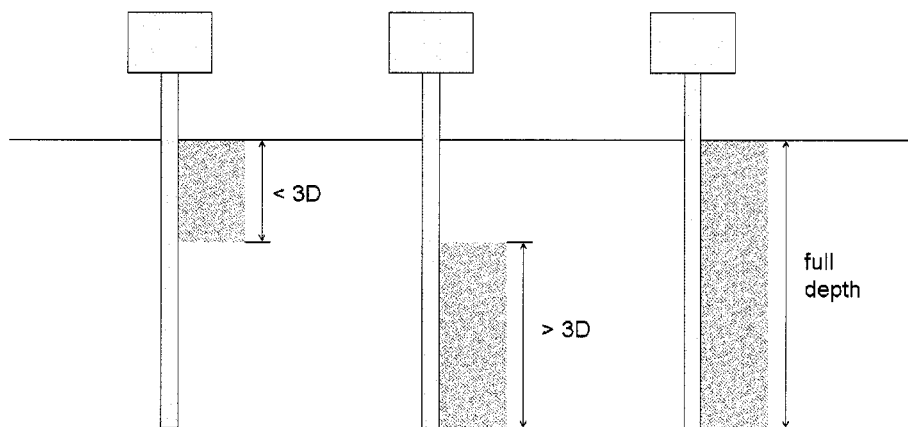


Figure A.1: p - y spring parameter regions for sensitivity study

Table A.2: Sensitivity study variables

Sensitivity Study Variables	Sensitivity Study Variable Values	related Figures
Soil stiffness and mass	$Gr = 91,000 \text{ kPa}, \rho = 1.3 \times 1.66$	Figure A.2
	$Gr = 91,000 \text{ kPa}, \rho = 1.5 \times 1.66$	Figure A.4
	$Gr = 130,000 \text{ kPa}, \rho = 2.0 \times 1.66$	Figure A.3
		Figure A.5
Depth of sensitivity of p - y spring	zone 1 (surface to $3D$)	Figure A.8
	zone 2 (greater than $3D$)	
	zone 3 (full depth)	
p - y parameter (y_{50})	80 %	Figure A.10
	100 % (base)	Figure A.12
	120 %	Figure A.11
		Figure A.13
p - y parameter (p_{ult})	80 %	Figure A.14
	100 % (base)	Figure A.16
	120 %	Figure A.15
		Figure A.17

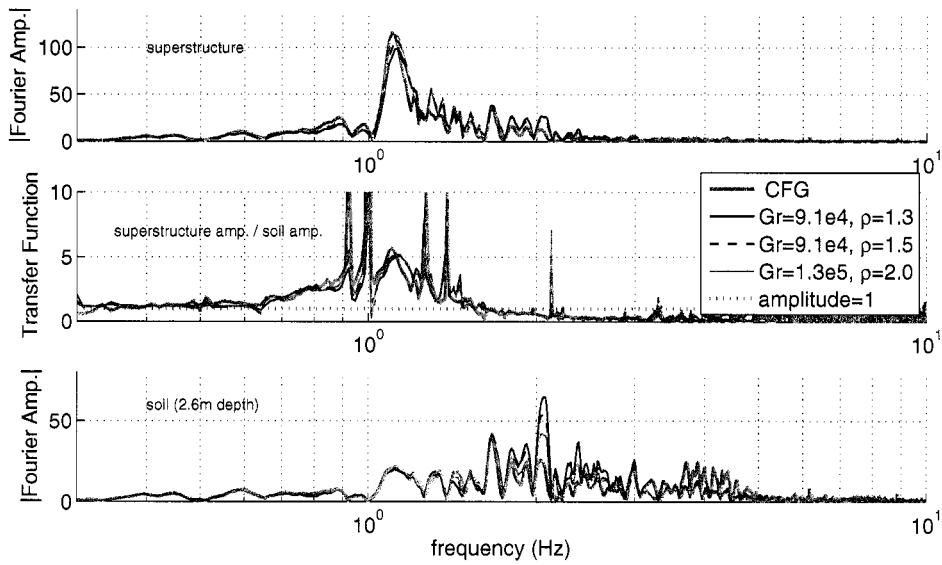
The results of each parametric variation are presented in figures where the Fourier spectrum corresponding to the soil response at 2.6 m depth is compared with the Fourier spectrum corresponding to the superstructure response. The ratio of the two Fourier amplitudes is the transfer function, from which the fundamental period of the soil-structure system can be identified. The transfer functions shown in the figures have noisy spikes which correspond to points where the soil frequency amplitudes are very small. The figures also show the response spectra for the soil and superstructure, pile force distribution, and mobilized soil resistance. The bending moment and shear force obtained at the time of maximum shear force. The same information is presented for a single pile.

A.0.5 Effect of Soil Motion Variation on Structure Response

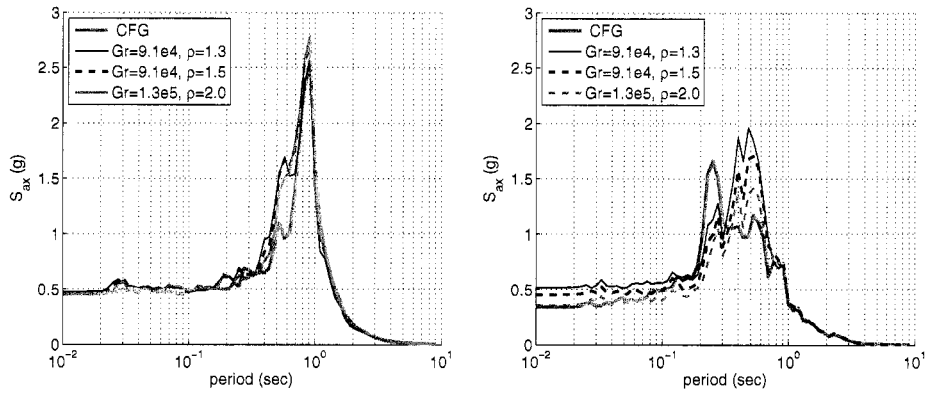
The use of the three soil properties (stiffness and mass) resulted in different soil motions with different peak accelerations. The difference in soil motion is clearly reflected in the soil Fourier spectra (especially at frequency $\cong 2.0$ Hz) and response spectra shown in Figures A.2 and A.3. However, the superstructure accelerations were insensitive to the soil motion change in both bent and single pile structures. This insensitivity of superstructure response can be explained evaluating the transfer function in Figure A.2a. The transfer function for frequencies greater than 1.5 Hz was less than one, which represents de-amplification. Therefore any effect observed at higher frequencies (> 1.5 Hz) did not influence the superstructure response significantly. This mechanism was more evident in a single pile as shown in Figure A.3a. Since the fundamental frequency of the soil-structure system (about 0.5 Hz in the transfer function shown in the figure) was far from the relevant soil frequencies, the superstructure response was insensitive to the change of soil motion. Figures A.2d and A.3d show that the maximum pile bending moment, shear force, and mobilized soil resistance were insensitive to soil parameter variation.

A.0.6 Natural Period of Soil-Structure System

In the previous section, the natural period of the soil-foundation system was identified using transfer functions. Figures A.2a and A.3a show that the OpenSees bent models

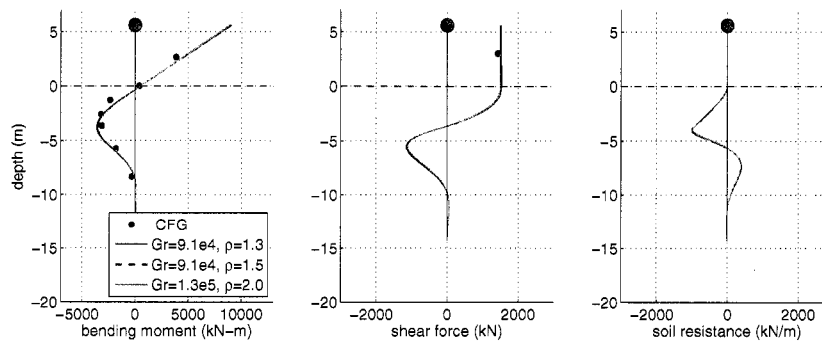


(a) transfer function between superstructure and soil (at 2.6m depth)



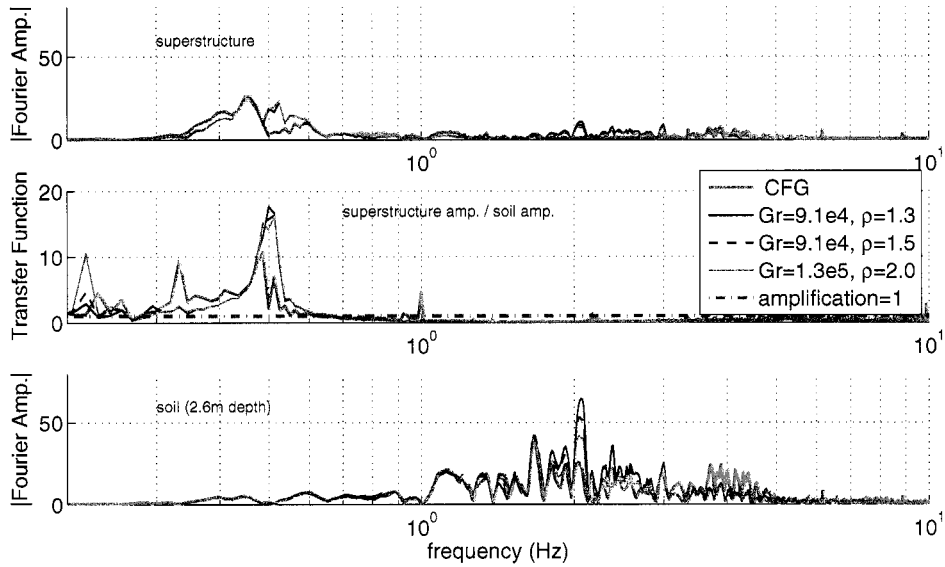
(b) superstructure response

(c) soil response (at 2.6m depth)

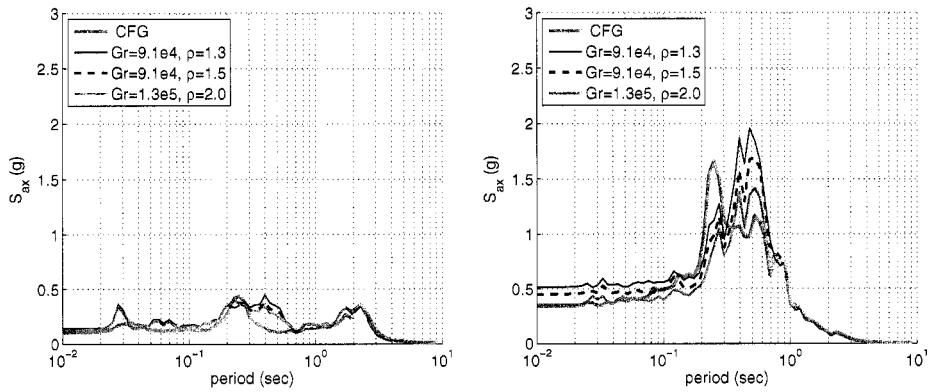


(d) pile force and soil resistance

Figure A.2: Effect of soil motion on bent response - Northridge motion, $a_{max} = 0.25g$

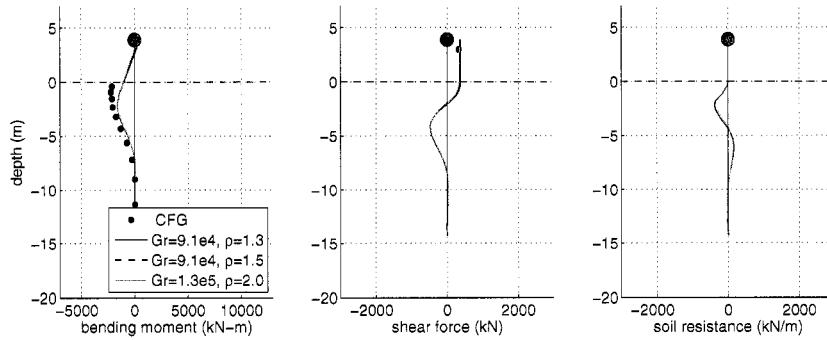


(a) transfer function between superstructure and soil (at 2.6m depth)



(b) superstructure response

(c) soil response (at 2.6m depth)



(d) pile force and soil resistance

Figure A.3: Effect of soil motion on single pile response - Northridge motion, $a_{max} = 0.25g$

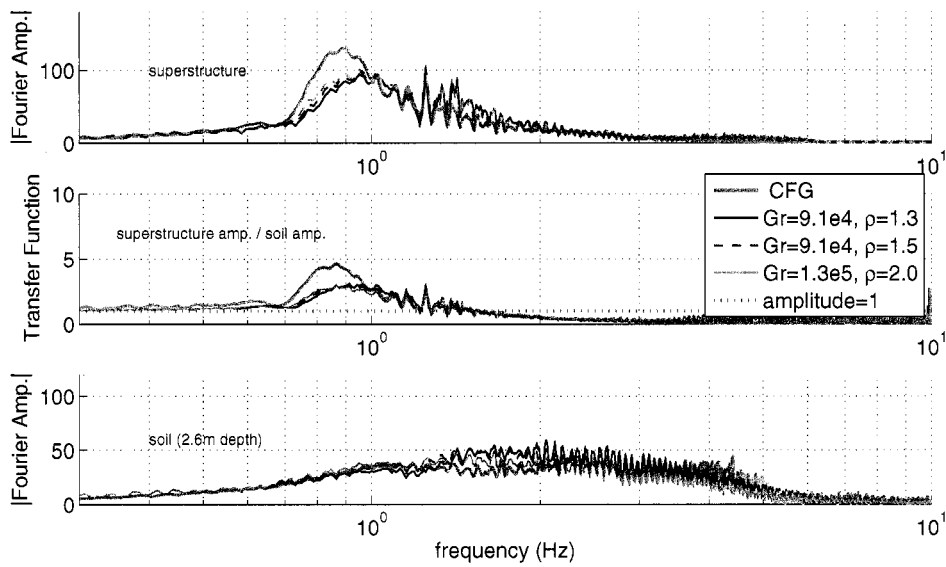
captured well the natural period of the soil-structure system for the Northridge ($a_{max} = 0.25g$) motion, while the natural period obtained from the single pile model was slightly underestimated. This discrepancy in the single pile model was reflected in the maximum bending moment difference between centrifuge results and OpenSees simulations as shown in Figure A.3d.

In addition, the natural period of the bent and single pile structures were investigated using a frequency sweeping motion, with larger peak acceleration ($a_{max} = 0.41g$). Figure A.4 clearly shows that the OpenSees bent model clearly underestimated the transfer function amplitude at 0.7 and 1.0 Hz, where the natural period is located. This led to smaller superstructure inertial and pile forces than those measured in centrifuge test. On the other hand, it is shown in Figure A.5 that, for this case, the transfer function in the single pile model was well captured especially at the natural period (about 0.25 second or 4 Hz), resulting in good estimation of maximum pile bending moments.

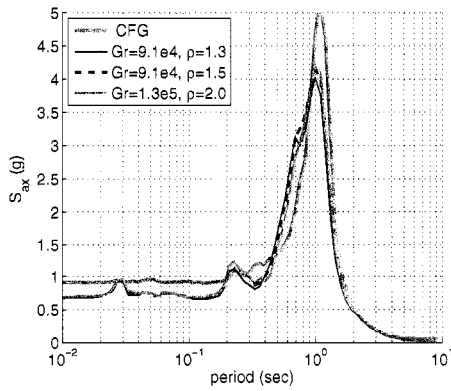
One interesting aspect was that the natural periods of the soil-structure system varied depending on motion characteristics and intensity. For the Northridge motion, the natural period of the bent and single pile were about 1.0 second and 2.5 second, respectively. However, when a frequency sweeping motion was used, the natural period became longer and close to 1.2 second and 3.2 second (about 15 % and 30% increase), respectively. The change in natural period was attributed to the system nonlinearity.

From these observations, it was found that the natural period of the soil-foundation system plays an important role on SPSI in bridges. Therefore, the natural periods of the bent and single pile structures were investigated in several ways. First, the natural periods of the bent and single pile structures were estimated using basic equations as shown in Figure A.6. In this calculations, the column was extended 3.0 m below the ground surface to approximate the soil interaction effect. From the calculation, the natural periods of the bent and single pile structures were about 0.8 and 1.6 second, respectively. These values were shorter than the natural periods (about 1.0 and 2.5 second) estimated from the transfer functions.

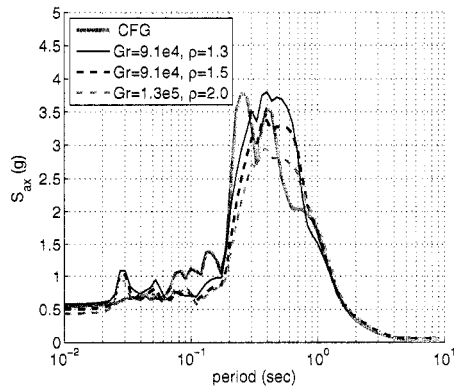
To investigate the natural period variation during shaking, eigenvalue analyses were performed in OpenSees at every time step for Bent-90 subjected to shaking in the longi-



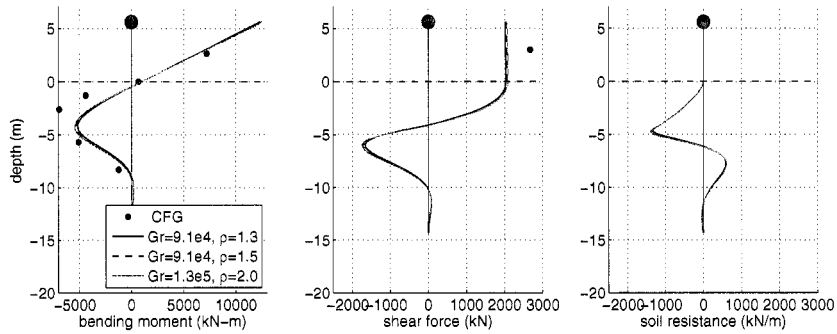
(a) transfer function between superstructure and soil (at 2.6m depth)



(b) superstructure response

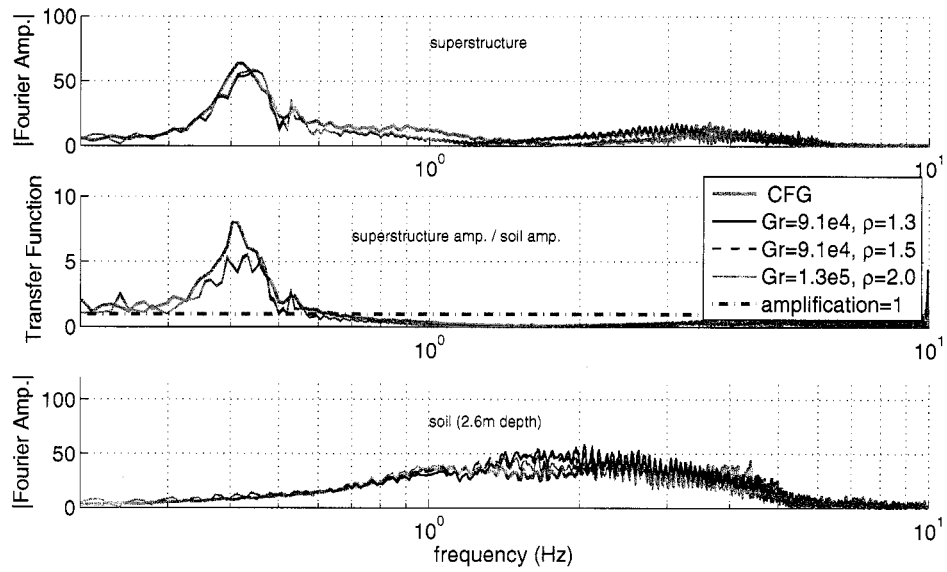


(c) soil response (at 2.6m depth)

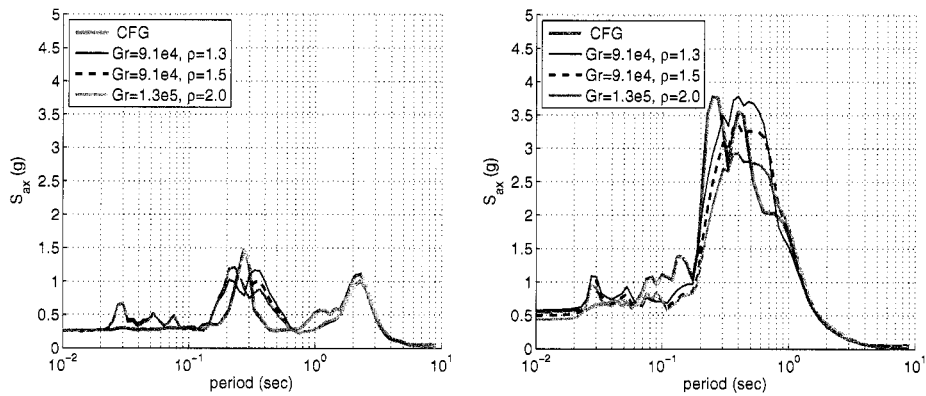


(d) pile force and soil resistance

Figure A.4: Effect of soil motion on bent response - Sweeping motion, PGA = 0.50g

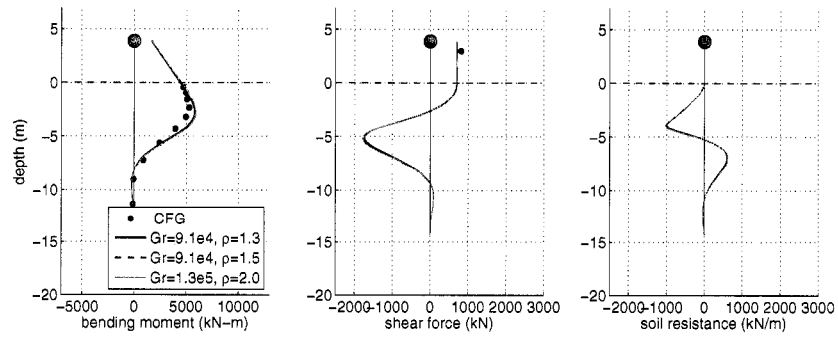


(a) transfer function between superstructure and soil (at 2.6m depth)



(b) superstructure response

(c) soil response (at 2.6m depth)



(d) pile force and soil resistance

Figure A.5: Effect of soil motion on single pile response - Sweeping motion, PGA = 0.50g

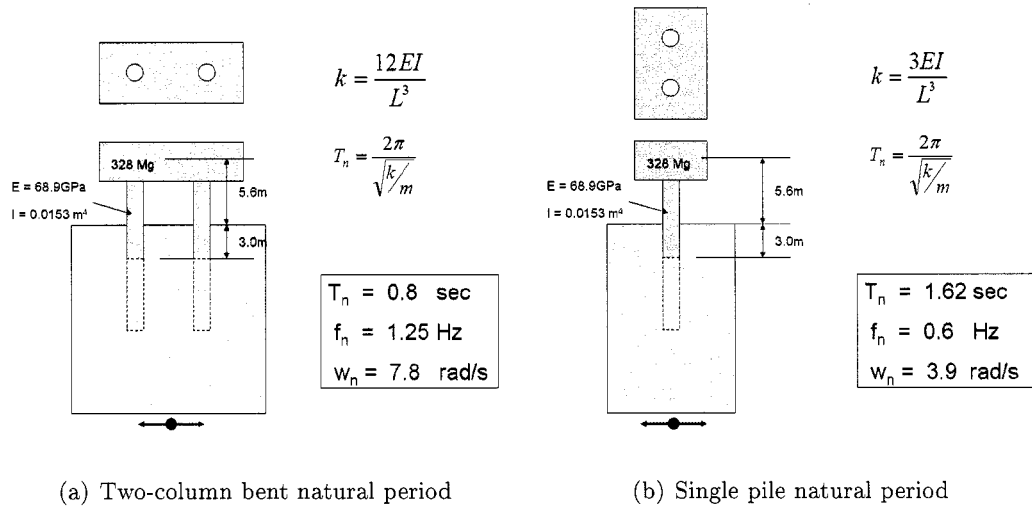
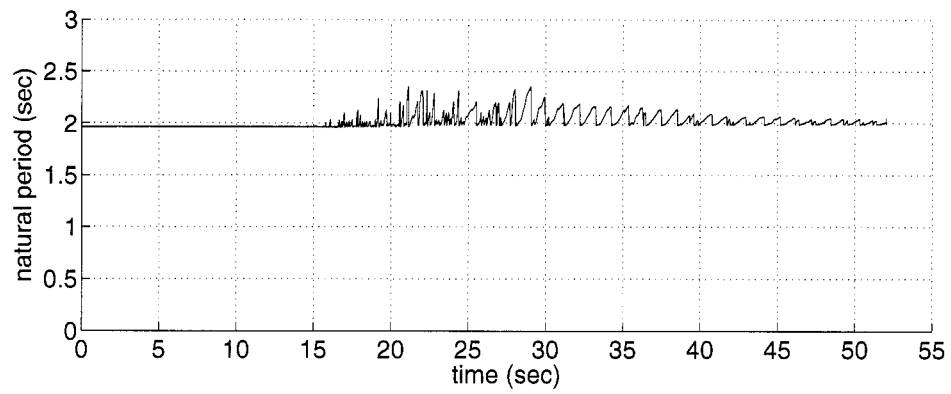


Figure A.6: Simple estimation of natural periods of bent and single pile structures

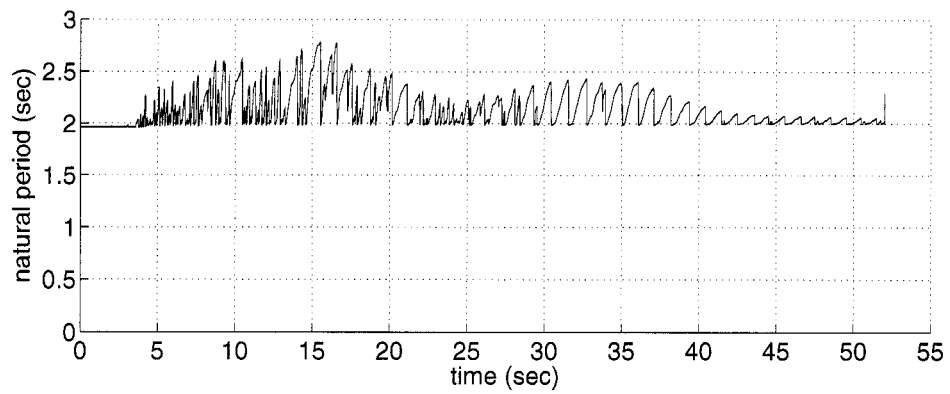
tudinal direction. The bent model consisted of the structure and interface springs without soil column. The eigenvalue analyses were performed for two different intensity motions to investigate the nonlinear SPSI effect on the fundamental period. Figure A.7 shows the eigenvalue analysis results. The initial natural period was about 2.0 second, but the natural period was increased up to 2.3 second (15% increase) during moderate shaking. This was attributed to the p - y spring stiffness change during shaking. For a stronger shaking, the natural period was increased up to 2.7 second (35% increase). This is similar to the natural period estimated from the transfer function.

A.0.7 Effect of p - y Parameter Change at Different Depths

The effect of p - y parameter variation at different depths was investigated. Values of y_{50} and p_{ult} in the three regions (zone 1, zone 2, and zone 3 in Figure A.1) were changed by $\pm 20\%$ with respect to the base p - y parameters while the p - y parameters at other depths were kept the same as those for the base model. The results (superstructure response and pile forces) due to p - y parameter change in zone 1 and zone 3 were similar indicating the variation of p - y parameter in zone 2 did not affect the structure response. Figure A.8 shows the superstructure accelerations were not affected by p - y parameter (e.g., p_{ult}) change at



(a) Northridge motion, $a_{max} = 0.25g$



(b) Northridge motion, $a_{max} = 0.74g$

Figure A.7: Natural period variation of single pile structure during shaking (eigenvalue analysis results)

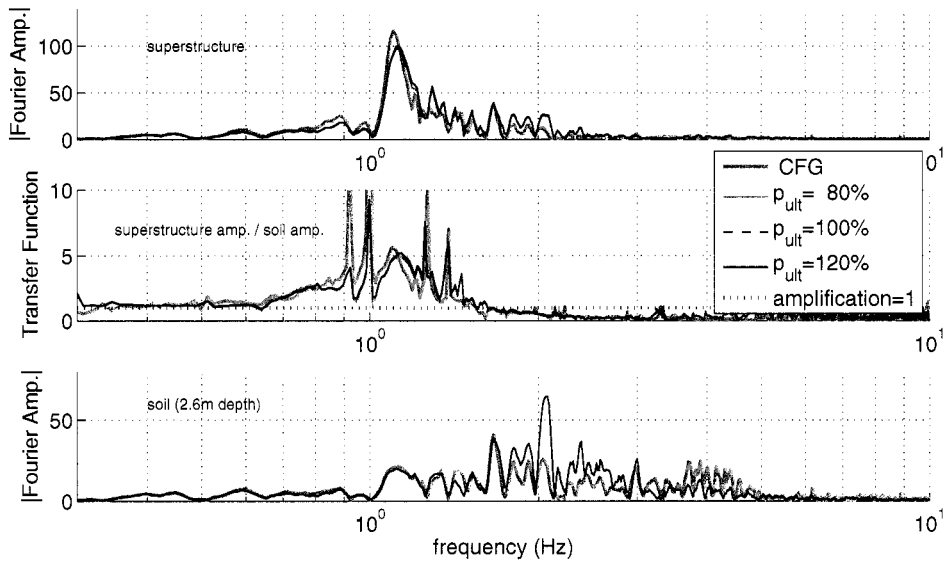


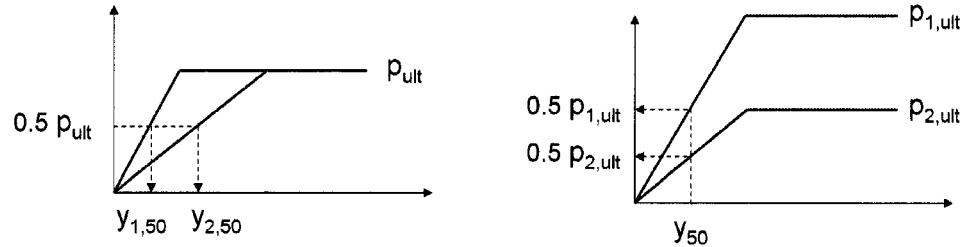
Figure A.8: Effect of p_{ult} change (p_{ult}) in greater-than-3D depth on bent superstructure response - Northridge motion, $a_{max} = 0.25g$

depths larger than 3D.

A.0.8 Effect of p - y Spring Stiffness (y_{50})

To evaluate the influence of y_{50} on the superstructure response, the value of y_{50} was increased and decreased by 20% of the base model's y_{50} . The results were clearly shown in Figure A.9b and A.9b. The change of y_{50} values did not affect the superstructure (peak) acceleration for moderate and strong motions.

For moderate and strong shaking, the maximum bending moment and shear force were slightly affected by the change of y_{50} , especially at depths greater than 3D. Figures A.10d and A.11d, and Figures A.12d and A.13d show that the soil resistance change due to y_{50} change occurred at larger depths (e.g., greater than 3D). This is because the p - y springs near the surface reached ultimate soil resistance even with different p - y spring stiffness resulting in similar mobilized soil resistance. The difference in soil resistance distribution at large depth did not affect the structural response. The same pattern was observed in both bent and single pile structures.



(a) Stiffness change due to y_{50} values with a constant p_{ult} (b) Stiffness change due to p_{ult} values with a constant y_{50}

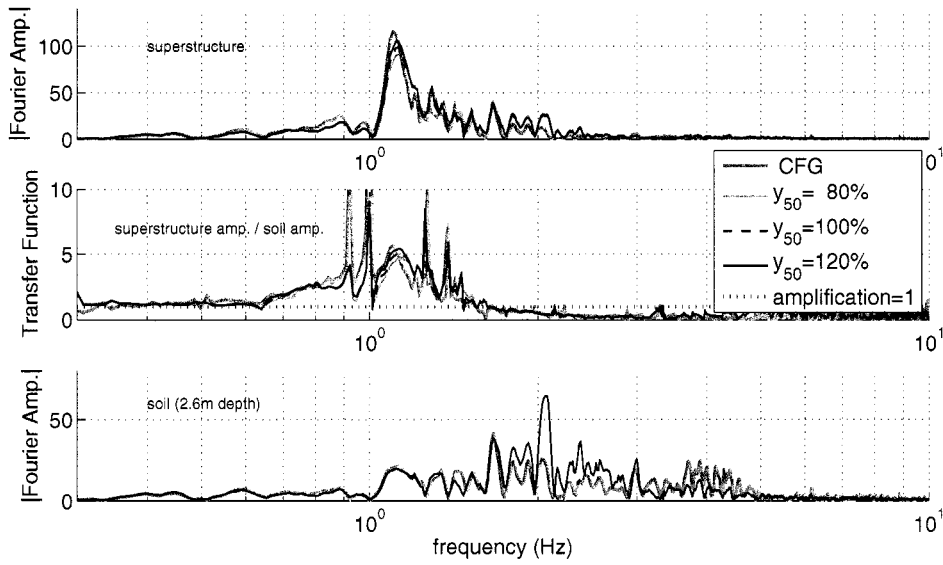
Figure A.9: Schematic drawing of Change of initial stiffness in p - y curve due to change of y_{50} and p_{ult}

A.0.9 Effect of p - y Spring Ultimate Resistance (p_{ult})

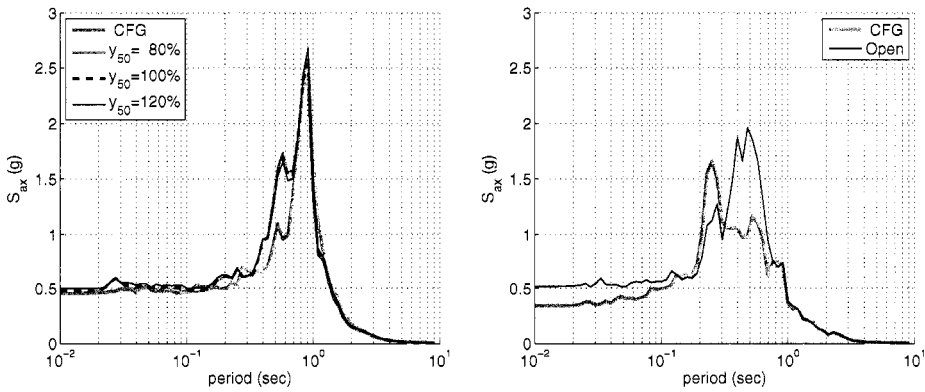
To evaluate the influence of p_{ult} on the superstructure response, the value of p_{ult} was increased and decreased by 20% of the base model's p_{ult} value, while the other parameters were kept constant and equal to those for the base model. Using a constant value of y_{50} , the change of p_{ult} value influenced not only the ultimate resistance but also the initial stiffness. This is illustrated in Figure A.9b. Since y_{50} did not affect the superstructure responses and pile force, in this parametric study, y_{50} value was not adjusted when p_{ult} was changed. The results for this study are shown in Figure A.14 and A.15 for the bent and single pile. The results for strong shaking are shown in Figures A.16 and A.17. From the results, it was concluded that, for moderate and strong shaking, the superstructure peak acceleration was not affected by p_{ult} change for this soil condition. However, pile force and mobilized soil resistance distribution below the ground surface were clearly affected, especially the maximum bending moment location (e.g. zero shear force depth). The maximum bending moment depth became shallower with increasing p_{ult} values.

A.0.10 Ratio of Near-Surface Soil Resistance to Maximum Inertial Force

From the p_{ult} parameter sensitivity study it was observed that the ultimate soil resistance, especially near the surface (from surface to 3D or 4D depth), affected the pile force

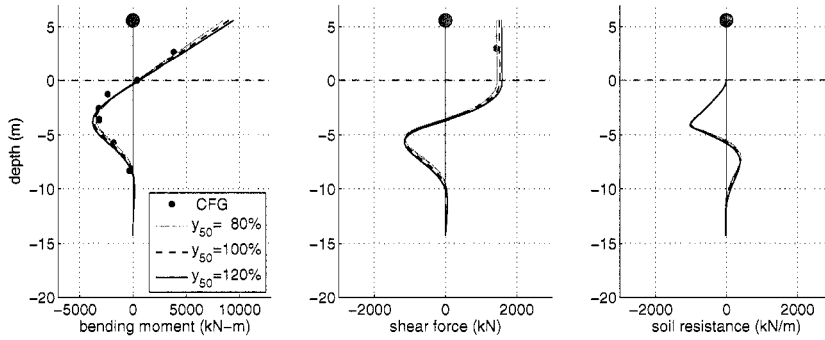


(a) transfer function between soil (at 2.6m depth) and superstructure



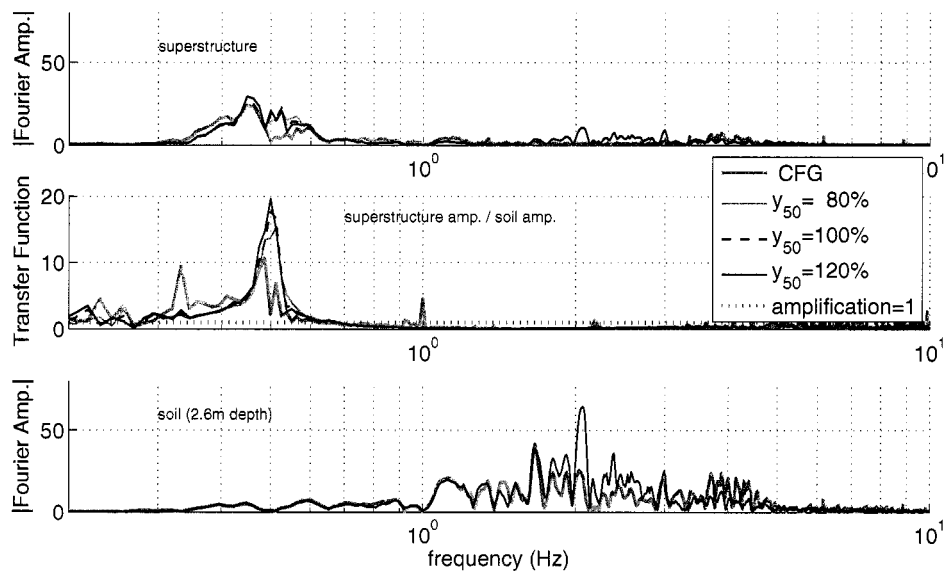
(b) superstructure response

(c) soil response (at 2.6m depth)

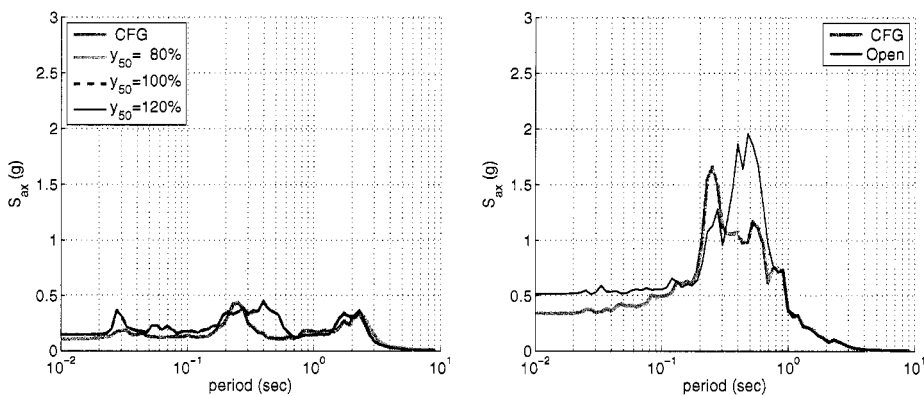


(d) pile force and soil resistance

Figure A.10: Effect of p - y spring stiffness (y_{50}) - bent; Northridge motion ($a_{max} = 0.25g$)

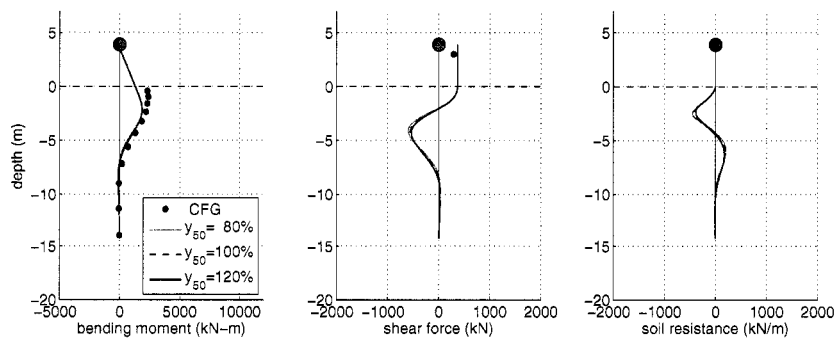


(a) transfer function between soil (at 2.6m depth) and superstructure



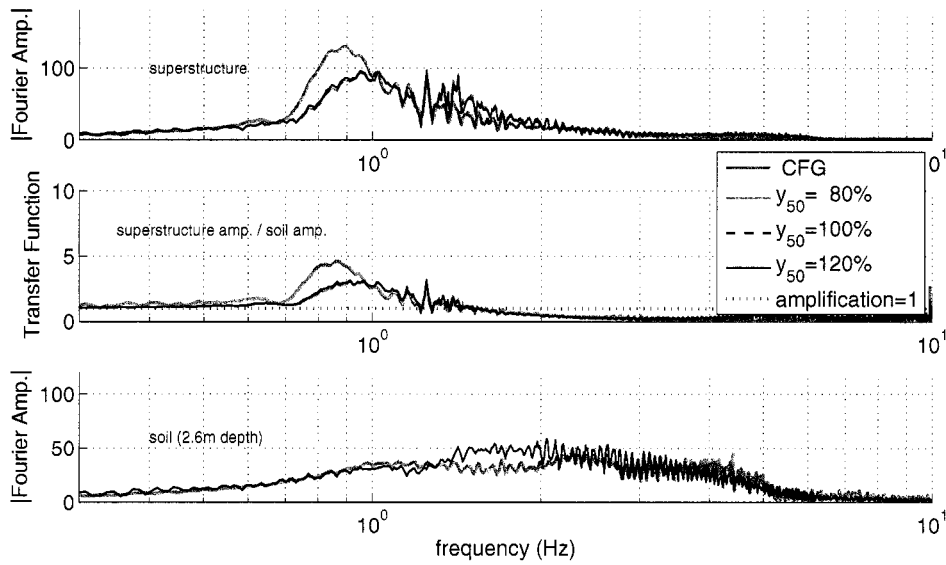
(b) superstructure response

(c) soil response (at 2.6m depth)

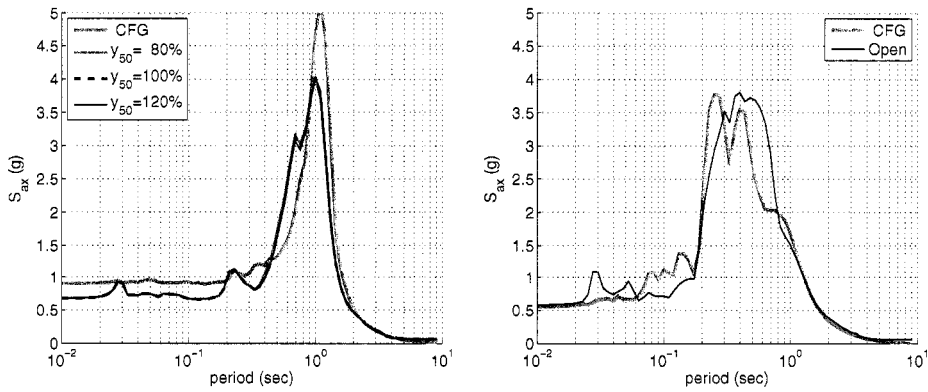


(d) pile force and soil resistance

Figure A.11: Effect of p - y spring stiffness (y_{50}) - single pile; Northridge motion ($a_{max} = 0.25g$)

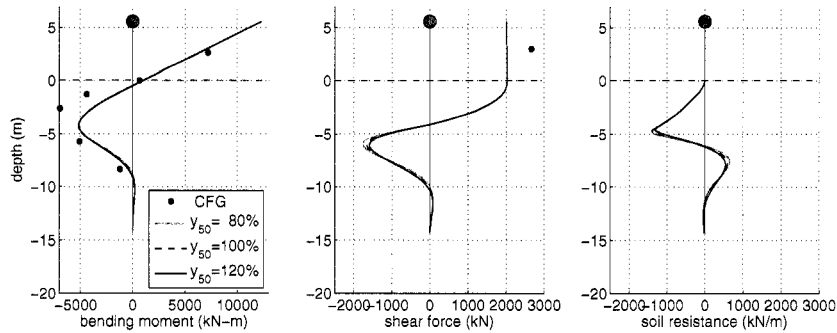


(a) transfer function between soil (at 2.6m depth) and superstructure



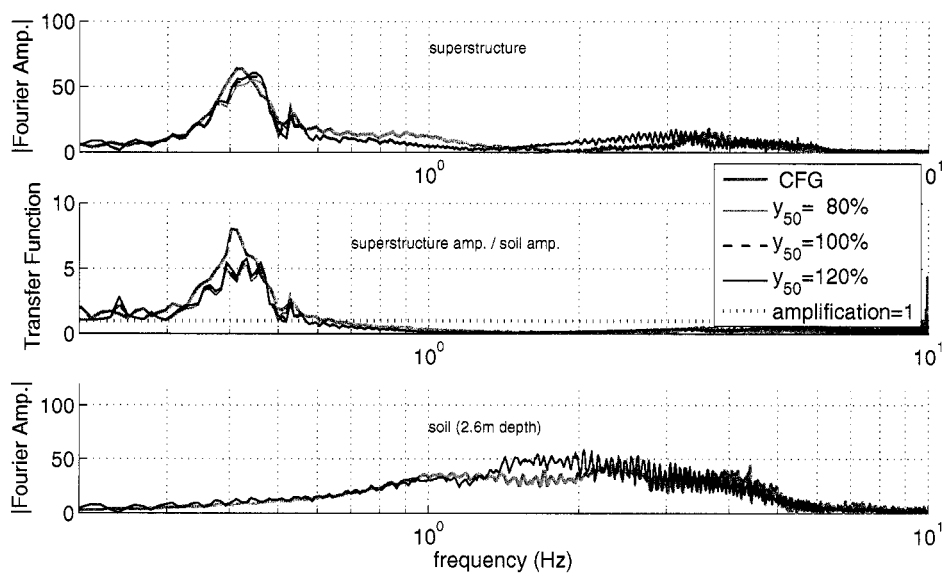
(b) superstructure response

(c) soil response (at 2.6m depth)

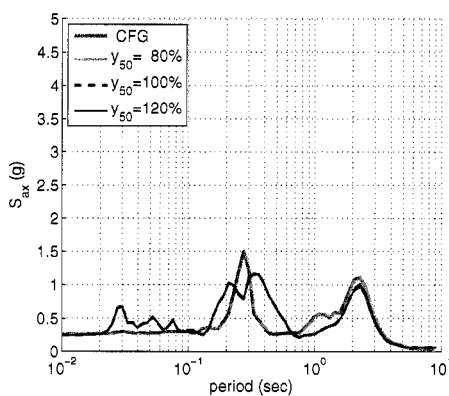


(d) pile force and soil resistance

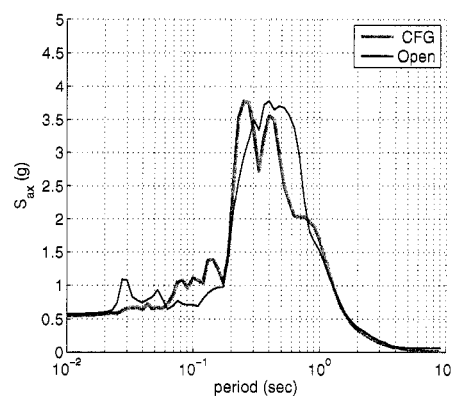
Figure A.12: Effect of p-y spring stiffness (y_{50}) - bent; Sweeping motion (PGA = 0.50g)



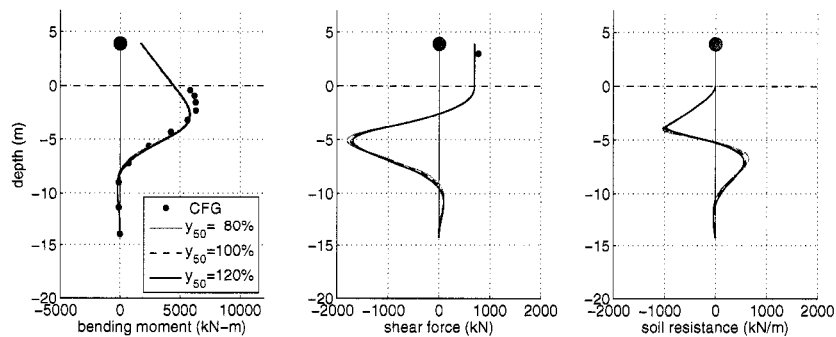
(a) transfer function between soil (at 2.6m depth) and superstructure



(b) superstructure response

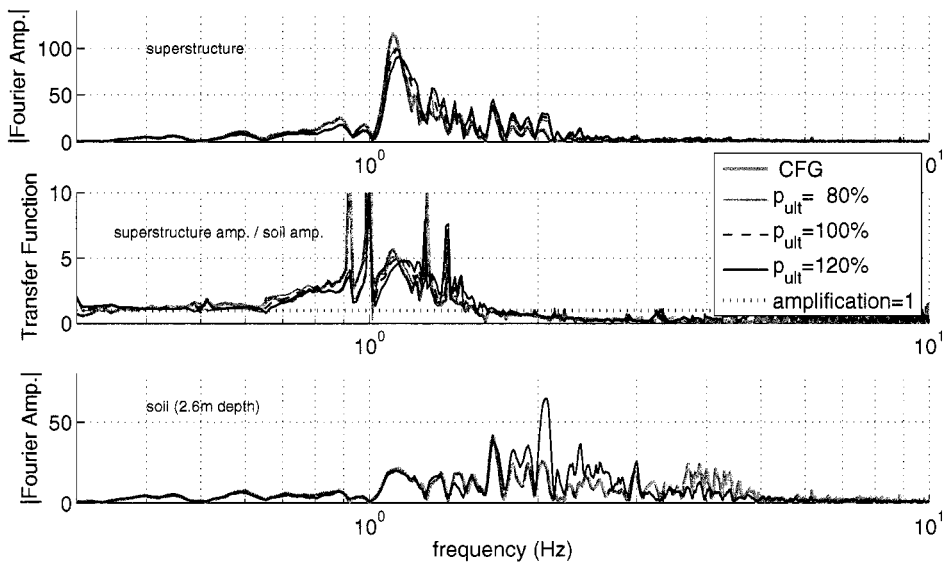


(c) soil response (at 2.6m depth)

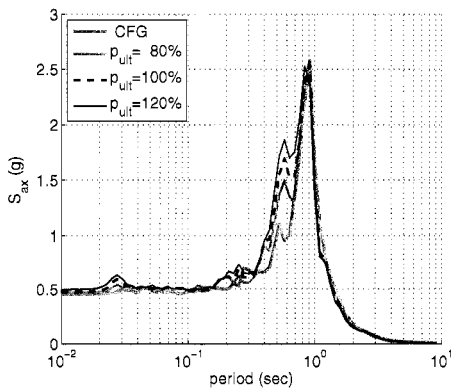


(d) pile force and soil resistance

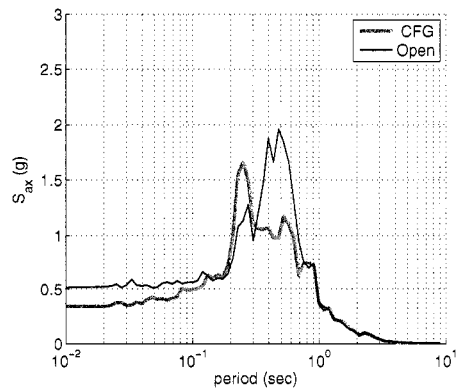
Figure A.13: Effect of p-y spring stiffness (y_{50}) - single pile; Sweeping motion (PGA = 0.50g)



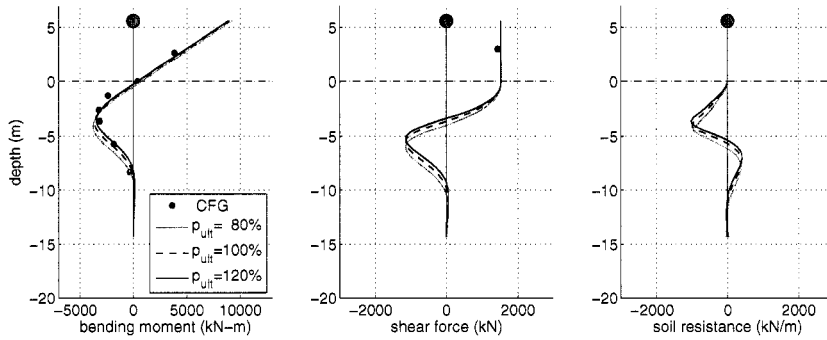
(a) transfer function between superstructure and soil (at 2.6m depth)



(b) superstructure response

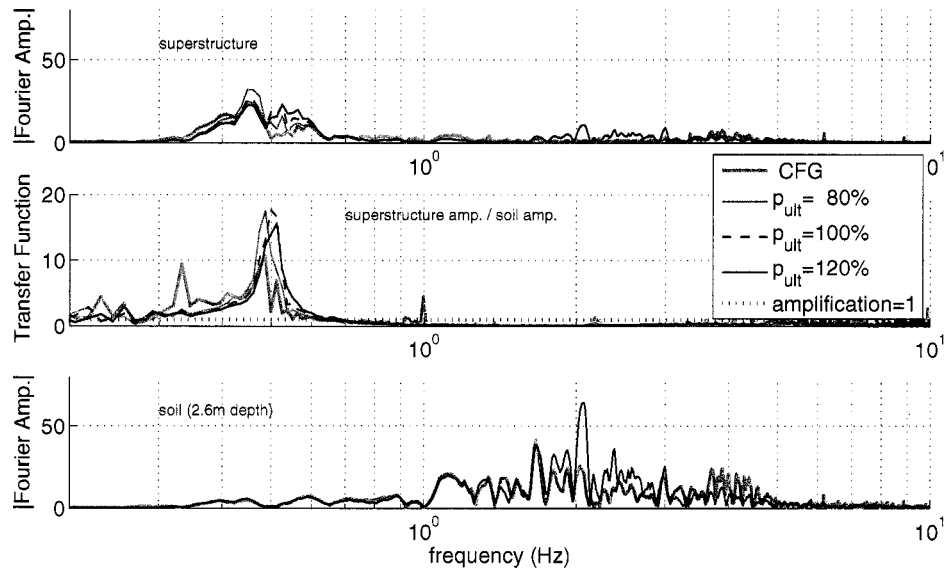


(c) soil response (at 2.6m depth)

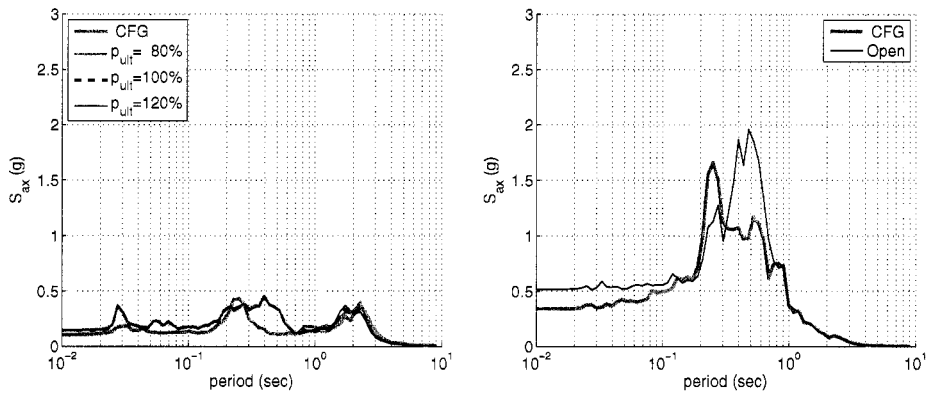


(d) pile force and soil resistance

Figure A.14: Effect of p - y spring ultimate soil resistance (p_{ult}) - bent; Northridge motion ($a_{max} = 0.25g$)

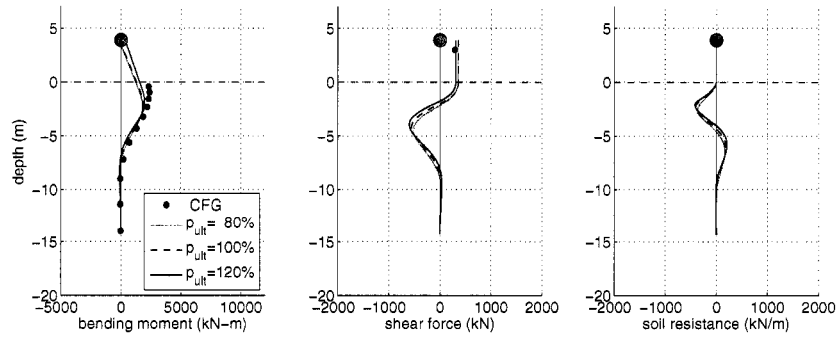


(a) transfer function between superstructure and soil (at 2.6m depth)



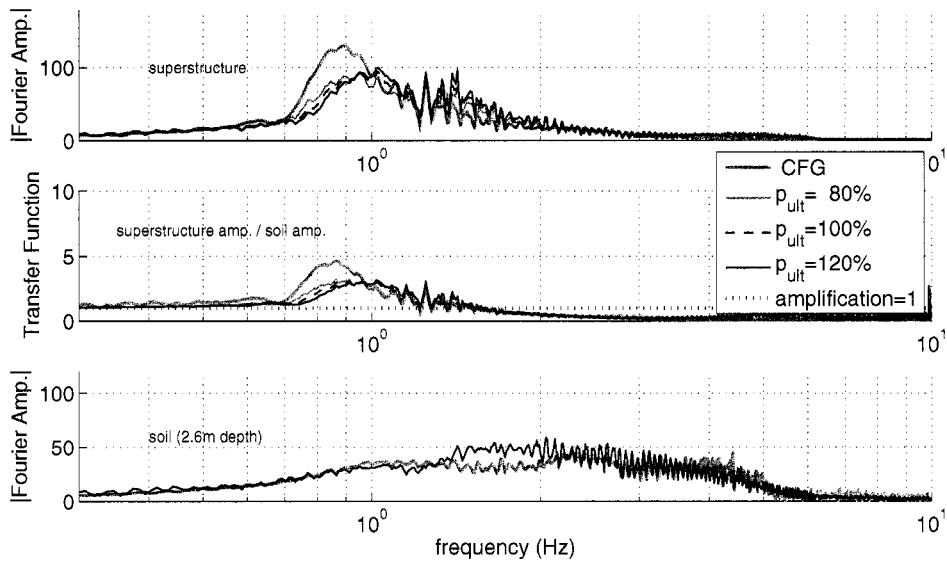
(b) superstructure response

(c) soil response (at 2.6m depth)

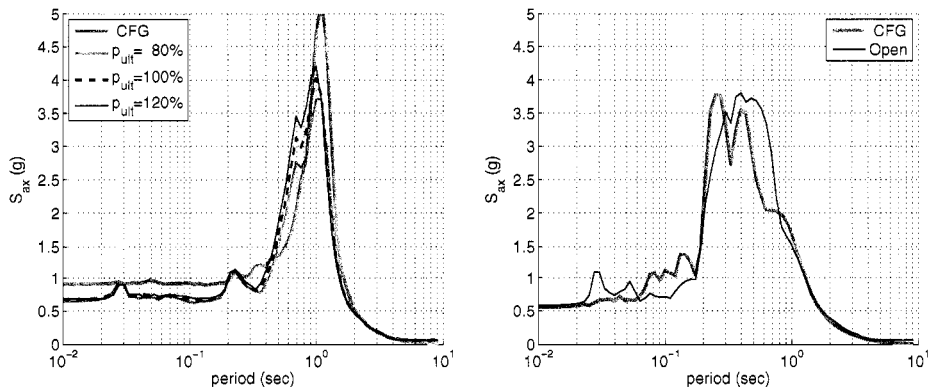


(d) pile force and soil resistance

Figure A.15: Effect of p - y spring ultimate soil resistance (p_{ult}) - single pile; Northridge motion ($a_{max} = 0.25g$)

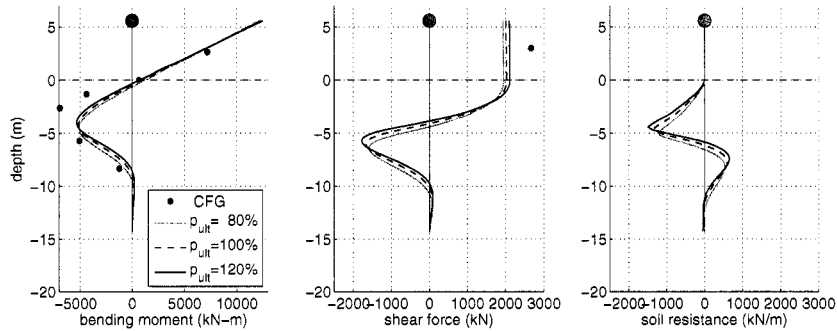


(a) transfer function between soil (at 2.6m depth) and superstructure



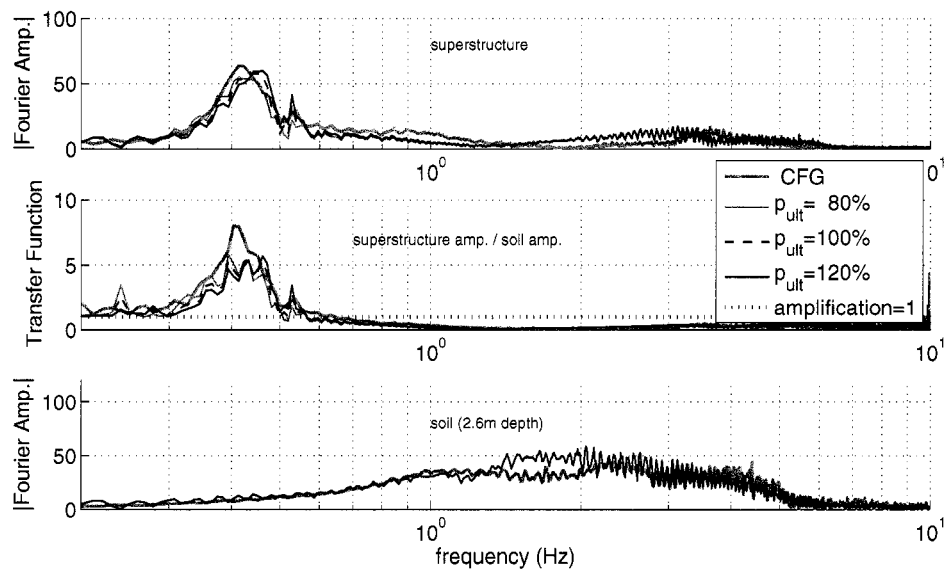
(b) superstructure response

(c) soil response (at 2.6m depth)

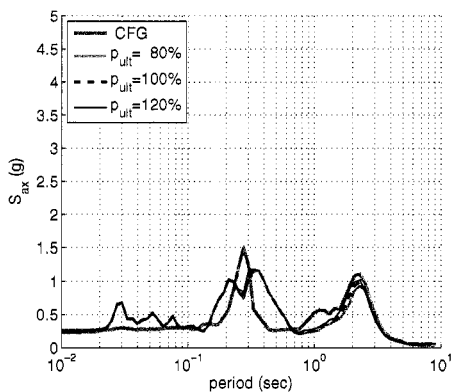


(d) pile force and soil resistance

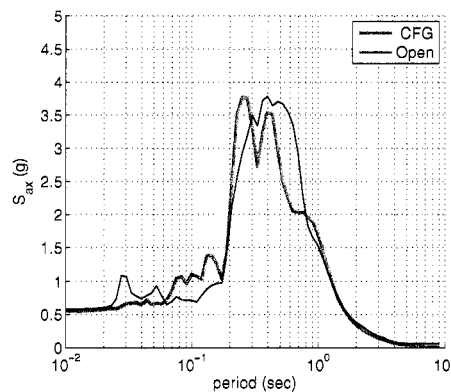
Figure A.16: Effect of p-y spring ultimate soil resistance (pult) - bent; Sweeping motion (PGA = 0.50g)



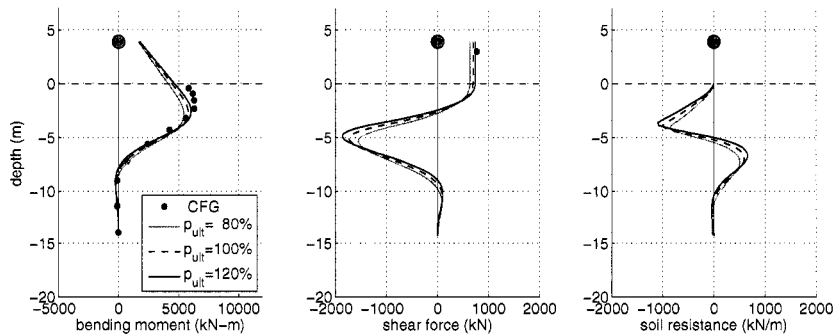
(a) transfer function between soil (at 2.6m depth) and superstructure



(b) superstructure response



(c) soil response (at 2.6m depth)



(d) pile force and soil resistance

Figure A.17: Effect of p-y spring ultimate soil resistance (p_{ult}) - single pile; Sweeping motion (PGA = 0.50g)

and soil resistance distribution. It was also observed that the depth of maximum bending moment was related to the mobilized soil resistance near the ground surface. In order to investigate the variation of mobilized soil resistance near the surface due to the p - y parameter change, the ratio of maximum inertial force to the p - y spring resultant force from the surface to 3D was calculated at the time of maximum bending moment/shear force. The ratio is defined as

$$R_{rs} = \frac{\text{maximum superstructure inertial force}}{\sum_{z=0}^{\text{depth}} p(z)} \quad (\text{A.1})$$

where $p(z)$ is the soil pressure at depth z . The influence of y_{50} and p_{ult} variation on $R_{rs} = \sum_{z=0}^{3D} p(z)$ is shown in Table A.3. The R_{rs} value shows about 4 % change due to the 20 % change in y_{50} change, and about 17 % change due to the 20 % of p_{ult} change, respectively. By changing the friction angle (2°) in the p - y parameter calculation, R_{rs} shows a 16 % increase and decrease. From these results, it is concluded that the mobilized soil resistance near the ground surface at the maximum inertial force time is affected more by p_{ult} change than by y_{50} change and that the pile force and soil pressure distribution (i.e., the maximum bending moment location) is more affected by p_{ult} change.

Table A.3: Ratio of Near-Surface Soil Resistance to Maximum Inertial Force, R_{rs}

Parameter change	y_{50}	p_{ult}	ϕ
80 %	$R_{rs} = 1.14$	$R_{rs} = 0.86$	$R_{rs} = 0.92$
100 % (base)	$R_{rs} = 1.10$	$R_{rs} = 1.10$	$R_{rs} = 1.10$
120 %	$R_{rs} = 1.06$	$R_{rs} = 1.29$	$R_{rs} = 1.28$

VITA

HyungSuk Shin was born in South Korea. He completed his Bachelor of Science of Civil Engineering at Chungnam National University in 1998, Korea. HyungSuk started graduate studies in the same school and continued his graduate program in South Dakota State University through University Exchange Program. He finished his Masters of Science at South Dakota State University in 2000. HyungSuk earned a Doctor of Philosophy degree in June 2007.